Estimation of the composition of cosmic rays using the radio signal

Florian Sylvain Gate

▶ **To cite this version:**

Florian Sylvain Gate. Estimation of the composition of cosmic rays using the radio signal. High Energy Physics - Theory [hep-th]. Ecole des Mines de Nantes, 2016. English. NNT : 2016EMNA0295 . tel-01427261

HAL Id: tel-01427261
https://theses.hal.science/tel-01427261

Submitted on 5 Jan 2017

HAL is a multi-disciplinary open access archive for the deposit and dissemination of scientific research documents, whether they are published or not. The documents may come from teaching and research institutions in France or abroad, or from public or private research centers.

L'archive ouverte pluridisciplinaire **HAL**, est destinée au dépôt et à la diffusion de documents scientifiques de niveau recherche, publiés ou non, émanant des établissements d'enseignement et de recherche français ou étrangers, des laboratoires publics ou privés.

UNIVERSITE BRETAGNE LOIRE

MINES Nantes

Thèse de Doctorat

Florian GATÉ

Mémoire présenté en vue de l'obtention du
grade de Docteur de l'Ecole des Mines de Nantes
sous le sceau de l'Université Bretagne Loire

École doctorale : *3MPL*

Discipline : Constituants élémentaires et physique théorique
Spécialité : *Cosmologie et astroparticules*
Unité de recherche : *Laboratoire Subatech UMR6457*

Soutenue le *26/10/2016*
Thèse N° : *2016EMNA0295*

Estimation of the composition of cosmic rays using the radio signal

JURY

Rapporteurs : **M. Jacob LAMBLIN**, MCF Université Grenoble Alpes, Laboratoire de Physique Subatomique et de Cosmologie de Grenoble.
M. Gilles MAURIN, MCF Université Savoie Mont-Blanc, Laboratoire d'Annecy-le-Vieux de Physique des Particules.

Examinateurs : **M. Pol-Bernard GOSSIAUX,** Professeur Ecole des Mines de Nantes, Laboratoire Subatech de Nantes.
Mme Marianne LEMOINE-GOUMARD, Chargée de Recherche CNRS, Centre Etudes Nucléaires de Bordeaux Gradignan.
Mme Isabelle LHENRY-YVON, Directrice de Recherche CNRS, Institut de Physique Nucléaire d'Orsay.
M. Vincent MARIN, Docteur en Physique, Incubateur de l'Ecole des Mines de Nantes.
M. Ginès MARTINEZ, Directeur de Recherche CNRS, Laboratoire Subatech de Nantes.

Directeur de Thèse : **M. Benoît REVENU**, Directeur de Recherche CNRS, Laboratoire Subatech de Nantes.

Acknowledgments

Je remercie Bernd Grambow, directeur du laboratoire Subatech, de m'avoir permis de réaliser cette thèse au sein de ce laboratoire. Je tiens également à remercier l'ensemble des personnes qui ont acceptés de faire partie de mon jury de thèse. Merci à Isabelle Lhenry-Yvon d'avoir présidé ce jury, merci à Marianne Lemoine-Goumard, Pol-Bernard Gossiaux et Ginès Martinez. Enfin, je remercie Gilles Maurin et Jacob Lamblin d'avoir chacun endossé le rôle de rapporteur.

J'ai découvert le groupe Astro de Subatech lors de mon stage de M2. Le courant est très vite passé avec l'ensemble de l'équipe et je tiens à remercier chacun d'entre eux pour leur disponibilité, leur franchise mais aussi pour leur amitié.

Je tiens à remercier tout particulièrement mon directeur de thèse Benoît Revenu. Travailler et apprendre à tes cotés au cours de ces trois années fut un réel plaisir. Merci pour tes conseils, ta patience et ton enthousiasme. Nos échanges quasi quotidiens m'ont apporté énormément. Je te remercie également pour la grande confiance que tu m'as accordée et pour la liberté dont j'ai pu profiter pour réaliser ces travaux.

Je veux remercier Vincent Marin qui m'a encadré depuis mon stage de M2 jusqu'à la première moitié de ma thèse. Merci pour cet enthousiasme qui te caractérise et qui est très communicatif. J'ai appris énormément à tes cotés. Nos échanges ont continué bien au-delà du cadre de la thèse même après ton départ du groupe. Les rendez-vous café du matin sont vite devenus indispensable, surtout en fin de thèse. Je te souhaite toute la réussite dans ta nouvelle aventure, tu le mérites.

Je remercie Richard Dallier, toujours disponible pour prêter une oreille attentive et formidable compagnon de voyage. Je garderai toujours un souvenir ému de nos assados en Argentine et de la collocation en péniche aux Pays-Bas.

Enfin je veux remercier Lilian Martin. Merci pour ta franchise et tes conseils lors de nos discussions ainsi que ton aide précieuse pour l'analyse des données CODALEMA.

Merci au groupe Astro, ça sera très compliqué de vous rendre tout ce que vous m'avez donné durant ces trois années.

Merci à Jean-Luc Beney, Didier Charrier et Fréderic Lefèvre pour leur enthousiasme. Merci Fréderic de m'avoir donné l'opportunité de participer au Café des Sciences, ce fut une super expérience.

Un grand Merci à Pol-Bernard Gossiaux d'avoir accepté de faire partie de mon jury de thèse et de m'avoir permis d'enseigner à l'Ecole des Mines de Nantes, qui a été une expérience très enrichissante.

Je voudrais également remercier Thierry Gousset, que j'ai eu la chance d'avoir comme enseignant de la première année de licence jusqu'à la dernière année de master.

Ses conseils m'ont été d'une grande aide lors de mes choix au cours du M2. Merci à Julien Masbou pour son aide et ses précieux conseils pour ma recherche de post doc. Merci à Rémi Maurice pour son aide sur la polarisabilité des molécules

I would like to address special thanks to the Auger Collaboration, in particular to Tim Huege, Julian Rautenberg, Sebastian Mathys, Qader Dorosti and Christian Glaser for the numerous discussions and advice related to AERA. Thanks for everything! I hope to see you during the next ICRCs.

Je remercie l'ensemble des personnes des services administratif et informatique de Subatech qui ont contribué à résoudre de nombreux problèmes et à me faciliter grandement la vie. Merci également à Delphine Turlier et Michelle Dauvé pour leur aide et leur disponibilité.

Je voudrais remercier les personnes avec lesquelles j'ai partagé le bureau H125, les nouveaux comme les anciens. Merci à Jennifer, Guillaume, Zak, Fanny, Grégoire, Loïc, Antony. Je remercie également l'ensemble des thésards et post docs de Subatech pour leur bonne humeur et pour tous les bons moments partagés. Merci à Alexandre S., Thiago, Thorben, Loïck, Kévin, Daniel, Benjamin, Audrey, Gabriel, Florian et Flavia. Enfin merci à ceux qui avec le temps sont devenu mes amis et qui ont donné une saveur particulière à ces trois années. Merci à vous, Javier, Lucia, Lucile, Guillaume, José, Martin, Alexandre P., Christophe et Roland.

Merci à l'équipe de tennis ASPIR, Alexandre, Benoît, Vincent, Christophe, Massoud et Catherine avec qui nous avons disputé des rencontres d'anthologie.

Merci à Nicolas Thiolière, Fréderic Yermia et Baptiste 'la gagne' Léniau d'avoir égayé avec autant de talent, la vie du bâtiment H. Merci à Arnaud Guertin pour ton amitié et ta bonne humeur. Je garderai un souvenir impérissable de cette soirée à Chicago.

Je tiens à remercier mes amis pour leur soutien et pour les très nécessaires phases de décompression. Merci, Pierre-Emmanuel, Brieuc, Edwige, Ségolène, Amaury, Thierry, Jean-Sébastien, Gauthier, Maxime, Zak, Nicolas.

Un grand merci à ma famille qui, depuis toujours, m'a apporté son soutien inconditionnel. Rien de tout cela n'aurait été possible sans vous. Je remercie aussi ma belle-famille, également venue en nombre le jour de la soutenance. Cela m'a fait très chaud au cœur.

Enfin merci à toi, Charlotte, d'avoir donné un sens à tout cela.

Contents

List of Figures

List of Tables

Introduction

The Earth is constantly bombarded by a flux of particles which extraterrestrial origin has been suggested by Domenico Pacini in 1911 and confirmed by Victor Hess in 1912. Many major progress in the fields of particle physics and astrophysics have been achieved thanks to the study of this radiation. The study of cosmic rays is a domain of the "astroparticles". Nowadays, the term "cosmic-ray" is used to qualify all charged particles detected on Earth, coming from extraterrestrial sources.

The comic rays energy spectrum extends on more than 32 orders of magnitude for the flux and 12 for the energy. It is described by a power law with a spectral index varying from 2.8 to 2.3. Thus, the number of cosmic-rays decreases very quickly as a function of the energy. The statistics is divided by a factor 100 for each decade in energy. Up to 10^{17} eV, the sources, the acceleration mechanisms and the mass composition of the cosmic-rays are well known. In this energy range, the number of events is high enough to allow a direct detection (satellites, balloons ...). Above 10^{17} eV, indirect detection techniques are used and allow the statistical determination of several parameters, as the mass of the primary cosmic rays, with a large number of events.

The indirect detection consists in the observation of the development of the cascade of secondary particles created when a primary cosmic ray interacts with the constituents of the atmosphere. After entering the atmosphere, the cosmic ray interacts after crossing an atmospheric depth called X_1: it is the first interaction point. The number of secondary particles increases as long as the energy available in the shower front is sufficient, until it reaches the depth of the shower maximum: $X_{\max}$, at which the number of particles is maximum. Beyond this point, the energy is too low to create new particles and their number decreases. Still above 10^{17} eV, the statistics is close to one particle per km^2 per day, and reaches one particle per km^2 per century at 10^{20} eV. Large detection areas are thus mandatory for the study of ultra-high energy cosmic rays.

It is the case of the Pierre Auger Observatory, in Argentina. This observatory is composed of 1660 Cerenkov tanks covering a surface of 3000 km^2, 27 fluorescence telescopes spread across four sites, 153 radio stations and the construction of 61 muon counters has begun. The Cerenkov tanks sample the secondary particles distribution reaching the ground. The muons counters are buried at 2.5 meters under the ground, allows the measurement of the muonic component of the shower, as the electrons and positrons are stopped before reaching this depth. When the air shower crosses the atmosphere, the secondary particles that composed it, excite the nitrogen molecules. These molecules go back to their ground energy state by emitting fluorescence light that is received isotropically by the telescopes. The intensity of the light is proportional to the number of particles composing the air shower at the time of the emission. This method

allows a calorimetric measurement of the air shower development in the atmosphere and especially the direct measurement of the $X_{\max}$ depth. This latter quantity is highly correlated to the mass of the primary cosmic ray as it depends, at the first order, on the interaction cross section of the primary with the atmosphere.

At the Pierre Auger Observatory, the mass of the cosmic rays with an energy higher than 10^{17} eV is statistically determined. The mean measured $X_{\max}$ by energy range are compared to the results given by the ultra-high energy hadronic interaction models. This method is effective within the condition that the number of detected air showers is high, which is the case up to 10^{19} eV. For higher energies, the statistics is very low. A cut-off in the energy spectrum is observed at 6×10^{19} eV with a confidence level higher than 20 σ. The GZK limit predicts this cut-off and attributes it to the interaction of the cosmic rays with the photons of the cosmic microwave background for which the energy threshold is estimated to be at 5×10^{19} eV. Moreover, the duty cycle of the fluorescence telescopes is around 14% as their sensitivity allow measurements during night without moon and without bad weather. Then, the number of detected events is too low above 4×10^{19} eV to precisely determine the mass of cosmic rays with this technique.

Nowadays, there is still some questions about ultra-high energy cosmic rays remain. The cut-off in the energy spectrum is experimentally highlighted but the reason is not clearly defined. The data from the Pierre Auger Observatory, in the Southern hemisphere, are compatible with an isotropic flux while the Telescope Array experiment, in the Northern hemisphere, observes an excess of events toward the Ursa Major galaxy cluster. The acceleration and propagation mechanism models at these energies are also poorly constrained due to the lack of data. Finally, at these energies, the main candidates are the protons and the iron nuclei due to their high abundance and binding energy. The Pierre Auger Observatory data, at the highest energies, are compatible with a progressively heavier composition. The data of the Telescope Array experiment are compatible with protons at all energies. The precise determination of the mass would allow to constrain the acceleration and propagation models and the type of sources. It is then the priority of all experiments devoted to the detection of ultra-high energy cosmic rays. Ideally, measurement of $X_{\max}$ should be done with a duty cycle, close to 100 %, as it is the case using radio stations. The atmospheric air showers are mainly made of positrons and electrons (which contribute to 90 % of the total energy, with the photons). The temporal evolution of the net charge of the shower front induces the emission of an electric field in the range detectable in the MHz range of few hundreds of micro Volts per meter for a vertical shower induced by a primary of 10^{17} eV. This detection method is sensitive to the full air shower development as for the fluorescence method.

The radio stations of the Pierre Auger Observatory are located on the AERA (Auger Engineering Radio Array) experimental site, close to one of the four sites of fluorescence telescopes. They allow the detection in coincidence with the telescopes and the Cerenkov tanks. These stations are equipped with two orthogonal antennas of butterfly

type or logarithmic dipole antenna type (LPDA). The stations record the electric field in two polarizations (North-South and East-West) in the frequency band [30-80] MHz in order to avoid the radio anthropic emitters (AM frequency band below 20 MHz and FM frequency band above 80 MHz). A detection involving several antennas allow the reconstruction of the lateral distribution function (LDF) of the electric field, calculated as the maximum electric field received by each antennas as a function of their position relatively to the air shower axis.

During my PhD thesis, a reconstruction method of the $X_{\max}$ depth with the radio signals has been developed in order to estimate the mass of the cosmic rays at energies above 10^{17} eV, with a duty cycle close to 100 %. It is now established that the LDF is highly correlated to the $X_{\max}$ depth. The electric field is highly beamed towards the direction of propagation of the air shower. A high $X_{\max}$ value gives a narrow distribution, as the emission of the electric field occurs close to the ground. On the contrary, a low $X_{\max}$ value gives a LDF less intense and more spread. The reconstruction method is based on the comparison of the LDF sampled by the radio stations to an LDF model.

In a first step, I have developed a model of angular distribution function of the radiation in agreement with experimental observations of the electric field induced by the development of an extensive air shower. A first emission mechanism is due to an excess of negative charges against the positive charges, predicted by Askaryan in 1962. Indeed, the positrons annihilate in the middle. The time variation of the current induced by the net charge of the air shower front produces an electric field radially polarized around the air shower axis. In 1967, Kahn and Lerche predicted another phenomenon. The presence of the terrestrial magnetic field causes a systematic and opposed deviation of the electrons and positrons under the effect of the Lorenz force. It induces a current oriented perpendicularly to the direction of propagation of the air shower. The time variation of this current creates an electric field polarized in the direction $\boldsymbol{v} \times B$, with $\boldsymbol{v}$ the direction of propagation of the air shower and $\boldsymbol{B}$ the direction of the geomagnetic field. The total electric field emitted by an atmospheric air shower is a superposition of the two mechanisms, which can interfere in a constructive or destructive way depending on the observer relative position around the air shower axis. The developed model takes into account these two mechanisms and has been parametrized with a simulation provided by the code SELFAS. This code uses a microscopic approach by summing up the individual contributions of all secondary particles to the total electric field. It appears that the maximum of emission can be associated to X_{inf}, the depth at which the production rate of the secondary particles is maximum. The parametrized model is thus an image of the radiation emitted by an air shower at this depth.

This model has been tested on a set of simulated events. In order to compare several air showers with different zenith angles, the atmospherical effects have been taken into account to convert this distance into atmospheric depth. The used atmosphere model is a parametrization of the US Standard model, giving the crossed atmospheric depth

corresponding to an altitude.

The comparison of the reconstructed atmospheric depths to the simulated X_{inf} depths are in good agreement. However, this model which predicts an exponential decay of the intensity of the electric field as a function of the distance to the shower axis has some limitations. Indeed, the topology of the electric field at the ground level is more complex. An effect similar to the Cerenkov emission occurs. This effect is due to the time compression (secondary particles are relativistic), and is responsible for a boost of the electric field intensity which appears under a particular angle of emission. The value of the angle depends on the velocity of the particles and on the air refractive index.

Thus, another method has been developed, using the SELFAS code as prediction. This method aims to reconstruct all the parameters describing an atmospheric air shower: the air shower core position on the array, the primary energy and X_{max}, allowing an estimation of the primary mass. The radio data allow a precise reconstruction of the arrival direction by studying the relative arrival time of the electric field at each antenna position. The method consists in the simulation of a set of events composed of air showers initiated by iron nuclei and protons with the same arrival direction as the one experimentally deduced. The electric field is computed for all antennas of a dense fictive array. After interpolation, the computed LDFs are compared to the experimental data. The first interaction depth of each simulation is randomly drawn in a realistic way with the use of a ultra-high energy hadronic interaction model. Each simulation has a particular X_{max} value. The energy of the primaries is arbitrary fixed, as the amplitude of the computed field varies linearly with the energy of the simulated primary particle. The best agreement is obtained for a particular core position of the air shower, a particular X_{max} and amplitude factor. The three reconstructed parameters are compared with the values obtained from the Cerenkov tanks and the fluorescence telescopes. However, a systematic shift of 17 g/cm^2 is observed.

In order to explain and correct this deviation, improvements have been applied to SELFAS. The atmosphere geometry was previously computed within a flat Earth approximation where the atmospheric layers were flat. Now, SELFAS uses a realistic and totally spherical description. Secondly, the data produced by the fluorescence telescopes take into account the daily and seasonal variations of the atmosphere density. The atmospheric conditions strongly affect the electric field distribution. It is then important to take it into account in order to precisely reconstruct the X_{max} depth. The GDAS (Global Data Assimilation System) provides meteorological data of interest everywhere on Earth every three hours. This database has been used in order to allow a dynamic simulation of the atmosphere, matching as much as possible the experimental conditions at the time of the event detection. Moreover, an estimation of the air refractive index more adapted to the problem is proposed. Indeed, the most widely used law is the Gladstone and Dale law, which proposes a linear variation of the air index as a function of the density. The relative humidity of the air is not taken into account while

it has an important influence on the calculation of the air index. In addition, this law is parameterized for optical wave lengths, which is not appropriate to the detection in the decametric range. Therefore, a law that has been specially parameterized for the high and very-high frequencies, taking into account the pressure, the temperature and the relative humidity, has been used. The improved version of SELFAS is finally used for the reconstruction of several events detected at the Pierre Auger Observatory. The estimation of the mass composition of the cosmic rays with energies above 10^{17} eV is proposed for both experiments.

CHAPTER 1

A history of high energy cosmic rays

Contents

After a century of observations, the composition, the sources location and the acceleration mechanisms of the ultra-high energy cosmic rays are still not clearly established. However, the study of these mysterious particles has led to major discoveries in astrophysics, particle physics and cosmology. In this first chapter, I give a review of the important discoveries that have led to the actual understanding of the cosmic rays at the highest energies, from the first detections to the modern giant experiments.

1.1 The radiation from above

1.1.1 1785 - The very first observation

The first observation of the existence of cosmic rays happened back in 1785. At that time Charles Augustin de Coulomb formalized the interaction between two static charges, known nowadays as the Coulomb's law, written in its scalar form as:

$$F = k_e \frac{q_1 \cdot q_1}{r^2} \tag{1.1}$$

Where $k_e = 8.99 \times 10^9$ N.m^2 C^{-2} is the Coulomb's constant, r is the distance between the charges and q_1 and q_2 are their signed magnitudes. To quantify the electrostatic force, he used a torsion balance (Figure 1.1).

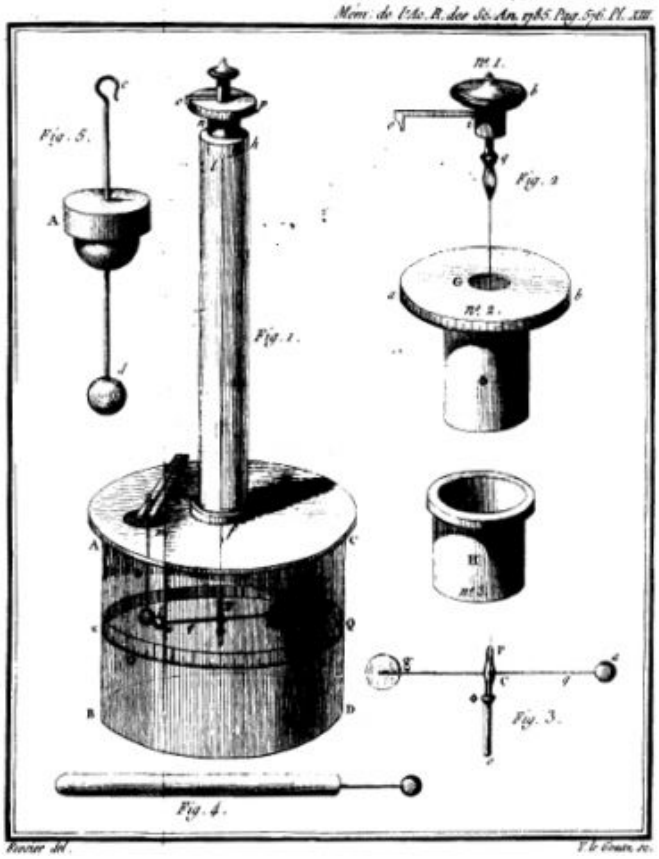

Figure 1.1: Sketch of a torsion balance [1].

The device is composed of a bar with a metal coated ball attached to one end, and suspended from its middle by a thin fiber acting as a torsion spring. The electric charge of the ball is known and an other ball of the same polarity was brought near to it. The two balls eventually repelled each other, twisting the torsion spring. The distance

between the two balls could be read with a scale integrated to the device and knowing the necessary force to twist the spring, Coulomb could estimate the intensity of the force between the two balls. Nevertheless, he also noticed that the device spontaneously discharge, which was eventually due to the flux of cosmic rays in the device but he imputed it to the action of the air and not to the defective insulation of the device, as notified in a report to the France's Royal Academy of Sciences [1].

1.1.2 1834 - The mystery of the ionization of the atmosphere

In 1834, Michael Faraday introduced the term of ion [41] to describe species that goes from one electrode to another in aqueous medium. One year later, Faraday confirmed Coulomb's observation with a better insulation of the device [42]. In 1850, Cano Matteucci followed by William Crookes [43] in 1879, observed that the rate of the discharge decreases at lower atmospheric pressure. Faraday's work allowed Crookes to conclude that the discharge was due to the air conductivity, thus to its ionization. The knowledge of the cause of the discharge kindled the question that will lead to the discovery of cosmic rays: what is causing the ionization of the atmosphere? The discovery of the radioactivity by Henry Becquerel in 1896 [44, 45] was of great interest to explain the origin of the ionization.

In 1898, Pierre and Marie Curie discovered that polonium and radium undergo transmutation through radioactive decay [46], for which they received the Nobel prize in 1903 with Henry Becquerel [47]. They also demonstrated that these radioactive substances can emit charged particles that cause discharge of electroscopes. The level of ionization was then used to gauge the amount of radioactivity [48]. At this point, the search for the main source of natural radioactivity began and the main candidates were the Sun, the soil and the atmosphere. The dominant belief were that the radioactive elements in the ground was the main source of the ionization of the atmosphere.

In the beginning of the 20^{th} century, Wilson [49], Elster and Geitel [50] improved the sensitivity of the technique by putting the electroscope in a closed vessel to ensure a good insulation. In 1901, Wilson's measurements in tunnels [51] showed no reduction of the ionization rate comparing to the surface and comforted the idea that the main source of radioactivity is in the soil. In 1909, Theodur Wulf perfected the electrometer making it transportable [52]. In 1910, during a holiday trip to Paris in which he brought few of his electroscopes, he measured the ionization of the atmosphere at the bottom and at the top of the Eiffel tower [53].

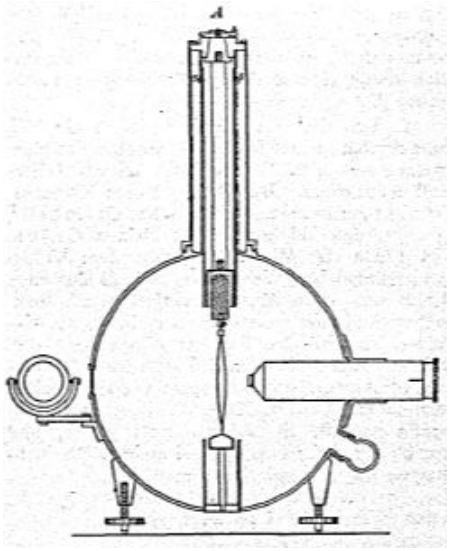

Figure 1.2: Sketch of Wulf's original electrometer [2].

Wulf's measurements show that the ionization rate fell from 6 ions by cm^3 at the ground level to 3.5 ions by cm^3 at 330 meters above the ground. However if the ionization was due to γ rays from the ground, as commonly believed, the ionization rate should have been halved before reaching 100 meters above the ground, following an exponential decrease. These results are incompatible with a source of radiation from the ground and suggested a source from above. In 1911, Domenico Pacini made a serie of measurements, in particular over the sea surface and at 3 meters under water at Livorno and later in Bracciano.

Figure 1.3: Dominco Pacini making a measurement of the air ionization [3].

He showed that the ionization rate was smaller below the sea level. He obtained

the confirmation of a 20% reduction of the ionization rate with a confidence level of 4.3σ [3]. Pacini concluded that *"a sizable cause of ionization exists in the atmosphere, originating from penetrating radiation, independent of the direct action of radioactive substances in the soil."* [54].

1.1.3 1910's - Time to go up!

The same year of 1911 Victor Hess, who was working on measuring the absorption coefficients of radioactivity in air, undertook two balloon flights (see Figure 1.4 (left) from Vienna up to 1300 meters to measure the possible variation of the radioactivity with the altitude using few Wulf's electrometers. As no effect was found, seven flights were scheduled from April to August 1912. During the final flight he reached the altitude of 5300 meters [55].

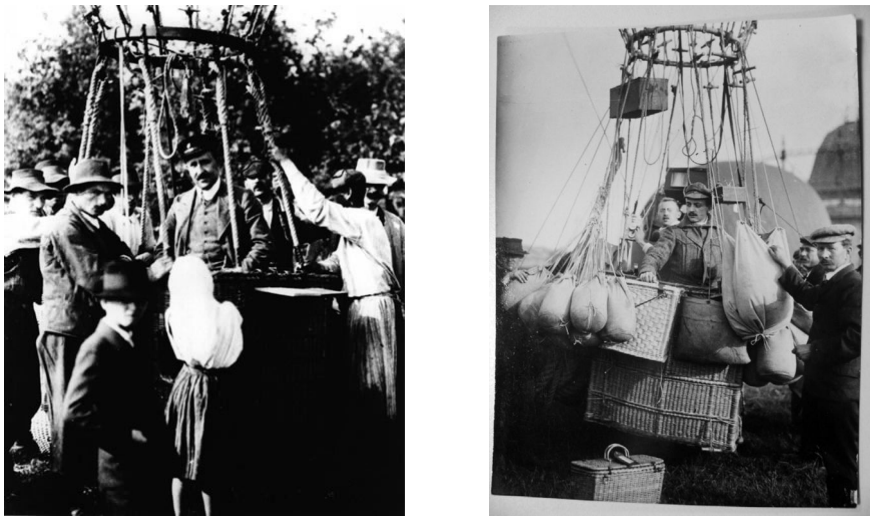

Figure 1.4: left: Victor Hess after the landing in 1912 [4]. - right: Werner Kolhörster during the flight of 1913 [5].

Hess' results, in Figure 1.5 (left), shows that the ionization rate is decreasing up to 1 km of height as expected. However, it increases as a function of altitude beyond this point. The flight took place during a nearly total sun eclipse. This experimental condition led him to conclude that, not only the ionization was caused by a source of radiation from above, but also that it was not coming from the sun, but further from outer space. The ionization rate reaches ten times the value at sea level. Hess's results were confirmed by Werner Kolhörster in 1913 (see Figure 1.5 (left)). Kolhörster made a series of flights between 1913 and 1914 during which he reached an altitude of 9300 meters (see Figure 1.4 (right)).

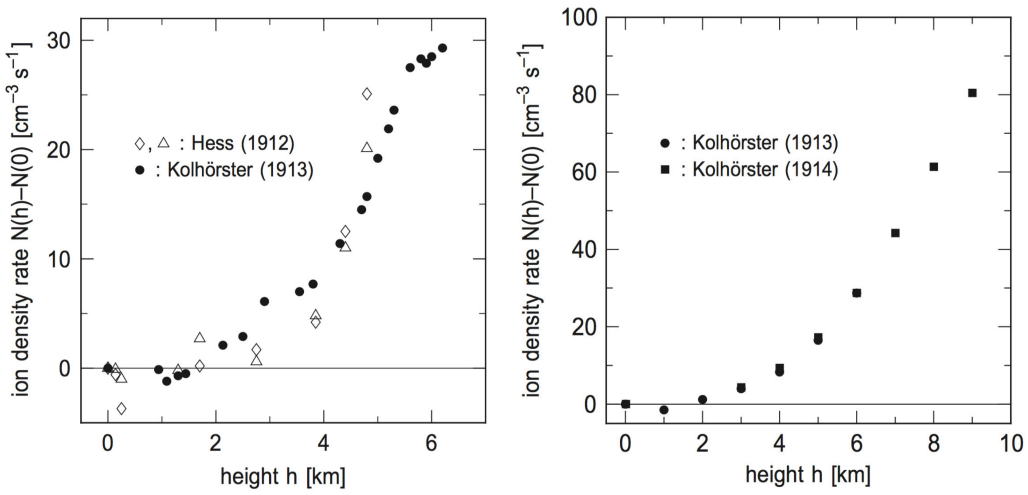

Figure 1.5: left: Hess measurements up to 5300 m compared to Kolhörster's results [6, 7]. - right: Kolhörster's measurements up to 9200 m [7, 8]. - Both plots are adapted from original papers [9].

The second flight of Kolhörster took place on 28th June 1914 (at 9300 meters), the results, presented in Figure 1.5 (right), are in agreement with his previous measurements. The same day the assassination of Archduke Franz Ferdinand of Austria took place, leading to the start of World War I. During this period and the years after, no new measurement series have been achieved and investigations stopped.

1.2 First steps towards the nature of cosmic rays

Around 1925, researches started again, mainly in the USA. The data transmission technology developed during the war was used by Millikan and Bowen to launch unmanned balloons carrying their newly engineered very light electrometer (around 200 g) and ion chamber. Throughout flights in Texas up to 1500 meters, they found a radiation intensity of one fourth the intensity reported by Hess and Kolhörster [56]. At that time they were unaware that a latitude geomagnetic effect exists and they explained this observation as an inversion of the radioactivity intensity at higher altitudes. Millikan concluded that there was no extraterrestrial radiation and stated to the American Physical Society: *"The whole of the penetrating radiation is of local origin."*, which will be strongly argued by Arthur Compton [57]. It was believed that cosmic rays were composed of γ rays due to their important penetrating power and also because the penetrating power of relativistic charges was unknown. In 1926, Millikan and Cameron reproduced Pacini's experiment, stating that these particles shoot through space equally in all directions, and called them *"cosmic rays"* [58]. Millikan was skillful at handling medias and, in the United States, the discovery of cosmic rays quickly became an american success. The geomagnetic effect experienced by Millikan was accidentally discovered in 1927

by Clay [59] when carrying his detector on a trip from Java to the Netherlands. He observed that the ionization rate was minimum at the magnetic equator and higher farther south or north. He confirmed his results with multiple measurements [60, 61]. Compton recognized the variation as a geomagnetic effect, giving evidence that the radiation consisted of charged particles [62, 63].

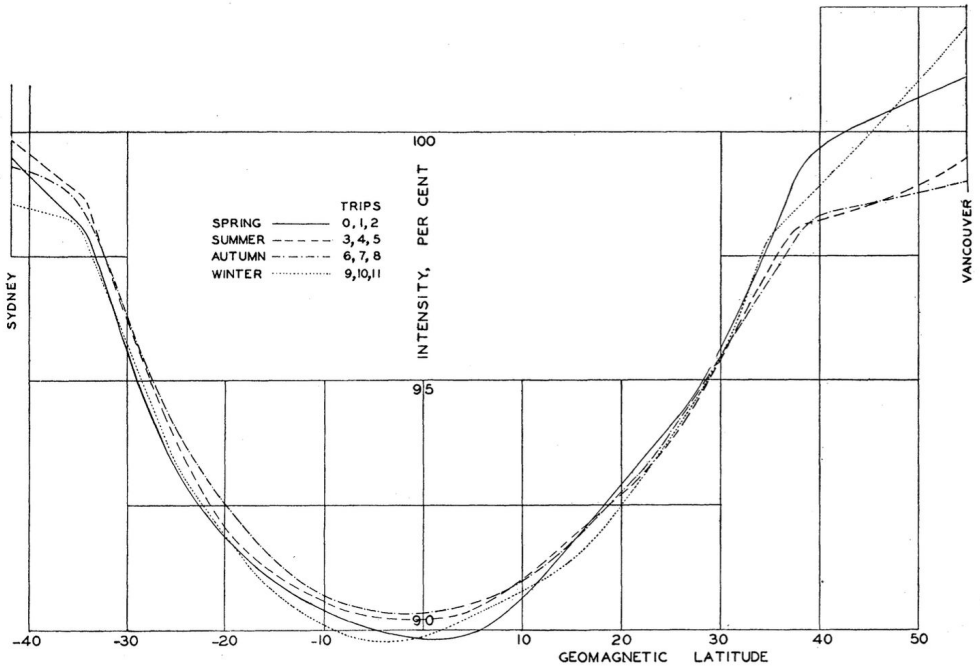

Figure 1.6: Latitude effect curves for the four seasons highlighted by Compton [10].

Measurements at 69 locations from 1931 to 1933 demonstrated the dependence of cosmic radiation intensity on geomagnetic latitude [64]. The record of cosmic rays intensities measured during 12 trips between Vancouver, Canada and Sydney, Australia, led by Compton from March 1936, to January 1937 [10] are shown in Figure 1.6. The charged particles approaching the Earth near the poles travel almost along the direction of the magnetic lines of force. They experienced no deviation and easily reach the surface of the Earth and hence maximum intensity at poles. But the charged particles that approach towards the equator have to travel in a perpendicular direction to the field and are deflected away. Only particles with sufficient energy can reach the equator, while the low energy particles are deflected back into cosmos and hence minimum intensity at the equator as depicted in Figure 1.7. This discovery put an end to the Millikan's theory, which specified that cosmic rays were composed of γ rays.

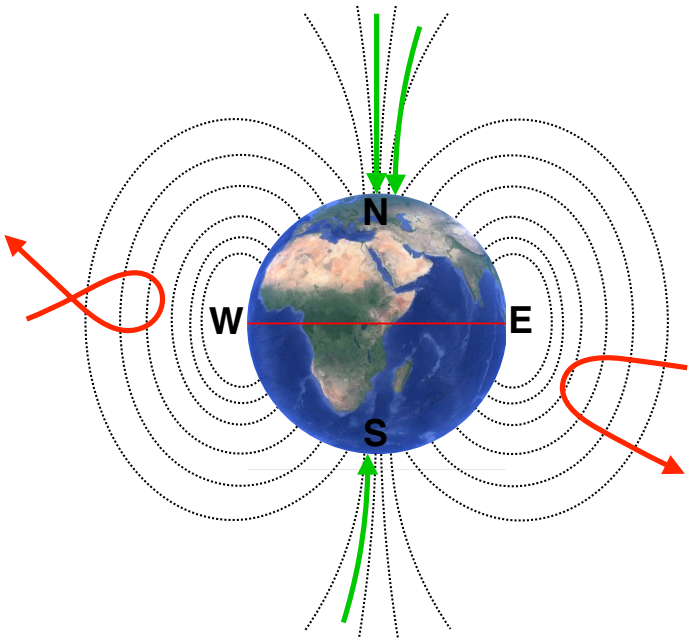

Figure 1.7: Latitude effect caused by the geomagnetic field. The particle arriving towards the poles are represented by the green arrows, those arriving towards the equator, by the red arrows and the red line represents the equator.

In 1932 and under the supervision of Millikan, Anderson began to investigate on cosmic rays in the frame of the preparation of its PhD thesis. During a course in which he was studying the tracks that cosmic particles produce in a Wilson chamber [65], he stumbled upon unexpected tracks that must have been created by a particle of the same mass as the electron but of opposite electric charge.

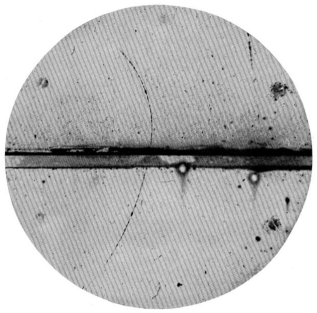

Figure 1.8: Picture of the track left by a positron in Anderson's cloud chamber, taken from [11]

He interpreted correctly the first observation of the positron [11], the antiparticle associated to the electron and theoretically predicted by P. Dirac in 1932 [66].

In 1933, Rossi and others demonstrated that the intensity of the cosmic radiation is larger from the east than from the west [67]. The trajectory of cosmic rays is eventually bended by the presence of the Earth magnetic field, as previously highlighted by Compton. As depicted in Figure 1.9 if more comic rays are detected from the east, it is because most of them are positively charged particles.

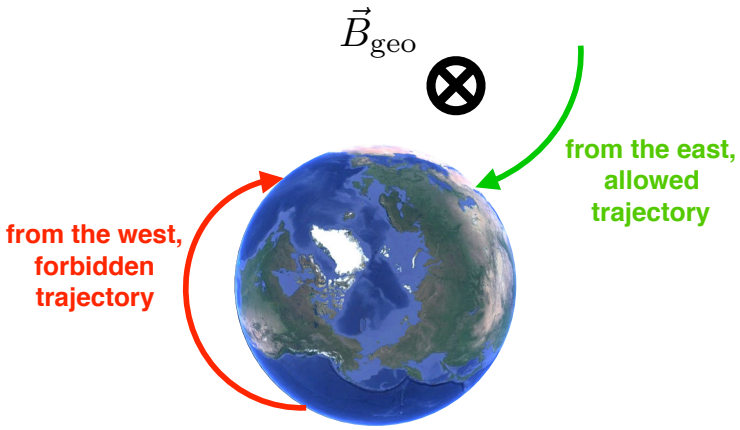

Figure 1.9: View of the north magnetic pole Earth.

In the 30's Rossi [68] also noticed simultaneous discharge in two Geiger counters separated by several meters, far in excess to be chance coincidences. At the time he stated: *"It would seem that occasionally very extensive groups of particles arrive on the equipment"*.

1.3 The discovery of the extensive air showers

1.3.1 1930's - Pierre Auger and the discovery of the extensive air showers

At the end of the 30's, Pierre Auger and collaborators observed the same phenomenon when they undertook a systematic survey [69], first at the Observatoire du Pic du Midi (2876 m) in France and at the scientific station of Jungfraujoch (3500 m) in Switzerland. Two detectors located many meters apart horizontally (as far as 75 meters) both have detected the arrival of particles at exactly the same time. In the meantime the rate of coincident detections dropped drastically with the distance between the detectors from 10 cm to 10 m and decreased slowly at larger distances but once again the event rates were too high to be due to chance coincidences.

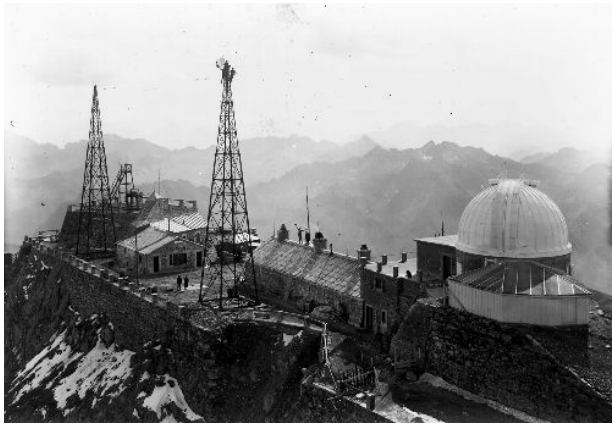

Figure 1.10: The Observatoire du Pic du Midi (1937) taken from [12].

The results allowed Pierre Auger's team to conclude that the detected particles are secondary charged particles produced by the interaction of a very energetic cosmic ray with the atmosphere constituents. They stated that the energy of the primary particles could exceed one million GeV, which is more energetic than the maximum energies that modern particle accelerators can reach, even with the Large Hadron Collider at CERN (Switzerland).

In 1940 and 1941, M. Schlein et al. determined that cosmic rays are mostly protons [70, 71]. In 1948, H. L. Bradt and B. Peters measured the relative flux of cosmic rays for different nuclei [40] and the distribution of atomic numbers among the primaries was determined without any energy cut:

nucleus	H	He	C, N, O	Z>10
relative ratio	4000	1000	35	10

Table 1.1: The relative magnitude of the fluxes of the H, He, C, N, O and Z>10 nuclei measured by H. L. Bradt and B. Peters [40].

They found that even if protons and helium nuclei are the main part of cosmic rays, heavy particles are a significant fraction of the total cosmic rays flux.

1.3.2 1949 - Enrico Fermi's *"On the origin of cosmic radiation"*

The first description of the energy spectrum was introduced by Enrico Fermi in the article *"On the origin of cosmic radiation"* in 1949 [72], where he exposed his theories on the acceleration mechanisms. Fermi's intuition, which led him to assume

a power law ($dN/dE \propto E^{\gamma}$) to describe the flux of cosmic rays, can be summarized as follow, according to [73]. The interstellar space is filled with clouds of matter which can have magnetic properties. Cosmic rays, as charged particles, can exchange energy with clouds and gain energy as depicted in Figure 1.11.

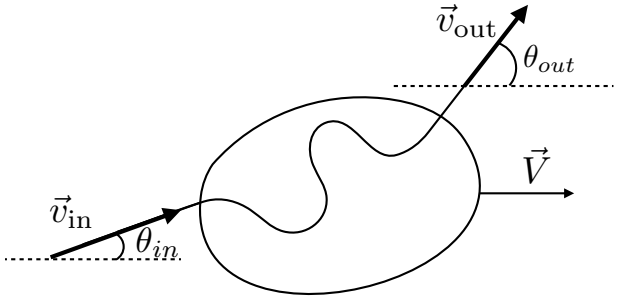

Figure 1.11: Kinematics of a particle entering an interstellar magnetic cloud. A particle enters a magnetic cloud with a velocity v_{in} and with a pitch angle θ_{in} with respect to velocity of the cloud $\vec{V}$. After exiting the cloud, the particle have a velocity v_{out} and under an angle θ_{out}.

On this sketch, a charged particle encounter a magnetic cloud moving at the velocity $\vec{V}$ with a pitch angle θ_{in} (angle between the velocity vector of the particle and the velocity vector of the cloud). One can write the initial energy of the particle before and after its interactions with the cloud, E_{in} and E_{out} measured in the galactic frame and their expression E'_{in} and E'_{out} in the frame of the cloud. By extent, the prime symbol denotes the quantities expressed in the cloud frame.

$$E'_{\text{in}} = \gamma E_{\text{in}}(1 - \beta \cos\theta_{\text{in}}) \tag{1.2}$$

$$E_{\text{out}} = \gamma E'_{\text{out}}(1 + \beta \cos\theta'_{\text{out}}) \tag{1.3}$$

In the cloud frame, the trajectory of the particle is modified inside the cloud without change of energy, so that $E'_{\text{in}} = E'_{\text{out}}$, from which we obtain:

$$E_{\text{out}} = \gamma^2 E_{\text{in}}(1 - \beta \cos\theta_{\text{in}})(1 + \beta \cos\theta'_{\text{out}}) \tag{1.4}$$

$$\frac{E_{\text{out}} - E_{\text{in}}}{E_{\text{in}}} = \frac{\Delta E}{E} = \frac{\beta(\cos\theta'_{\text{out}} - \cos\theta_{\text{in}}) + \beta^2(1 - \cos\theta'_{\text{out}}\cos\theta_{\text{in}})}{1 - \beta^2} \tag{1.5}$$

To calculate the mean energy gain for one encounter between a particle and a cloud, one must calculate $< \cos\theta_{\text{in}} >$ and $< \cos\theta'_{\text{out}} >$. From the assumption that the direction of the particles becomes isotropic in the cloud frame due to the magnetic field, $< \cos\theta'_{\text{out}} >= 0$; $< \cos\theta_{\text{in}} >$ depends on the relative velocities of the particle and the cloud as depicted in Figure 1.12.

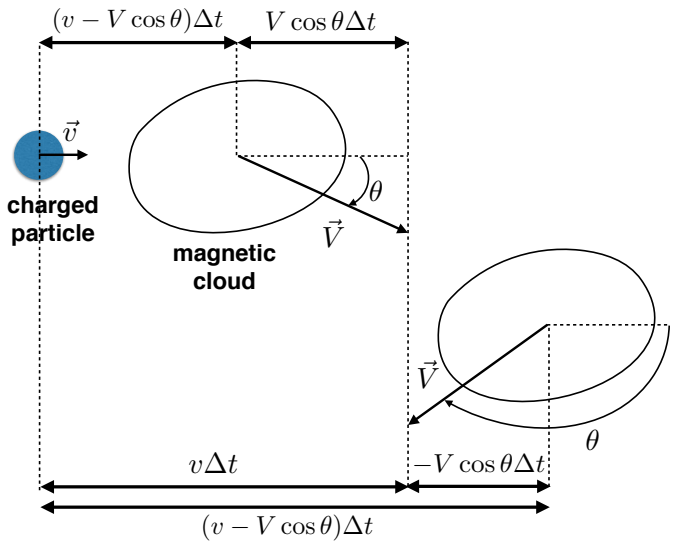

Figure 1.12: Stochastic distributions of the pitch angle of a particle in a magnetic cloud.

From this sketch, one sees that the mean number of encountered clouds during Δt is proportional to $(v - V\cos\theta)\Delta t$. The probability distribution function for θ_{in} is thus:

$$P(\theta_{\text{in}}) \propto (v - V\cos\theta_{\text{in}}) \tag{1.6}$$

And the mean $\cos\theta_{\text{in}}$ can be approximated as:

$$< \cos\theta_{\text{in}} >= \frac{\int_{-1}^{1} \cos\theta_{\text{in}}(v - V\cos\theta_{\text{in}})\mathrm{d}(\cos\theta_{\text{in}})}{\int_{-1}^{1}(v - V\cos\theta_{\text{in}})\mathrm{d}(\cos\theta_{\text{in}})} = \frac{-2V/3}{2v} \simeq -\frac{1}{3}\beta \tag{1.7}$$

Assuming that particles are relativistic ($v \simeq c$), thus $\beta = V/c$. If one replace the expression of $< \cos\theta_{\text{in}} >$ in Equation (2), we obtain at the first order:

$$\left\langle \frac{\Delta E}{E} \right\rangle = \frac{4}{3}\frac{\beta^2}{1-\beta^2} \simeq \frac{4}{3}\beta^2 \tag{1.8}$$

which gives a mean relative acceleration of the second order ($\propto \beta^2$). The mean acceleration is positive due to an excess of head-on collisions comparing to head-tail collisions in the galactic frame. However, this stochastic acceleration mechanism has some limitations. The differential spectrum obtained with such mechanism is:

$$N(E) = \dot{N}_0 \frac{\tau_{\text{acc}}}{E_0}\left(\frac{E}{E_0}\right)^{-x}, \quad \text{with} \quad x = 1 + \frac{\tau_{\text{acc}}}{\tau_{\text{esc}}} \tag{1.9}$$

With τ_{acc} the acceleration time, τ_{esc} the escaping time of the particles out of the acceleration region and $\dot{N}_0$ the injection rate of the particle at the energy E_0. Even if

Fermi's theory leads to an energy spectrum described as a power law, its spectral index is not precisely estimated due to the dependence with the distance between clouds, the velocity of the clouds and the size of the region of the acceleration. Moreover, the acceleration time is too long. If we consider a typical speed of $\beta \simeq 10^{-4}$ for the clouds in the interstellar medium, the mean relative energy gain is around 10^{-8} per collision as the process is proportional to β^2. For a mean distance between clouds of 1 pc, it takes 10^9 years to triple the energy whereas the age of cosmic rays is estimated around 10^7 years. Finally, at low energy (< 200 MeV for protons) the particles loose energy from coulombian interaction and the time between two collisions with clouds is to slow to compensate the energy loss. To let the second order fermi mechanisms effectively accelerate cosmic rays, an other mechanism must accelerate protons up to 200 MeV (higher energy for heavier nuclei). In the late 70's, a theory of a first order Fermi acceleration was established involving many physicists (for an extensive review see [74]), solving the injection problem. This mechanism is detailed more extensively in Section 1.8.2. Nevertheless, at the end of the 1940's, a first acceleration model was introduced. In the mean time, the first steps towards gamma astronomy were about to be taken.

1.3.3 The 1950's - The birth of gamma astronomy.

In 1948, Patrick Blackett suggested for the first time that Cerenkov radiation induced by cosmic rays in the atmosphere should contribute to the light in the night sky [75]. In 1952, two young researchers, Galbraith and Jelley, built a detector out of a dustbin painted in black, a recycled 25 cm searchlight mirror and a 5 cm phototube in order to measure flashes of Cerenkov light in the night sky and to confirm Blackett's statements.

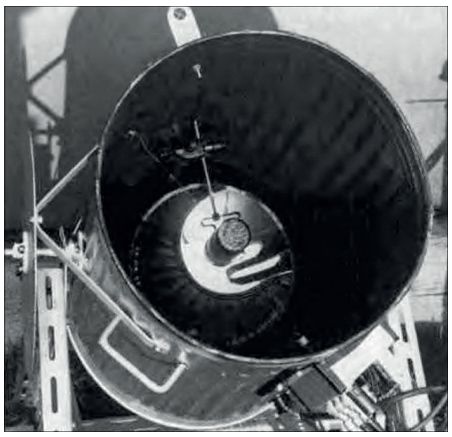

Figure 1.13: Galbraith and Jelley's detector composed of a dustbin painted in black, a recycled 25 cm searchlight mirror and a 5 cm phototube, taken from [13].

They indeed observed flashlights with a counting rate of about one pulse per minute [76]. However, there was no proof at the time that these pulses, detected in coincidence with air showers, were due to a Cerenkov emission. They were aware that the origin of the light could be produced by bremsstrahlung or by recombination after the ionization of the constituents of the atmosphere during the development of the shower. To lift this uncertainty and to avoid the vagaries of the British weather, they headed to the Observatoire du Pic du Midi to carry out experiments and take advantage of the greater number of clear nights with an improved apparatus [77, 78]. This time, they successfully demonstrated that the polarization and the spectral distribution of the detected light were characteristic of the Cerenkov emission. These series of experiments gave birth to the Cerenkov astronomy.

1.3.4 Exploring the highest energies.

In 1946, Bruno Rossi left the Los Alamos National Laboratory (New-Mexico, USA) for the MIT in Cambridge, where he was recruited as professor and became the leader of a comic ray research group [79]. In 1952 and 1953, he took advantage of the extremely fast response of the newly developed scintillation counters to study the structure of air showers and three devices were deployed on the roof of the MIT Physics building. This detection method allowed the determination of the arrival direction and the location of the shower axis. With this success, Rossi became the head of a major experiment in high energy cosmic rays detection [80]. After several years of measurements with eleven then fifteen liquid scintillators of one square meter arranged in a circular area of about 460 m at the Agassiz astronomical Station of Harvard University, multiple findings were made. They got a precise measurement of the density of shower particles as a function of the distance from the shower center, a measurement of the energy spectrum of the primary particles responsible for the showers from 10^{15} to 10^{18} eV and the proof that these particles arrive in practically equal numbers from all directions. Their energy is too high to let their trajectories be affected enough by the geomagnetic field to observe the east-west effect. At fixed energy, the number of detected events decreases with the zenith angle. This is consistent with the fact that the showers arriving with large zenith angle have to cross more matter that the vertical ones and are more likely not to reach the ground due to the energy loss during the development. The maximum energy of a detected particle by the Agassiz experiment is around 10^{19} eV. At these energies, the events are very rare. Thus, the decision was made to build an array of greater dimension to detect showers induced by ultra-high energy particles.

1.4 The era of the ground detectors

1.4.1 1960 - The detection of the secondary particles

The construction of an array of nineteen scintillation counters between 1957 and 1958 was led by John Linsley at Volcano Ranch near Albuquerque in New Mexico at an altitude of 1800 meters above the sea level. In 1960, the detectors spreading reached a surface of 10^7 m^2 [81]. The first observations were made in 1959 and then in 1962, Linsley observed an air shower induced by a particle with an energy above 10^{20} eV. Linsley also stated that this kind of highly energetic particle could not be confined within our galaxy [14]. The region where originates such an energetic particle must be large enough and possess also a strong enough magnetic field to verify the following relation, known nowadays as the Hillas criteria [82]:

$$R.H \gg (1/300) \times (E/Z) \tag{1.10}$$

Where R is the radius of the region [cm], H is the intensity of the magnetic field [Gauss], E is the total energy of the detected particle [eV] and Z is its electric charge. For $E \simeq 10^{20}$ eV, and considering the best case scenario where the particle is a proton ($Z = 1$), the condition is $R.H >> 3 \times 10^{17}$. The condition is not satisfied by our galaxy for which H is estimated by $H \simeq 10^{-5}$ Gauss, and $R \simeq 15$ kpc$= 5.25 \times 10^{22}$ cm (including the galactic halo), giving $R \times H \simeq 5 \times 10^{17}$.

In 1965, Penzias and Wilson, two physicists were experimenting with an antenna designed to detect radio waves at the Bell Telephone Laboratories. After removing the known interferences such as radar, radio broadcasting and even the heat due to the receiver itself by a cooling system, they found a unknown low and steady noise remaining in the antenna. After checking all possible other sources they concluded that the detected radiation was not coming from Earth, the Sun or the Milky Way, was present during night and day and evenly spread in the sky [83]. The observed radiation was eventually the cosmic microwave background (CMB), formed when the universe was 380 000 years old, when its expansion together with an adiabatic cooling reached a state (known as recombination) that allows electrons to interact with protons, forming hydrogen atoms. Photons could no longer interact with the neutral atoms and could travel freely in space. The CMB is the relic of these photons from the time of the decoupling of matter and radiation which intensity corresponds nowadays to a 2.7 K black-body radiation. Penzias and Wilson shared the Nobel Prize in Physics (1978) *"for their discovery of cosmic microwave background radiation"*. In 1966, Greisen [84] and Zatsepin and Kuz'min [85] noted an important effect on the propagation of extremely energetic protons. Indeed, at the threshold energy of 4×10^{19} eV, the pion production from the interaction of protons with the photon of the CMB via the Δ resonance is allowed.

$$p + \gamma_{\mathrm{CMB}} \rightarrow \Delta^{+} \rightarrow p + \pi^{0} \tag{1.11}$$

$$p + \gamma_{\mathrm{CMB}} \rightarrow \Delta^{+} \rightarrow n + \pi^{+} \tag{1.12}$$

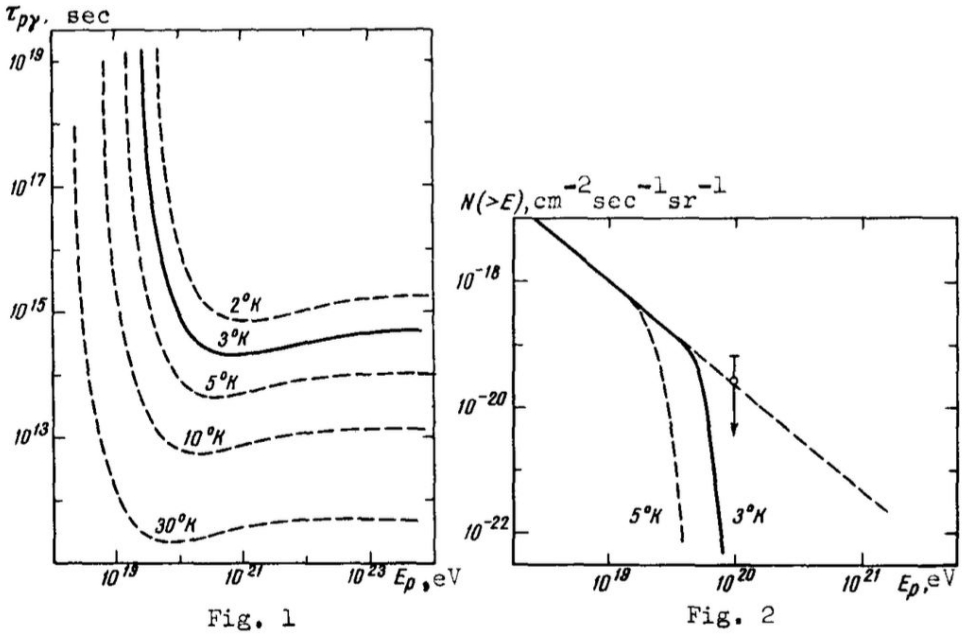

Figure 1.14: Fig 1) Theoretical time between two collision interactions CMB for as a function of the energy of the proton (10^7 years for 10^{20} eV proton). - Fig 2) Expected suppression of the energy spectrum for a 5°K and 3°K photon background including the data point from the highest event of Vulcano Ranch Experiment [14].

Figure 1.14 shows the key results of the work of Zatsepin and Kuz'min predicting a fast suppression of the flux of protons beyond 4×10^{19} eV. Resulting from prediction, known as the Greisen - Zatsepin - Kuz'min (GZK) limit, the high expectation of detecting events with greater energy than 10^{20} eV, as it has been the case at the Vulcano Ranch experiment, has became more moderate. It was now expected that events beyond the GZK limit must come from a very close region of space as the farther a cosmic ray comes from the greater the chance to loose energy on the CMB. The pion produced in the process drains 20% of the total energy of the proton and the mean path of this reaction is of the order of few Mpc. Several large-scale experiments such as Yakutsk in Siberia, SUGAR in Australia and Haverah Park in England were developed, before knowing the existence of the GZK limit, to study the upper part of the energy spectrum, beyond 10^{17} eV, in the 70's and the 80's. For these experiments, the main goal became the test of the predicted GZK limit.

1.4.2 1967 - The ground particle detectors

With the success of the Volcano Ranch experiment, several experiments dedicated to the detection of cosmic rays at the highest energies succeeded to each other as shown in Figure 1.15.

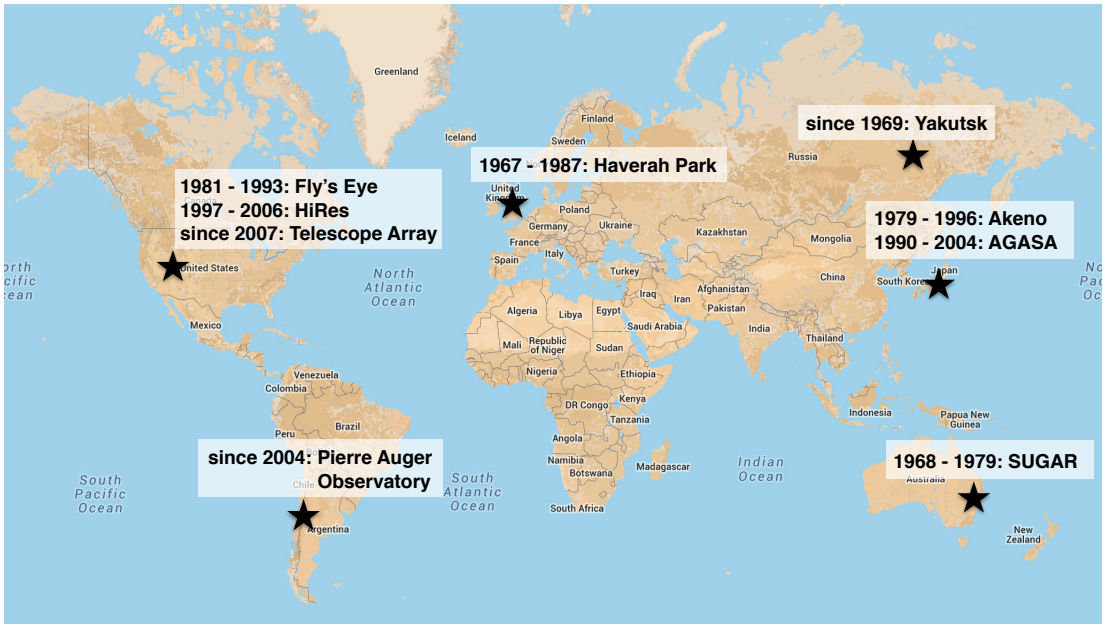

Figure 1.15: Location of several major cosmic rays experiments. The dates are the data taking periods.

The experiments Yakutsk in Russia (1967), SUGAR in Australia (1968) and Haverah Park in England (1968) measured (and still measures for Yakutsk) the cosmic particles at the highest energies. The detection method consists in sampling the secondary particles at the ground level with scintillator counters (as for the Volcano Ranch Experiment) or Cerenkov tanks. However, another technique will quickly compete with the ground detection experiments: the fluorescence detection.

1.5 The fluorescence technique

In 1981, the Fly's Eye experiment introduced the fluorescence technique to the detection of extensive air showers [86]. The charged particles composing a shower can excite the nitrogen molecules of the atmosphere, according to the following reaction:

$$h\nu' + N_2 \rightarrow N_2^* \rightarrow N_2 + h\nu \tag{1.13}$$

Where $h\nu'$ is the energy of the absorbed photon, ν is its wavelength, h is the Planck's constant, N_2 is a nitrogen molecule at the ground energy state, N_2^* corresponds to the excited state and $h\nu$ is the energy of the emitted photon. The emitted photon has generally less energy than the absorbed one. This effect, known as the Stokes shift, can be explained through the Jablonski diagram corresponding to the fluorescence process shown in Figure 1.16, which is useful to illustrate the electronic states of a molecule and the transitions between them.

The nitrogen molecule, after being excited, can experience an energetic relaxation though vibrational heat production, loosing a part of the energy gained during the absorption of a photon, before emitting a photon to finally reach its ground energy state. The fluorescence light produced by the development of the secondary particles of an air shower is mainly composed of ultraviolet light. After a successful test at Volcano Ranch in 1976, consisting in three modules of fluorescence detectors in coincidence with extensive air showers, the 67 modules of the Fly's Eye experiment were built atop Little Granite Mountain in 1981 by the University of Utah Cosmic Ray group, led by George Cassiday. Each module was composed of a mirror that reflects the fluorescence light to PMTs placed at the focal surface of the mirror as illustrated in Figure 1.17.

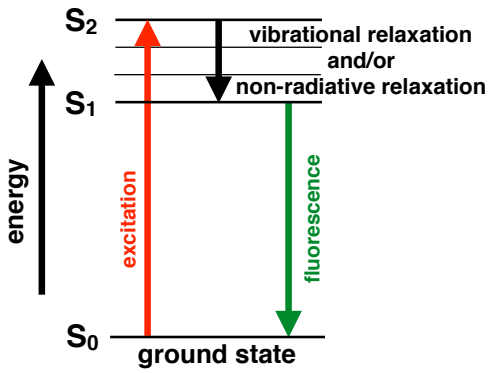

Figure 1.16: Jablonski's diagram for the fluorescence process.

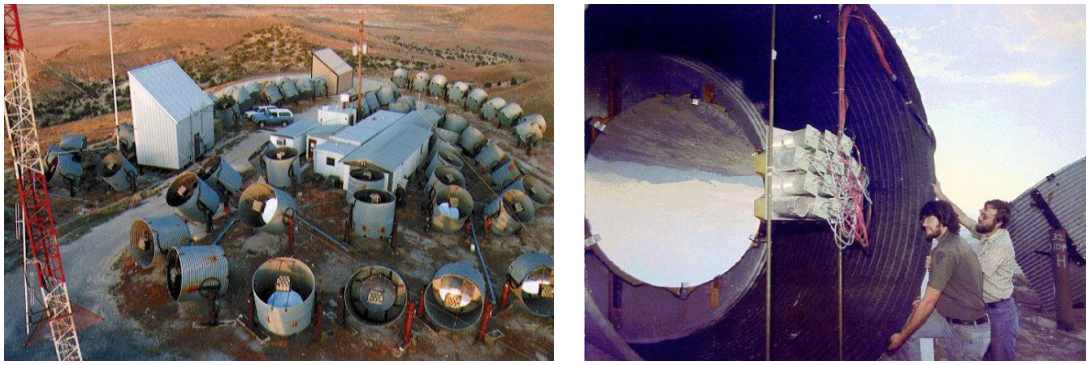

Figure 1.17: left: picture of the Fly's Eye experiment showing the 67 modules. - right: arrangement of the mirror along with the PMTs at the focal surface. Taken from [15].

The huge asset of the fluorescence detection technique is that the detected light is directly proportional to the number of particles composing the shower. The light collected

by each pixel corresponds to different ages of the shower. Thus, the fluorescence technique allows a direct measurement of the longitudinal profile of the shower using the atmosphere as calorimeter. Whereas detections based on the sampling of the particles at the ground level with scintillators or Cerenkov tanks require a longitudinal profile model. The model is constrained using the reconstructed arrival direction, energy and density of the particles on the ground. The estimation of the evolution of the number of particles is thus very dependent of the model that is used and moreover considering the uncertainties on the latter parameters. In 1991, the Fly's Eye experiment recorded an extensive air shower initiated by a particle with an energy of 3.2×10^{20} eV and a consistent depth of the shower maximum of $X_{\max} \simeq 800$ g/cm^2 for a hadron-initiated shower at this energy. It was the most energetic particle ever detected at the time. The event display and the longitudinal profile of the event are shown Figure 1.18.

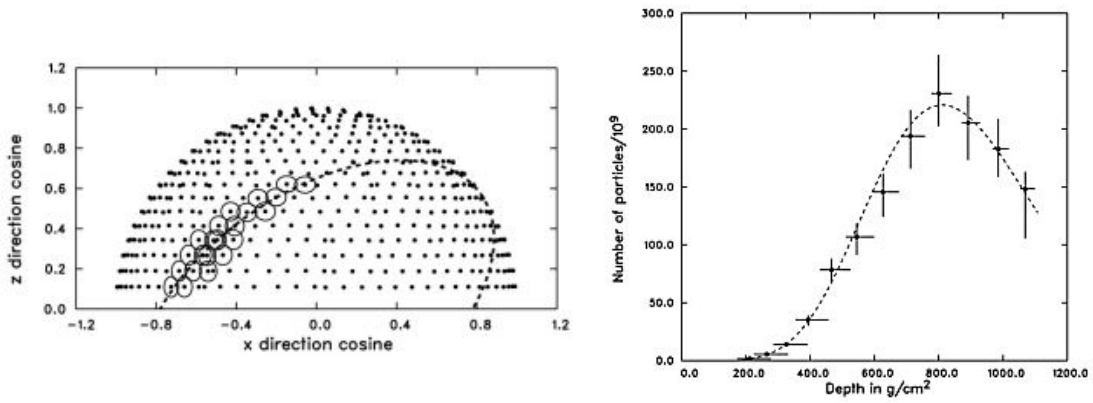

Figure 1.18: left: event display for the detected air shower initiated by a 3.2×10^{20} eV primary. - right: longitudinal profile for this event with $X_{\max} \simeq 800$ g/cm^2 [16].

In 1986, the addition of a second detection site, Fly's Eye-II [87], at 3.7 km away from the original site, Fly's Eye, and composed of 36 additional mirrors, allowed stereoscopic observations and has considerably enhanced the precision of the $X_{\max}$ measurement and the energy estimation. At the time of its shutdown in 1993, Fly's Eye had constituted the largest ultra high energy cosmic rays database. The important set of data has been used to determine the energy spectrum beyond 10^{17} eV. At this time a comparison is made between the four biggest experiment: Yakutsk, Haverah Park, Akeno and Fly's Eye. The comparison can be found in [17] and is presented in Figure 1.19, Figure 1.20 and Figure 1.21.

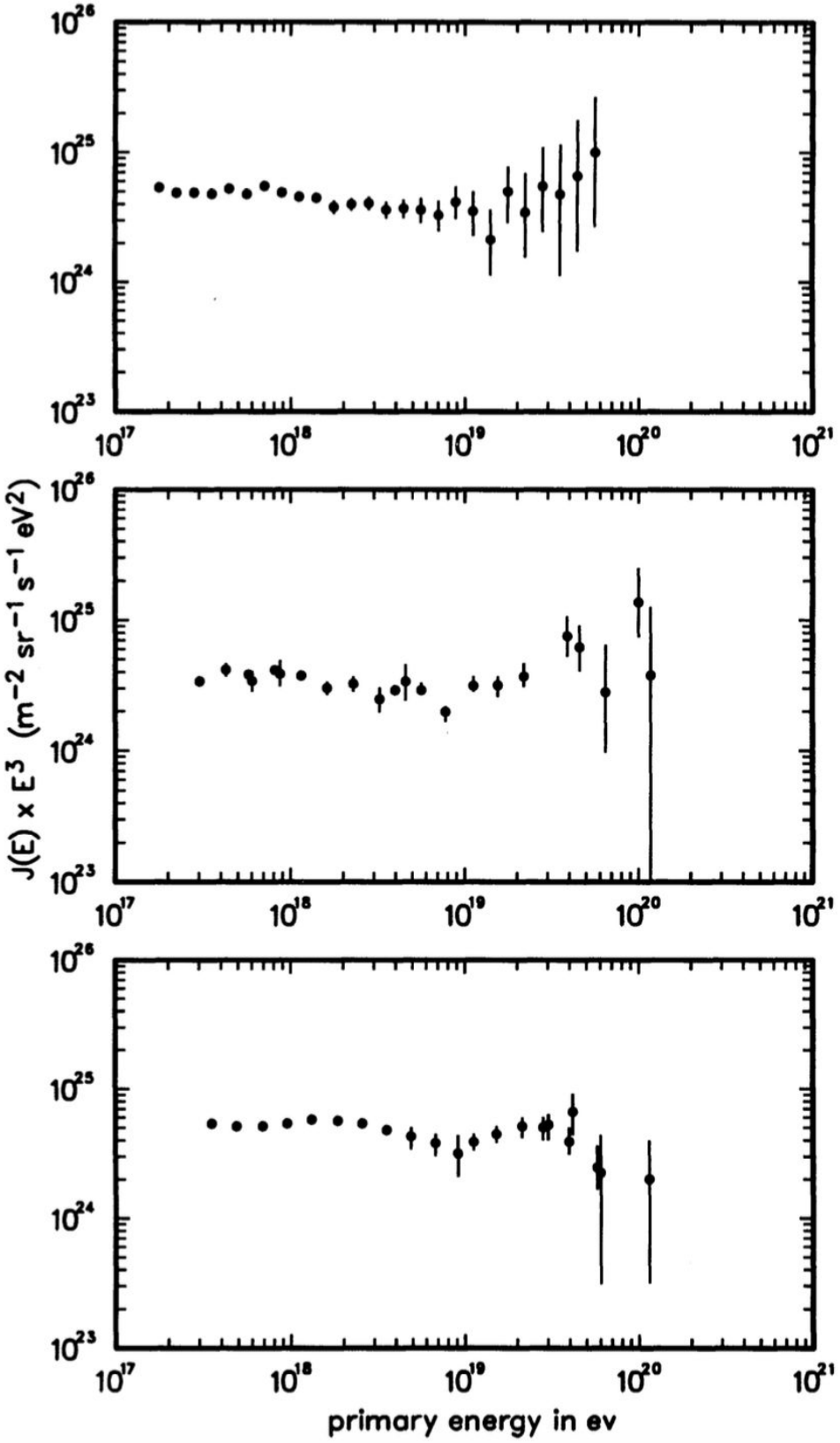

Figure 1.19: Energy spectra for (top) Akeno, (middle) Haverah Park, (bottom) Yakutsk [17].

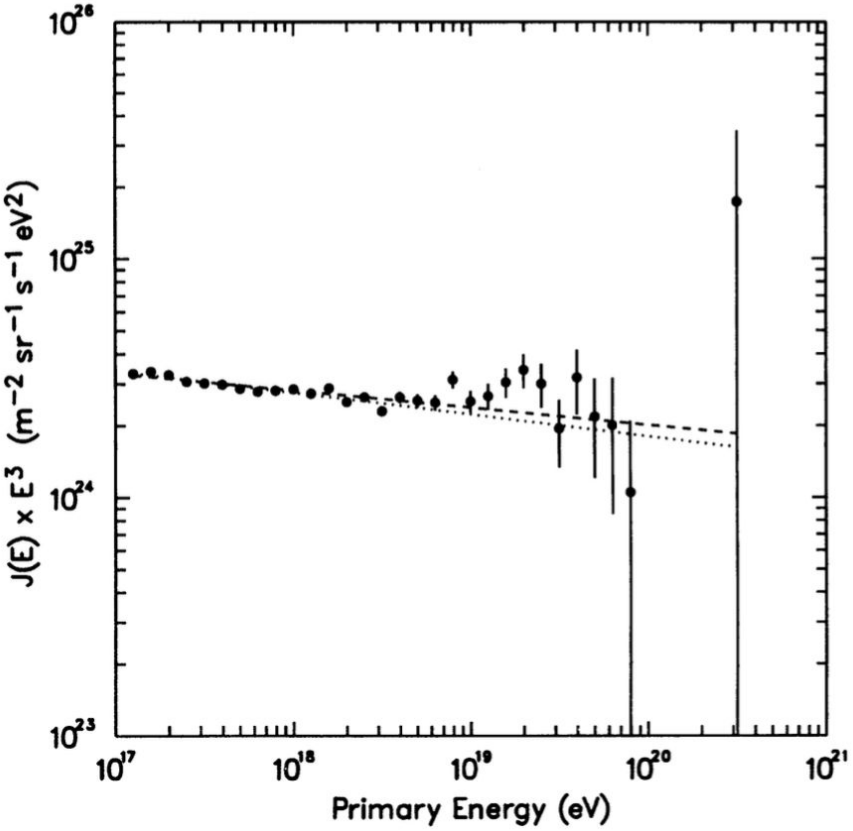

Figure 1.20: Energy spectrum obtained with monocular events with Fly's Eye [17].

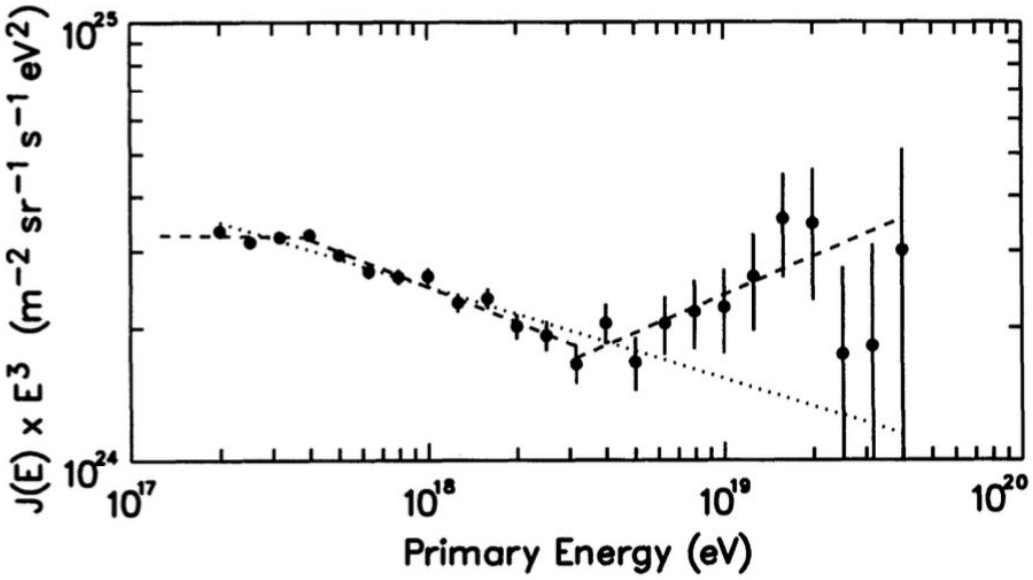

Figure 1.21: Energy spectrum obtained with stereoscopic events with Fly's Eye [17].

From this results, the existence of the GZK cutoff can not be clearly established. One can nevertheless notice that the power law of the spectrum presented by the Akeno

experiment seems to show a lower spectral index in comparison of the other experiments and could be incompatible with the GZK limit. In 1990, the Akeno experiment was upgraded to the Akeno Giant Air Shower Array (AGASA) [88] and its 111 surface detectors and 27 muon detectors, covering an area of 100 km^2, to study more precisely the arrival directions and the energy spectrum. In 1998, the obtained energy spectrum was presented [18] with the title: *'Extension of the Cosmic-Ray Energy Spectrum beyond the Predicted Greisen-Zatsepin-Kuz'min Cutoff'*.

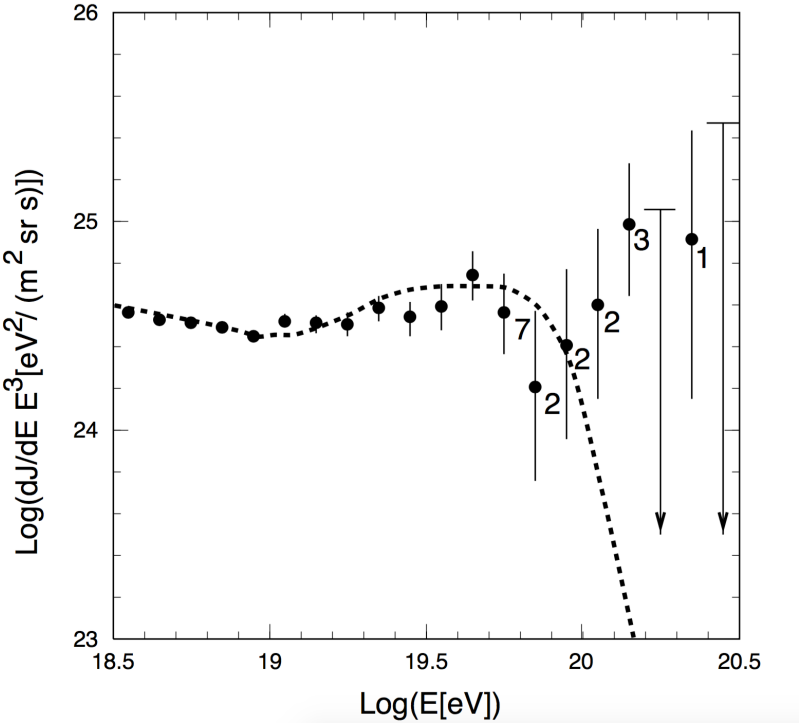

Figure 1.22: Final results of the energy spectrum from AGASA [18].

From the obtained spectrum, the conclusion was that *'the cosmic-ray energy spectrum extends beyond* 10^{20} *eV'* [18]. The successor of the Fly's Eye experiment, the High Resolution Fly's Eye Cosmic Ray Detector (HiRes) operated from 1997 to 2006, also using the fluorescence technique. HiRes used larger mirrors (3.72 m^2) and smaller pixels (a camera is composed of 256 PMTs) compared to Fly's Eye, dividing the sky into $1°\times1°$ pixels. The full experiment consists in two sites (HiRes-I with 22 mirrors and HiRes-II with 42 mirrors) separated by 12.6 km with a full azimuth coverage, respectively a field of view from 3° to 17° and 3° to 31° in elevation and a duty cycle close to 10%. The instantaneous aperture of HiRes is around 10,000 km^{2}sr at 10^{20} eV. The HiRes spectrum [19] is presented in Figure 1.23.

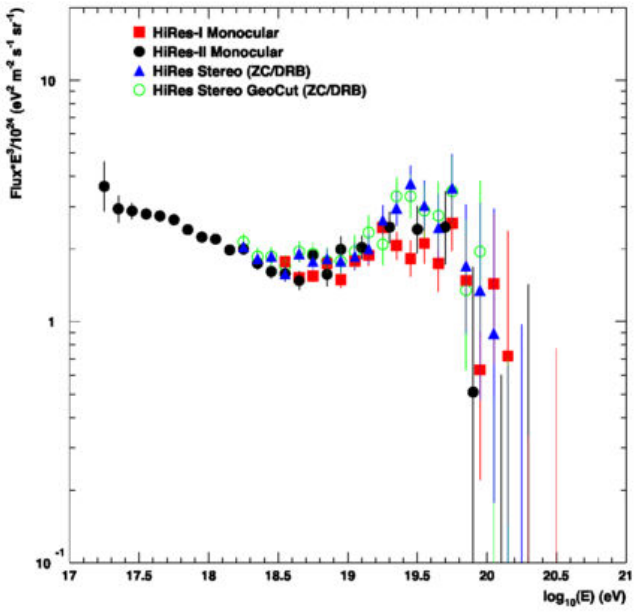

Figure 1.23: Final results of the energy spectrum from HiRes [19].

The spectrum shows clear evidence of a cutoff at the GZK limit energy. The $X_{\max}$ distributions presented in Figure 1.24 are consistent with a light nuclei composition.

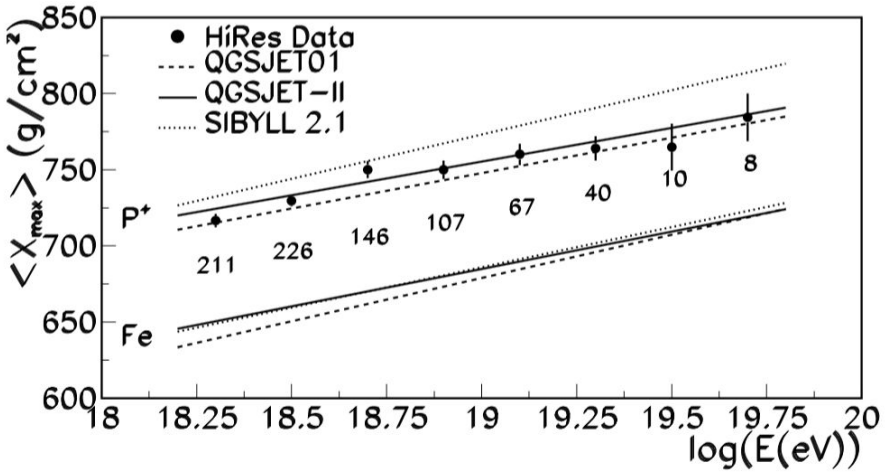

Figure 1.24: The atmospheric depth at which the number of secondary particles is maximum as a function of the energy, compared to the mean proton and iron nucleus behavior predicted by three high energy hadronic interaction models [19].

From this point, the building of experiments with huge detection surfaces were scheduled, such as the Pierre Auger Observatory, in Argentina, with 3000 km^2 and Telescope Array in the United States with 730 km^2, gathering scientists from AGASA

and HiRes, in order to make progress on the energy spectrum potential cutoff, the possible anisotropies and the mass composition at the highest energies via the detection of the extensive air showers.

1.6 Physics of the extensive air showers

From their first detection in the 1930's and the dedicated experiments in the 1940's, the extensive air showers (EAS) became of strong interest because they were the only way to study cosmic rays at the highest energies. Beyond 10^{15} eV, the flux of cosmic particles is indeed very low: the primary cosmic ray cannot be directly detected under a reasonable time scale and instrumental area (1 event / km^2 / year at 10^{19} eV). However, particles arriving on Earth with enough energy will interact with the constituents of the atmosphere and create a shower of secondary particles (around 10^9 particles) which can be detected from the ground.

1.6.1 The constituents of the EAS

An extensive air shower can be divided in three components as summarized in Figure 1.25.

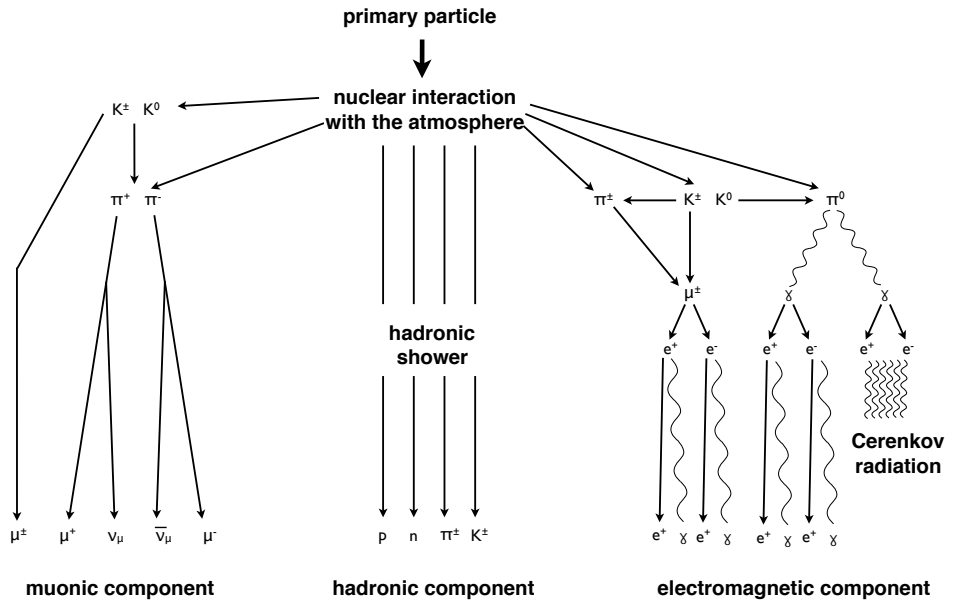

Figure 1.25: Schematic view of an extensive air shower initiated by a hadron [20] (see text for details).

When a highly energetic hadron enters the atmosphere, it eventually interacts with

an air molecule. This interaction will produce several pions (π^0, π^+, π^-), some mesons (K^0, $K^\pm$) and baryons (p,n,..). Depending on the mass of the primary hadron, nuclear fragments can also be produced and they remain very close to the shower axis, forming the hadronic component.

For the charged pions ($\pi^\pm$), decay and interaction mechanisms are in competition, depending of the density of the medium and the Lorentz factor of the particle. The density of the atmosphere decreases almost exponentially as a function of the altitude. In the upper part of the atmosphere, the density is low (1.4×10^{-5} g/cm^3 at an altitude of 30 km which is the mean height of the first interaction point for vertical events at 0.1 EeV) and the Lorentz factor is high because the shower has not yet divided its energy into too many particles, resulting in a high rate of decays comparing to interaction mechanisms. They will produce mostly muons:

$$\pi^\pm \rightarrow \mu^\pm + \nu \tag{1.14}$$

They will feed the muonic component together with kaons decay (which can also decay into pions):

$$K^\pm \rightarrow \mu^\pm + \nu \tag{1.15}$$

$$K^\pm \rightarrow \pi^\pm \rightarrow \mu^\pm + \nu \tag{1.16}$$

This component represents 10% of the total number of particles. In the lower part of the atmosphere, the probability of interaction between charged pions and the medium is more important and they can produce more pions of smaller energy. The neutral pions decay immediately into pairs of photons due to their lifetime of 10^{-16} s:

$$\pi^0 \rightarrow \gamma\gamma \tag{1.17}$$

The photons will initiate a chain reaction, forming the electromagnetic component by creating pairs of electron / positron. The positrons and the electrons will themselves create photons through annihilation and bremsstrahlung. The electromagnetic component accounts for 90% of the total energy of the shower. The evolution of the composition of a shower as a function of the atmospheric depth is presented in Figure 1.26.

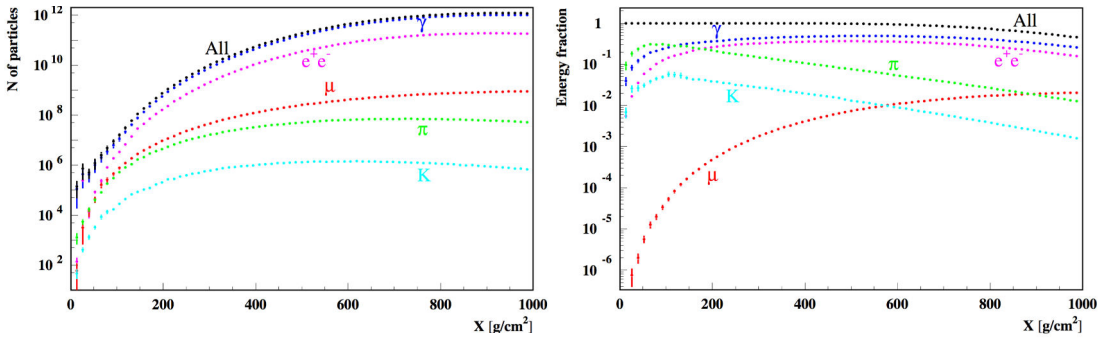

Figure 1.26: Left: Number of particles composing a shower initiated by a 3×10^{20} eV vertical proton as a function of the atmospheric depth, sampled by 13 g/cm^2 steps. - Right: Energy fraction of each type of particle [21].

1.6.2 Geometry of the EAS

1.6.2.1 The longitudinal profile

The Figure 1.27 summarizes the different steps of an EAS development.

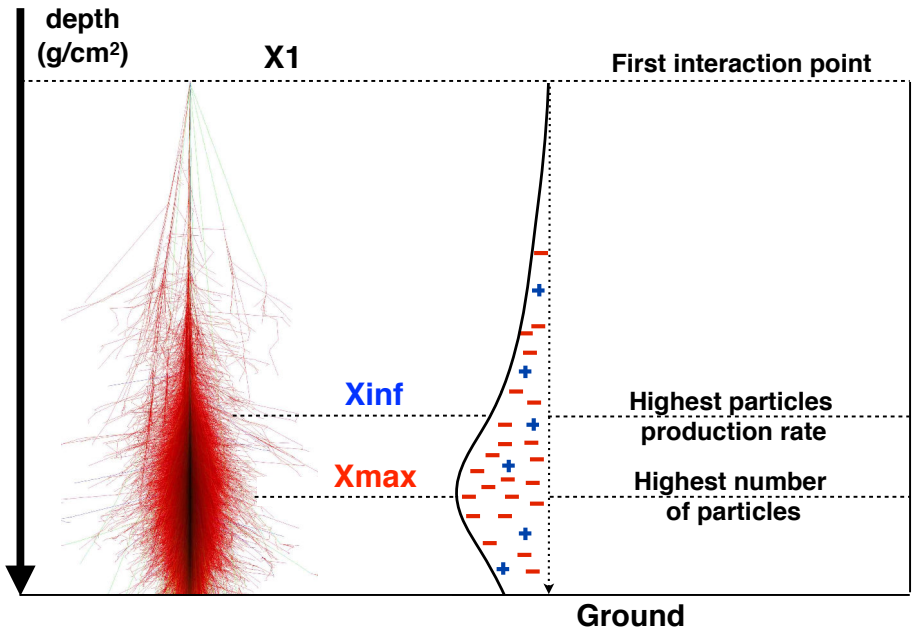

Figure 1.27: The geometry of an EAS with the key parameters X_1, $X_{\max}$, $X_{\inf}$.

The characteristic steps of the shower development are described in term of crossed atmospheric depth. It permits to compare showers with different arrival direction. The

density of the atmosphere is not constant in space (nor in time) and an EAS arriving with a zenith angle of 30° will cross a greater atmospheric depth up to the ground compared to a vertical one. When a high energy cosmic ray enters the atmosphere, after it has crossed a certain quantity of matter, it eventually interacts with dioxygen or dinitrogen molecules. This is the first interaction point: X_1, from which the chain reaction of secondary particles creation is initiated. The number of secondary particles grows to reach the depth X_{inf} at which the particles production rate is maximum. The number of particles as a function of the atmospheric depth is called the longitudinal profile and X_{inf} is the inflection point of the profile. The number of particles still grows up to the depth X_{max} at which the shower reaches its maximum number of particles. Beyond this point, the total energy in the shower front is such that the rate of particles that are absorbed in the medium is greater than the particle production rate. Therefor, the number of particles decreases.

The number of particles in the shower front initiated by any primary as a function of the travelled atmospheric depth is described by the Gaisser-Hillas function [89].

$$N(X) = N_{\text{max}} \left(\frac{X - X_1}{X_{\text{max}} - X_1} \right)^{\frac{X_{\text{max}} - X_1}{\lambda}} \exp\left(\frac{X_{\text{max}} - X}{\lambda} \right) \tag{1.18}$$

Where $N(X)$ is the number of particles at the depth X (in g/cm^2), N_{max} is the maximum number of particles, X_{max} is the atmospheric depth (in g/cm^2) at which $N = N_{\text{max}}$, X_1 is the depth of the first interaction point (in g/cm^2) and $\lambda = 70$ g/cm^2 the attenuation length of the secondary particles in the atmosphere. The maximum number of secondary particles is roughly 5×10^9 for a shower induced by a primary with an energy of 10^{19} eV. The longitudinal profile can also be described by the Greisen - Iljina - Linsley parametrization (GIL) [90], introducing the concept of the age of the shower. It is derived from the Greisen relations [91] and describes the number of electrons and positrons, N, for nucleus-initiated showers [92] as a function of the mass of the primary A and its energy E_p.

$$N(E_p, A, t) = \frac{E_p}{E_\ell} e^{(t(1-2\ln(s)) - t_{\text{max}})} \tag{1.19}$$

With:

$$t = \frac{X - X_1}{X_0}, \quad t_{\text{max}} = a + b\left(\ln \frac{E_p}{E_c} - \ln A \right) \quad \text{and} \quad s = \frac{2t}{t + t_{\text{max}}} \tag{1.20}$$

This parametrization takes also into account the first interaction depth X_1. $X_0 = 36.7$ g/cm^2 is the radiation length via bremsstrahlung of electrons in the air, $E_\ell = 1450$ MeV is a normalization factor, the Greisen formula gives the critical energy $E_c = 81$ MeV (at which the ionization and bremsstrahlung rates become equal). $b = 0.76$ is the value of the elongation rate obtained from adjusted data (see [90]) and $a = 1.7$ is an offset parameter. X is the atmospheric depth in g/cm^2 measured from $X = 0$ g/cm^2 so that

if $X < X_1$, then $s < 0$ and N is undefined, interpreted as no secondary particles are yet created before the first interaction depth.

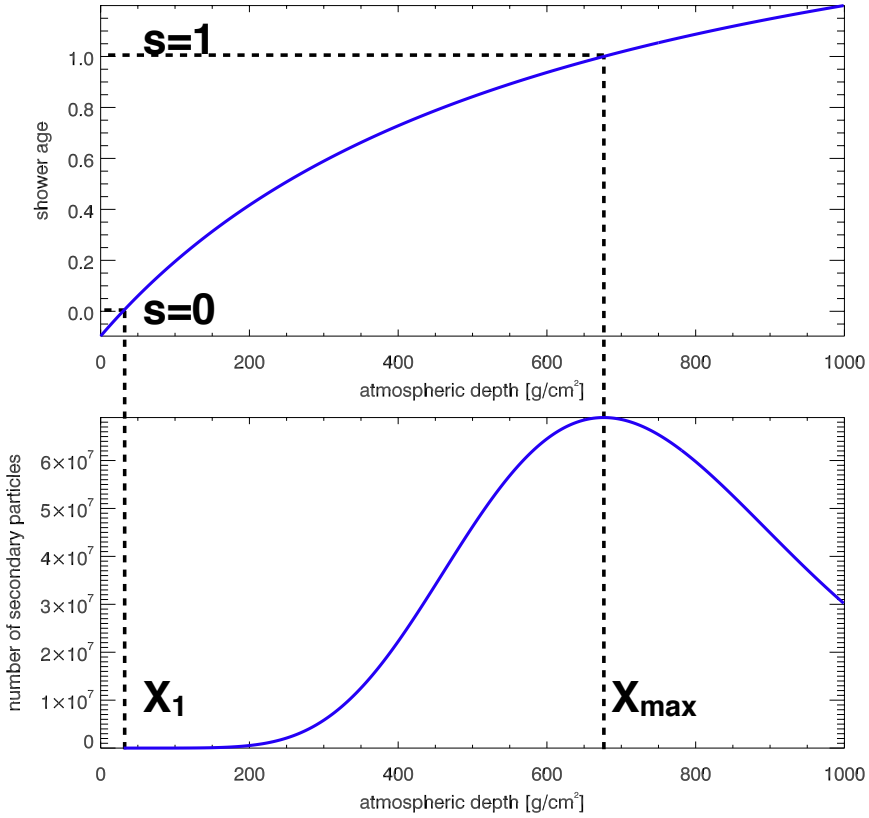

Figure 1.28: Top: the shower age (s) as a function of the atmospheric depth - Bottom: number of secondary electrons and positrons calculated with the GIL parametrization as a function of the atmospheric depth.

Figure 1.28 shows that the shower age is $s = 0$ at the first interaction depth X_1 and $s = 1$ corresponds to $X = X\text{max}$.

1.6.2.2 The lateral profile

The lateral profile, also called the particles lateral distribution function (LDF) accounts for the particle density as a function of the distance from the shower axis and the age of the shower. A lateral distribution has been proposed by Nishimura, Kamata, and Greisen [93] and can be written as:

$$\rho(r) = N.C(s)\left(\frac{r}{r_m}\right)^{s-2}\left(1+\frac{r}{r_m}\right)^{s-4.5} \tag{1.21}$$

With:

$$C(s) = \frac{\Gamma(4.5-s)}{2\pi r_m^2 \Gamma(s)\Gamma(4.5-2s)} \tag{1.22}$$

Where r is the distance to the shower axis in meter, s is the shower age parameter, r_m is the Molière radius, N is the shower size, which is the integrated number of particles in the shower. The Molière radius depends on the characteristics of the material (the air in this case) and is the radius around the shower axis wherein 90% of the secondary particles are located.

1.6.3 Correlation to the primary cosmic ray

The probability of the first interaction depth, X_1, depends of the interaction cross section of the primary hadron with the air. The probability can be written as:

$$\frac{dP}{dX_1} = \frac{1}{\lambda}\exp\left(-\frac{X_1}{\lambda}\right) \quad \text{with} \quad \lambda = \frac{< M_{\text{air}} >}{\sigma} \tag{1.23}$$

Where $< M_{\text{air}} >$ is the atomic mass of the air (in g) and σ is the interaction cross section of the primary hadron with the air (in cm^2).

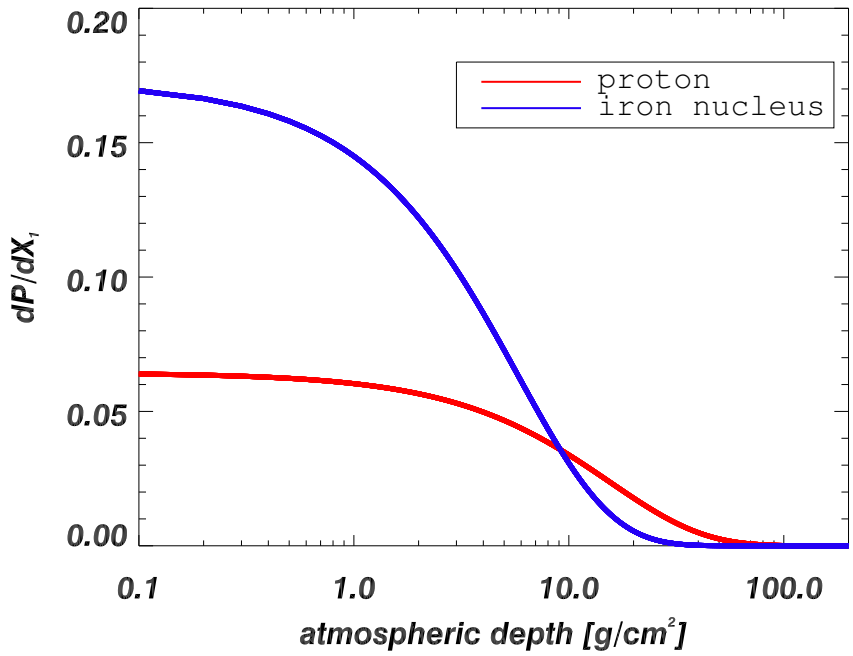

Figure 1.29: p-air and Fe-air probability of the first interaction depth for an energy of 10^{17} eV.

In Figure 1.29, one can see that iron nuclei are more likely to interact quicker (few g/cm^2) than protons after entering the atmosphere. The slope is also smoother in the case of protons, indicating larger fluctuations of the first interaction depth. At any energy, $\sigma_{\text{Fe,air}} > \sigma_{\text{p,air}}$. The depth X_{max} is also highly correlated to the mass of the primary as it depends on the first interaction depth X_1. The Figure 1.30 shows the relation between X_{max} and X_1 according to the GIL parametrization. The difference

between the two depths is 110 g/cm^2 (see Figure 1.30), which seems to be enough to discriminate between protons and iron nuclei as the modern fluorescence detection technique has a resolution of 70 g/cm^2 in monocular detection and less than 20 g/cm^2 in stereo. As the flux of cosmic rays is very low beyond 10^{15} eV, it is not possible to measure X_1 to estimate the mass of the primary, which would be possible only with direct detection. However, it is possible to measure $X_{\max}$ from the ground.

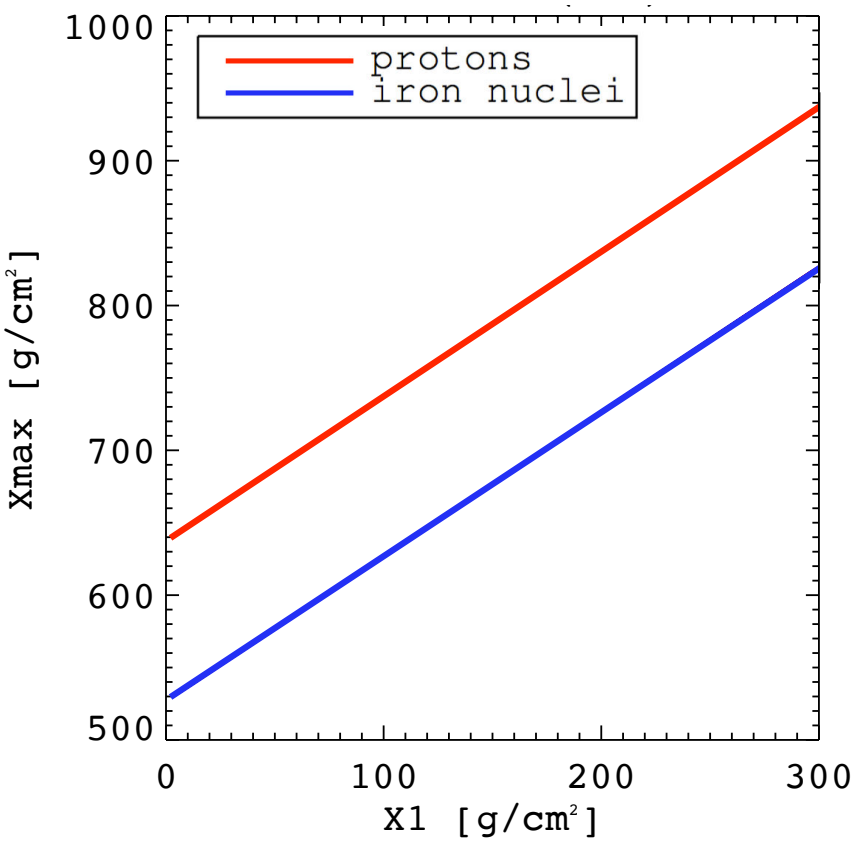

Figure 1.30: $X_{\max}$ as a function of X_1 according to the GIL parametrization of the longitudinal profile.

However, the depth ($X_{\max} - X1$) actually fluctuates and the Figure 1.30 only shows the mean values. First of all, some fluctuations of the first interaction depth are expected and predicted by high energy hadronic interaction models such as QGSJET [94] or EPOS [95]. In Figure 1.31, are shown the distributions of the X_1 depths of 1076 proton and 1076 iron nucleus-induced showers with an energy of 10^{18} eV, simulated with QGSJET. The distributions are clearly overlapping each other. One can calculate the overlapping coefficient (O_c) of the two discrete normalized distributions $f_{\rm p}$ and $f_{\rm Fe}$:

$$O_c = \sum_i \min[f_{\rm P}(X_1^i), f_{\rm Fe}(X_1^i)] \times 100 \tag{1.24}$$

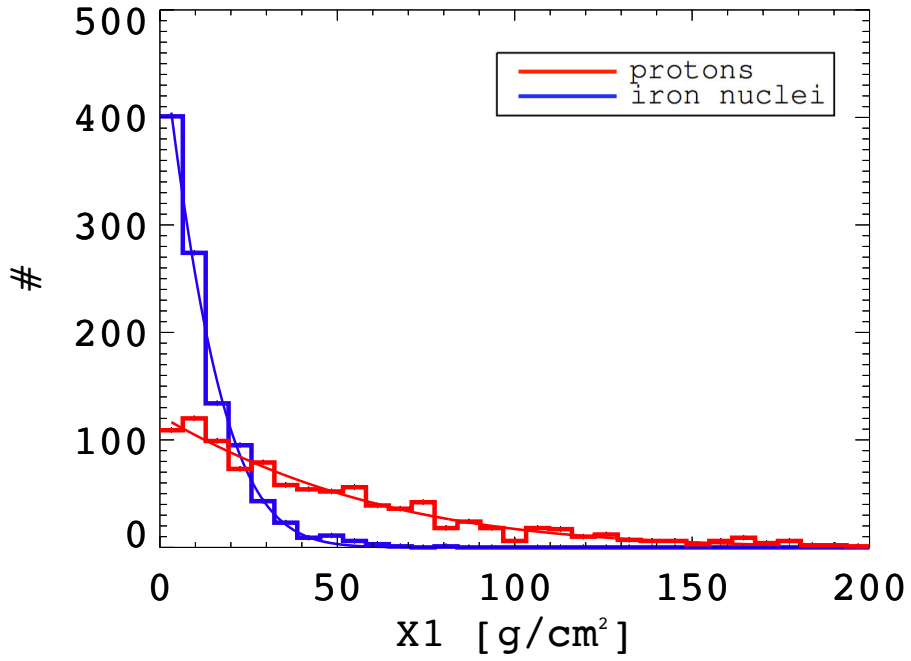

Figure 1.31: X_1 distributions of 1076 protons and 1076 iron nuclei induced shower at 10^{18} eV, simulated with QGSJET-II.04.

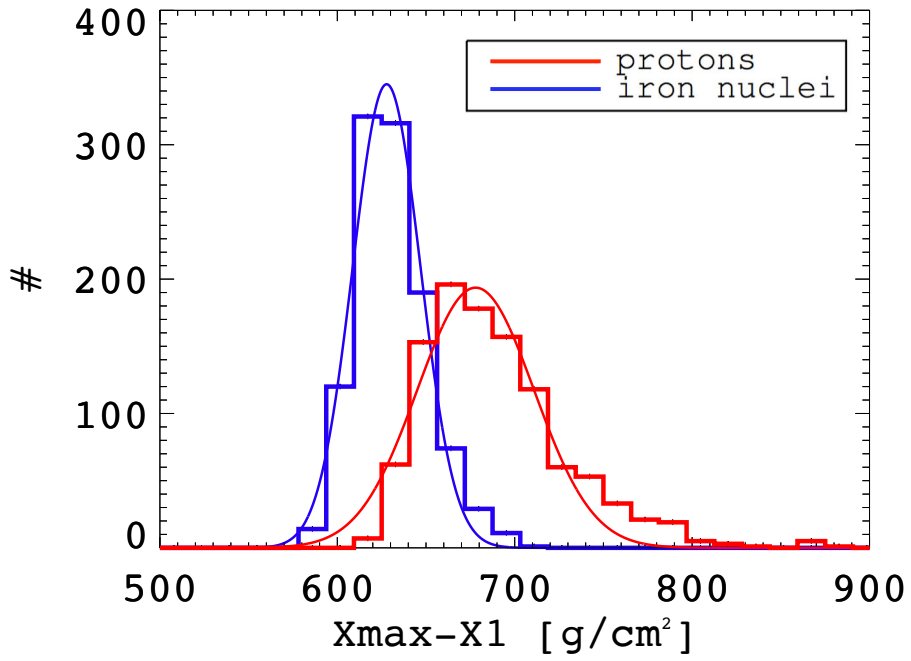

Figure 1.32: $(X_{\max} - X_1)$ distributions for the same set of events than in Figure 1.31.

From the values presented in Figure 1.31, we obtain $O_c \simeq 50\%$, which is the main source of overlapping of the longitudinal profiles of showers induced by protons and iron nuclei. A second source of uncertainty is that the elongation rate $(X_{\max} - X1)$ is not of fixed value. From the same set of events, simulated with QGSJET-II, the distributions of the elongation rate have been obtained and are presented in Figure 1.32. One can see that the elongation rate $(X_{\max} - X_1)$ is fluctuating at fixed energy. The distributions are fitted with a gaussian function with:

$$G(X_{\max} - X_1) = A.\frac{1}{\sigma\sqrt{2\pi}} e^{-\frac{((X_{\max}-X_1)-\mu)^2}{2\sigma^2}} \tag{1.25}$$

And we obtain:

primary	μ	σ
Protons	677.9	32.9
Iron nuclei	627.8	19.1

Table 1.2: Results of the gaussian fit of the $(X_{\max} - X_1)$ distributions.

The fit results give three informations:

a) The elongation rate is not fixed and can vary significantly from one shower to one other, in particular for proton-induced showers. The estimation of the mass of the primary relies on determining the interaction cross section of the primary, that has initiated the shower, with the atmosphere. This is done by the direct measurement of $X_{\max}$ which is strongly correlated to X_1, itself highly correlated to the interaction cross section, thus the mass of the primary. However, $X_{\max}(X_1)$ fluctuates and the distributions for proton-induced showers and iron-induced showers are again overlapping. The overlapping factor for the two distributions is of $O_c \simeq 33.3\%$, which also causes uncertainties to the determination of the mass of the primary from the $X_{\max}$ information. The calculation was made using the values of the histogram rather than the fitted gaussian distributions.

b) The elongation rate is significantly higher in the case of proton-induced showers. According to [96], the electromagnetic component can be described as a superposition of showers initiated by the neutral pions produced during the first interaction of the primary with the atmosphere. The more neutral pions are produced, the more showers are superimposed. The demonstration is made that the elongation rate (and number of particles) of the electromagnetic sub-showers initiated by the first generation of pions is higher. It is also demonstrated that the major part of the electromagnetic sub-showers were generated by these pions. We can conclude that, statistically, more energetic neutral pions are created during the first interaction in the case of proton-induced showers. It appears that the fluctuations of the number of produced π^0 is greater in the case of proton initiated showers than in the case of iron nucleus initiated showers. Thus the

fluctuations of X_{max} are greater in the case of proton initiated showers.

c) The spread of the proton distribution is wider. The fluctuation of the first generation neutral pions is higher in the case of proton-induced showers. Thus, we expect smaller mean X_{max} depth values for iron nucleus induced showers and a sharper distribution, as shown in Figure 1.33.

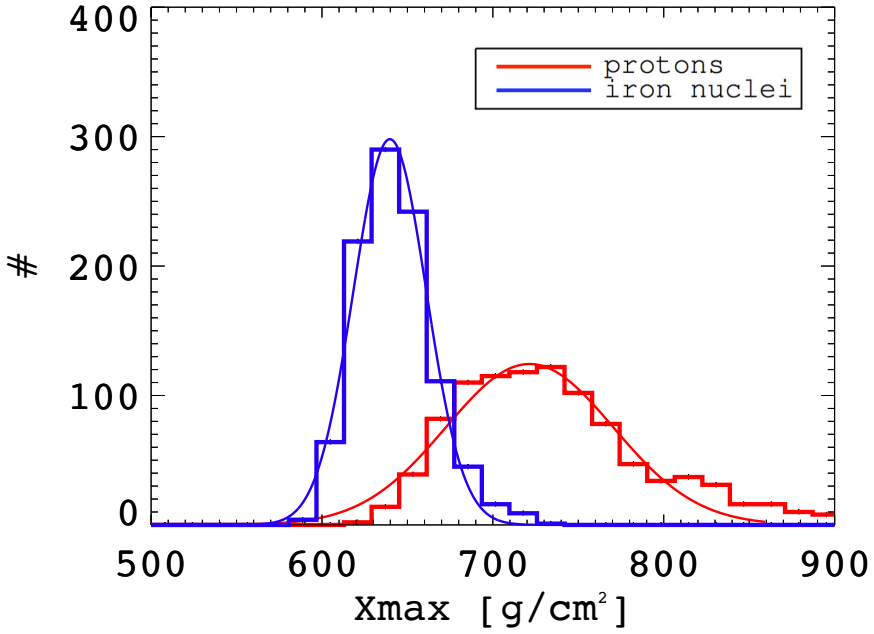

Figure 1.33: X_{max} distributions of the same set of events.

The two primary populations have a different distribution. Both the mean X_{max} and its fluctuations are an estimator of the mass of the primary. From the gaussian fit, we obtain:

primary	μ	σ
Protons	721.482	49.0
Iron nuclei	639.7	21.3

Table 1.3: Results of the gaussian fit of the X_{max} distributions.

The overlapping factor for X_{max} is $O_c \simeq 20.1\%$ at 10^{18} eV, according to QGSJET-II. Thus, the precise determination of the mass of cosmic rays through the detection of the extensive air showers can only be made statistically with a very high number of events, like it was the case at the KASCADE-Grande experiment [97] from 10^{16} eV to 10^{18} eV. To acquire an important rate of detected events, the Pierre Auger Observatory, which the goal is the characterization of cosmic rays above 10^{18} eV, is composed of a detection array covering 3000 km^2. Its main features are discussed in the next section.

1.7 The Pierre Auger Observatory

In order to raise the statistics of detected cosmic rays at the highest energies, giant observatories were built. This is the case of the Pierre Auger Observatory, gathering around 600 researchers, spread over 100 institutes and 15 countries. I took part into this collaboration during the three years of my PhD thesis. The Pierre Auger Observatory is the world's biggest detector dedicated to the characterization of ultra high energy cosmic rays, with a surface of detection that reaches 3000 km^2. It is located in Malargüe in Argentina.

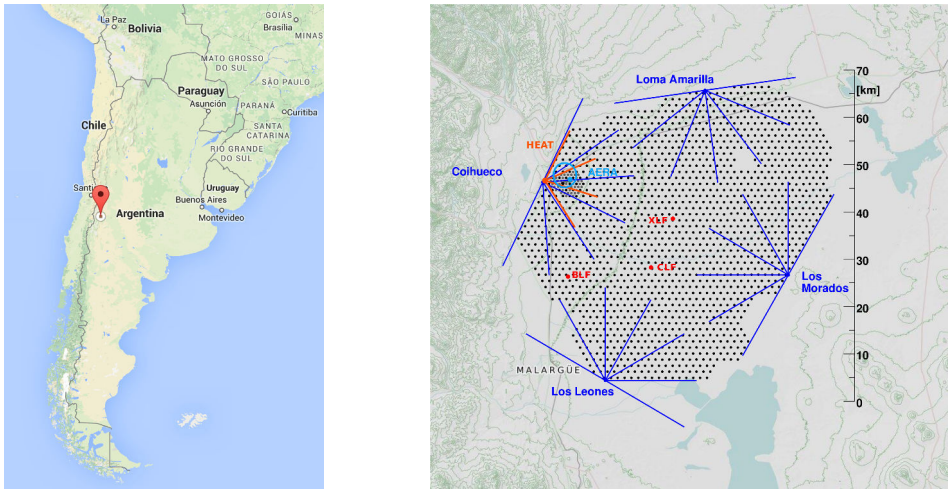

Figure 1.34: left: Location of the Pierre Auger Observatory. - right The detection array.

The data acquisition started in 2004 and the inauguration took place in 2008. It is an hybrid observatory as it is composed of multiple types of detectors. In Figure 1.34 (right) the different features are presented. The black dots represent the 1660 Cerenkov tanks that sample the secondary particles reaching the ground. The blue lines show the azimuthal field of view of the 27 fluorescence telescopes, gathered in four sites. 153 radio stations recording the electric field induced by the development of extensive air showers have been added to the detection array, near the fluorescence site of Coihueco. The emission mechanisms and their detection with the Auger Engineering Radio Array (AERA) are presented extensively in the next chapter.

1.7.1 The fluorescence telescopes

As described in Section 1.5, the fluorescence telescopes receive the light emitted by the nitrogen molecules after their excitation by the interaction with the charged particles of the shower. When falling back to their ground state the fluorescence light is emitted isotropically in the ultra violet domain. The four sites are located in Los Leones, Los Morados, Loma Amarilla and Coihueco with six telescopes housed at each site. At Coihueco three additional telescopes are installed. They can be tilted by up to 29°

upwards and are called the *high elevation Auger telescopes* (HEAT) [98]. HEAT is designed to observed lower energy showers, down to 10^{17} eV. At this energy a shower statistically develops farther away from the ground comparing to showers at higher energies.

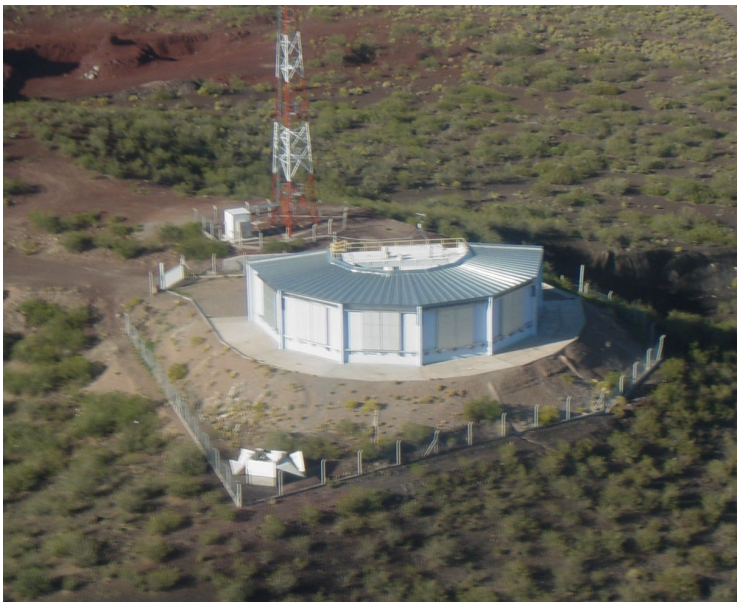

Figure 1.35: Aerial view of one of the four fluorescence sites.

A schematic view of one of these telescopes is shown in Figure 1.36.

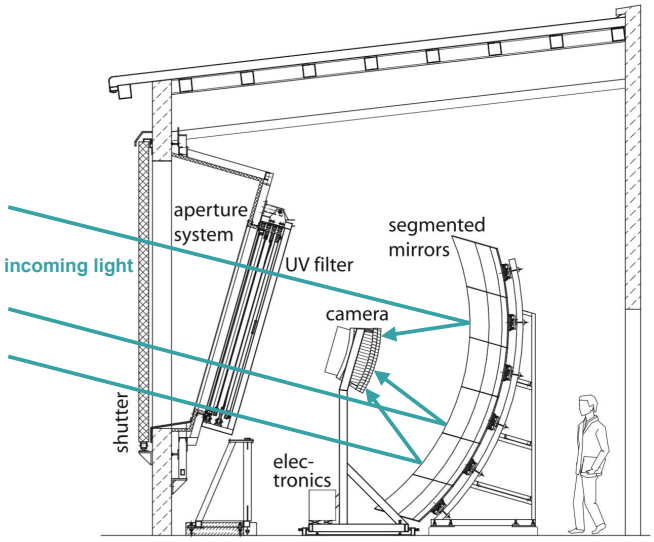

Figure 1.36: Schematic view of a fluorescence telescope of the Pierre Auger Observatory [22].

The fluorescence light is reflected on the mirror to its focus point where is placed a camera composed of 440 photo-multiplier tubes (PMTs). The signals are then digitized and the threshold and geometry triggers are generated.

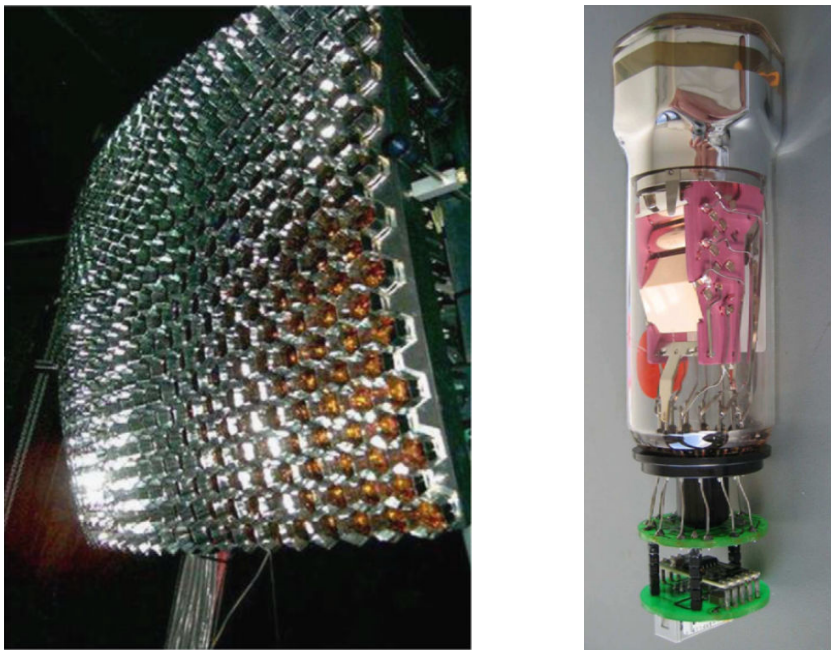

Figure 1.37: Left: Picture of a camera completely assembled with all PMTs and light collectors in place - Right: Picture of a PMT unit [22].

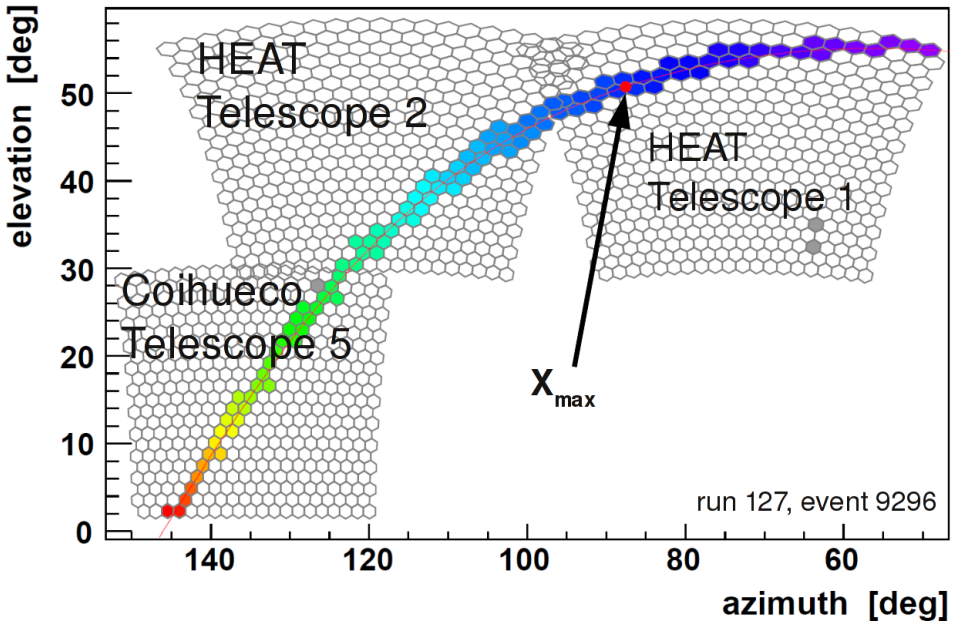

Figure 1.38: Event in the field of view of HEAT (telescopes 1 and 2) and Coihueco (telescope 5) [23].

The field of view of each mirror is of 30° × 30°, then each site provides a 180° coverage in azimuth. Knowing the geometry of the shower, the light collected as a function of time is converted into the energy deposited by the shower in the atmosphere as a function of the slant depth. Figure 1.38 shows an event in the field of view of HEAT (telescopes 1 and 2) and Coihueco (telescope 5). The color of the pixels indicates the arrival time of the light in the PMTs.

The fluorescence technique provides a calorimetric measurement of the development of the shower. The electromagnetically-deposited energy accounts for around 90% of the total energy of the shower [22]. The calorimetric energy of a shower is estimated by fitting a Gaisser–Hillas function [89] to the reconstructed energy deposit profile and integrating it. To constrain the shower axis geometry and timing of the impact of the secondary particles on the ground, at least one surface detection station must be trigged by the same shower measured by the fluorescence telescope [99].

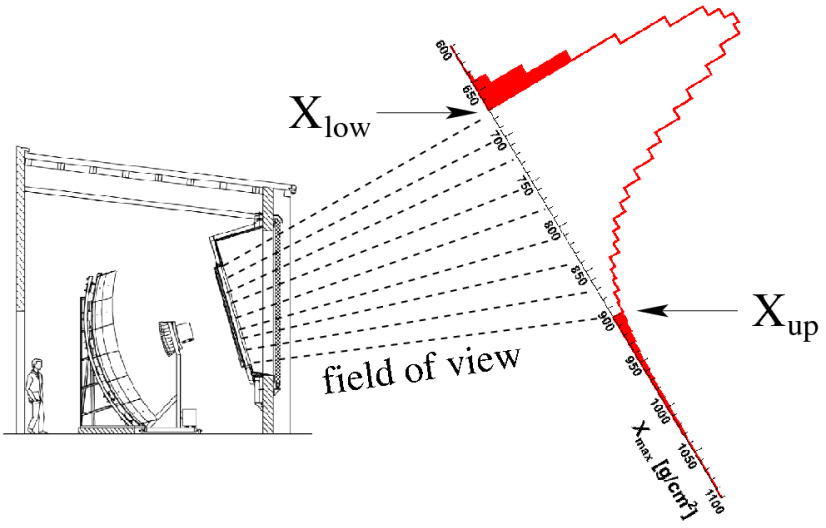

Figure 1.39: Schematic view of the conversion of the received light into the energy deposited as a function of the atmospheric depth, taken from [24]. The field of view of the telescope is delimited by X_{low} and X_{up}.

To calculate the energy deposit, the attenuation of the fluorescence light from the shower to the telescope must be accounted for and the different light sources must be disentangled [100] such as direct and scattered Cerenkov light [101, 102], multiple-scattered light [103, 104] and fluorescence light [105, 106, 107, 108]. The aerosols are also responsible for light scattering and the vertical aerosol optical depth (VAOD) is measured with hourly laser shots. Figure 1.40 (left) shows the measured light at the telescope with detailed contribution of light sources. The mass composition of ultra high energy cosmic rays is currently done with the fluorescence telescopes with the reconstruction of the X_{max} depth, highly correlated with the mass of the primary cosmic ray.

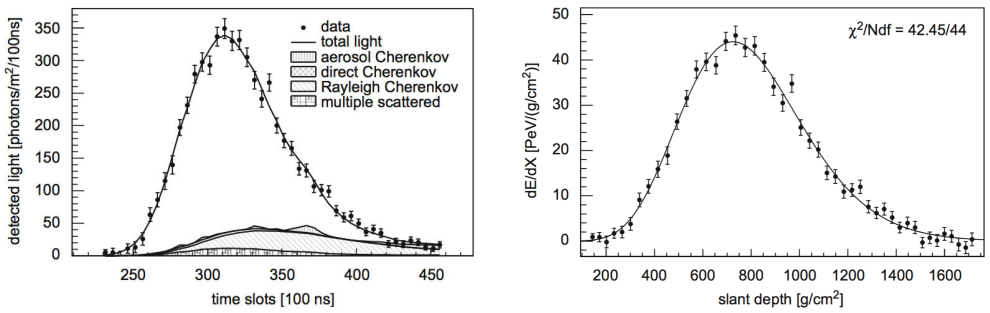

Figure 1.40: Left: An example of the measured light at the telescope - Right: The energy deposit profile reconstructed from the measured light shown in on the left panel. The line shows a Gaisser–Hillas fit of the profile. The reconstruction of the energy of the primary that induced this shower gives 3×10^{19} eV [22].

1.7.2 The Cerenkov tanks

The array of ground detectors of the Pierre Auger Observatory consists in 1660 Cerenkov tanks, spread over a triangular grid. The spacing between the detectors is 1500 m. A schematic view of a tank is shown in Figure 1.41.

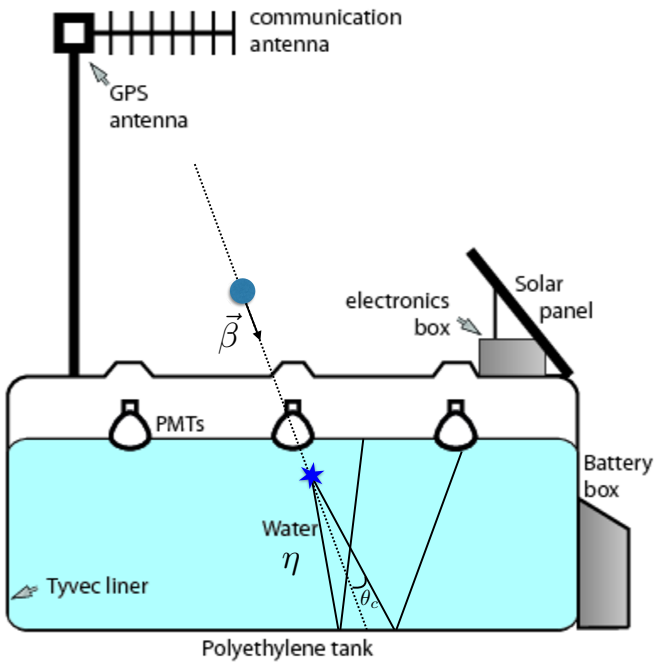

Figure 1.41: Schematic view of a Cerenkov tank, adapted from [25].

The tanks are filled with 12 t of purified water. The secondary charged particles have supra luminous velocity in water and produce a Cerenkov radiation in the tank.

The Cerenkov light is emitted under the angle defined by:

$$\theta_c = \text{acos}\left(\frac{1}{\eta\beta}\right) \tag{1.26}$$

With respect to the particle direction, β is the reduced velocity of the particle and η is the refractive index of the purified water. The Cerenkov light will mostly be emitted downward and reflected upward on the reflective liner that coats the inner part of the tank. The light is finally collected by PMTs (three for each tank) oriented downward. The PMTs and the electronics are powered by batteries charged with solar panels. The GPS module is used for timing detection purposes with a precision of 10 ns. The wireless communication with the central data acquisition system (CDAS) is ensured by the communication antenna. The signal strength is converted into vertical equivalent muons (VEM) which account for the total amount of light that would have been measured if a muon has travelled vertically through the center of the tank. The signal strength is proportional to the number of particles crossing the tank and to their track length. A Cerenkov tank is triggered if all three PMTs measure a signal of at least 3 VEM that would send an alert to the CDAS. If three neighbors tanks have trigged within 25 μs, the data are recorded and form an event. The ground detectors allow the reconstruction of the geometry of the air shower. The arrival timing in the tanks as a function of their relative positions to each other is fitted to a curved particle front model to reconstruct the arrival direction, the time of the impact of the particle core on the ground and the curvature of the particle front. The core impact location is estimated by fitting the signal strength with a NKG function [109] as shown in Figure 1.42. This NKG function describes also the lateral distribution of the signal strength as it is proportional to the number of particles crossing the tanks [110].

$$S(r) = S_{1000}\left(\frac{r}{r_{1000}}\right)^{\beta}\left(\frac{r+r_{700}}{r_{700}+r_{1000}}\right)^{\beta} \tag{1.27}$$

Where $S(r)$ is the signal at the distance to the shower axis r, $r_{700} = 700$ m and $r_{1000} = 1000$ m. S_{1000} is the signal at 1000 m from the shower axis. The fit of the signal strength with this function depends on the orientation of the shower axis and the core position. The minimal signal fluctuations were found to be at a distance of 1000 m [110] from the shower axis so that S_{1000} is used as an energy estimator for the surface detector. The parametrization of the factor β is [110]:

$$\begin{aligned}\beta(\theta) = &-3.35 - 0.125\log S_{1000} + (1.33 - 0.0324\log S_{1000})\sec\theta \\ &+ (-0.191 - 0.00573\log S_{1000})\sec^2\theta\end{aligned} \tag{1.28}$$

The arrival direction is determined by the arrival time fit, the remaining three free parameters are S_{1000} and the coordinates of the core position (x_c, y_c).

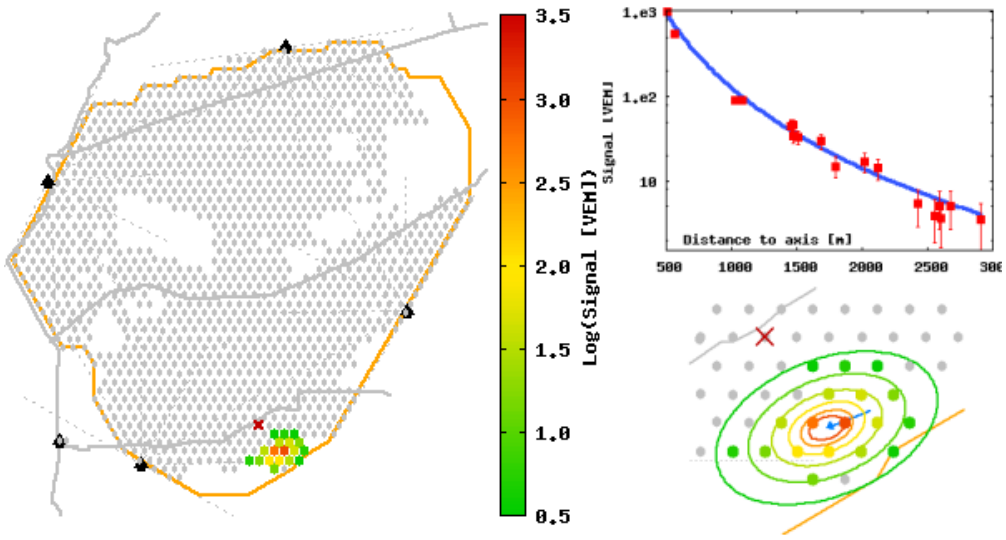

Figure 1.42: An example of a SD event detected by the surface detector array. On the left: particle footprint on the array, the color scale accounts for the signal strength relative to each trigged tank. On the top right: the signal strength as a function of the axis distance, the blue curve is the adjusted NKG function. On the bottom right: zoom on the particle footprint, the color scale accounts for signal strength, thus the particle density at the ground level.

1.8 Actual status of cosmic rays

Thanks to the deployment of giant detections areas like the Pierre Auger Observatory, and to a slightly lesser extent, Telescope Array Project, progress have been made concerning the ultra high energy cosmic rays. However several questions remain and some major results are in disagreement.

1.8.1 Energy spectrum

The energy spectrum of the cosmic rays is presented in Figure 1.43.

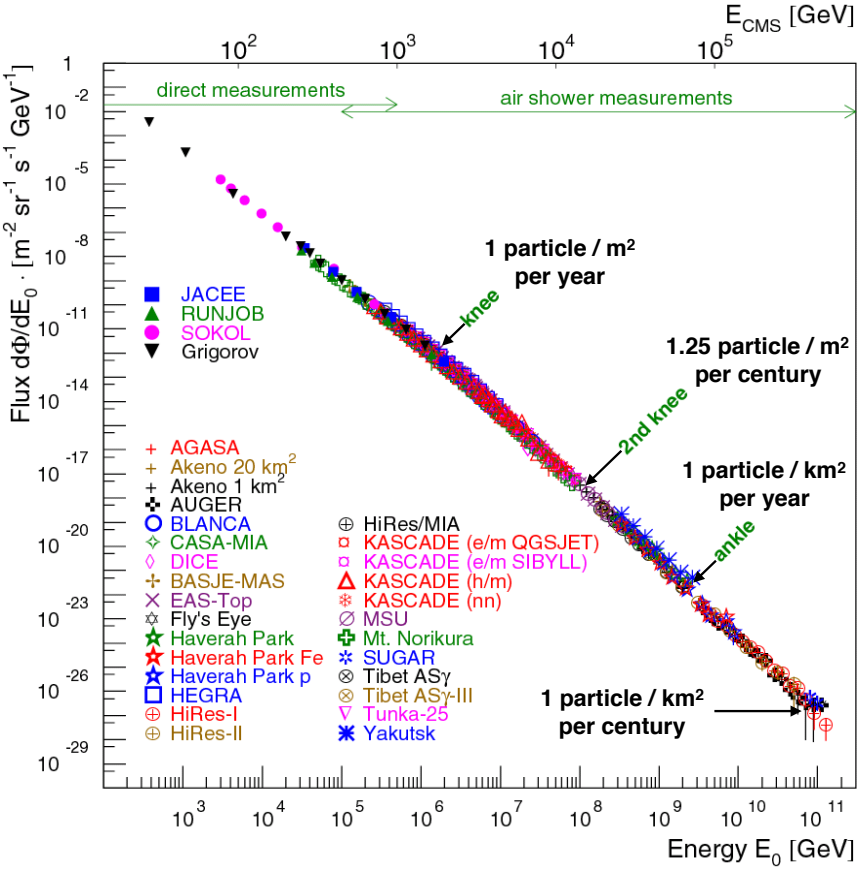

Figure 1.43: Cosmic ray spectrum, compilation of experimental results.

It is a compilation of experimental results from various experiments, regardless the nature of the cosmic rays. The spectrum is described by a power law $\mathrm{d}N/\mathrm{d}E \propto E^{-3}$ of spectral index $\gamma \simeq -3$. The differential flux is given in [m^2 sr^{-1} s^{-1} GeV^{-1}]. At each energy decade, the flux of cosmic rays is divided by 100. A first hardening of the spectrum is observed around 3×10^{15} eV called the "knee". Considering the Hillas criteria, the Larmor radius of the accelerated particle must be smaller than the radius of the accelerator site otherwise it escapes the source. With this principle we have:

$$R_{\mathrm{L}} = \frac{\gamma\beta_{\perp}mc}{ZeB} = 3.1875\frac{\gamma\beta_{\perp}m[\mathrm{GeV/c^2}]}{ZB[\mathrm{Gauss}]} \leq L[\mathrm{pc}] \tag{1.29}$$

With L, the size of the acceleration region, $\beta_{\perp}$ is the reduced velocity of the particle in the direction perpendicular to the direction of the magnetic field and γ is its Lorentz factor. From this equation, considering the worst case scenario where $<\beta_{\perp}> \simeq 1/3\beta$, and $\beta \simeq 1$, we obtain:

$$E \leqslant E_{\mathrm{max}} = \frac{Z.B[\mathrm{Gauss}].L[\mathrm{pc}]}{3.1875}\frac{1}{3} \tag{1.30}$$

It is interesting to notice that the maximum energy does not depend on the mass of the particle at rest. For protons we obtain $E_{\mathrm{max,p}} \simeq 3.2 \times 10^{15}$ eV, considering a magnetic field of 1μGauss and 1 pc for galactic supernovae. Beyond this energy, galactic protons escape the sources and less particles are received. Heavier nuclei are present in smaller quantities and will also escape the galactic sources of acceleration with higher energy. Iron nuclei are the last species to escape at around $E_{\mathrm{max,Fe}} \simeq 10^{17}$ eV. Beyond this point, galactic cosmic rays are no longer expected and this assertion is observed at 10^{17} eV: the second knee. Considering the Hillas criteria, the ankle region at 4×10^{18} eV corresponds to the energy at which particles start to escape the galaxy because their Larmor radius is larger than the size of the Milky Way. Beyond this energy, the detected cosmic rays are expected to come from extra galactic sources.

1.8.2 Sources and acceleration mechanisms

The most considered acceleration mechanism is the first order Fermi's acceleration mechanism, introduced by Bell in 1978 [111]. In this model, the magnetic cloud is replace by a shock wave. A shock wave is created when matter travels faster than the speed of sound. The principle of the mechanism can be resumed as follow, according to [26], where a review of the subject can be found. A charged particle can diffuse on either sides of the shock as depicted in Figure 1.44. The shock propagates with a velocity β_{sh} into the undisturbed medium (upstream). The velocity of the shocked region (downstream) relative to the upstream one is noted β_{rel}. A particule can cross the shock surface from both sides. The initial energy before the crossing at an incidence angle $\theta_{\rightarrow \mathrm{d}}$ is noted E_{i} and the final energy after the re-crossing at an angle $\theta_{\rightarrow \mathrm{u}}$ is noted E_{f}. The magnetic irregularities near the shock wave allow a charged particle to cross the shock several times through magnetic scattering process.

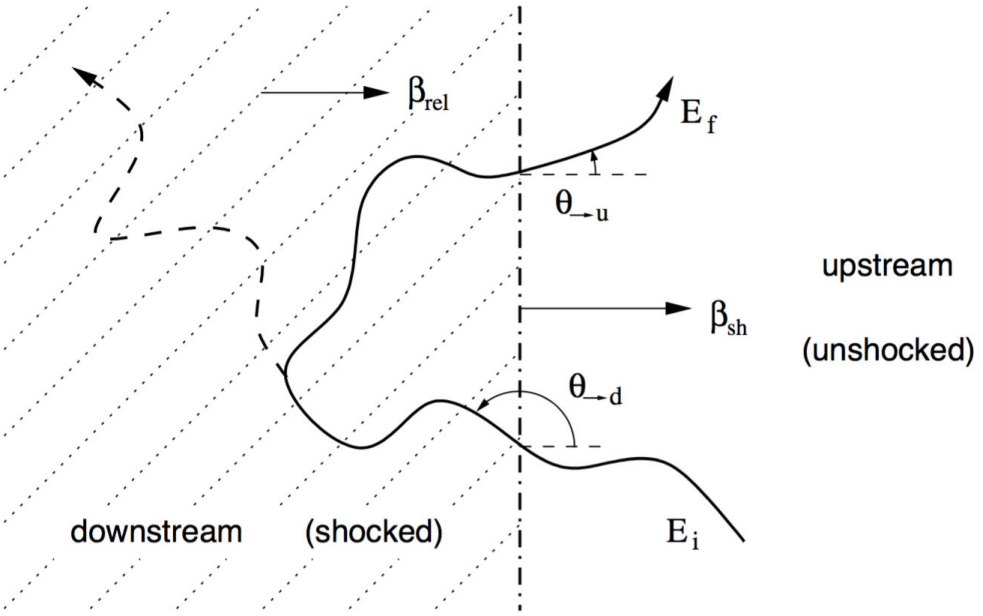

Figure 1.44: Sketch of the shock acceleration mechanism, taken from [26] (see text for details).

One consider the case of a relativistic particle whose initial and final energies expressed in the upstream frame are noted E_i and E_f and E'_f and E'_f in the downstream frame from the Lorentz transformations. The Equation (1.5) giving the relative energy gain for the first order Fermi mechanism can be applied. However in this case, there is only head-on collisions between the particle and the shock wave. For a non-relativistic shock, ($\beta_\mathrm{sh} \ll 1$), the angular distribution of the incidence angles can be considered as isotropic, thus we obtain:

$$< \cos\theta'_{\to \mathrm{u}} > \simeq 2/3 \quad \text{and} \quad < \cos\theta_{\to \mathrm{d}} > \simeq -2/3 \tag{1.31}$$

Using Equation (1.5) with these values leads to the expression of the relative energy gain per crossing cycle:

$$\left\langle \frac{\Delta E}{E} \right\rangle = \frac{4}{3}\beta_\mathrm{rel} \tag{1.32}$$

One can express the relative gain as a function of the shock velocity ratio $r = \beta_\mathrm{u}/\beta_\mathrm{d}$ and the reduced velocity of the shock β_sh so that:

$$\left\langle \frac{\Delta E}{E} \right\rangle = \frac{4}{3}\frac{r-1}{r}\beta_\mathrm{sh} \tag{1.33}$$

The particle gains an energy proportional to the shock wave reduced velocity $< \Delta E/E > \propto \beta_{sh}$, it is thus a first order acceleration mechanism. The energy spectrum obtained for such acceleration mechanism is given by:

$$N(E) = (x-1)\frac{N_0}{E_0}\left(\frac{E}{E_0}\right)^{-x} \quad \text{with} \quad x = \frac{r+2}{r-1} \tag{1.34}$$

The Fermi's first order acceleration mechanism solves the problems of the second order mechanism. First, this is a first order mechanism, the speed of the shock created by a supernova ($\beta_{sh} \sim 10^{-2}$) is greater than the typical speed of the Fermi's clouds ($\beta_{cloud} \sim 10^{-4} \rightarrow \beta^2_{cloud} \sim 10^{-8}$). For the first order mechanism, the acceleration time $\tau_{acc} \sim t_{cycle}/\beta_{sh} \sim 10^6$ seconds for a typical value of $t_{cycle} \sim 10^4$ secondes. In comparison, the acceleration time of the first order mechanism is 10^9 years. The reduction of the acceleration time solves the injection problem. The Larmor radius of the particles must be larger than the thickness of the front to be seen as a sharp discontinuity by the particles. The thermal distribution of the downstream medium is sufficient to provide protons with enough energy to be accelerated by this process. For a strong shock wave $r \rightarrow 4$ leading to a spectral index $x = 2$, the energy spectrum is then very close to the experimental observations. By adjusting the parameters B, L and Z, one can calculate the maximum energy that can acquire a particle in different types of sources, as shown on the Hillas diagram in Figure 1.45.

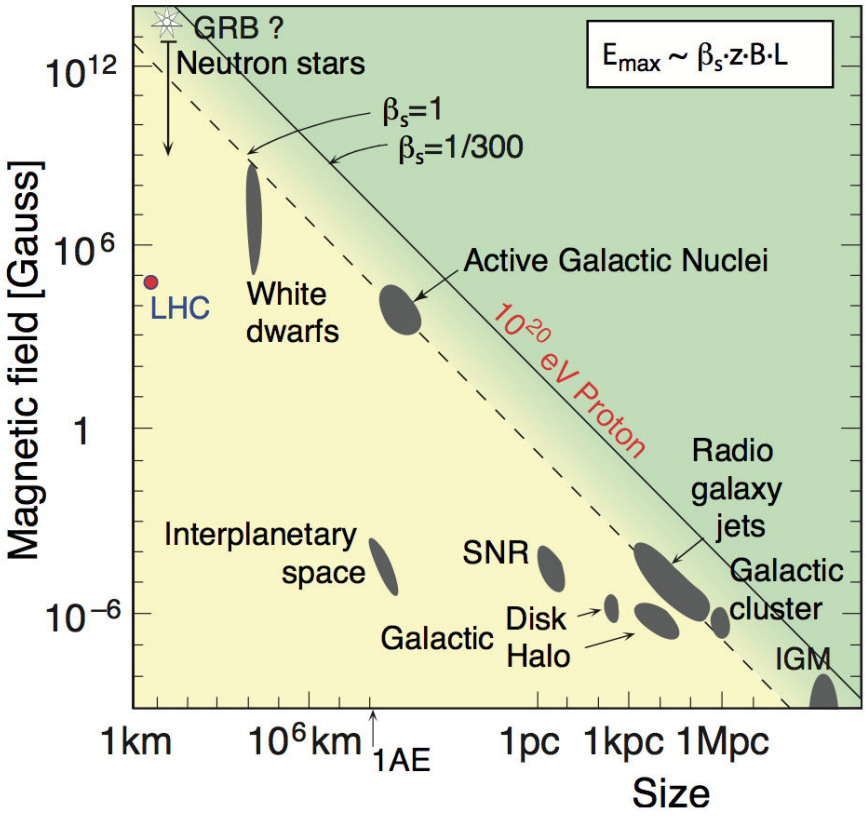

Figure 1.45: The Hillas diagram [27] (see text for details).

Very few objects reach the conditions to accelerate protons at an energy beyond 10^{20} eV. The active galactic nuclei are a solid candidate as a source of cosmic rays at the highest energies. On the Hillas diagram, known astrophysical objects are displayed as a function of their magnetic field intensity and their size. The necessary conditions to produce a proton with an energy of 10^{20} eV are shown by the straight lines for different values of the velocity of the shock wave. It appears that none of the known objects seem to be able to match the conditions for small shock velocities. Only relativistic shocks are compatible with the characteristics of theses objects.

1.8.3 Flux suppression

In the northern hemisphere a flux suppression, known as the energy cut-off, is observed at the HiRes experiment as well as at the Telescope Array Project. The most recent energy spectrum measured by the Telescope Array collaboration is presented in Figure 1.46. In the south hemisphere, the Pierre Auger Observatory also observes the cut-off, as shown on the Auger spectrum in Figure 1.47. The existence of the cutoff is now clearly established. However, the origin of the cutoff is still debated. The GZK limit is a serious candidate ($E_{\mathrm{GZK}} = 4 \times 10^{19}$ eV) but the flux suppression could also be due to a limit of the acceleration mechanisms or an extinction of the sources.

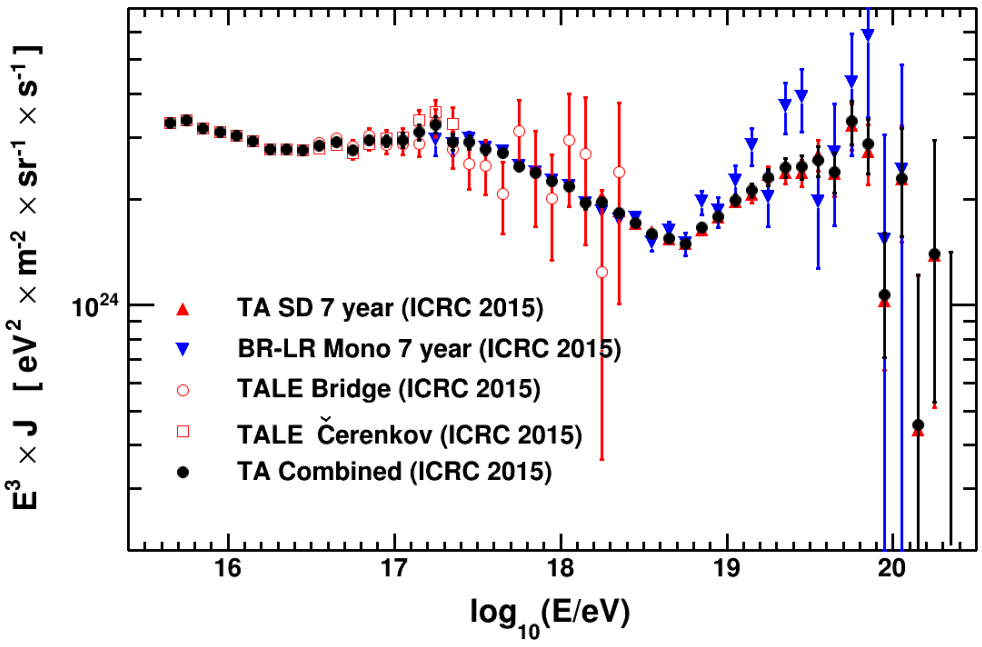

Figure 1.46: Results of the Telescope Array Project on the energy spectrum [28].

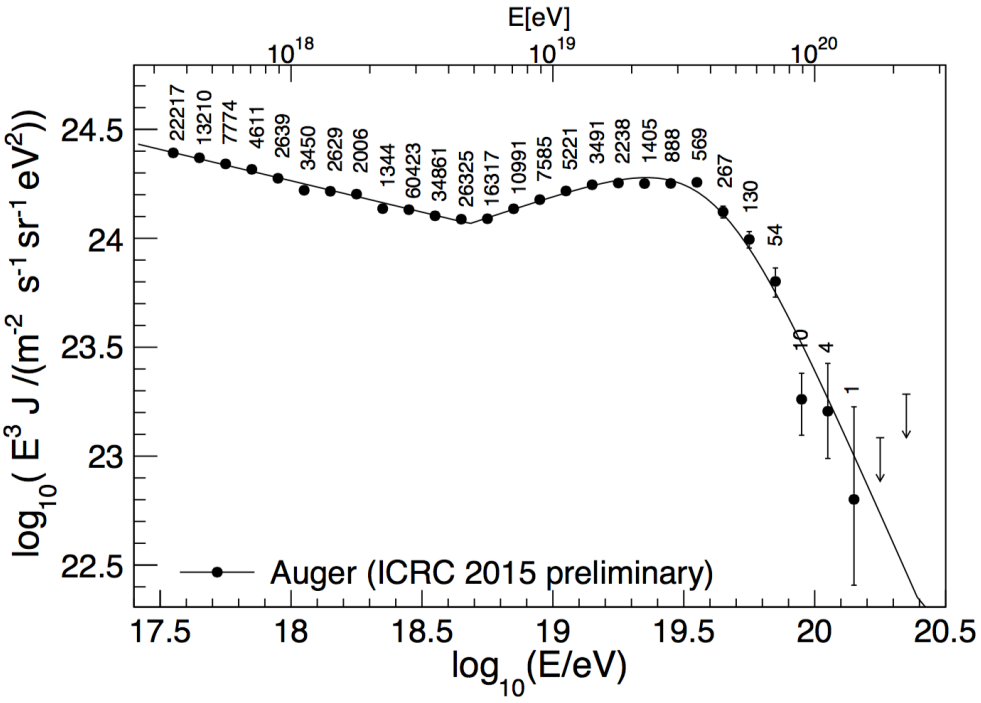

Figure 1.47: Results of the Pierre Auger Observatory on the energy spectrum [29].

The results of the three experiments are presented below:

Experiment	HiRes	Telescope Array Project	Pierre Auger Observatory
cutoff energy (eV)	$(5.6 \pm 0.7) \times 10^{19}$	$(6.0 \pm 0.9) \times 10^{19}$	$(4.2 \pm 0.1) \times 10^{19}$
significance	$5.3\ \sigma$	3.9σ	$> 20\sigma$

Table 1.4: Energy at which the flux suppression is observed for HiRes, Telescope Array and the Pierre Auger Observatory.

1.8.4 Anisotropy

The HiRes experiment tested the excess of arrival direction in correlation with active galactic nuclei (AGN) of the Veron catalogue [112]. Nothing was found beyond expected random coincidences and no correlation was found either with large scale structure. Above $4 \times 10^{19} eV$, the data are compatible with an isotropic flux with a 95% confidence level. The excess map produced by Telescope Array Project with seven years of data is presented in Figure 1.48. An excess if observed around the Ursa Major cluster with a significance of 5.3σ for $E > 54$ EeV. The excess is consistent with random fluctuations and the post-trial chance for the excess is of 3.7×10^{-4} with a sig-

nificance of 3.4σ. Several candidate sources have been proposed within the Ursa Major cluster but the statistics remains too low to draw any conclusions as the uncertainties remain about the deflection of cosmic rays in the galactic and extragalactic magnetic fields.

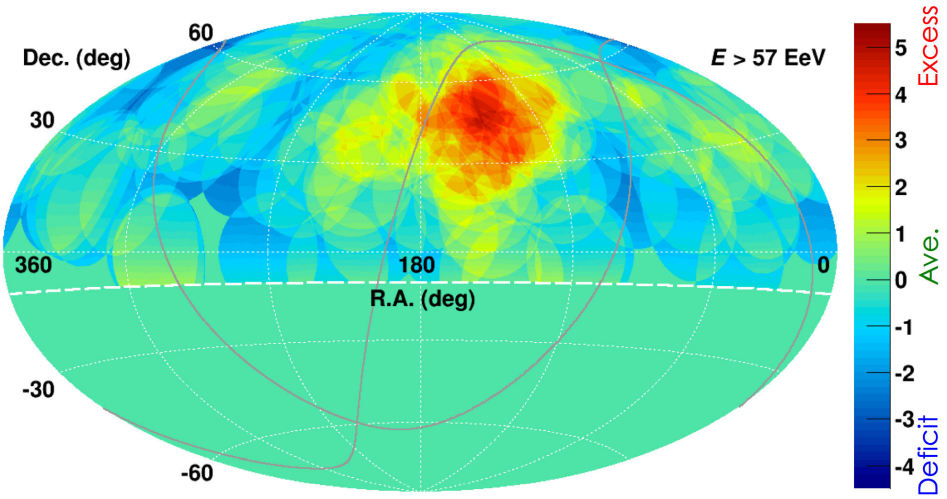

Figure 1.48: Sky map in equatorial coordinates highlighting the excess and the deficit of cosmic rays according to their arrival directions at the Telescope Array experiment, compared to isotropic expectations. The size of the angular window is 20° [28].

The data of the Pierre Auger Observatory in the southern hemisphere are shown in Figure 1.49. An excess is present with a significance of 4.5σ but the data remain compatible with an isotropic flux for $E > 54$ EeV. Nowadays it is still not clear if indeed there are anisotropies in the flux of cosmic rays. For the moment, the data are compatible with an isotropic flux but this statement may change in the near future. For highly energetic light nuclei, the arrival direction (the orientation of the shower axis) can be associated to the location of the source. Indeed, galactic and extra-galactic magnetic fields induce a Lorenz force on the cosmic rays, which are charged particles and heavy nuclei with a high electric charge (Z = 26 for an iron nuclei) will suffer larger deviations. The Larmor radius (or gyroradius) for a relativistic particle is defined as:

$$R_{\mathrm{L}} \propto \frac{\gamma mc^2 \beta_{\perp}}{Z.e.B}[\mathrm{pc}] \tag{1.35}$$

With $\beta_{\perp}$, the reduced velocity in the direction perpendicular to the direction of the magnetic field. For an energy of 10^{20} eV the Larmor radii for a proton and an iron nuclei are $R_{\mathrm{L,P}} \simeq 1$ Mpc and $R_{\mathrm{L,Fe}} \simeq 40$ kpc and the ratio $R_{\mathrm{L,P}}/R_{\mathrm{L,Fe}} \simeq 26$. Proton astronomy

seems more likely possible than with iron nuclei. However very little is known of the direction and the magnitude of the extragalactic magnetic fields.

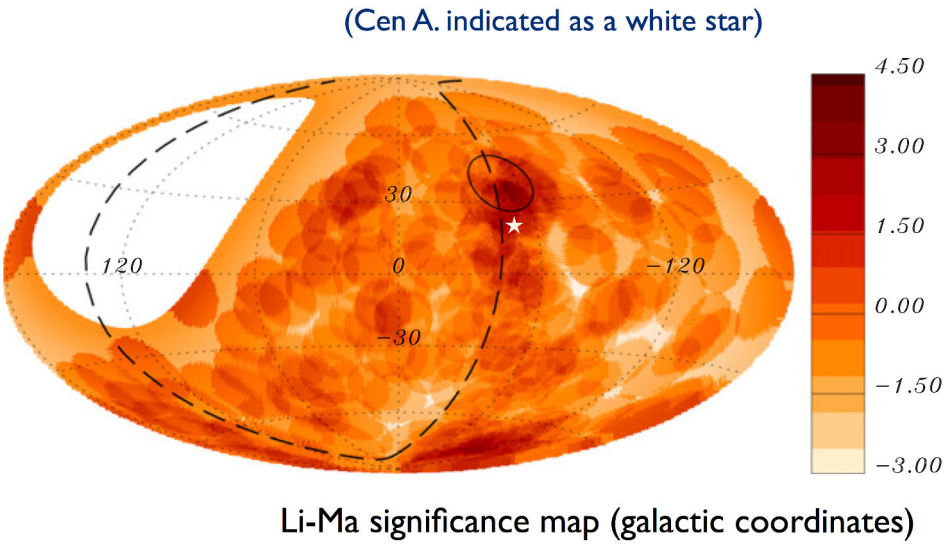

Figure 1.49: Sky map in galactic coordinates highlighting the excess and the deficit of cosmic rays according to their arrival directions at the Pierre Auger Observatory, compared to isotropic expectations. The size of the angular window is 20° [29].

1.8.5 Composition

The mass composition is deducted statistically by the direct measurement of the shower maximum $X_{\max}$. The moments measured by the Pierre Auger Observatory are presented in Figures 1.50 and 1.51. The data of the Telescope Array experiment (see Figure 1.52) are compatible with the data from the Pierre Auger Observatory up to an energy of $\mathrm{Log}_{10}(E) < 18.5$ eV. Beyond this energy, the data of the Telescope Array experiment show a rather light composition but are compatible with the data from the Pierre Auger Observatory within the uncertainties. The data show a composition heavier than protons above 3×10^{18} eV together with a modification of the slope of the spectrum. The RMS($X_{\max}$) values are shown in Figure 1.51 and also indicate a heavy composition. The mass composition of cosmic rays at the highest energies is not clearly established. If the cosmic rays beyond the GZK cutoff are composed of protons, particle astronomy would be possible due to their very low deviation in the extra galactic magnetic field comparing to iron nuclei, for which astronomy would be impossible.

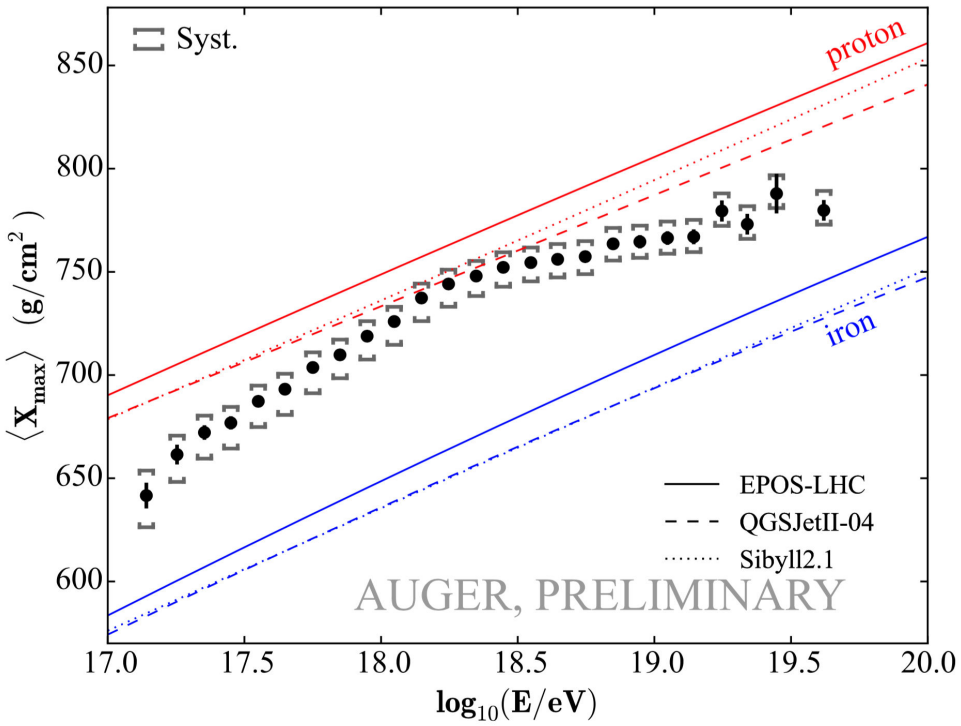

Figure 1.50: Measured <X_{max}> at the Pierre Auger Observatory [29].

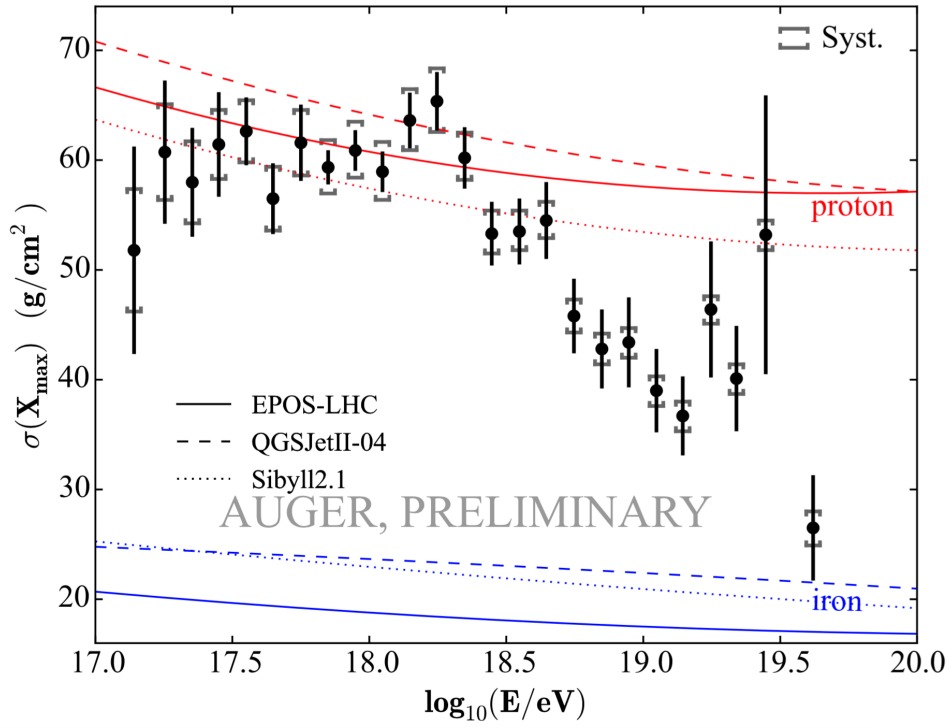

Figure 1.51: RMS(X_{max}) at the Pierre Auger Observatory [29].

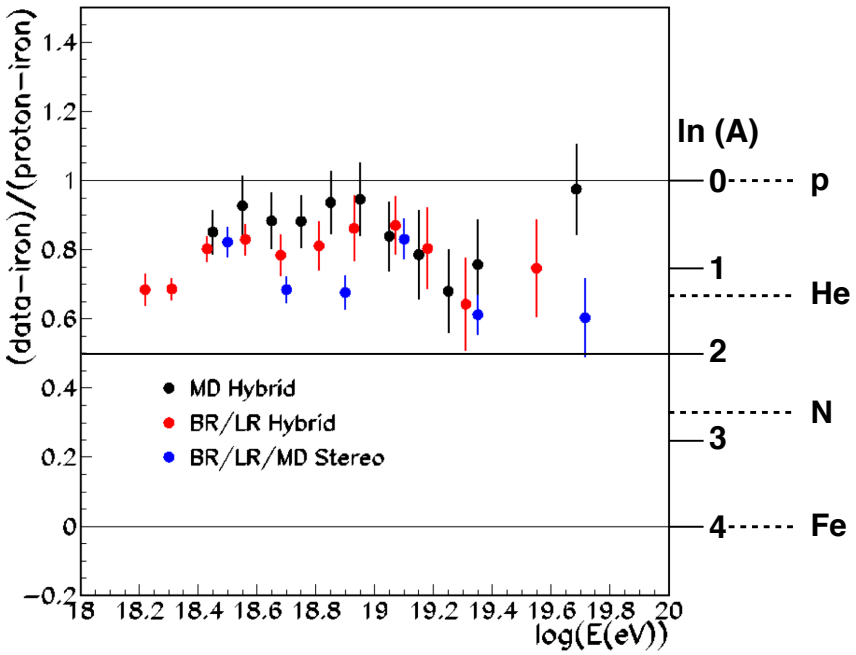

Figure 1.52: Mass composition estimation at the highest energies from Telescope Array [28].

1.9 Conclusions

After more than 100 years of investigations of cosmic rays, very rich in discoveries, several interrogations remain at the highest energies. A clear flux suppression is observed around 4×10^{19} eV but the origin of the cutoff is not established. In the southern hemisphere, the arrival directions are compatible with an isotropic flux whereas in the northern hemisphere an excess (compatible with statistical fluctuations) is observed in the region of Ursa Major. For the moment the data are compatible with an isotropic flux. The mass composition is not clearly determined. It is statistically determined from the measurement of the longitudinal profiles of the showers with fluorescence detectors. The main difficulty is the lack of statistics at the highest energies added to the low duty cycle of the fluorescence technique, which is around 14%. A significant improvement of the Cerenkov tanks of the Pierre Auger network is planned; a scintillator will be added on the top of each tank to get a better sensitivity for the electron/muon ratio of the hadronic air showers, in order to estimate the cosmic ray mass and determine why the particle flux is suppressed beyond 30 EeV. In the next chapters, I will introduce an other detection technique sensitive to the whole EAS profile, as the fluorescence technique, and with a duty around 100%. Although the acceptance and efficiency of the radio detectors have not been studied extensively. This technique is the radio detection

of the electric field emitted by an EAS during its development. In particular, I developed a method using only the radio signal and its simulation to reconstruct the characteristic depth X_{max} in order to significantly raise the number of detected events and reduce the error bars of the X_{max} measurement.

CHAPTER 2

EAS induced electric field

Contents

2.1 Radio detection

2.1.1 The pioneer experiments

After the detection of air Cerenkov emission in coincidence with EAS by Jelley and Galbraith [76], Jelley proposed the idea of an emission in the radio domain. At that time, the shower was though to contain an equal number of positrons and electrons, leading to destructive interferences of the two components. However, in 1962 Askaryan, suggested an excess of electrons in the particle front of air showers caused by the annihilation of the positrons [113]. Due to the excess, inducing a net negative charge, an emission in the radio frequencies is possible. The charge excess effect is presented in more details in Section 2.2.2. The first radio detection experiment was installed by Jelley and Smith at Jodrell bank, near Manchester [114] in 1964. Other experiments were deployed like at Haverah Park [115] and other locations. The experimental setup was essentially composed of oscilloscopes, of which pictures were taken, triggered by particle detectors. In 1966, F.D. Kahn and I. Lerche worked on a more complete description of the mechanisms susceptible to produce a radio emission [116]. They proposed three mechanisms:

- the charge excess mechanism, proposed by Askaryan
- an electric dipole, created by the separation of the electrons and positrons caused by the Lorentz force induced by the geomagnetic field
- under the influence of the Lorentz, force the permanently created electrons and positrons are deviated in opposite directions. It induces a transverse current with respect to the direction of propagation of the shower.

The electric field emission due to the variation of the transverse current is known as the geomagnetic effect and is presented in more details in Section 2.2.1. The early experiments permitted to establish correlations between the radio signal and the shower parameters. A detailed review of the pioneer experiments has been made by Allan in 1971 [117]. From the detections operated at Haverah Park, Allan composed a set of a hundred of events with an energy between 10^{17} eV and 10^{18} eV, a zenith angle lower than 35° and antennas closer than 300 meters from the shower axis. Several conclusions were drawn from the analysis of this data set [117]:

- the strength of the electric field is proportional to $\sin\alpha$, where α is the geomagnetic angle (the angle between the geomagnetic field and the shower arrival direction).
- measurements in different polarizations show that the geomagnetic effect is the dominant mechanism.
- the strength of the electric field is proportional to the energy of the primary cosmic ray.

- the strength of the electric field as a function of the distance to the shower axis (lateral profile) can be described by an exponential decrease.

Allan proposed the following parametrization of the lateral profile of the electric field for $\theta \leqslant 35^\circ$ and $\nu = 54$ MHz:

$$E(d) = 20 \left(\frac{E_p}{10^{17}\text{eV}} \right) \sin\alpha \cos\theta \exp\left[-\frac{d}{d_0(\nu,\theta)} \right] \mu\text{V m}^{-1}\,\text{MHz}^{-1} \tag{2.1}$$

Where d is the distance to the shower axis, E_p is the energy of the cosmic ray and d_0 is the distance from the shower axis at which the fluctuation of the strength of the electric field are minimum. This equation will be used extensively by the next experiments. Significant disagreements of the measurement of the electric field strength between the different experiments were obtained. The lack of accuracy of the radio detection did not allow the estimation of the depth of the shower maximum or the energy of the primary. Most of the radio detection experiments ended in the 1970's due to technological limitations, in favor of the fluorescence and particle detectors. Since the 2000's, new radio experiments were built, taking benefit of the technological progress during the 1980's and the 1990's. The first experiments of the digital era are CODALEMA [118] and LOPES [119] whose prototypes have proven the potential of the radio detection. Since then, considerable progress have been made in the understanding of the emission mechanisms and the correlation of the features of the electric field to the characteristics of the extensive air showers.

2.1.2 The modern detection

2.1.2.1 Basic principles

The radio instrument

A radio station is composed of a radiator (the antenna), a signal amplifier, a digitizer, a GPS device (for timing and position) and way of communication to a central data acquisition system. Radio detection experiments such as AERA [120] and CODALEMA share common features from the data acquisition to the production of high level data. These two experiments are described in the next sections. A typical logical acquisition chain is described in Figure 2.1.

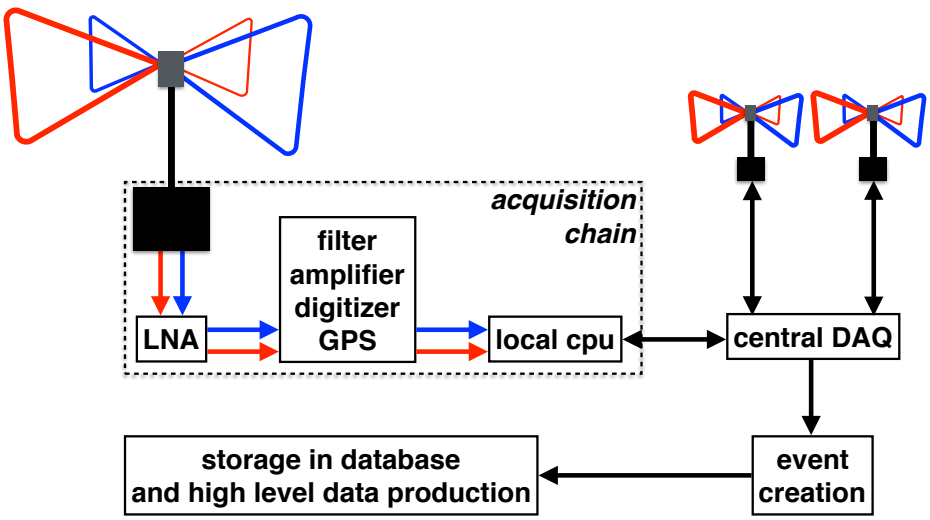

Figure 2.1: The main features necessary for a radio detection experiment and their logical interactions. In this sketch, the stations are equipped with two antennas. The signals recorded by the antennas with two polarizations are represented by the red and blue arrows.

The electromagnetic wave induces a difference in electric potential at the antenna level. If the station is composed of two or more antennas, their analog tensions are treated independently and are first amplified by the low noise amplifiers (LNAs). The signals are then filtered in the requested frequency band before or after being sampled by a digitizer. During this phase, a first level trigger can be evaluated on the analog or digital signals and the data passing the trigger are kept. At this point, a second trigger level can be applied on the rise time and the shape of the pulses. If they are consistent with a shower event, the header (composed among other parameters by the GPS time of the detection) is sent to the central data acquisition system (DAQ) which will search for coincident detection based on the GPS (global positioning system) time sent by other stations. If a coincidence is found, the latter stations will receive a request from the central DAQ for the event data which are gathered to compose a radio event.

The antenna response

The electromagnetic wave induces a tension (in V) at the antenna level. To retrieve the electric field $\boldsymbol{E}$ (in Vm^{-1}) one must take into account the antenna response. The measured tension depends on the electric field ($\boldsymbol{E}$) and the antenna vector effective length (VEL) $H_{\mathrm{ant}}(\nu,\theta,\phi)$, which depends on the wave frequency (ν) and its arrival direction in spherical coordinates (θ,ϕ). At AERA and CODALEMA the stations are composed of two horizontal perpendicular antennas (noted 1 and 2 in the following). The deconvolution procedure is detailed in [121]. One can write the measured tension for each antenna arm $V_{1,2}(t)$ as:

$$V_{1,2}(t) = \boldsymbol{E}(t)\boldsymbol{H}^{\text{ant}}_{1,2}(t) \tag{2.2}$$

For antenna response calculation, it is convenient to define a frame in spherical coordinates $(\boldsymbol{e}_r, \boldsymbol{e}_\theta, \boldsymbol{e}_\phi)$ which origin is the center of the antenna. In this frame, the electric field of a plane wave arriving from a given direction (θ, ϕ) is contained in the plane defined by the unity vectors $\boldsymbol{e}_\theta$ and $\boldsymbol{e}_\phi$ and the center of the antenna, as depicted in Figure 2.2.

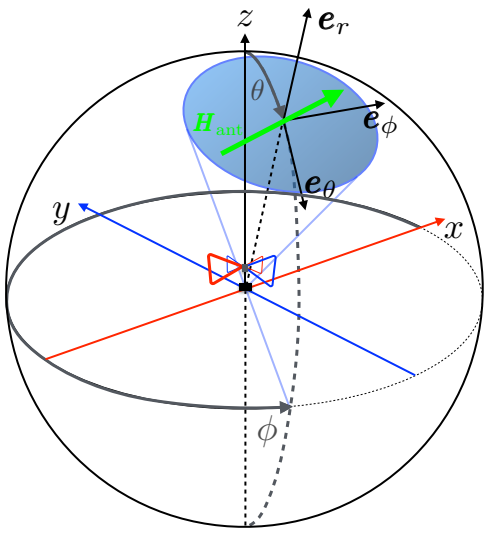

Figure 2.2: The spherical coordinate system used to calculate the vector effective length of an antenna. The VEL is indicated by the green arrow.

The unity vectors of the spherical frame are calculated as:

$$\boldsymbol{e}_r = \begin{pmatrix} \sin\theta\cos\phi \\ \sin\theta\sin\phi \\ \cos\theta \end{pmatrix}, \quad \boldsymbol{e}_\theta = \begin{pmatrix} \cos\theta\cos\phi \\ \cos\theta\sin\phi \\ -\sin\theta \end{pmatrix}, \quad \boldsymbol{e}_\phi = \begin{pmatrix} -\sin\phi \\ \cos\phi \\ 0 \end{pmatrix} \tag{2.3}$$

From the convolution theorem [122], the voltage at the antenna can be written in the frequency domain as:

$$\begin{aligned} \mathcal{V}_1(\omega) &= \mathcal{E}_\theta(\omega)\ \mathcal{H}^{\text{ant}}_{\theta,1}(\omega) + \mathcal{E}_\phi(\omega)\ \mathcal{H}^{\text{ant}}_{\phi,1}(\omega) \\ \mathcal{V}_2(\omega) &= \mathcal{E}_\theta(\omega)\ \mathcal{H}^{\text{ant}}_{\theta,2}(\omega) + \mathcal{E}_\phi(\omega)\ \mathcal{H}^{\text{ant}}_{\phi,2}(\omega) \end{aligned} \tag{2.4}$$

Where $\mathcal{V}(\omega)$, $\mathcal{E}(\omega)$ and $\mathcal{H}(\omega)$ are the Fourier transforms of $V(t)$, $E(t)$ and $H(t)$ and $\omega = 2\pi\nu$ is the angular frequency. The electronics and the digitizer transfer functions (respectively $\mathcal{H}^{\text{elec}}(\omega)$ and $\mathcal{H}^{\text{dig}}(\omega)$) must be accounted for to retrieve the electric field, cleared from all the effects of the antenna and the acquisition chain. The sum of the effects can be written as:

$$\mathcal{H}^{\text{tot}}_{\phi,2} = \mathcal{H}^{\text{ant}}(\omega)\ \mathcal{H}^{\text{elec}}(\omega)\ \mathcal{H}^{\text{dig}}(\omega) \tag{2.5}$$

Ultimately the electric field measured by the two antennas can be expressed in a cartesian frame in the temporal domain:

$$\begin{aligned} E_x(t) &= \cos\theta\ \cos\phi\ \mathcal{F}^{-1}(\mathcal{R}) + \sin\phi\ \mathcal{F}^{-1}(\mathcal{R}) \\ E_y(t) &= \cos\theta\ \sin\phi\ \mathcal{F}^{-1}(\mathcal{R}) - \cos\phi\ \mathcal{F}^{-1}(\mathcal{R}) \end{aligned} \tag{2.6}$$

For an antenna oriented vertically, the electric field is given by:

$$E_z(t) = -\sin\theta\ \mathcal{F}^{-1}(\mathcal{R})$$

Where $\mathcal{F}^{-1}$ is the inverse Fourier transform and with:

$$\mathcal{R} = \left(\frac{\mathcal{H}^{\text{tot}}_{\phi,2}\ \mathcal{V}_1 - \mathcal{H}^{\text{tot}}_{\theta,1}\ \mathcal{V}_2}{\mathcal{H}^{\text{tot}}_{\phi,2}\ \mathcal{H}^{\text{tot}}_{\theta,1} - \mathcal{H}^{\text{tot}}_{\phi,1}\ \mathcal{H}^{\text{tot}}_{\theta,2}} \right) \tag{2.7}$$

The analog electronic chain, including the LNA, the filter, the amplifier and the coaxial cables induces frequency dependent gain and group delays degrading the signal. The contribution of each component is measured in laboratory and is described by the parameter $\mathcal{H}^{\text{elec}}(\omega)$. The response of the digitizers $\mathcal{H}^{\text{dig}}(\omega)$ are not identical and their calibration is also performed in laboratory [123].

Calibration of the antenna response

At AERA, the antenna response calibration is made *in situ*. The latest measurements were made using an octocopter drone carrying a known pulsing electromagnetic source [30]. The setup is depicted in the left panel of Figure 2.3.

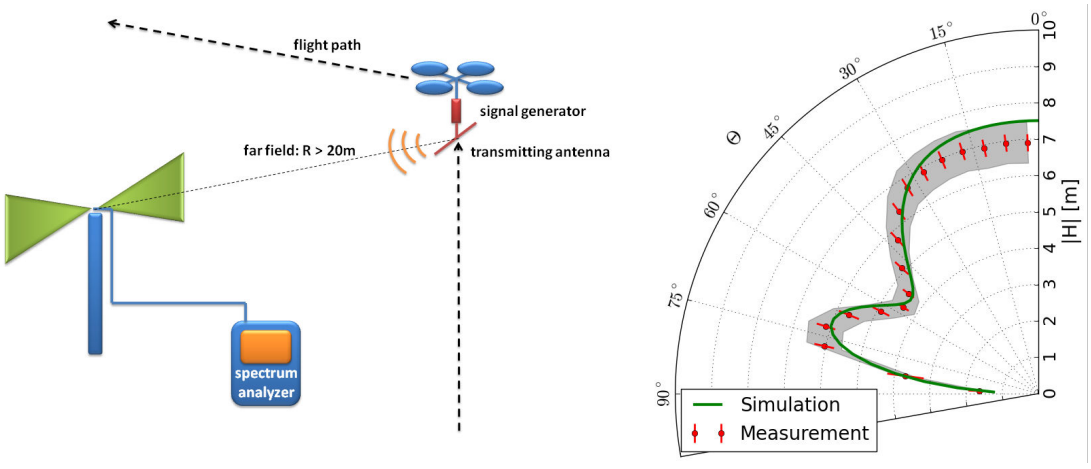

Figure 2.3: Left: setup of the antenna response calibration (see text for details). Right: Comparison of the measured (red dots) and simulated VEL of the LPDA station at 55 MHz. The error bars and the grey band account respectively for the statistic and systematic uncertainties. Both figures are taken from [30].

The octocopter is flew around the antenna at different zenith angles. The antenna response corresponding the each arrival direction is measured by a spectrum analyzer. In the right panel, one can see the measured VEL of the stations equipped with logarithmic periodic dipole antennas (LPDA). It is compared to the simulation at 55 MHz for which the NEC2 [124] simulation code is used.

Time calibration

Two methods are employed at AERA to correct for possible GPS clock drifts. The first way consists in the use of the beacon, continuously emitting four sine waves at different frequencies (58.887 MHz, 61.523 MHz, 68.555 MHz and 71.191 MHz). The waves superpose to a specific beat of approximately 1.1 μs [125], as shown in Figure 2.4. The relative positions of the antennas with respect to the position of the beacon emitter are measured with a resolution better than 10 cm by a differential GPS. The expected propagation times from the beacon to the antennas is determined with an accuracy better than 1 ns. Deviations of the measured beat times from the expected ones are used to correct for the relative time offsets of the GPS clocks. The stations are continuously calibrated by correcting the measured time drifts. The typical drift is of few dozens of nano seconds within few hours. The second way used for the timing relative calibration is the detection of aircrafts flying above the array.

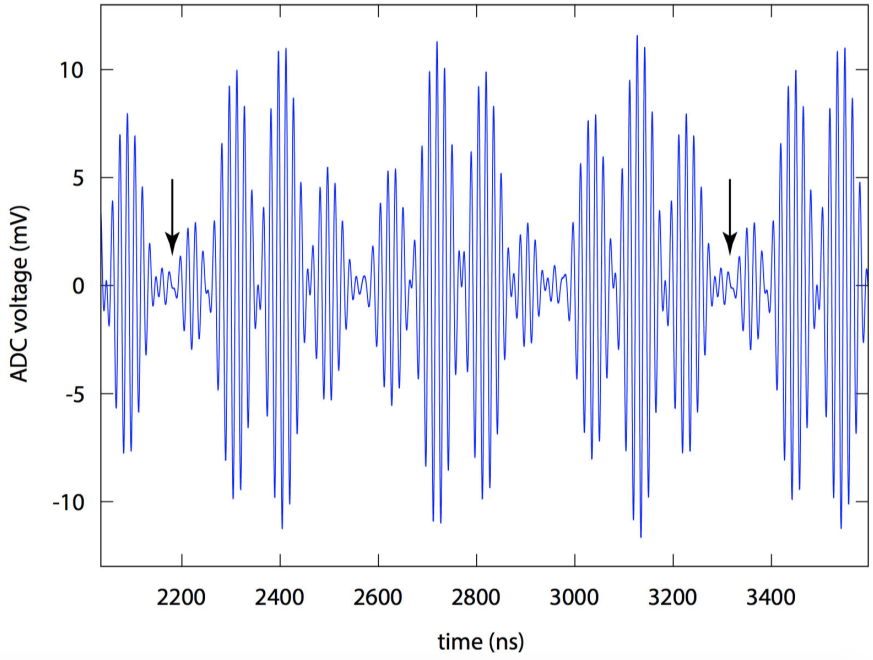

Figure 2.4: Time series of the voltage recorded with the analog-to-digital converter of an AERA antenna. The signal is filtered to contain only the four beacon frequencies. The periodicity of the beacon beat (around 1.1 μs) is indicated by the two arrows.

As shown in Figure 2.5, commercial planes broadcast their position via digital ADS-B packets at 1090 MHz that are received by a dedicated device. In addition some planes

emit radio pulses in the range 30 - 80 MHz that are recorded by the stations.

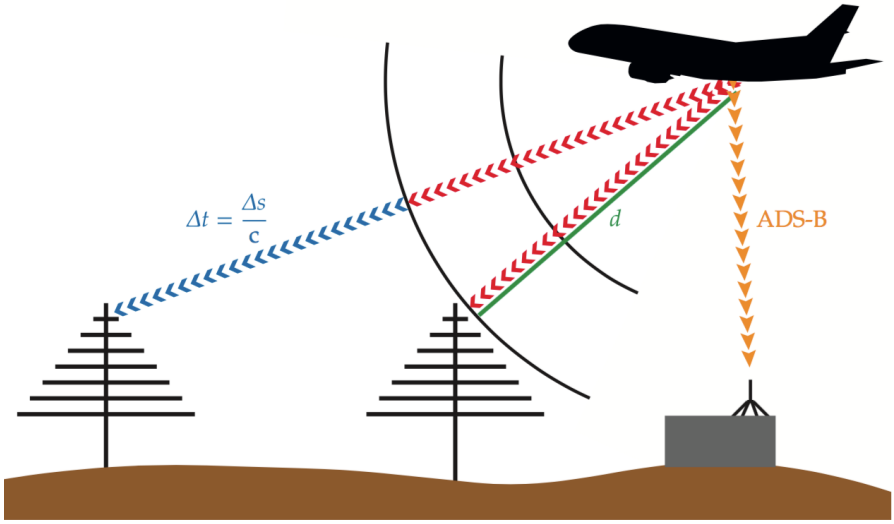

Figure 2.5: Sketch of a plane flying above the AERA array. The ADS-B packets signaling the position of the plane is received by a dedicated device and the radio stations detect the radio pulses.

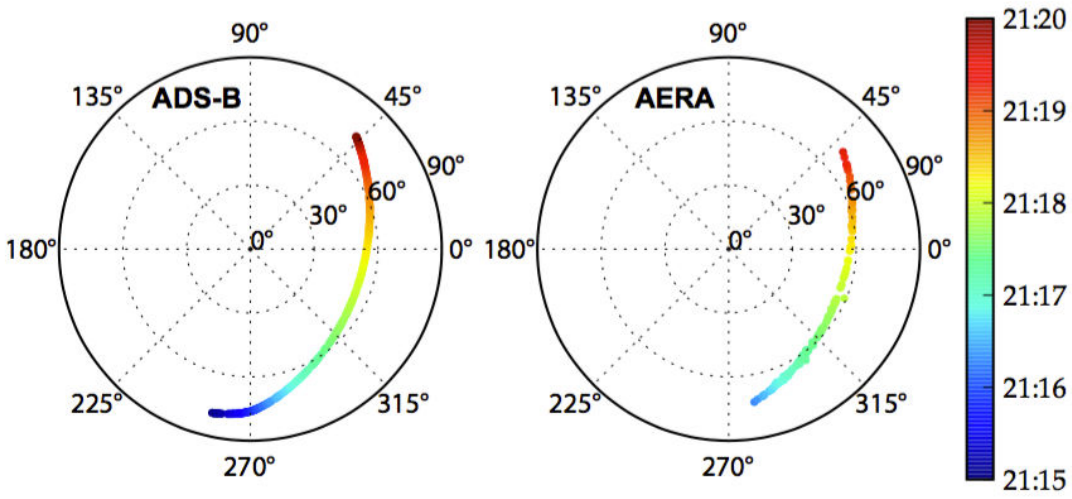

Figure 2.6: Left: the broadcasted positions of a plane flying above AERA. Right: the reconstructed positions from the timing of the pulses at the antennas.

The broadcasted position is compared to the one reconstructed with the stations by triangulation of the pulses arrival times, as shown in Figure 2.6. The deviations of the reconstructed positions from the broadcasted ones are used to eliminate clock drifts. The overall time resolution using the two calibration methods is of 2 nano seconds.

2.1.2.2 CODALEMA

The CODALEMA experiment is located in the Observatoire de radioastronomie de Nançay in France. The acronym CODALEMA stands for "Cosmic ray Detection Array with Logarithmic Electromagnetic Antennas". The name was given to the first setup CODALEMA1 [118] that used spiral logarithmic antennas. These antennas were replaced by more compact and sensitive radio stations, composed of dipole antennas [126]. A particle detector array was also added to detect extensive air showers in coincidence with the radio stations. This setup formed CODALEMA2. CODALEMA3 is the latest setup and consists in 13 scintillators, 57 autonomous radio stations with butterfly antennas and 10 radio stations forming a compact array. The map of the current setup is presented on Figure 2.7.

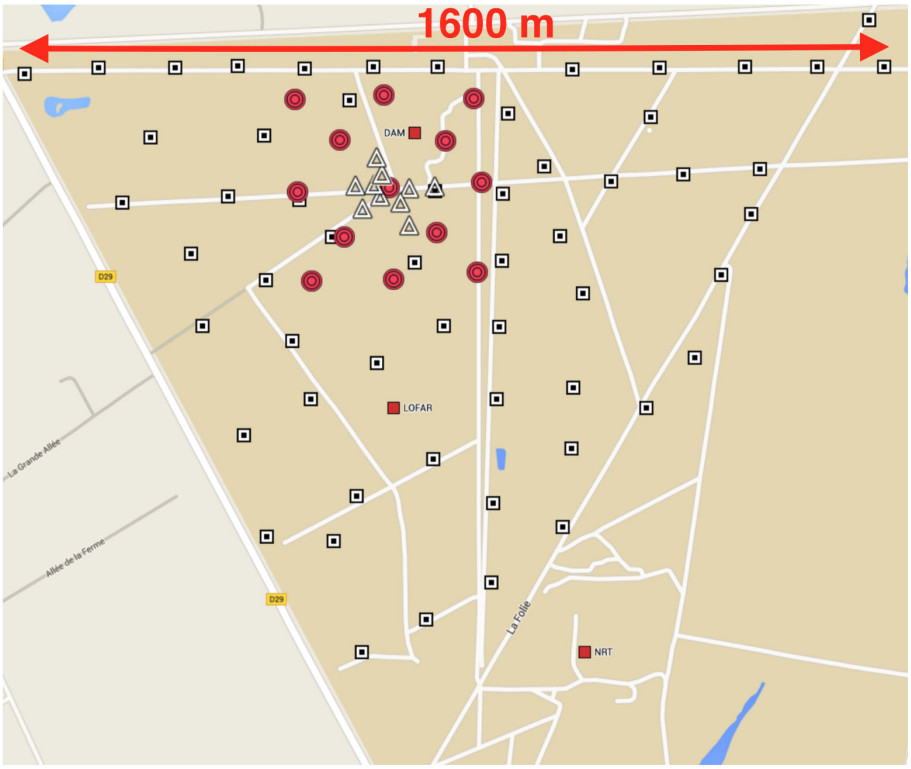

Figure 2.7: The detection array at CODALEMA with the scintillators represented by the red circles, the radio stations displayed as the black and white squares and the stations of the compact array displayed as the triangles.

The stations of the compact array record the electric field in the band [30 - 80] MHz whereas the autonomous stations record it in the band [20 - 200] MHz, excluding the FM band that emits between 80 MHz and 120 MHz. CODALEMA provides the largest detection frequency band. The filtered analog signal is compared to a fixed threshold, constituting the first level trigger. If the signal matches the requirements, it is digitized and kept on the local CPU which performs a discrimination procedure on the

wave shape and the rise time of the signal. This verification is the second level trigger. If the signal is considered as a potential event, the header of the event is sent to the central DAQ. The third trigger level is performed by the central DAQ which looks for coincidences among other stations of the array. If a time coincidence is found, the DAQ requests all the event data from the concerned stations and creates the event from all the informations.

2.1.2.3 AERA

The Auger Engineering Radio Array (AERA), located at the Pierre Auger Observatory is composed of 153 radio antennas, as shown in Figure 2.8.

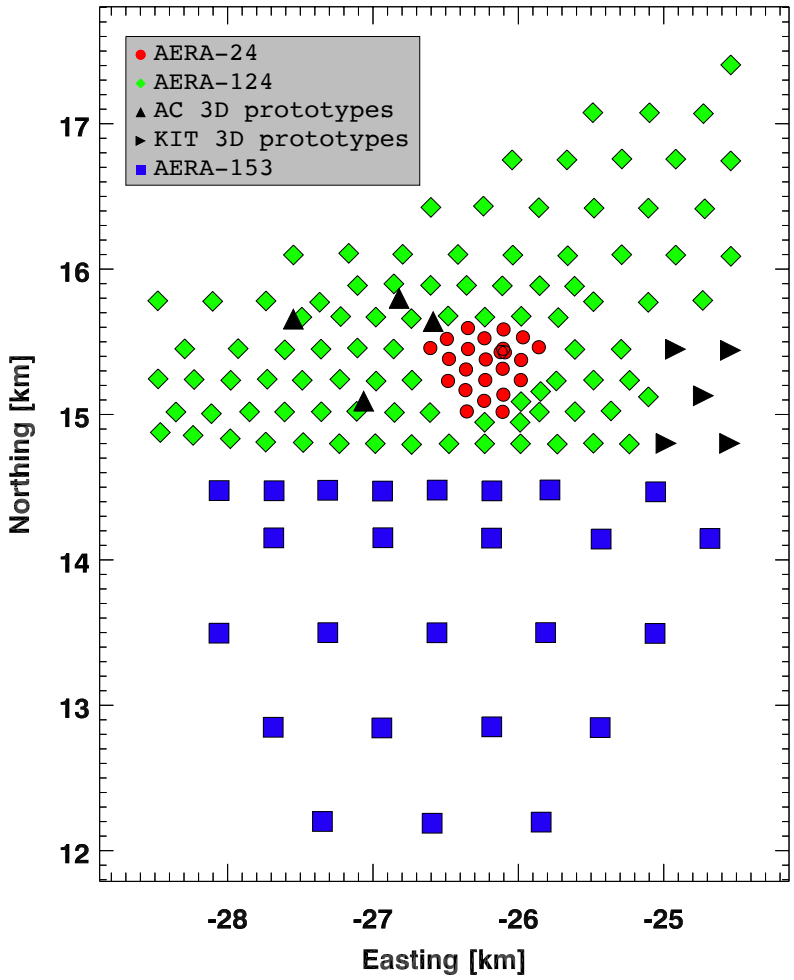

Figure 2.8: The map of AERA, showing the different deployment stages. The triangles are the 3D antennas developed at the Aachen University (upward triangles) and at the KIT (right-facing triangles).

Its purpose is to record the electric field in the frequency band [30 - 80] MHz emit-

ted by the development of extensive air showers in the atmosphere, in coincidence with other detection techniques. AERA went through different development phases, involving several prototypes. The phase one of AERA (AERA24) is composed of 24 logarithmic periodic dipole antennas (LPDA), with a spacing of 144 meters, covering 400 m^2. The data acquisition started in 2011. In 2013, the phase two (AERA124) is completed. The addition of 100 butterfly antennas with a spacing of 250 meters and 375 meters, upgraded the surface of the detection array to 6 km^2. In 2015, the last enhancement of AERA with 29 additional butterfly antennas with a spacing of 750 meters at the south, rises the surface of detection to 17 km^2 (AERA153). The array of antennas is located near the fluorescence site of Coihueco.

The antennas are presented on the pictures in Figure 2.9.

Figure 2.9: Left: a logarithmic periodic dipole antenna (LPDA) installed at AERA (phase one). Right: butterfly antennas installed during phase two or three. Both set up have two horizontal polarizations.

Two setups coexist at AERA, based on two trigger strategies depending on the equipped digitizer. The KIT/BUW digitizers sample the signal at 180 MS/s with a 12 bits ADC resolution. The radio stations equipped with KIT/BUW digitizers can trigger from different ways:

- autonomous trigger (same setup as for CODALEMA but the signal strength is compared to a threshold after digitization)
- trigger received from the surface detectors or fluorescence detectors (HEAT or Coihueco)

The radio stations equipped with Nikhef/RU digitizers are operated only in self trigger mode and are equipped with a scintillator. The first level trigger can be sent by the following possibilities

- trigger from the strength of the electric field
- trigger from the scintillator
- a combination of the two latter trigger modes

The Nikhef/RU digitizers sample the signal at 200 MS/s with a 14 bits ADC resolution. The recorded radio background is presented in Figure 2.10.

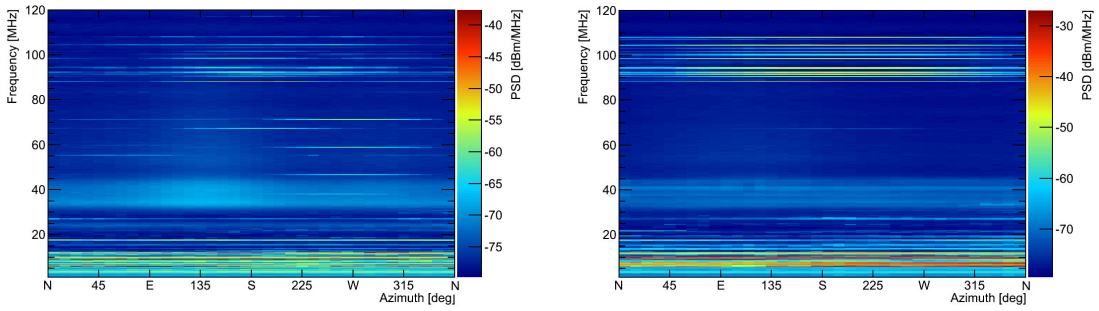

Figure 2.10: Power spectra measured at AERA as a function of the azimuthal directions for the horizontal polarization (left) and for the vertical polarization (right) in the 1 to 120 MHz frequency band (see text for details). The color scale represents the spectral power in dBm/MHz. Plots are taken from [31].

The measurements were made with a directional antenna. The AM emissions, below 20 MHz and FM emissions beyond 80 MHz are clearly visible. The most powerful noise source in this frequency range is the galactic plane, which measurement is presented in Figure 2.11. The color scale represents the intensity of the measured signal. The source of the radio galactic noise is the synchrotron emission from cosmic electrons in presence of the galactic magnetic field. The cycle of the presence of the galactic plane is visible on both polarizations and coincides with the maximum received signal. The radio environment of the AERA experiment is well measured and taken into account in the noise rejection algorithms. The stations are equipped with a bandpass filter, making possible the radio detection in the [30 - 80] MHz frequency band, without major noise emission.

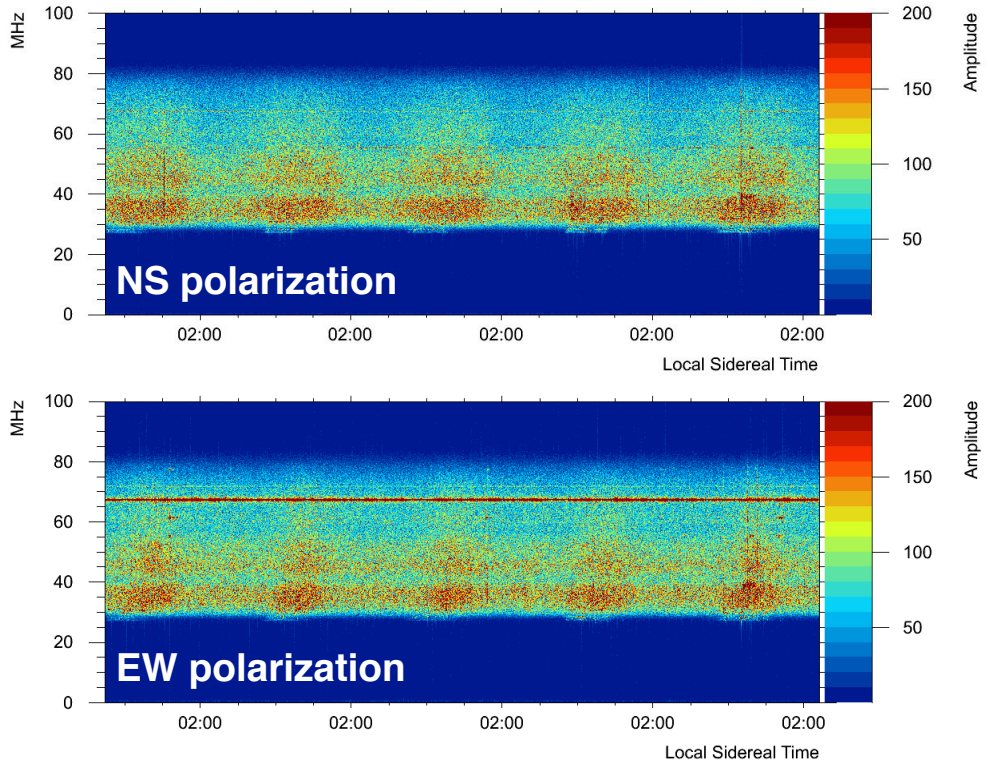

Figure 2.11: Power spectra measured at AERA as a function of the local sidereal time for the north-south polarization (top) and east-west polarization (bottom) in the 1 to 100 MHz frequency band (see text for details). Plots are taken from [31].

An example of recorded electric field deconvoluted from the responses of the antenna and the electronics is shown in Figure 2.12. After the deconvolution it is possible to compare the electric field measured by the LPDA and the butterfly antennas. For cosmic rays, the signal duration is smaller than 20 ns.

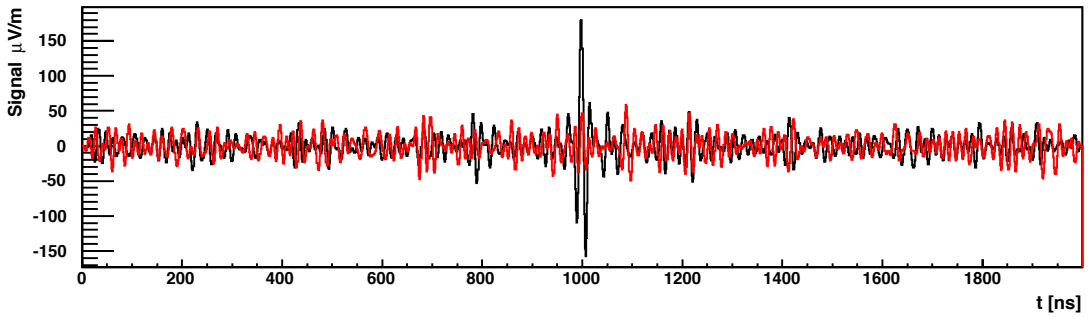

Figure 2.12: Time series of the electric field induced by a shower event and recorded by an AERA antenna in the east-west polarization (black) and north-south polarization (red), filtered in the band 30 - 80 MHz.

The vertical component is calculated afterwards, knowing the arrival direction of the

wave in the far field approximation. The total electric field is represented by the dashed line and is calculated as the square root of the quadratic sum of Hilbert envelopes of the three polarizations. The maximum of the total Hilbert envelope is the pulse maximum as shown in Figure 2.13.

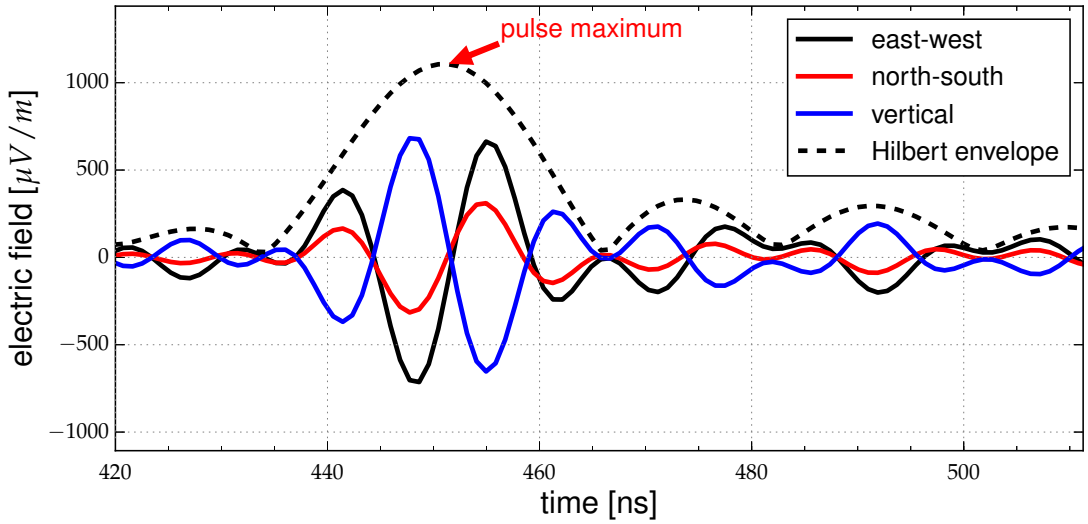

Figure 2.13: Time series of the electric field in the three polarizations. The total electric field is represented by the dashed line and is calculated as the square root of the quadratic sum of Hilbert envelops (see text for details). Taken from [32, 33].

The lateral distribution function of the electric field is calculated as the values of the pulse maximum as a function of the positions of the antennas with respect to the shower axis.

2.1.3 Progress of the characterization of the radio signal

The lateral distribution of the electric field

The lateral profile parametrized by Allan was applied on CODALEMA2 and LOPES data. A majority of events are well described by this parametrization, but some ($\sim 20\%$) are better described by a constant profile close to the shower axis ($d < 150$ m). The emitted electric field is a combination of several mechanisms leading to a complex topology at the ground level due to polarization effects and causing an asymmetry around the shower axis. A two dimensional model has been developed by Nelles et al [127]:

$$u(\boldsymbol{r}) = A\left[\exp\left(\frac{-(\boldsymbol{r}+C_1\boldsymbol{e}_{\boldsymbol{v}\times\boldsymbol{B}}-\boldsymbol{r}_{\text{core}})}{\sigma^2}\right) - C_0\exp\left(\frac{-(\boldsymbol{r}+C_2\boldsymbol{e}_{\boldsymbol{v}\times\boldsymbol{B}}-\boldsymbol{r}_{\text{core}})}{(C_3e^{C_4\sigma})^2}\right)\right] \quad (2.8)$$

Where $\boldsymbol{r}$ is the position at which the electric field is evaluated and $\boldsymbol{r}_{\text{core}}$ is the position of the shower core, both expressed in the shower frame. The parameter σ accounts for the width of the radio footprint on the ground and is highly correlated to the geometric distance to the maximum emission of the electric field. The subtraction of the two

gaussian functions describes well the asymmetry of the electric field amplitude around the shower axis.

Correlation to the energy of the primary

A clear correlation between the energy of the primary has been obtained by the CODALEMA [35] and LOPES [34] experiments. The results are shown in Figure 2.14.

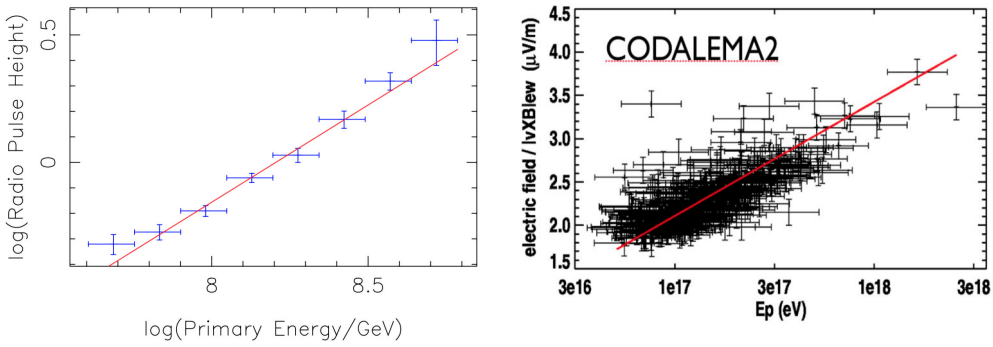

Figure 2.14: Correlation between the energy of the primary and the strength of the electric field as measured by the LOPES experiment [34] by energy bin (left) and by the CODALEMA experiment (right) [35]

The LOPES experiment is deployed within the KASCADE experiment, which dense array of particle detectors allows a precise determination of the energy of the detected showers and a discrimination of the type of the secondary particles at the ground level. The energy of the primaries is derived from the combined electron and muon number. At CODALEMA the energy is estimated by scintillators. In both cases the correlation is linear and is observed by other experiment such as RAugerI [128] and AERA [129]. If the shower to shower fluctuations induce an energy resolution of 30% for the particle detectors, recent publications evaluate the energy resolution from the radio signal at 17% for events with five or more stations [32, 33] at AERA. The energy deposited per area in eV m^{-2} is calculated from the total electric field. The energy fluence at each station is calculated by the integrating of the Poynting vector over time. The squared magnitude of the total electric field (as shown in Figure 2.13) is summed over a time of 200 ns center at the position of the pulse maximum. The local energy fluence at the location of the triggered antennas is fitted by the two dimensional model presented in the previous paragraph. An example of the fit procedure is shown in Figure 2.15 and the result is presented in Figure 2.16.

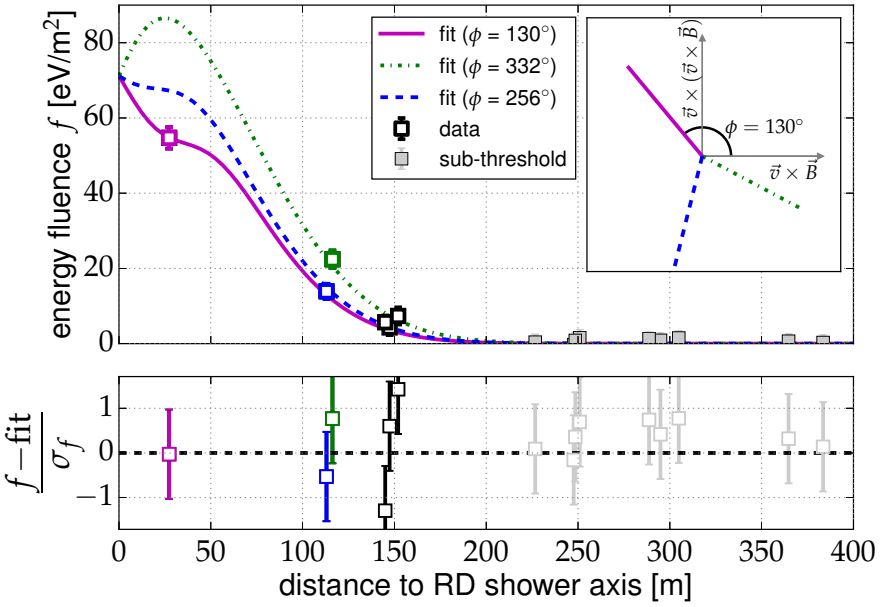

Figure 2.15: A fit example of the energy fluence with the two dimensional model. The curves are the model values, fitted on experimental data displayed as points, for different directions around the shower axis as a function of the axis distance [33].

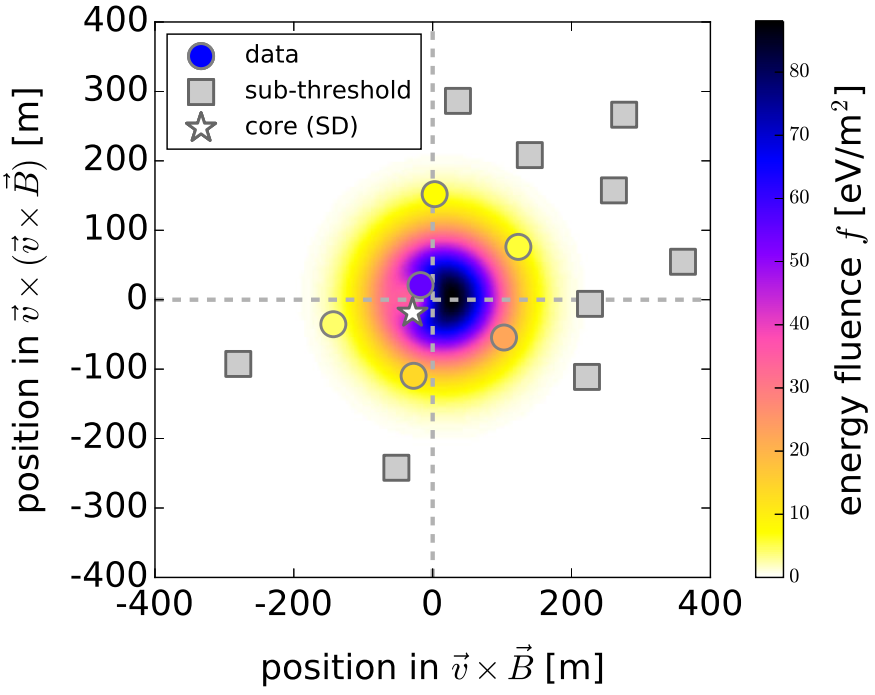

Figure 2.16: Deposited energy per unit area for radio stations together with the values given by the model after the fit procedure, the color scale accounts for the deposited energy [33].

The total deposited energy in the [30 - 80] MHz frequency range is obtained by integrating the fitted model over the plane perpendicular to the shower axis.

$$E_{30-80\,\mathrm{MHz}} = \iint u(\boldsymbol{r})\, d^2\boldsymbol{r}' \tag{2.9}$$

The correlation to the energy estimated by the surface detectors of the Pierre Auger Observatory is shown in Figure 2.17 with the energy resolution of the technique. The right panel of Figure 2.17 shows the scatter around the correlation curve for events with five or more stations with signal. The obtained mean deviation is 24%. The radio-energy resolution is obtained from the subtraction of the known resolution of the surface detector from the combined scatter. The combined scatter is calculated through a Monte Carlo simulation, taking into account the energy and the zenith angle dependence of the SD energy resolution and according to the number of air showers and the zenith and energy distribution of the data set. The obtained energy resolution of the radio detector is 22% for the full data set and 17% for showers detected by five or more stations. The radio detection of extensive air showers can be used to perform a reliable energy estimation.

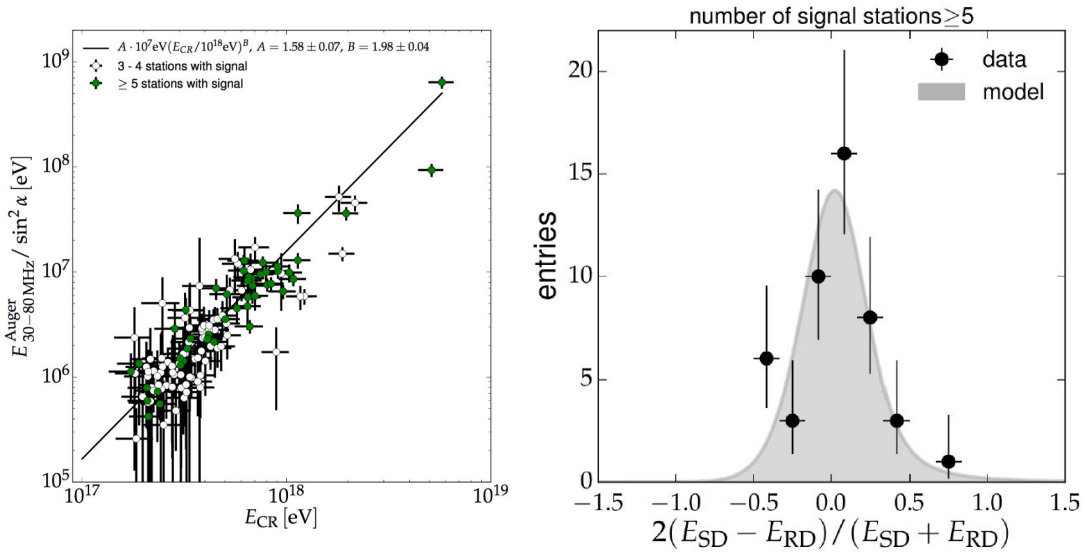

Figure 2.17: Left: Correlation between the calculated deposited energy from the radio signal and the energy estimated by the particle detectors. The white points are events with 3 or 4 stations with signal and the green ones account for events involving 5 or more stations. The black line is the correlation curve [33]. Right: Scatter around the correlation curve of the left panel for events with five or more antennas [32]. See text for details.

Correlation to the mass of the primary

The first correlation of the radio signal to the mass of the primary cosmic ray was established by the LOPES collaboration [36], by taking advantage of the very complete

array of particle detectors of the KASCADE experiment.

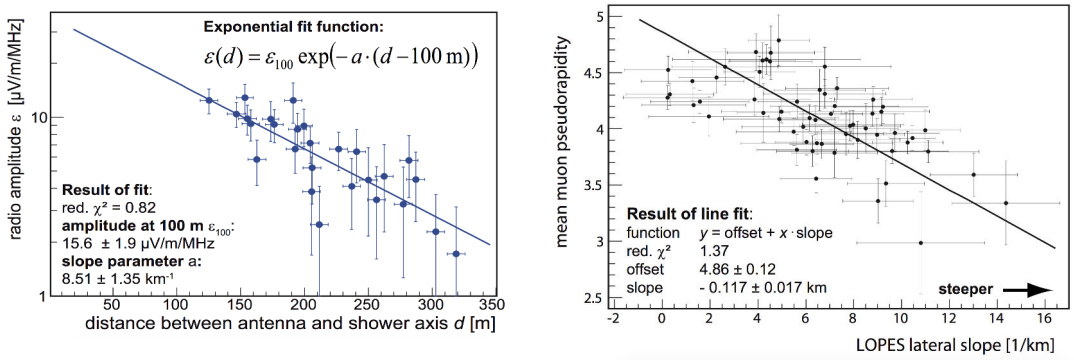

Figure 2.18: Left: Example of a LDF detected with LOPES, described by a one dimensional exponential decrease. - Right: Correlation of the lateral slope of the electric field and the muon pseudo rapidity measured at the LOPES and KASCADE experiments. Both figures are taken from [36].

A correlation was established by KASCADE between the muon pseudorapidity and the depth of the shower maximum. The correlation between the mean muon pseudorapidity to the longitudinal profile of air showers has been established in [130, 131, 132]. Figure 2.18 shows the correlation of the lateral slope of the electric field, described by a one dimensional exponential decrease and the muon pseudorapidity. In this case, the pseudo rapidity describes the angle of a particle relative to the shower axis. A linear correlation is obtained proving the sensitivity of the radio signal to the mass of the primary cosmic ray. Very recently, new methods to estimate the mass of the primary have been developed, including the one developed during this thesis which is detailed extensively in the next chapter. The dependence of the radio signal to the mass of the primary appears clearly in the simulations, as depicted in Figure 2.19.

The LOFAR [133] and Tunka-Rex [134] experiment is using the two dimensional model to reconstruct the depth of the shower maximum. The obtained precision of the X_{max} reconstruction is around 20 g/cm^2. However no comparison to direct X_{max} measurements is made, contrary to the Pierre Auger Observatory where the reconstructed values can be compared to the measurements of the fluorescence telescopes. Other features of the electric field are correlated to X_{max}, such as the shape of the radio wave front [135] and the spectral index of the frequency spectrum [136].

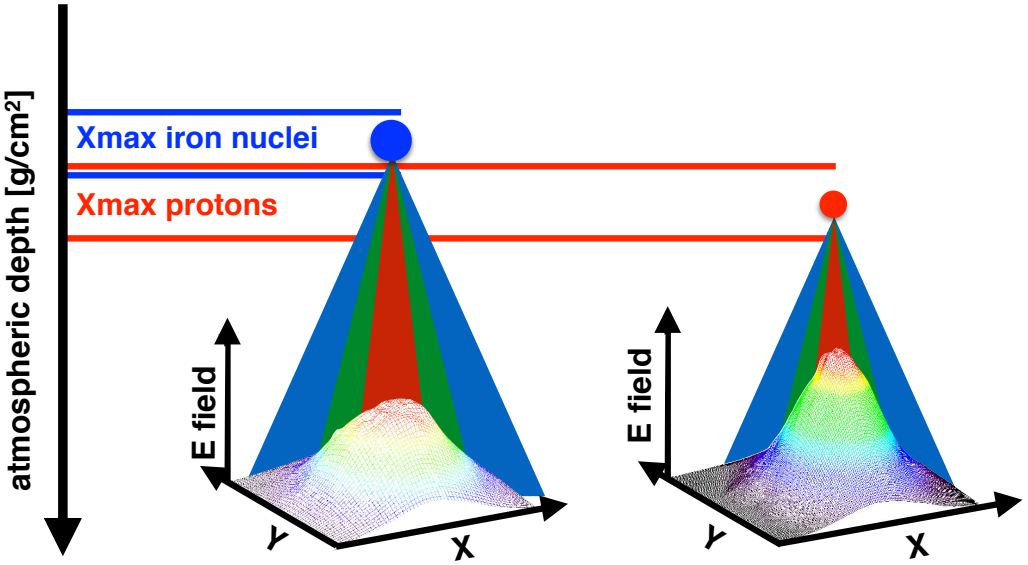

Figure 2.19: Difference of the LDF depending on the mass of the primary. Two LDF are simulated with SELFAS, on the left induced by an iron nucleus, on the right induced by a proton. The vertical axis represents the atmospheric depth and the horizontal lines accounts for the relative $X_{\max}$ depth distributions for proton induced showers and iron nucleus induced showers.

2.2 Emission mechanisms

The development of an extensive air shower, especially the electromagnetic component, creates an electric field that can be detected at the ground level. The generated signal is a combination of several mechanisms that are detailed in this section.

2.2.1 Geomagnetic effect

Among the emission mechanisms listed by F.D. Kahn and I. Lerche in 1966 [116], they estimated from simple shower models that geomagnetic effect was the dominant contribution to the electric field (in most cases), in particular the transverse current whereas the dipole effect was the less effective. The first radio detection experiments quickly provided evidence of this effect which is depicted in Figure 2.20.

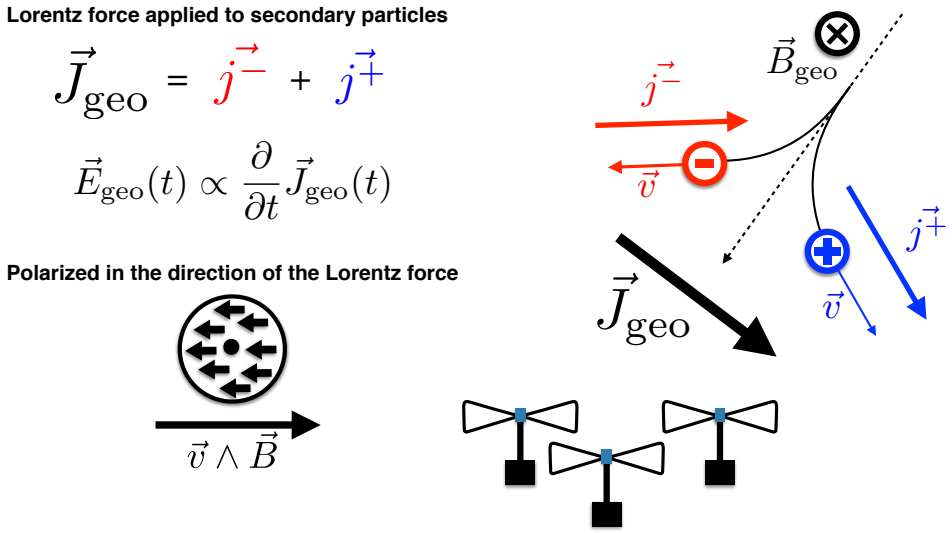

Figure 2.20: Schematic explanation of the geomagnetic effect.

The geomagnetic field induces a Lorentz force on the charged secondary particles. They undergo a systematic deviation in opposite directions, depending on the sign of the electric charge so that a current is established in the direction perpendicular to the direction of propagation of the shower. The intensity of the transverse current depends on the production rate of the secondary particles. The time variation of the transverse current is responsible for the creation of an electric field:

$$\boldsymbol{E}_{\rm geo}(t) \propto \frac{\partial}{\partial t}\boldsymbol{J}_{\rm geo}(t) \neq 0 \tag{2.10}$$

It is polarized in the direction ($\boldsymbol{v} \wedge \boldsymbol{B}$). The intensity of the electric field induced by this mechanism depends on the arrival direction of the shower with respect to the orien-

tation of the geomagnetic field. It is maximum for $\boldsymbol{v}.\boldsymbol{B} = 0$ and minimum for $|\boldsymbol{v}.\boldsymbol{B}| = 1$ after normalization, in which case there is no emission induced by the geomagnetic effect. The number of detected events is expected to be maximum for an arrival direction corresponding to high values of $\boldsymbol{v} \wedge \boldsymbol{B}$. This behavior is a clear evidence of the existence of the geomagnetic emission and has been observed in the northern hemisphere at CODALEMA [37].

In the northern hemisphere, the geomagnetic field is oriented downward and towards the south, inducing a higher intensity of the electric field produced by the geomagnetic effect for events from the north, thus more detected events from this direction. The CODALEMA data are compatible with this assertion as shown in Figure 2.21. The geomagnetic origin of the electric field has also been highlighted in the southern hemisphere by RAugerI, RAugerII and AERA.

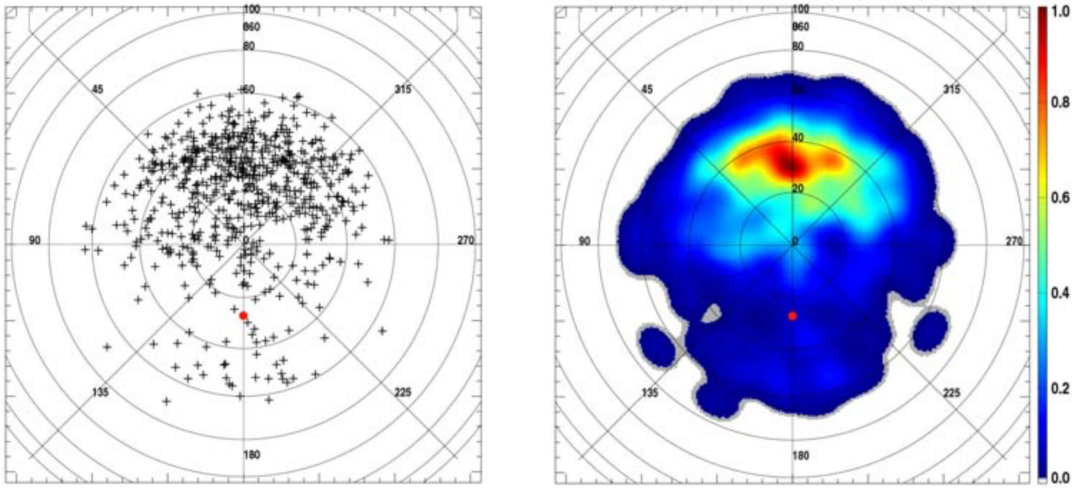

Figure 2.21: Left: sky map of events detected at CODALEMA, the geographic north is located to an azimuth angle of 0° (top) and the east to an angle of 270° (right). The direction of the geomagnetic field is indicated by the red point. Right: the corresponding 10° gaussian smoothed sky map. Both plots are taken from [37].

In the southern hemisphere, the geomagnetic field is oriented upwards and towards the north, so that the sky map of events detected at AERA is symmetric to the CODALEMA sky map with respect to the east-west axis.

2.2.2 Charge excess

In 1962, the Russian physicist Gurgen Askaryan, was studying the development of air showers in dense media [113]. He focused on demonstrating the radio-transparency of the lunar regolith in order to use the moon as a target to detect cosmic neutrinos. He also determined that the electromagnetic component of the shower should be composed of

more electrons than positrons, even if they are created in equal number by pair creation. The reason is that positrons annihilate with electrons of the medium. Furthermore, more electrons are created by Compton effect and delta electrons. These mechanisms lead to a negative charge excess and their coherent radiation: the charge excess effect. To obtain a coherent radiation (from constructive interferences), the particles have to be located at the same distance from the observer. The coherent radiation can be detected at wavelengths larger than the size of the spatial distribution of the secondary particles, also nicknamed the pancake due to its shape. The thickness of the pancake is approximately of 2 to 3 meters near the shower axis. Thus, the coherent emission must be detected at less than few hundreds of MHz. A schematic view of the charge excess effect is presented in Figure 2.22.

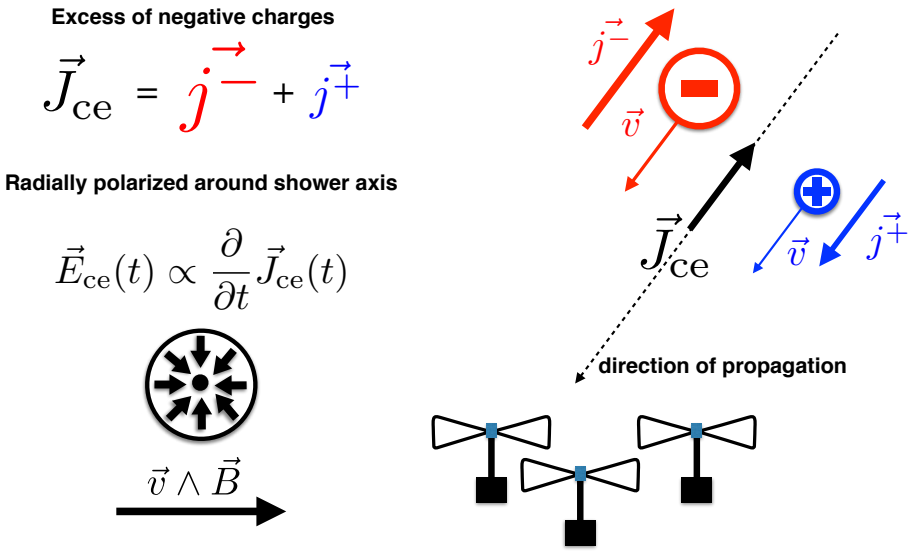

Figure 2.22: Schematic explanation of the charge excess effect.

The electrons create a current $\boldsymbol{j}^-$ and the positrons, a current $\boldsymbol{j}^+$. The total current, $\boldsymbol{j}^- = \boldsymbol{j}_{ce} + \boldsymbol{j}^+ \neq 0$ because of the excess of negative charge. The total current varies as a function of time, proportionally to the number of secondary particles.

$$\boldsymbol{E}_{ce}(t) \propto \frac{\partial}{\partial t}\boldsymbol{J}_{ce}(t) \neq 0 \tag{2.11}$$

The time variation induces an electric field detectable in the radio domain and radially polarized around the shower axis in the shower frame defined as:

$$\begin{pmatrix} \boldsymbol{v} \times \boldsymbol{B} \\ \boldsymbol{v} \times (\boldsymbol{v} \times \boldsymbol{B}) \end{pmatrix} \tag{2.12}$$

Where $\boldsymbol{v}$ is the axis direction of the shower front and $\boldsymbol{B}$ is the geomagnetic field. Recently the experiments of the digital era highlighted the mechanism predicted by

Askaryan in 1962: the charge excess mechanism. Several evidences have been observed. The data of the CODALEMA experiment show a systematic shift between the radio core and the particle core [38]. This results are shown in Figure 2.23.

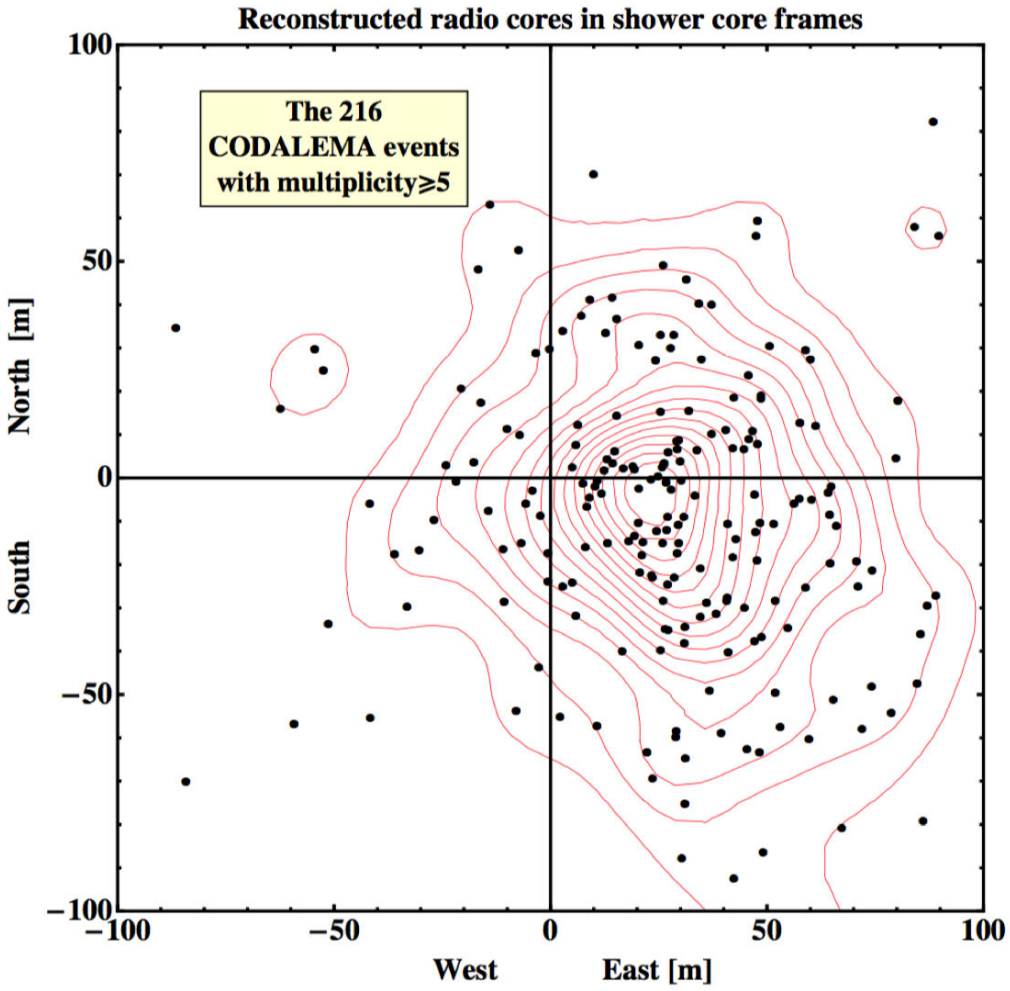

Figure 2.23: The experimentally observed core shift from CODALEMA data. The data set is composed of 216 events. The black dots are the radio core positions with respect to the particle core positions [38].

By fitting the LDF with a one dimensional model as the one proposed by Allan, the radio core is defined as the location of the maximum electric field on the ground. However, a systematic shift of the core position is observed compared the particle core position. The average radio core shift with respect to the particle core position is of 30 meters in the eastern direction. The geomagnetic effect, already observed by various experiments, induces an electric field polarized in the direction $\boldsymbol{v} \times \boldsymbol{B}$. To explain the shift, a second mechanism must produce an electric field, polarized radially around the shower axis. The charge excess mechanism is expected to have such a feature. The total electric field, composed of the two latter mechanisms, is asymmetric around the

shower axis as depicted in Figure 2.24. The 1D model does not take into account the asymmetry, the radio core is thus predicted at a position which is shifted to the east direction with respect the true core position.

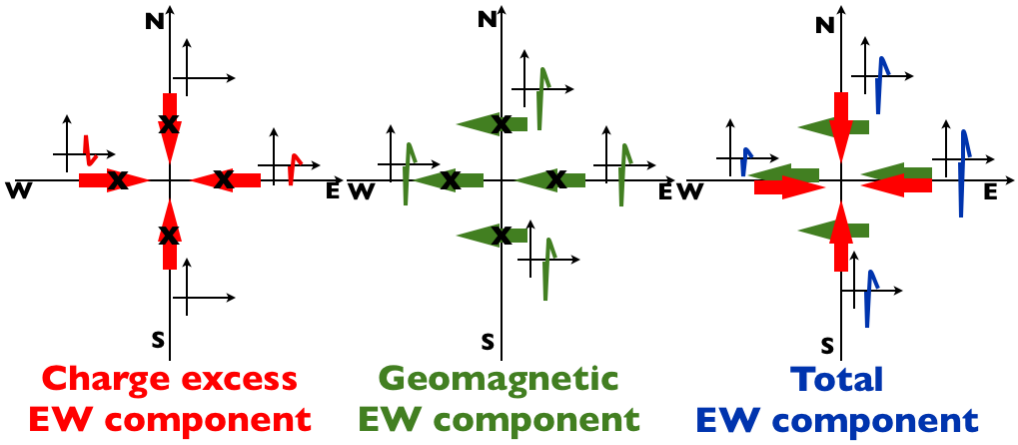

Figure 2.24: Constructive and destructive interferences of the two emission mechanisms and the resulting amplitude asymmetry around the shower axis and core shift of the total electric field [38].

Depending on the position of the observer around the shower axis, the interference of the two mechanisms can be destructive or constructive. The second observation of the charge excess effect was made through the analysis of the polarization of the detected electric field. Particularly at the MAXIMA experiment (the prototype of AERA) and more recently by AERA with a better resolution due to the simultaneous measurements in both horizontal polarization [39]. In this analysis, the total electric field received by a radio station at the position (x, y) is defined as:

$$\boldsymbol{E}(x,y) = \boldsymbol{E}_{\text{geo},(x,y)} + \boldsymbol{E}_{\text{ce},(x,y)} \tag{2.13}$$

Where $\boldsymbol{E}_{\text{geo}}$ and $\boldsymbol{E}_{\text{ce}}$ are respectively the electric field induced by the geomagnetic and charge excess effects. x and y are the ground coordinates along the north and east geographic directions, with respect to the position of the particle core. Several quantities are introduced for the calculation of the polarization. The direction of the incoming wave is denoted $\boldsymbol{v}$ with respect to the position of the radio station $\boldsymbol{p}$ indicated by an antenna in Figure 2.25. $\boldsymbol{B}$ is the geomagnetic field vector, ξ is the direction of the projection of the vector $-\boldsymbol{v}\times\boldsymbol{B}$ The direction η in the ground plane is perpendicular to ξ. α is the angle between the directions of the shower axis the geomagnetic field. ψ is the angle between ξ and the direction of the position of the antenna with respect to the position of the shower core. The polarization angle is defined as:

$$\phi_p = \tan^{-1}\left(\frac{E_{\text{geo},y}+E_{\text{ce,y}}}{E_{\text{geo},x}+E_{\text{ce},x}}\right) = \tan^{-1}\left(\frac{\sin(\phi_{\text{geo}})\sin(\phi)+a\sin(\phi_{\text{ce}})}{\cos(\phi_{\text{geo}})\sin(\alpha)+a\cos(\phi_{\text{ce}})}\right) \tag{2.14}$$

ϕ_{geo} and ϕ_{ce} are respectively the azimuthal angle of the geomagnetic and charge-excess contribution with respect to the geographic east. α denotes the geomagnetic angle (the angle between the arrival direction and the geomagnetic field).

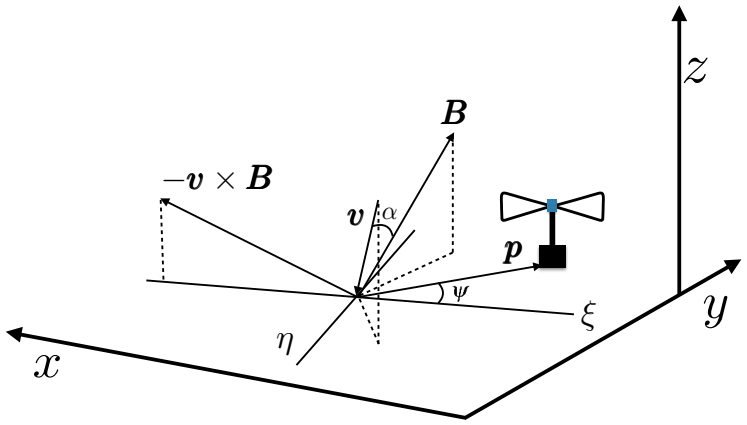

Figure 2.25: Schematic view of the different quantities used in the calculation of the polarization (see text for details). The figure is adapted from [39].

For a shower axis defined by a zenith angle θ_a and an azimuth angle ϕ_a, ϕ^{A} is defined as:

$$\phi^{\text{A}} = \tan^{-1}\left(\frac{\sin^2(\theta_a)\cos(\psi-\theta_a)\sin\phi_a - \sin\psi}{\sin^2(\theta_a)\cos(\psi-\theta_a)\sin\phi_a - \cos\psi}\right) \tag{2.15}$$

Where ψ is the angle between the projection of the direction ($\boldsymbol{v}\times\boldsymbol{B}$) and the radial position of a radio station around the shower axis. Finally, the relative intensity of the two emissions is given by the following relation:

$$a \equiv \sin(\alpha)\frac{|E_{\text{ce}}|}{|E_{\text{geo}}|} \tag{2.16}$$

Estimations of the parameter a have been performed with the antennas of AERA24. The measurements are shown in Figure 2.26. Each point is a single measurement and the value of the parameter a depends on the arrival direction of the shower with respect to the geomagnetic field. The blue vertical line accounts for the mean value of a, calculated for the displayed measurements. The value of the parameter a is estimated at 14% and the predicted polarization angles are compared to a AERA24 data set for $a = 0$ and $a = 14\%$, the results are presented in Figure 2.27. The predicted values show a very good agreement to the measured values for a non-zero contribution (14%) of the charge excess mechanism to the total electric field. Although the addition of a radially polarized contribution is consistent with experimental data, further investigation are required to attribute it to the net negative charge of the extensive air showers.

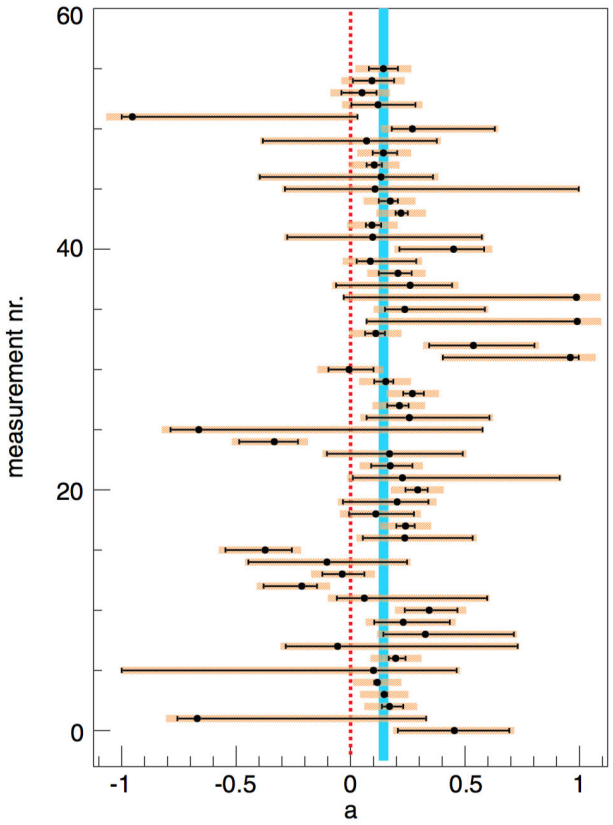

Figure 2.26: Distribution of the measurements of the parameters a at AERA24. The blue line represents the one σ confidence level of the most probable value. The figure is taken from [39].

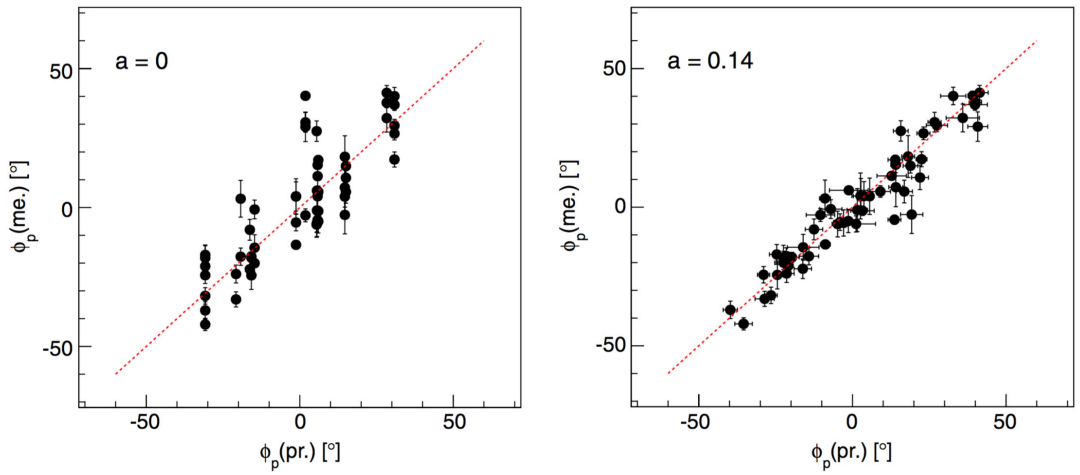

Figure 2.27: Measured polarization angle at AERA as a function of the predicted ones for a pure geomagnetic emission (left) and a contribution of 14% of the charge excess mechanism to the total electric field (right).

The combination of the two mechanisms leads to a total electric electric field for which both the polarization angle and amplitude depend on the observation position around the shower axis. Indeed the interferences between the two contributions that can be constructive or destructive produce an asymmetry of the electric field distribution around the shower axis.

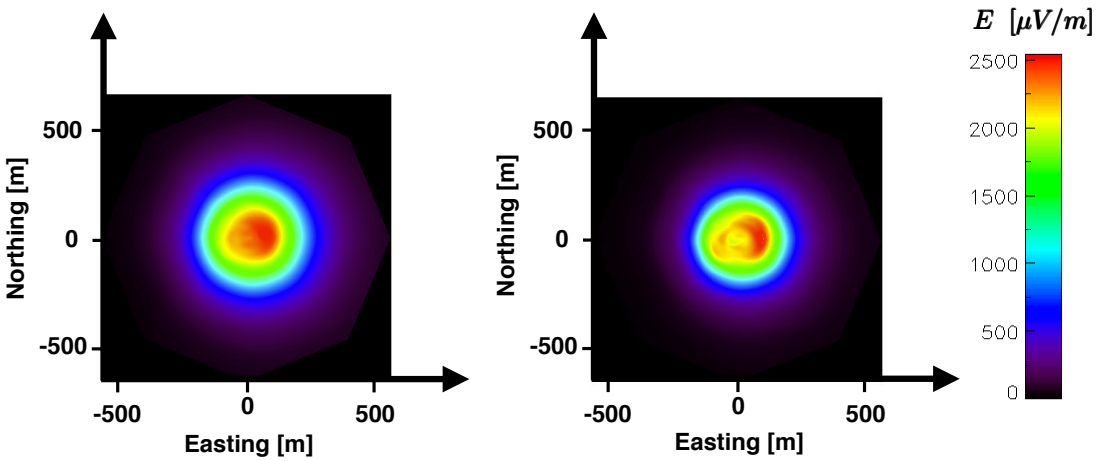

Figure 2.28: Electric field induced by a 10^{18} eV proton arriving from the east with a zenith angle of 30°. It is computed with SELFAS in the conditions of the CODALEMA experiment. The maximum electric field at each antenna is calculated as the maximum of the Hilbert envelop using the 3 polarizations and filtered in the band [1 - 100] MHz (left) and [100 - 200] MHz (right). In both cases, the intersection of the shower axis on the ground plane is located at the origin of the frame.

Two examples of total electric field computed with the simulation code SELFAS (which is described in Section 2.3.2) are shown in Figure 2.28. On the right panel, the electric field is filtered in the band [1 - 100] MHz. One can see that the radio core is shifted in the eastern direction, due to the interferences of the geomagnetic and charge excess emissions. On the right panel, the electric field is filtered in the band [100 - 200] MHz, an other effect appears. Due to time compression, a boost of the amplitude of the electric field occurs under a particular angle around the shower axis, matching the angle of the Cerenkov radiation. This leads to a ring-like structure where the electric field amplitude is maximum. This effect, that depends on the air refractive index will be detailed more extensively in the next chapters.

The frequency component of the electric field received by an antenna depends on its distance to the shower axis. As shown in Figure 2.29, the farther an antenna is from the shower axis, the larger is the source of emission and the conditions for the coherent emission of the secondary particles favors the lower frequencies. On the contrary, an antenna located very close to the shower axis will receive all the electric field, induced by the shower development, in a very short time period. For different energies of the primary cosmic ray, the amplitude of the spectra will change but their relative

distributions will remain the same.

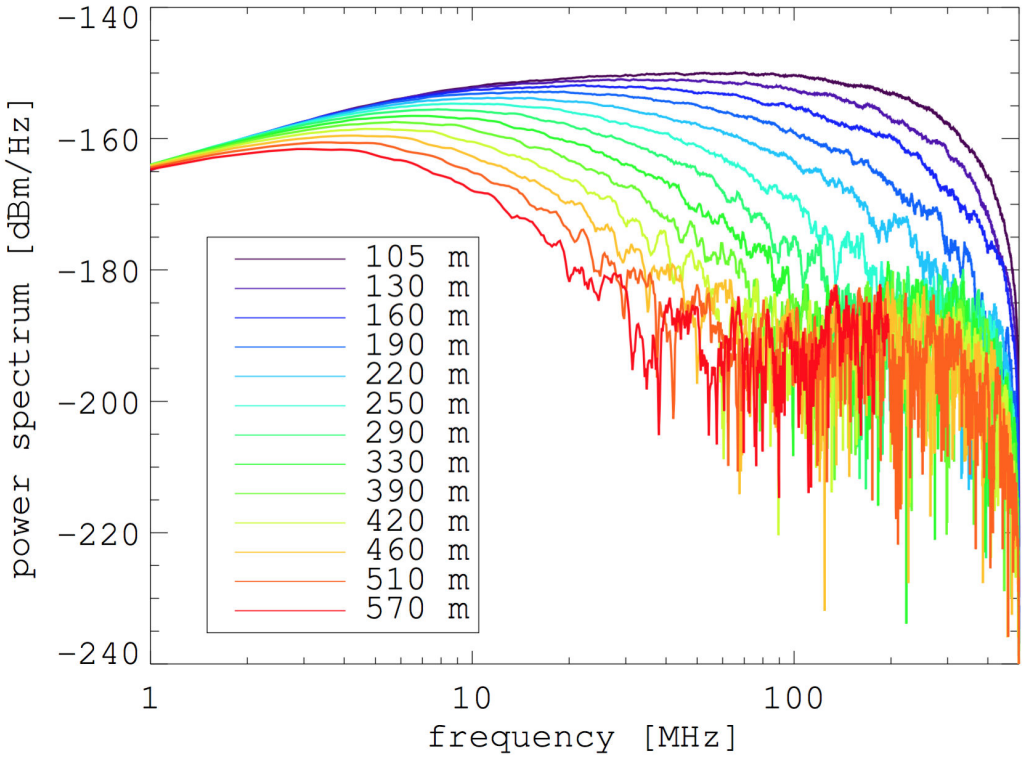

Figure 2.29: Power spectrum of the electric field simulated in the same conditions as for Figure 2.28 for different distances to the shower axis.

2.3 Simulation

2.3.1 Hadronic interaction model

The modern simulation of the electric field induced by extensive air showers is done by summing up the individual contributions of each secondary particle. Thus the profile of the shower must be estimated to know the number of particles that contribute at each atmospheric depth. The profile is determined using a high energy hadronic interaction model. Beyond few GeV in the center of mass, several models exist to predict the interaction cross sections beyond the energies available in laboratories.

QGSJET-II.04, for Quark Gluon String model [94] with Jet is based on the pomerons phenomenology [137]. The pomerons, act as microscopic partonic cascades. The multiple scattering processes are described as exchange of pomerons. This version of the QGSJET model takes into account the LHC data to constrain the cross sections.

Sibyll 2.1 [138] also uses the pomerons description for the soft interactions. The semi-hard interactions are estimated with the mini-jet approach [139]. The interaction

between nuclei are calculated considering a superposition of free nucleons.

EPOS LHC [95] also uses the pomerons approach. The main difference with the other models is that it takes into account the energy-momentum correlations between multiple re-scatterings [140]. Like the latest version of the QGSJET model, the parameters are adjusted from LHC data. This model predicts a muon production 20% more important than QGSJET.

2.3.2 SELFAS

SELFAS (Simulation of ELectric Field emitted by Air Showers) [141], is a simulation code that computes the electric field emitted during the development of an extensive air shower. It uses a microscopic description and calculates the sum of the individual contributions of all secondary particles. The requested input parameters are:

- the arrival direction of the shower
- the three components of the geomagnetic field, at the desired location
- the number secondary particles N_p to be simulated
- the energy of the primary cosmic ray
- the mass of the primary cosmic ray
- the time step at which the simulated antennas sample the electric field
- the positions of the antennas
- the first interaction depth (X_1), is optional

If the first interaction depth is set, the longitudinal profile is calculated using the Gaisser-Hillas function. If not, SELFAS can use QGSJET, Sibyll or EPOS to draw a first interaction depth. Then, CONEX [142] is used to compute the Gaisser-Hillas profile simulated by one of the latter hadronic simulation codes and returned to SELFAS for the electric field computation. Not all secondary particles are considered and only N_p particles are randomly chosen, their longitudinal distribution matches the longitudinal profile. The distributions describing the behavior of the secondary particles have been parametrized by Lafebre et al. [143], as a function of the crossed atmospheric depth since the first interaction. The initial conditions of a secondary particle are taken from the following distribution at a particular shower age:

- the energy distribution
- the angular distributions with respect to the direction of the shower axis
- the lateral distribution (the distance from the shower axis)

- the distribution of the time delay with respect to a virtual particle with a velocity of c along the shower axis (the pancake thickness)

The time delay accounts for the thickness of the particle front. All considered particles have a finite lifetime, the charge and current density associated to a single particle is given by:

$$\rho(\boldsymbol{x},t) = q[\theta(t-t_1) - \theta(t-t_2)]\delta^3(\boldsymbol{x}-\boldsymbol{x}_0(t)) \tag{2.17}$$

$$\boldsymbol{J}(\boldsymbol{x},t) = \rho(\boldsymbol{x},t)\boldsymbol{v}(t) \tag{2.18}$$

The expression of the electric field is given by the Maxwell's equations.

$$\boldsymbol{E} = -\boldsymbol{\nabla}\Phi - \frac{\partial \boldsymbol{A}}{\partial t} \tag{2.19}$$

With the Liénard–Wiechert scalar (Φ) and vector ($\boldsymbol{A}$) potential fields.

$$\Phi(\boldsymbol{x},t) = \frac{q}{R(1-\boldsymbol{n}\boldsymbol{\beta})} \quad \text{and} \quad \boldsymbol{A}(\boldsymbol{x},t) = \frac{\boldsymbol{J}}{R(1-\boldsymbol{n}\boldsymbol{\beta})} \tag{2.20}$$

For a point-like charge q with a reduced velocity $\boldsymbol{\beta}$, at a distance R to an observer and $\boldsymbol{n}$ is the unit vector between the observation position and the source, oriented toward the observation position. The wave equations are written as:

$$\nabla^2\Phi - \frac{1}{c^2}\frac{\partial^2\Phi}{\partial t^2} = \frac{\rho}{\varepsilon_0} \tag{2.21}$$

$$\nabla^2\boldsymbol{A} - \frac{1}{c^2}\frac{\partial^2\boldsymbol{A}}{\partial t^2} = -\mu_0\boldsymbol{J} \tag{2.22}$$

The electric field can thus be expressed as a function of the charge and current density:

$$\nabla^2\boldsymbol{E} - \frac{1}{c^2}\frac{\partial^2\boldsymbol{E}}{\partial t^2} = -\frac{1}{\varepsilon_0}\left(-\boldsymbol{\nabla}\rho\frac{1}{c^2}\frac{\partial \boldsymbol{J}}{\partial t}\right) \tag{2.23}$$

The equation is solved using retarded solution and after integration over space and time, the total electric field $\boldsymbol{E}(\boldsymbol{x},t)$ received by an observer at a position $\boldsymbol{x}$ and at the time t in Lorenz gauge is:

$$\begin{aligned} E_i(\boldsymbol{x},t) = \frac{1}{4\pi\varepsilon_0}\Bigg(&\frac{\boldsymbol{n}_i q_i(t_{ret})}{R_i^2(1-\eta\boldsymbol{\beta}_i\boldsymbol{n}_i)} \\ &+\frac{1}{c}\frac{\partial}{\partial t}\frac{\boldsymbol{n}_i q_i(t_{ret})}{R_i(1-\eta\boldsymbol{\beta}_i\boldsymbol{n}_i)} - \frac{1}{c^2}\frac{\partial}{\partial t}\frac{\boldsymbol{n}_i q_i(t_{ret})}{R_i(1-\eta\boldsymbol{\beta}_i\boldsymbol{n}_i)}\Bigg)_{\text{ret}} \end{aligned} \tag{2.24}$$

The details of the calculation can be found in [141]. R_i is the distance between a particle and the observer, $\boldsymbol{n}_i$ is the vector pointing from the particle to the observer, q_i

is the charge of the particle, η is the air refractive index and $\boldsymbol{\beta}_i$ is the reduced velocity of the particle. The notation "ret" means that the different quantities are evaluated at a delayed time. The delayed time (t_{ret}) corresponds to the time at which the electric field has been emitted, with respect to the time t at which it is detected by an observer. The delayed time is calculated as:

$$t_{\text{ret}} = t - \frac{<\eta> R(t_{\text{ret}})}{c} \tag{2.25}$$

Where $<\eta>$ is the mean value of the air refractive index between the position of the particle and the position of the antenna. Equation (1.24) contains the three contributions to the total electric field emission. It is composed of a static part:

- $\frac{\boldsymbol{n}_i q_i(t_{ret})}{R_i^2(1-\eta\boldsymbol{\beta}_i\boldsymbol{n}_i)}$ accounts for the Coulombian contribution.

And two radiative parts:

- $\frac{1}{c}\frac{\partial}{\partial t}\frac{\boldsymbol{n}_i q_i(t_{ret})}{R_i(1-\eta\boldsymbol{\beta}_i\boldsymbol{n}_i)}$ accounts for the net charge contribution.
- $\frac{1}{c^2}\frac{\partial}{\partial t}\frac{\boldsymbol{n}_i q_i(t_{ret})}{R_i(1-\eta\boldsymbol{\beta}_i\boldsymbol{n}_i)}$ accounts for the total current.

The electric field is computed at the time of the observer for the total number of particles (ζ) according to the equation:

$$\begin{aligned} E_{tot}(\boldsymbol{x},t) = \frac{1}{4\pi\varepsilon_0}\Bigg\{ & \sum_{i=1}^{\zeta}\left[\frac{\boldsymbol{n}_i q_i(t_{ret})}{R_i^2(1-\eta\boldsymbol{\beta}_i\boldsymbol{n}_i)}\right]_{\text{ret}} \\ & + \frac{1}{c}\frac{\partial}{\partial t}\sum_{i=1}^{\zeta}\left[\frac{\boldsymbol{n}_i q_i(t_{ret})}{R_i(1-\eta\boldsymbol{\beta}_i\boldsymbol{n}_i)}\right]_{\text{ret}} \\ & - \frac{1}{c^2}\frac{\partial}{\partial t}\sum_{i=1}^{\zeta}\left[\frac{\boldsymbol{n}_i q_i(t_{ret})}{R_i(1-\eta\boldsymbol{\beta}_i\boldsymbol{n}_i)}\right]_{\text{ret}}\Bigg\} \end{aligned} \tag{2.26}$$

In SELFAS, the length of the particle track is of 15 g/cm^2, divided into sub tracks of 0.3 g/cm^2 as depicted in Figure 2.30. The atmospheric depth along the shower axis at which the particles are created are randomly chosen with a probability matching the longitudinal profile. At the first propagation step (step 0 in Figure 2.30), the initial conditions are randomly calculated from Lafebre's distributions. For the next steps, the Lorentz force applied to the particle is calculated and the scattering probability is evaluated according the energy of the particle and the atmospheric density, from which, the new kinematic parameters are calculated. The same procedure is repeated for all sub tracks. SELFAS uses an absolute thinning for computational performance purpose, the particles with an energy smaller than 0.8 MeV are not considered.

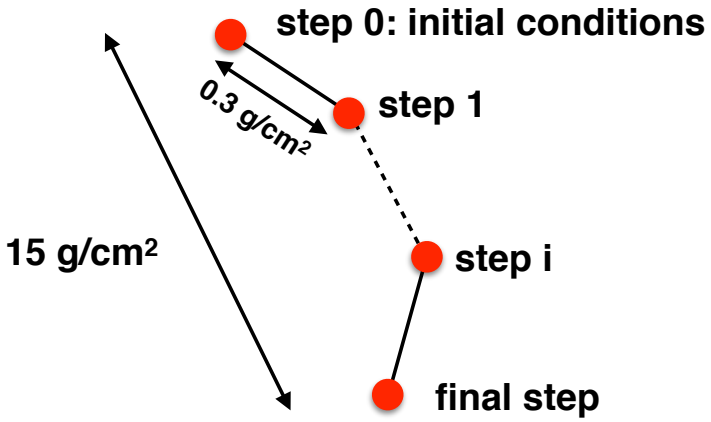

Figure 2.30: A total particle track of 15 g/cm^2 and the sub tracks of 0.3 g/cm^2 as defined in SELFAS.

2.3.3 Other codes

Macroscopic models

The simulation code MGMR (Macroscopic Geo-Magnetic Radiation) considers a point-like particle distribution [144]. The net charge $Q(t)$ is calculated as $Q(t) = a \times N_p(t)$, where N_p is the number of electrons and positrons and a is the negative charge excess ratio (evaluated at around 22%). The lateral deviation of the electrons and positrons with respect to the shower axis is estimated considering the Lorentz force and the possibility of multiple scattering (for vertical showers only). MGMR and its successor EVA [145] predicts a bipolar signal.

Microscopic models

CoREAS, is the result of the implementation of REAS3 [146], that computes the electric field as a sum of the contributions of the secondary particles, in electromagnetic interaction model CORSIKA. ZHAireS [147] uses the formalism developed by Zas, Halzen and Stanev [148] and computes the electric of showers generated by AIRES. The computing times of these two codes are quite high if one compares to SELFAS. The reason is that CoREAS and ZHAireS simulate the full shower, including the energy, position and momentum of all the secondary particles created during the shower development, before computing the electric field induced by the latter particles. The calculation of the shower development is made using one hadronic interaction model presented in this section. On the contrary, SELFAS uses parametrized distributions for the secondary particles which initial conditions are randomly chosen. Either accordingly to a Gaisser-Hillas longitudinal profile or a profile computed by CONEX from a hadronic interaction model. The advantage of SELFAS is that it computes only a

fraction of the total number of the secondary particles. The computing time is very competitive and the results are in very good agreement with experimental observations. To avoid large shower-to-shower fluctuations, we must consider at least 20×10^6 particles.

CHAPTER 3

Radio reconstruction of the EAS parameters

Contents

3.1 Introduction

The precise determination of the mass of the primary (associated with the energy and the arrival direction) is the key to constrain theoretical models of mechanisms of acceleration, propagation and the type of sources. As described in the previous Chapter, the mass estimation is performed statistically from measurements of the shower maximum with the fluorescence technique. The low duty cycle of this type of detection does not allow a precise mass discrimination at the highest energies. The duty cycle of the radio detection is around 100% and it is now established that the electric field induced by an extensive air shower is strongly correlated to the parameters of the primary cosmic ray. More precisely, the parameters of the lateral distribution function of the electric field contain all the informations about the primary and the correlations are summarized below:

- intensity $\longrightarrow$ energy of the primary
- slope of the lateral distribution $\longrightarrow$ mass of the primary
- frequency spectra $\longrightarrow$ mass of the primary
- timing of the pulses $\longrightarrow$ arrival direction
- position of the radio core $\longrightarrow$ position of the particle core

The radio detection appears as a perfect complement or alternative to the fluorescence detection to raise the statistics of detected event. In this chapter, I detail the different ideas that have been developed during this thesis in order to constrain the longitudinal profile of an extensive air shower, using only the radio signal and its computation. The main idea is to compare a model of electric field lateral distribution to the experimental one, sampled by an array of antennas.

3.2 A model of angular distribution of radiation

This study is based on the concept of shower universality, first introduced in [149] to describe the longitudinal profile of electromagnetic showers. According to this principle, a profile is fully described by the energy of the primary. The original idea was to develop a parametrized model describing the angular distribution of radiation. One of the free parameters of the model is the geometrical distance to the maximum emission. The main emission mechanism is the geomagnetic effect, causing an acceleration of the secondary particles in the direction $(\boldsymbol{v} \times \boldsymbol{B}_{\text{geo}})$ perpendicular to the direction of propagation of the particles $(\boldsymbol{v})$. The angular distribution of radiated power by unit of solid angle for a particle is calculated in [150] and is expressed as:

$$\frac{\mathrm{d}P}{\mathrm{d}\Omega} = \frac{2}{\pi}\frac{e^2}{c^3}\gamma^6 \frac{|\dot{\boldsymbol{v}}|}{(1+\gamma^2\theta^2)^3}\left[1 - \frac{4\gamma^2\theta^2\cos^2\phi}{(1+\gamma^2\theta^2)^2}\right] \tag{3.1}$$

Where θ denotes the zenith angle of emission with respect to the direction of propagation of the particle, ϕ is the azimuth angle of emission with respect to the acceleration direction of the particle in the plan perpendicular to $\boldsymbol{v}$ and parallel to $\boldsymbol{a}$. γ is the Lorentz factor of the particle. Thus one can calculate the relative electric field radiation diagrams for different values of γ for the best case scenario ($\cos\phi = 1$):

$$\frac{\mathrm{d}E}{\mathrm{d}\Omega} \propto \sqrt{\frac{\gamma^6}{(1+\gamma^2\theta^2)^3}\left[1-\frac{4\gamma^2\theta^2}{(1+\gamma^2\theta^2)^2}\right]} \tag{3.2}$$

as displayed in Figure 3.1:

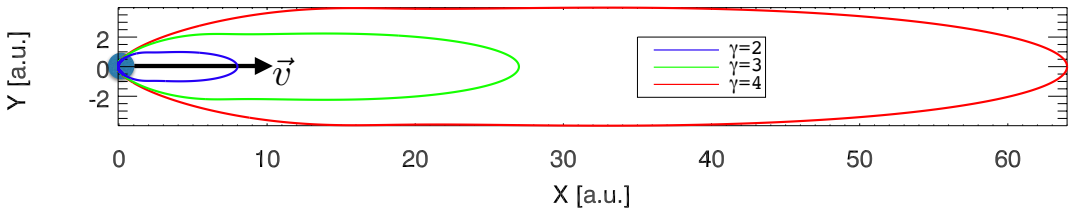

Figure 3.1: Absolute radiation diagrams for different values of γ. X and Y are respectively the direction of propagation of the particle and the direction transverse to the direction of propagation.

The emitted electric field is extremely focalized in the direction of propagation of the particle and the intensity varies at the first order as a function of γ^3. The angular distribution is also modified by the γ factor. In Figure 3.2, each distribution is normalized to its maximum value ($\simeq \gamma^3$) to highlight the effect.

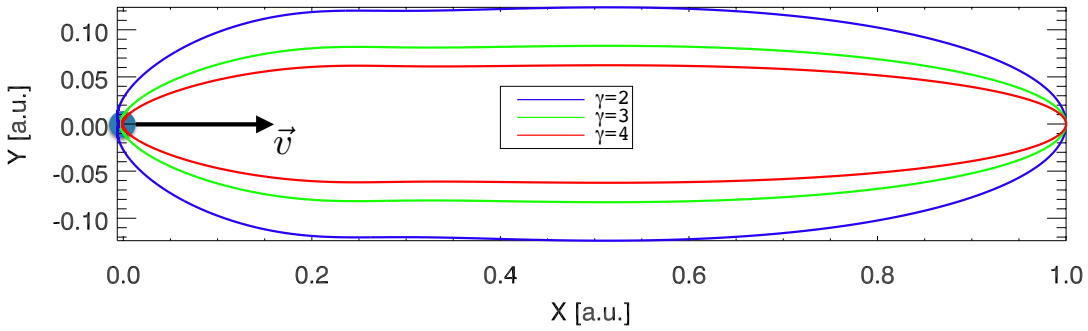

Figure 3.2: Normalized radiation diagrams for different values of γ.

$$\frac{1}{\gamma^3}\frac{\mathrm{d}E}{\mathrm{d}\Omega} \propto \sqrt{\frac{1}{(1+\gamma^2\theta^2)^3}\left[1-\frac{4\gamma^2\theta^2}{(1+\gamma^2\theta^2)^2}\right]} \tag{3.3}$$

The root mean square angle of the emission of radiation, the angle under which 68% of the emitted power is located, is proportional to $1/\gamma$.

$$\left\langle \theta^2 \right\rangle^{1/2} = \frac{1}{\gamma} \tag{3.4}$$

The angular distribution of the electric field is sharper, the greater the Lorentz factor of the particle is. This angular distribution describes the full-band emission and can be used to estimate the distribution of the electric field emitted at a particular moment of the shower development as a function of the Lorentz factor of the particle. In Figure 3.3, the comparison is made with the electric field induced by a vertical proton with an energy of 10^{18} eV simulated with SELFAS, for which the air refractive index equals 1. The simulated antennas form a star shape array.

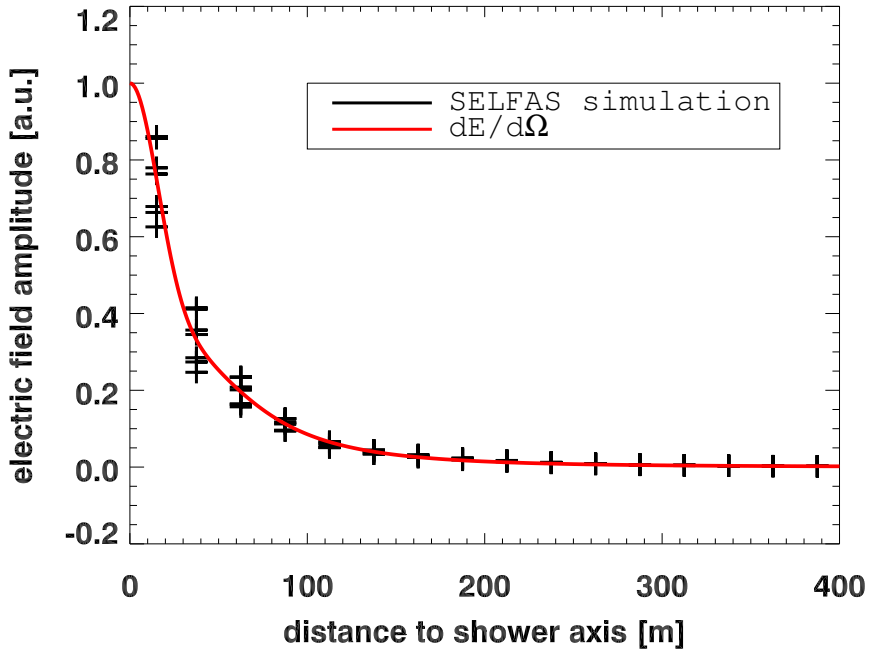

Figure 3.3: Normalized distribution of the electric field simulated with SELFAS compared to the model given by Equation (3.3) and fitted on SELFAS simulation. Each black cross represents a simulated antenna. The dispersion at fixed axis distance are due to the asymmetry of the amplitude of the electric field around the shower axis.

The mean energy of the secondary particles in the shower is around 30 MeV, corresponding to $\gamma = 60$ for electrons and positrons. On this plot, the electric field is not filtered and one can see that the distribution matches nicely the distribution of Equation (3.3). However it is not possible to detect the electric field in full band. Most of the detections are made in the [30 - 80] MHz frequency band. In Figure 3.4, the electric field computed with SELFAS is filtered in the frequency band [30 - 80] MHz. We can see that the angular model do not matches the simulation anymore as the slopes are different. The expression of the angular density written in Equation (3.3) as a function of

the frequency band would be difficult to obtain and not convenient due to the multiple presence of the Lorentz factor.

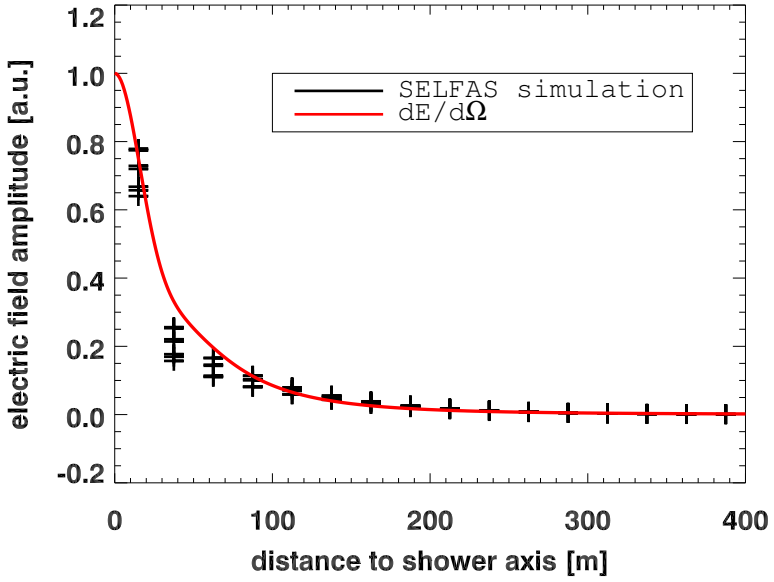

Figure 3.4: Normalized distribution of the electric field simulated with SELFAS and filtered in the frequency band [30 - 80] MHz, compared to the model given by Equation (3.3).

A convenient option is to parametrize a more simple model in the frequency band of interest using the simulation. The model to be parametrized must satisfy the conditions of Equation (3.2), thus it must satisfy Equation (3.4). The electric field decreases exponentially as a function of γ and the axis distance (i.e. the angle at which the radiation is observed). We thus choose to use a function of this type:

$$E(\theta_{\text{rad}}) \propto \exp\left[-\frac{\theta_{\text{rad}}^2}{2/\gamma^2}\right] \tag{3.5}$$

We then verify the condition established by Equation (3.4) for this model. In Figure 3.5 the angle of emission at which 1σ of the electric field distribution is contained is plotted as a function of the Lorentz factor of the particles. A comparison is made with the function $f(\gamma) = 1/\gamma$ and we observe a perfect match (see Figure 3.5). The displayed values are obtained by integrating the angular distribution obtained with Equation (3.5) along the angle of emission until reaching 68% of the total emission, for different values of γ. Thus one can begin the parametrization of the model. Some changes are applied to Equation (3.5). First, the Lorentz factor of the secondary particles does not need to appear clearly in the parametrization. The reason is that the angular density model we are building will be parametrized on a lateral distribution function simulated with SELFAS. The LDF is calculated for the maximum electric field received on the ground and is a

"picture" of the emission at a particular moment of the development of the shower.

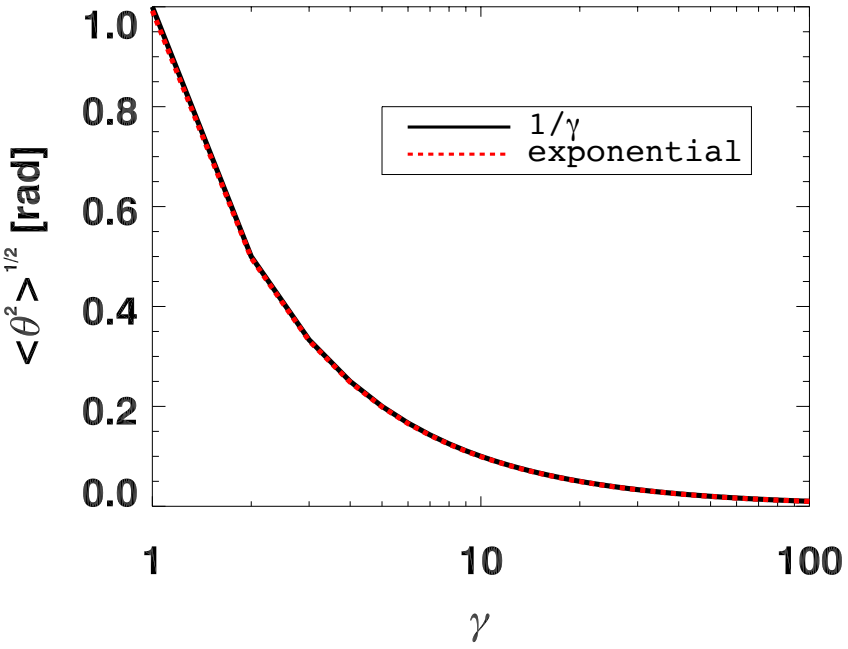

Figure 3.5: The root mean square angle of the emission of radiation as a function of γ for the model proposed in Equation (3.5) (see text for details).

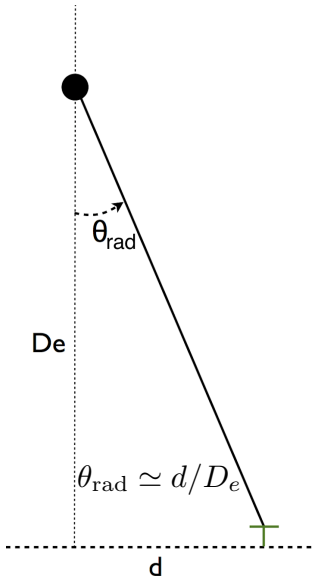

Figure 3.6: Geometry of the problem (see text for details).

The model is written as follow:

$$E(\theta_{\text{rad}}) = E_0.\exp\left[-\alpha.\theta_{\text{rad}}^{P}\right] \quad (3.6)$$

The parameter γ is likely to vary from shower to shower. It is hidden in the slope parameter α that will remain free. Also the exponent on θ_{rad} will be let free during the parametrization as the slope changes when the electric field is filtered. The geometry of the problem is depicted in Figure 3.6. The electric field is emitted at an altitude D_e under an angle θ_{rad} and detected by an antenna at a distance d from the shower axis. $D_e \gg d$ so that $\tan\theta_{\text{rad}} \simeq \theta_{\text{rad}} = d/D_e$. The model can now be written as:

$$E(D_e) = E_0.\exp\left[-\alpha.\left(\frac{d}{De}\right)^{P}\right] \quad (3.7)$$

In Figure 3.7, the LDF of a simulated event is plotted as a function of the axis distance and of the radiation angle.

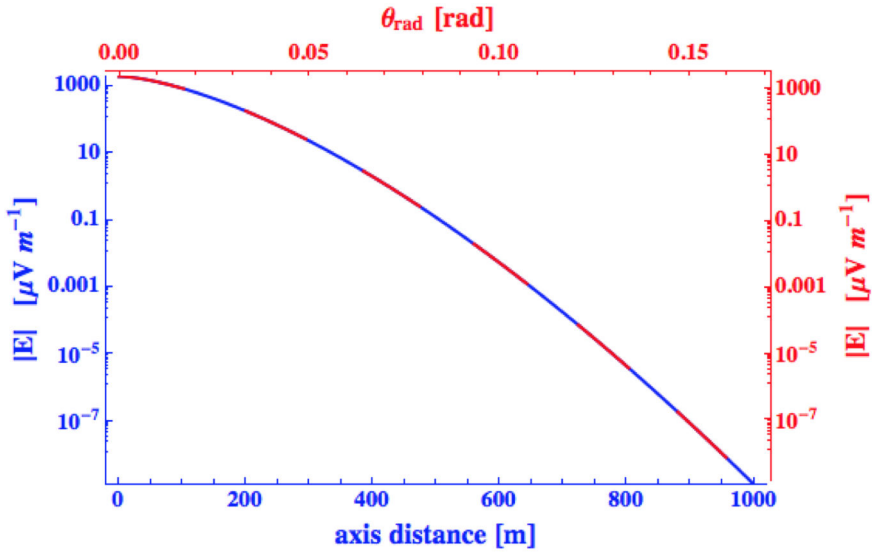

Figure 3.7: Amplitude of the electric field of a simulated event as a function of the angle of emission and the distance to the shower axis.

To parametrize the model, the electric field induced by an EAS is simulated with SELFAS. The EAS is initiated by a 10^{18}eV proton with a 30° zenith angle and a 270° azimuth angle. All this study is done in the filtered range [30 - 80] MHz. The best fit is obtained for $P = 1.54$, $\alpha = 420$ and $D_e = 5958.2$ m. From now on P and α are fixed and will not be let free during the fits to other simulation. The latter assertion is based on the universality principle according to which all extensive air showers can be described with two parameters: the energy of the primary, the first interaction depth. The energy of the primary influences the amplitude of the electric field and the first interaction depth influences the slope of the electric field distribution.

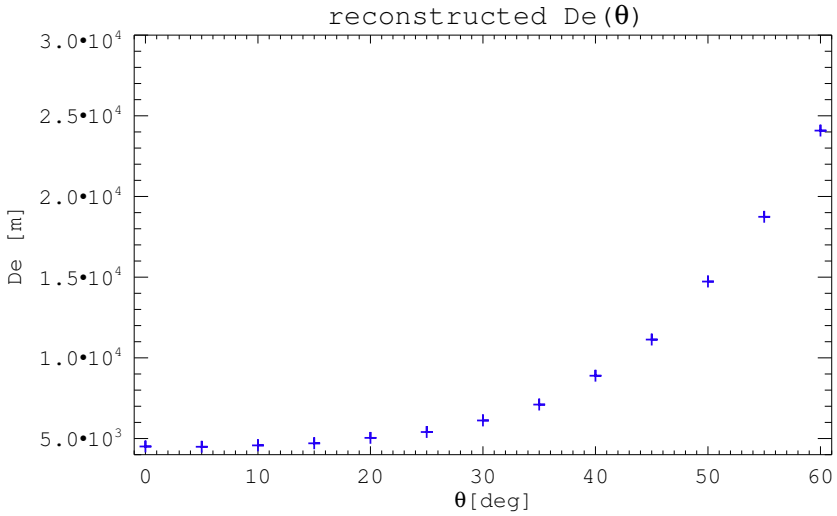

Figure 3.8: D_e values reconstructed for identical events but with different zenith angles

In the model, these parameters are described by E_0 and D_e respectively. The model has been tested on several events for which only the zenith angles vary from 0° to 60° by 5° steps. E_0 and D_e are free parameters. For each event, the simulated LDF is fitted with the model, estimating $D_e = f(\theta)$ (see Figure 3.8). Before testing the model on other events, where the geometrical distance to the maximum emission D_e is a free parameter, an estimation of the depth at which the maximum electric field has been emitted has been performed. To estimate the crossed atmospheric depth corresponding to an altitude above the mean see level, one can use the atmospheric parametrization made by Linsley [14]. With this model the atmosphere is divided in four layers and the coefficient are calculated from the U.S. Standard Atmosphere model [151].

$$f(z) = \begin{cases} -186.5562 + 1222.6562\exp(-z/9941.8638) & \text{if} \quad 0 < z \leq 4000 \text{ m} \\ -94.9199 + 1144.9069\exp(-z/8781.5355) & \text{if} \quad 4000 \text{ m} < z < 10000 \text{ m} \\ 0.61289 + 1305.5948\exp(-z/6361.4304) & \text{if} \quad 10000 \text{ m} \leq z < 40000 \text{ m} \\ 540.1778\exp(-z/7721.7016) & \text{if} \quad 40000 \text{ m} \leq z < 100000 \text{ m} \end{cases} \tag{3.8}$$

This function calculates the atmospheric depth in g/cm^2, crossed by a vertical particle, knowing its altitude z. The reciprocal function is given by:

$$f(X)^{-1} = \begin{cases} -9941.8638\ln\left(\frac{186.5562+X}{1222.6562}\right) & \text{if} \quad 631.1 \text{ g/cm}^2 \leq X \\ -8781.5355\ln\left(\frac{94.9199+X}{1144.9069}\right) & \text{if} \quad 271.7 \text{ g/cm}^2 < X < 631.1 \text{ g/cm}^2 \\ -6361.4304\ln\left(\frac{-0.61289+X}{1305.5948}\right) & \text{if} \quad 3.039 \text{ g/cm}^2 < X \leq 271.7 \text{ g/cm}^2 \\ -7721.7016\ln\left(\frac{X}{540.1778}\right) & \text{if} \quad 0.00182 \text{ g/cm}^2 \leq X \leq 3.039 \text{ g/cm}^2 \end{cases} \tag{3.9}$$

Then, these functions are tested on several events for which only the zenithal angle vary from 0° to 60° by 5° steps. For each event, the model fits the LDF and a correction is applied for inclined events with a zenith angle of θ. The atmospheric depth is calculated as:

$$X = f(D_e)/\cos\theta \tag{3.10}$$

The inverse deconvolution function is applied to these reconstructed values to calculate the corresponding depth. The results are shown in Figure 3.9. The depths of the maximum emission are very close to the depth of the inflection point of the longitudinal profiles. This result is coherent with the description of the electric field detailed in the previous chapter, as the intensity is proportional to the production rate of the secondary particles, which is maximum at X_{inf}. Nowadays the depth at which the maximum emission is produced is not clearly established.

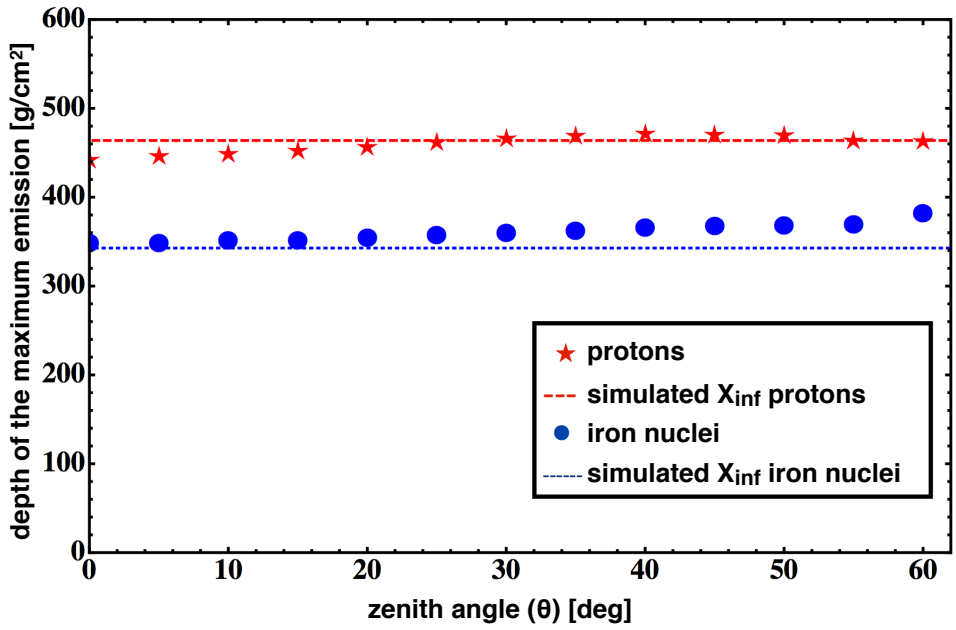

Figure 3.9: Reconstructed depth of the emission maximum, compared to the depth of the first inflection point of the shower profiles (X_{inf}) used to simulate the electric field with SELFAS. The simulated primaries have an energy of 10^{18} eV.

The main agreement is that the moment of the maximum emission is located between X_{inf} and X_{max}. The results shown in Figure 3.9 prove that it is possible to disentangle the atmospheric effects, to reconstruct the depth of the maximum emission (to which I will now refer to as X_{inf}) and to compare EAS that come from different zenith angles. We now try to improve the model by taking into account the asymmetry of the electric field intensity around the shower axis.

3.2.1 Two dimensional model

The charge excess mechanism produces an electric field radially polarized around the shower axis whereas the geomagnetic effect produces an electric field polarized in the $\boldsymbol{v} \times \boldsymbol{B}$ direction. The superposition of the two effects leads to a rather important (for this study) asymmetry around the shower axis (see Section 2.2), as we can see on the following plot. Figure 3.10 shows the density map of the electric field's maximum value received at ground level. The EAS is initiated by a vertical proton with an energy of 10^{18} eV. In order to describe the asymmetry effect, we add a second dimension to our model: the parameter φ, defined as the oriented angle between $\boldsymbol{v} \times \boldsymbol{B}$ and the vector $\boldsymbol{r}$ directed from the shower particle core to the observer position, projected into the plane perpendicular to the shower arrival direction.

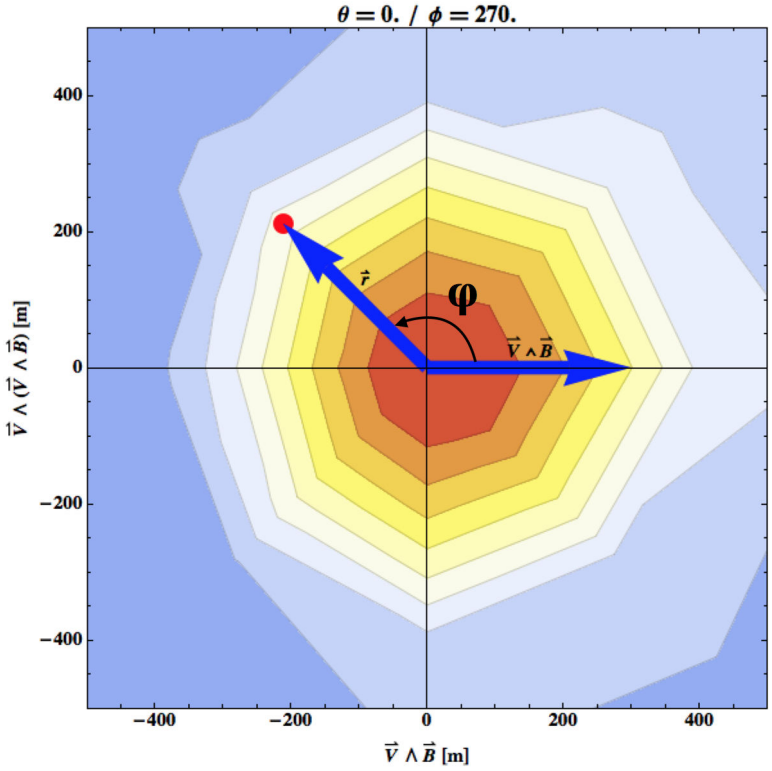

Figure 3.10: Density map of the maximum electric field received by several antennas, projected into the plane perpendicular to shower arrival direction.

The model is now written as:

$$E(d,\varphi) = E_0.\exp\left[-\alpha\left(\frac{d}{De(1+\beta\cos\varphi)}\right)^P\right] \tag{3.11}$$

The parameter β will remain free. Its purpose is to account for the ratio of the amplitudes of the electric field produced by the charge excess and geomagnetic mechanisms. We parametrize the two dimensional model with the same event as described previously. We estimate a relative value of the SNR for each antenna for the East-West polarization and in the frequency range [30 - 80] MHz in order to exclude antennas presenting a low SNR. The fit gives $\alpha = 376.13$, P = 1.60 and for this example: $\beta = 0.16$. In Figure 3.11 and Figure 3.12, the one and two dimensional models are compared for different directions around the shower axis. In the North - South direction the LDF is symmetric with respect to the shower axis.

In the East-West direction, the two mechanisms produce constructive interferences in the East direction whereas the interferences are destructive in the West direction (see Section 2.2). The two dimensional model accounts for this effect. The two dimensional model improves the fit, compared to the one dimensional model: $\chi^2_{1D} = 18.9$ and $\chi^2_{2D} = 1.5$ (normalized by the number of degrees of freedom).

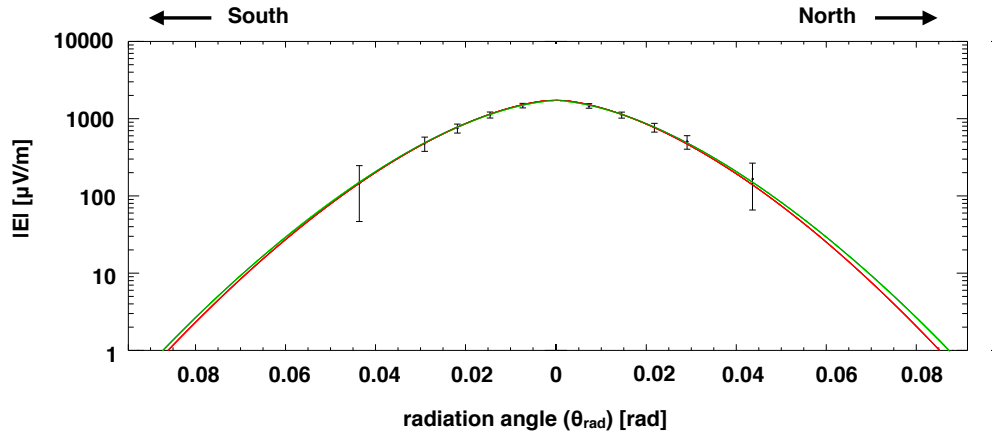

Figure 3.11: The one dimensional model (green curve) is fitted on the simulated data points (black points) along the North - South direction. The two dimensional fit is represented by the red curve.

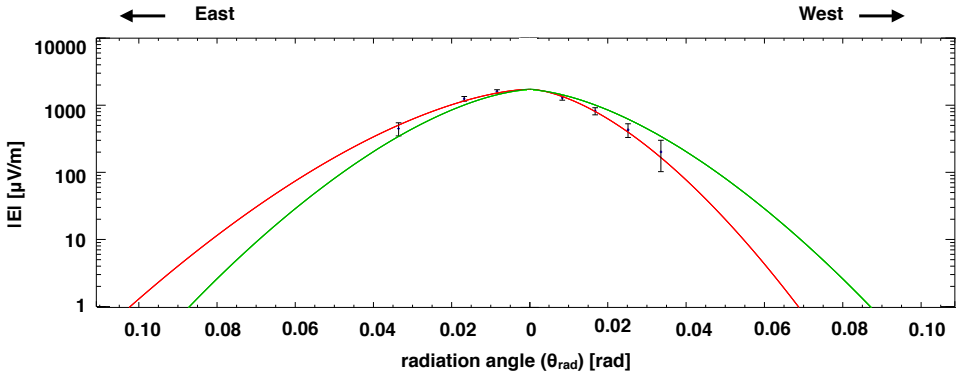

Figure 3.12: The same fit as above but in the East - West direction.

The two dimensional model is tested on proton induced events with the same arrival direction and the same energy. The first interaction depth varying from 5 to 85 g/cm^2. The reconstructed X_{inf} are plotted as a function of the simulated ones in Figure 3.13. It shows small deviations appearing when X_1 takes values far from the one we used to set the model ($X_1 = 40$ g/cm^2, corresponding to $X_{\text{inf}} \simeq 515$ g/cm^2).

These differences with the expected value can be explained by the fact that events with same characteristics (energy, arrival direction, primary particle), but different X_1 can generate EAS which develop in different ways because they do not experience the same variation of the atmosphere's density. Therefore the electric field's angular distribution can vary a few.

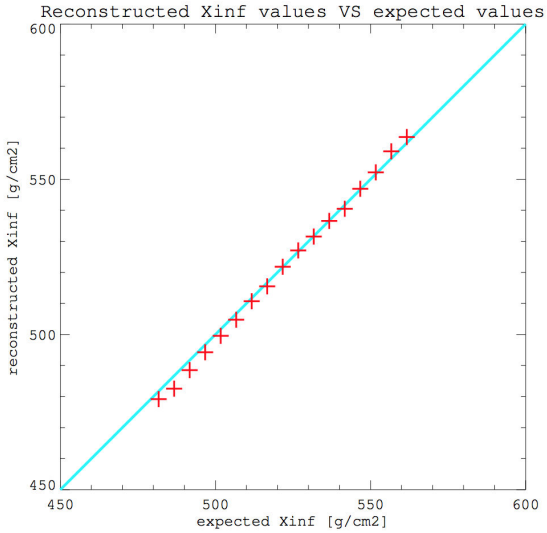

Figure 3.13: Reconstructed X_{inf} values using the 2D model as a function of the simulated ones for different first interaction depths (X_1). The blue line represents a one to one correlation.

In Figure 3.14, the histogram of the differences of the simulated X_{inf} and the reconstructed ones is presented.

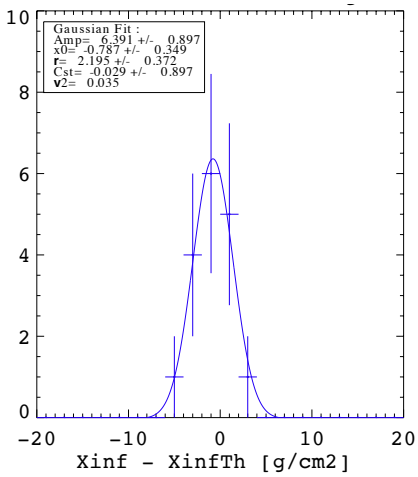

Figure 3.14: Histogram of the differences of the simulated X_{inf} and the reconstructed ones for different values of the first interaction depths (X_1).

The deviations can reach 5 g/cm^2. The deviations can be fitted by a gaussian function from which the center (μ) and standard deviation (σ) can be used to estimate the quality of the reconstruction, defined as $D^{\text{th}} = \mu \pm \sigma$. The precision of the reconstruction reached for different first interaction depth is $D^{\text{th}} = X_{\text{inf}}^{\text{rec}} - X_{\text{inf}}^{\text{th}} = -0.79 \pm 2.2$ g/cm^2. The deviation is very small and this effect will not be considered in the following of this study. The model is also tested on identical events to the event which we used for parameterization but with zenith angles from 0° to 80° by 5° steps and azimuthal

angle of 0° (East) and 180° (Weast).

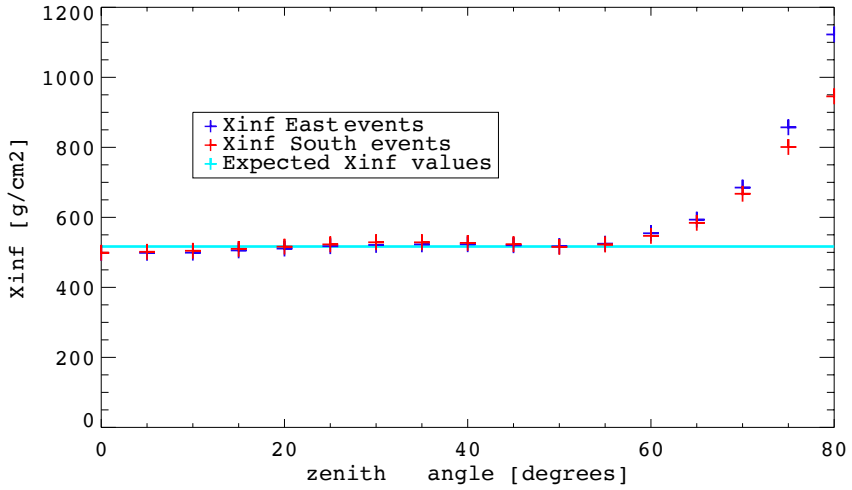

Figure 3.15: Reconstructed X_{inf} depths for showers induced by protons of 10^{17} eV, for different zenith and azimuth angles. The East direction corresponds to an azimuthal angle of 0° and the South to an angle of 270°.

In Figure 3.15 the reconstruction is satisfactory for $\theta < 60°$ and for different azimuth angles (the distance to the true value is smaller than 20 g/cm^2). It also shows that, for $\theta > 60°$ some deviations appear, obviously strongly correlated with the zenith angle. The calculation performed to reconstruct X_{inf} from D_e involves a flat approximation of the atmosphere, corrected for the zenith angle $X_{\text{inf}} = f(D_e)/\cos\theta$. However, on a segment of an inclined shower, the crossed atmospheric depth cannot be calculated as $X_{\text{vertical}}/\cos\theta$ due to the Earth curvature. The amount of discrepancies increases with the height of the zenith angle using this approximation. In the following, only events having a zenith angle under 60° are considered.

3.2.2 Results of X_{inf} depth reconstruction

To test the model at a higher scale, SELFAS is used to generate around 6000 events (representing 60,000 hours of computing time) with the following characteristics:

- The energy of the primary (E_P) is randomly selected: $\log_{10}(E_P) \in [17, 20]$
- θ is randomly selected: $\cos\theta \in [\frac{1}{2}, 1]$ corresponding to $\theta \in [0°, 60°]$
- ϕ is randomly selected: $\phi \in [0°, 360°]$
- 4200 protons, 1500 iron nuclei
- The antenna pattern of the AERA array
- The shower core position is randomly drawn inside of the AERA array (with an increased probability in the dense core of the array)

More protons are simulated due to their larger fluctuations compared to iron nuclei. The arrival directions and the shower core positions are displayed in Figure 3.17.

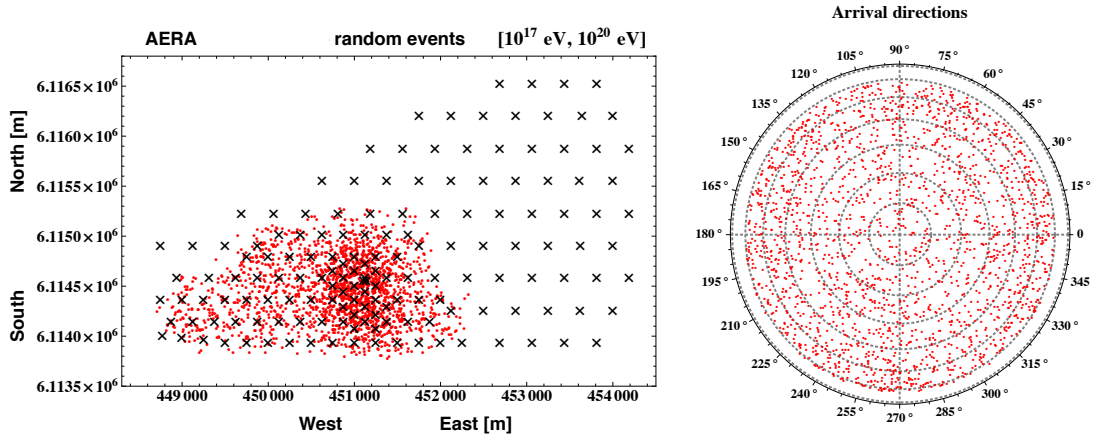

Figure 3.16: Left: Core position of the simulated events on the AERA frame, the black crosses refer to the antennas. - Right: Arrival direction of the simulated events, the difference of zenith angle between two grey dashed lines is of 10°.

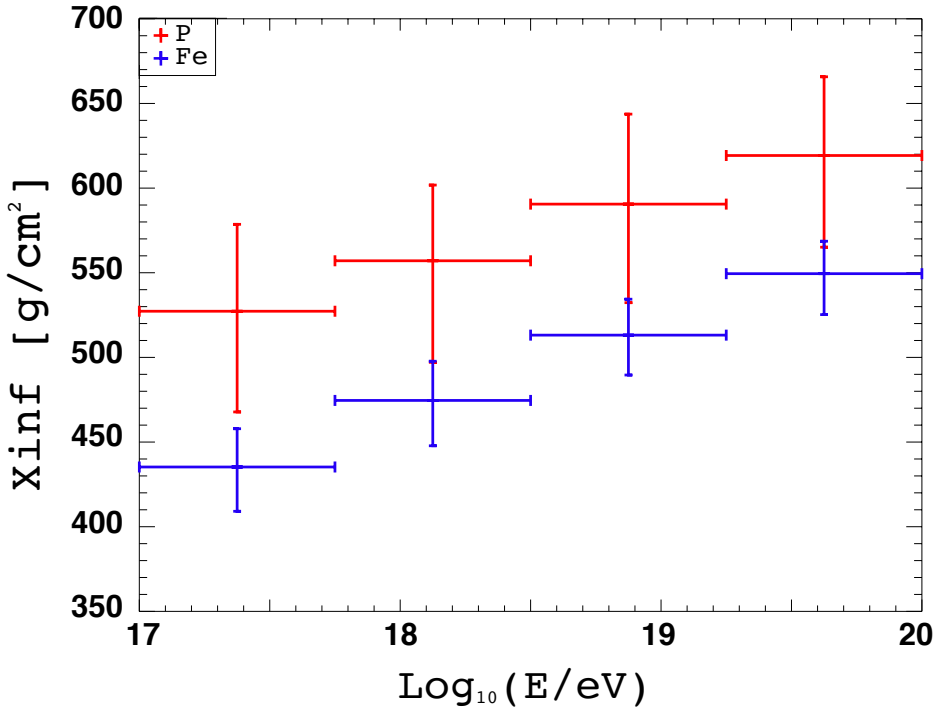

Figure 3.17: Simulated X_{inf} values as a function of the energy of the primary. The red points are the values of the proton-induced showers and the blue points are the values of the iron nuclei-induced showers.

The simulated X_{inf} are presented in Figure 3.17 as a function of the energy and the nature of the primary cosmic rays. The points are the mean X_{inf} values. The width of

the horizontal error bars are the width of the energy bins. The vertical error bars account for the statistical fluctuations and are calculated from the cumulative distribution function for each energy bin, explaining the asymmetry around the mean values. The reconstruction method is applied on the set of simulated events and the scatter plot of the reconstructed X_{inf} as a function of the simulated X_{inf} is shown in Figure 3.18.

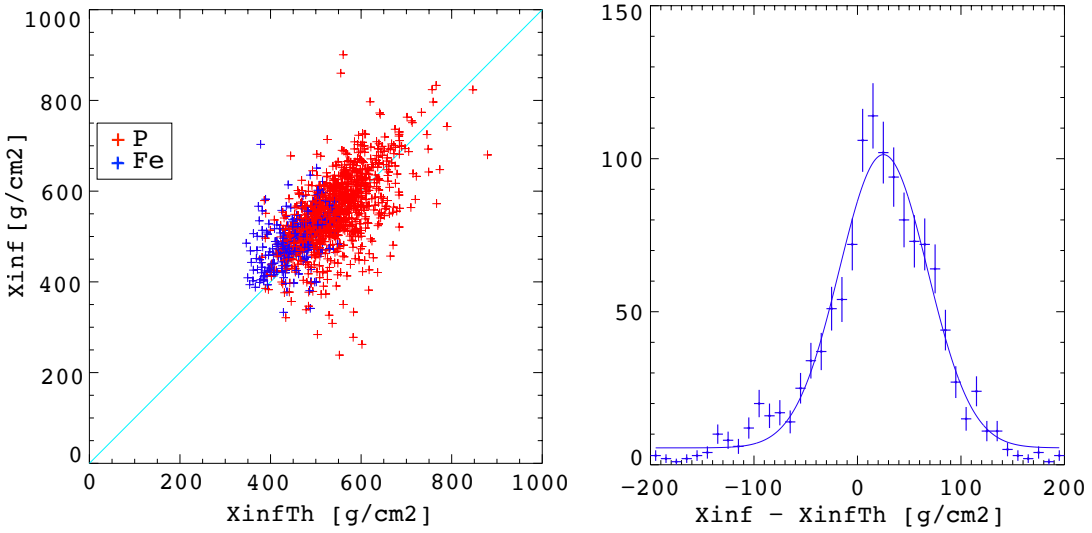

Figure 3.18: Left: Reconstructed X_{inf} values with the two dimensional model as a function of the expected ones. Right: Histogram of the differences between the reconstructed values and the reconstructed ones.

The reconstruction method gives a clear correlation to the expected values. To estimate the deviations, the histogram of the differences between the reconstructed and expected values is fitted by a gaussian function. The two dimensional model overestimates the expected X_{inf} values, $\overline{D^{\text{th}}} = 25 \pm 42$ g/cm^2 at 68% confidence level. The comparison is made with of the 1D model, which reveals the improvement due to the use of the 2D model, the result is: $\overline{D^{\text{th}}} = 40 \pm 55$ g/cm^2 for the 1D model. The overestimation caused by the use of the 1D model is reduced when using the 2D model.

The true advantage of the 2D model compared to the 1D model is that some showers will hit the edges of the array. In this case, only a fraction of the electric field around the shower axis is detected and due to the asymmetry, we will use a biased LDF slope using the one dimensional model, depending on which side of the shower is detected. With the two dimensional model one can evaluate the missing signal around the shower axis and thus, fits properly the LDF. The reconstructed values by energy bins are presented in Figure 3.19.

The mean difference of the reconstructed X_{inf} values between protons and iron nuclei is around 70 g/cm^2. The simulated values have a mean difference of 100 g/cm^2. The reconstruction method permits a good separation of the mass of the primary cosmic rays, although the differences are smaller than for the simulated values. The statistical

fluctuations of the reconstructed values and the protons and iron nuclei distributions are clearly overlapping for all energy bins.

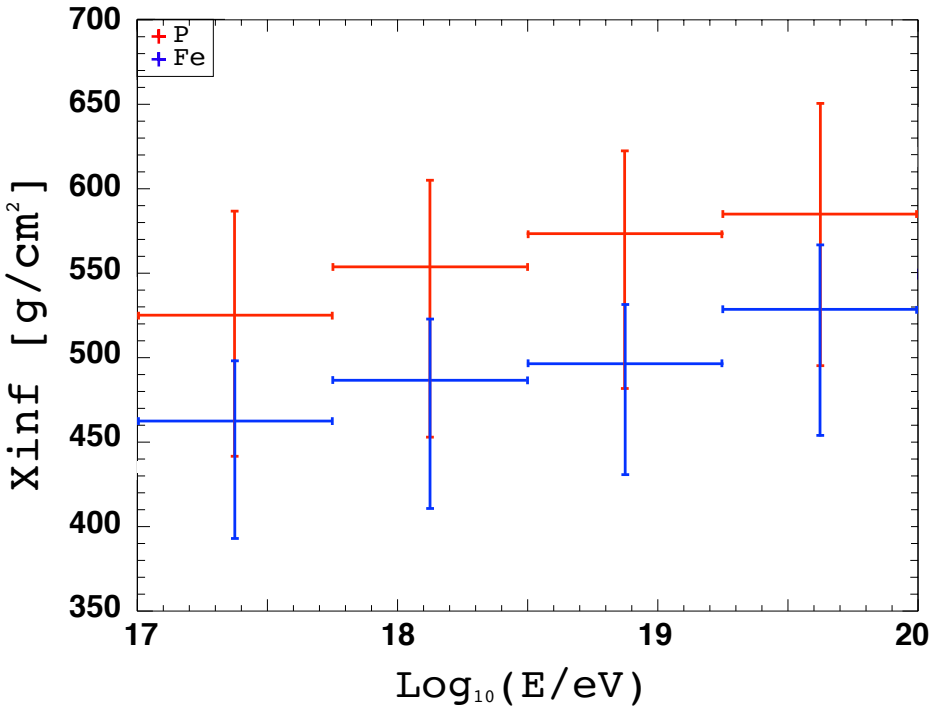

Figure 3.19: Reconstructed X_{inf} values as a function of the energy of the primary. The red points are the values of the proton-induced showers and the blue points are the values of the iron nuclei-induced showers.

The fluctuations are larger than for the simulated values which distributions have very narrow overlapping regions. In order to evaluate the influence of the uncertainties on the detected electric field on the reconstruction, the errors are propagated. A random error is added to the simulated electric field within a normal law, centered on the value of the electric field and a standard deviation of 10%. The reconstructed mean X_{inf} depth with error propagation are shown in Figure 3.20. The influence of errors of the detected electric field on the mean reconstructed values is negligible. Figure 3.20 shows that the mean X_{inf} depth as a function of energy can be employed to discriminate the mass of the primary cosmic rays. Figure 3.21 shows the error propagation on the standard deviation of the X_{inf} by energy bin.

The result is coherent with the expectations of larger fluctuations of the X_{inf} for proton induced showers comparing to shower induced by iron nuclei. The distributions of the standard deviations, as the distributions of the mean values, are also clearly separated. This result indicates that two parameters can be used for the mass discrimination

for a given energy range:

- the mean of the X_{inf} depths;
- the standard deviation of the X_{inf} depths.

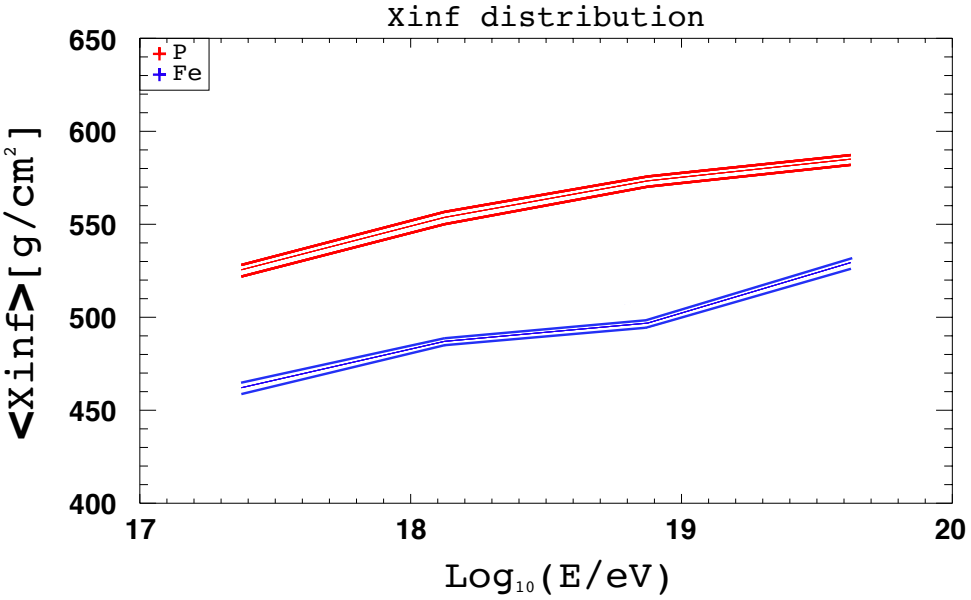

Figure 3.20: The reconstructed X_{inf} distributions with errors propagation.

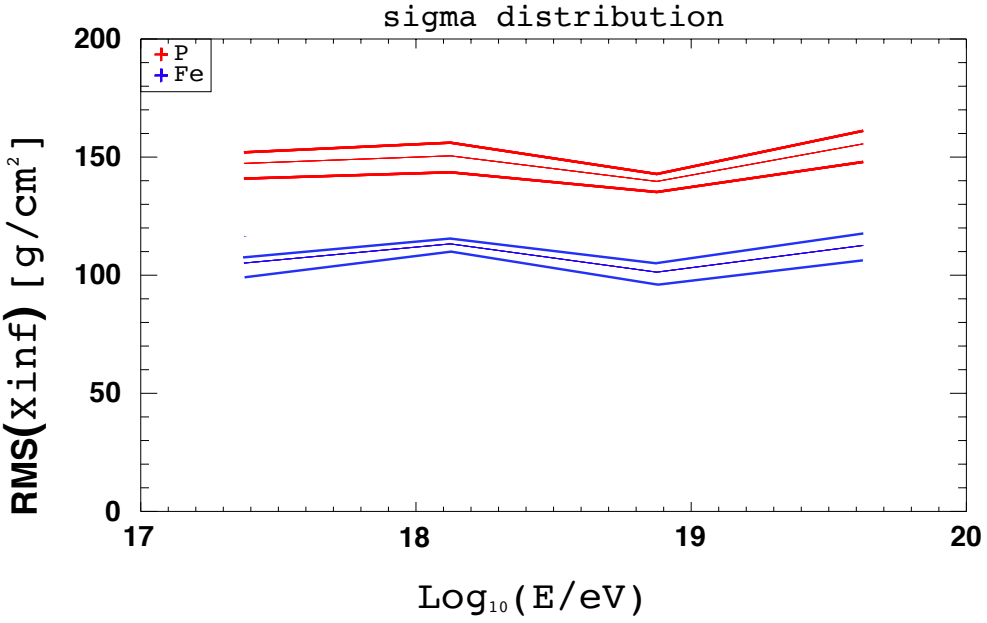

Figure 3.21: Reconstructed RMS(X_{inf}) distribution with errors propagation.

Some cuts are applied for different values of θ, ϕ and E_P, in order to see for which range of the latter parameters the reconstruction is the most accurate.

3.2.3 Influence of the zenith angle

First, all events with $\theta > 50°$ are removed from the data set. The reconstruction method is applied with the 2D model. $\overline{D^{\text{th}}}$ value is almost divided by 2 and sigma is around 10 g/cm^2 smaller, $\overline{D^{\text{th}}} = 13$ g/cm^2 with a dispersion of 34 g/cm^2 which is way better than the reconstruction using all the events. The comparison to the results obtained with the 1D model is made. The 1D model gives $\overline{D^{\text{th}}} = 22\pm$ g/cm^2 with a dispersion of 44 g/cm^2. The precision is better for the two models. This shows that the large angle problem appears earlier than expected and is more influent than previously though. In the following section only the events with $\theta < 50°$ are considered.

3.2.4 Influence of the azimuth angle

The events arriving from the North are removed from the data set to study a potential azimuthal effect. Only the events with $180° < \phi < 360°$ and $\theta < 50°$ are considered. The reconstruction is performed on the subset of events with the two dimensional model. The azimuth angle has nearly no influence on the agreement of the reconstructed values to the expected ones. $\overline{D^{\text{th}}} = 13$ g/cm^2 with a dispersion of 34 g/cm^2 for the subset with all azimuthal directions and $\overline{D^{\text{th}}} = 16$ g/cm^2 with a dispersion of 31 g/cm^2 for the subset without the events coming from the North.

3.2.5 Influence of the primary energy

Then we only look after events that have an energy of $\log(E_P) \in [17.5, 18.5]$, all ϕ values are considered and $\theta < 50°$. The 2D model is applied on the latter subset of events and the histograms of the differences between the reconstructed values gives $\overline{D^{\text{th}}} = 13$ g/cm^2 with a dispersion of 34 g/cm^2 for all energies and $\overline{D^{\text{th}}} = 16$ g/cm^2 with a dispersion of 29 g/cm^2 for the current subset. The energy of the primaries does not affect the reconstruction either. The deviation from the expected values will be tested as a function of the primary mass.

3.2.6 Influence of the nature of the primary

The two dimensional model has been parametrized using the electric field from proton induced shower. The set of all events for which $\theta < 50°$ is divided in two subsets: the proton induced showers and the iron nucleus induced showers. The 2D model is applied on both subsets. For proton-induced showers: $\overline{D^{\text{th}}} = -6$ g/cm^2 with a dispersion of 33 g/cm^2 and for iron-induced showers: $\overline{D^{\text{th}}} = 18$ g/cm^2 with a dispersion of 23 g/cm^2. The mean difference is smaller for the protons. It is coherent considering that the model was parametrized with a proton event. However, the standard deviation of

the difference is smaller for iron nuclei. The results show that the reconstruction is sensitive to the deviations between the longitudinal profile of the reconstructed event and the one that has been used to parametrized the model: the reference profile. Proton induced showers are more likely to match the reference profile. In the mean time, the large fluctuations inherent to the proton-air cross section produce a wide distribution of the differences between the reconstructed and expected values. The root mean square of the distribution of the differences is correlated to the root mean square of the X_{inf} distribution for $\log(E_P) \in [17.5, 18.5]$. On the contrary, longitudinal profiles of iron-induced showers are shifted with respect to the profiles of proton induced showers. Their fluctuation is also smaller than light nuclei. The results show that the deviation is due to the bias of the longitudinal profiles to the reference profile, and is induced by the mass of the primary cosmic rays.

3.2.7 Large zenith angles divergence

The previous results have shown that the model do not reconstruct correctly X_{inf} when the zenith angles are higher than 60°. Beyond this limit, an other structure appears in the LDF. Several LDF are presented in Figure 3.22 corresponding to several zenith angles. The red curves are the calculated LDF considering an air refractive index of $\eta = 1$ and the blue ones with an index of $\eta = 1.00029$, corresponding to the mean value at sea level. One can see that the topology of the LDFs calculated with a more realistic air refractive index of $\eta = 1.00029$ cannot be described by an exponential decrease when $\theta > 60°$. The deviations from the exponential decrease intensify as a function of the zenith angle. Indeed, the model does not take into account the air refractive index whereas it is taken into account in SELFAS. This parameter plays an important role in the topology of the electric field at the ground level. In SELFAS, the electric field is proportional to:

$$\boldsymbol{E} \propto \frac{\partial}{\partial t} \frac{1}{(1 - \eta \boldsymbol{\beta} \boldsymbol{n})} \tag{3.12}$$

Due to the time compression, the denominator can vanish and produce a boost of the electric field amplitude under a particular angle of observation, which corresponds to the angle at which the Cerenkov radiation is emitted. Thus, the variation of the electric field is not monotonous as a function of the distance to the shower axis. The electric field is maximum at the position of the projection of the cerenkov boost on the ground. From this position, the amplitude of the electric field decreases as a function of the axis distance in both directions. The boost is amplified at higher frequencies (> 120 MHz). In the frequency range [30 -80] MHz, the effect of the boost is negligible for showers having their maximum close to the ground. As the electric field is sampled by an array of antenna, the probability to detect it is quite low, as this component is located very close to the shower axis and its spatial distribution is very sharp. However, for shower having their maximum far from the ground, the boosted emission is located farther away from the shower axis and, due the the thickness and spread of the secondary particles, the spatial distribution of the boost is wider and more likely to be detected.

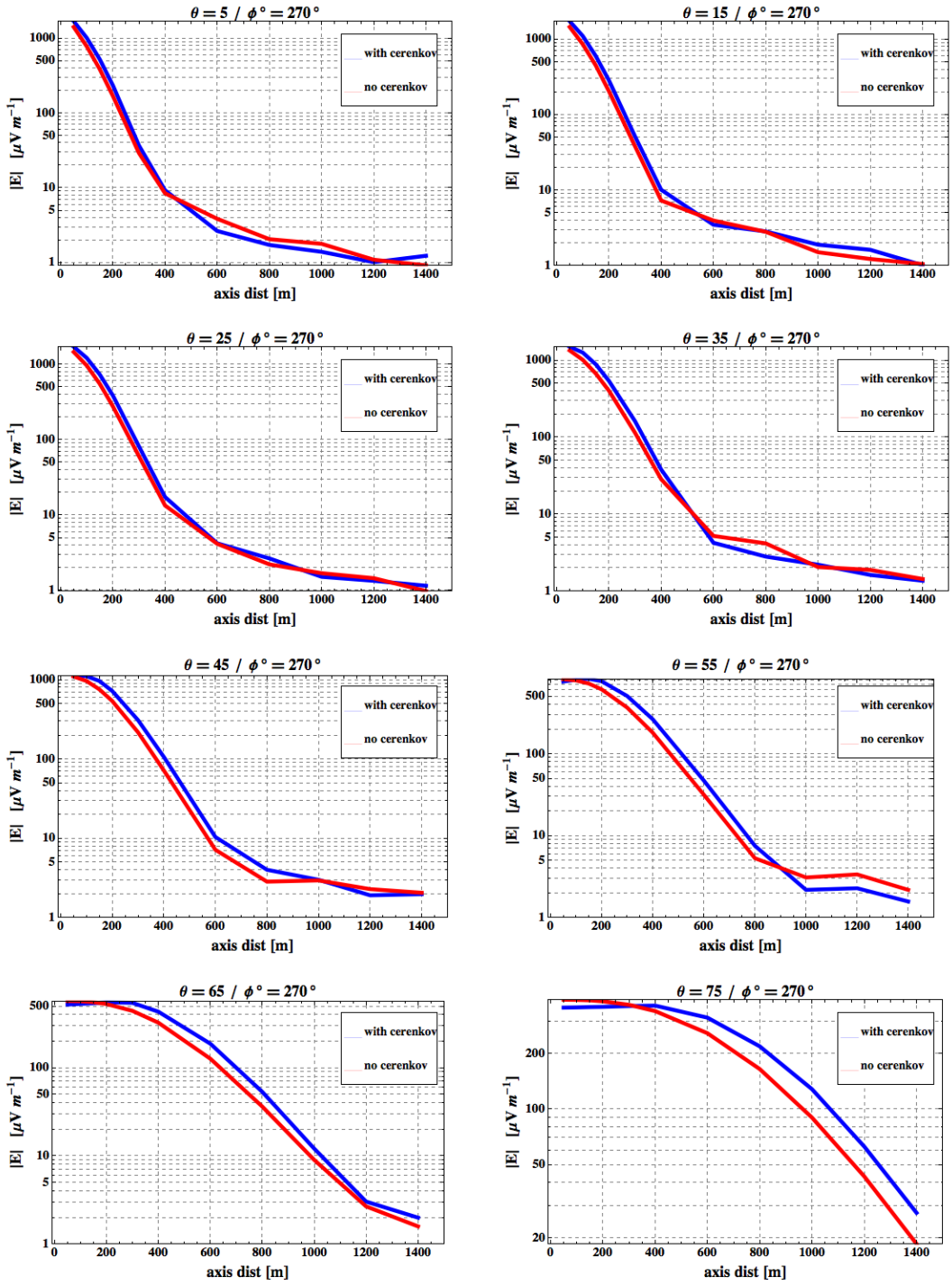

Figure 3.22: Simulated LDF with SELFAS for an azimuthal angle of 270° (South) and zenith angles from 5° to 75° with step of 10°. The red curves are the calculated LDF considering an air refractive index of $\eta = 1$ (no Cerenkov) and the blue ones with an index of $\eta = 1.00029$ (with Cerenkov), corresponding to the mean value at sea level.

These events are statistically more inclined than the one for which the Cerenkov

boost is not detected. The reconstructed X_{inf} for these events are completely inaccurate as the fitted model does not match the distribution.

3.2.8 conclusions

The addition of a second variable, accounting for the asymmetry of the intensity of the electric field around the shower axis, permits a significative improvement of the model of LDF. The results are summarized below for the total data set and the subset of events with $\theta < 50°$.

	$\theta \in [0°,60°]$		$\theta \in [0°,50°]$	
model	mean	dispersion	mean	dispersion
1D	39 g/cm^2	55 g/cm^2	21 g/cm^2	44 g/cm^2
2D	25 g/cm^2	42 g/cm^2	12 g/cm^2	33 g/cm^2

Table 3.1: Mean deviations and dispersions of the reconstructed X_{inf} values to the simulated ones for the 1D and 2D models and for different cuts of the zenith angle.

This first study has shown that the reconstruction discrepancies are nearly independent of the energy or the azimuth angle. Beyond a 50° zenith angle, the results of the reconstruction are biased. The 2D model needs to be adapted by the addition of a term describing the contribution of the Cerenkov effect. Nevertheless, the reconstruction is accurate for zenith angles smaller than 50° even if the model still overestimates the depth of the inflection point. However, this simple model does not take into account the air refractive index. The electric field distribution induced by a proton of 10^{18} eV with a first interaction depth of 5 g/cm^2 and a zenith angle of 80° in the frequency band [30 - 80] MHz is displayed in Figure 3.23.

One can see that the distribution of the electric field cannot be described by the 2D model. This method to estimate the mass of the primary presents several weaknesses:

1. for a consequent amount of events the model is inaccurate (especially when the zenith angle is greater than 50°).
2. the model needs to be parametrized for a specific frequency band.
3. taking into account the air refractive index would lead to a too important number of free parameters
4. to diminish the number of free parameters, some of them must be parametrized specifically for an experiment (pattern and spacing of the antenna array, geomagnetic field,...)

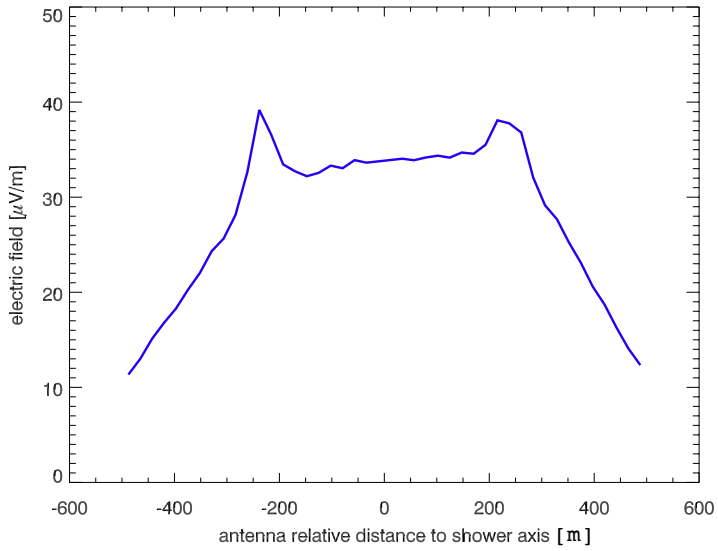

Figure 3.23: The electric field distribution in the east-west direction, induced by a proton of 10^{18} eV with a first interaction depth of 5 g/cm^2 and a zenith angle of 80° and an azimuth angle of 0° (North) in the frequency band [30 - 80] MHz.

For all this reasons, I decided to approach the problem from a different angle. We will test the agreement between the electric field sampled by an array of antennas to a Monte Carlo set of simulated events. The idea is to determine the combination of shower parameters (primary energy, $X_{\max}$ and particle core position) that needs to be simulated with SELFAS to obtain the best agreement to the experimental data.

3.3 A full radio method for EAS reconstruction

This method is based on a comparison of the detected electric field to its simulation. We aim to estimate the combination of primary mass, energy and the EAS core position that gives the best agreement between data and simulation. A summary of the method is presented in Figure 3.24. The different steps are detailed in the next Sections.

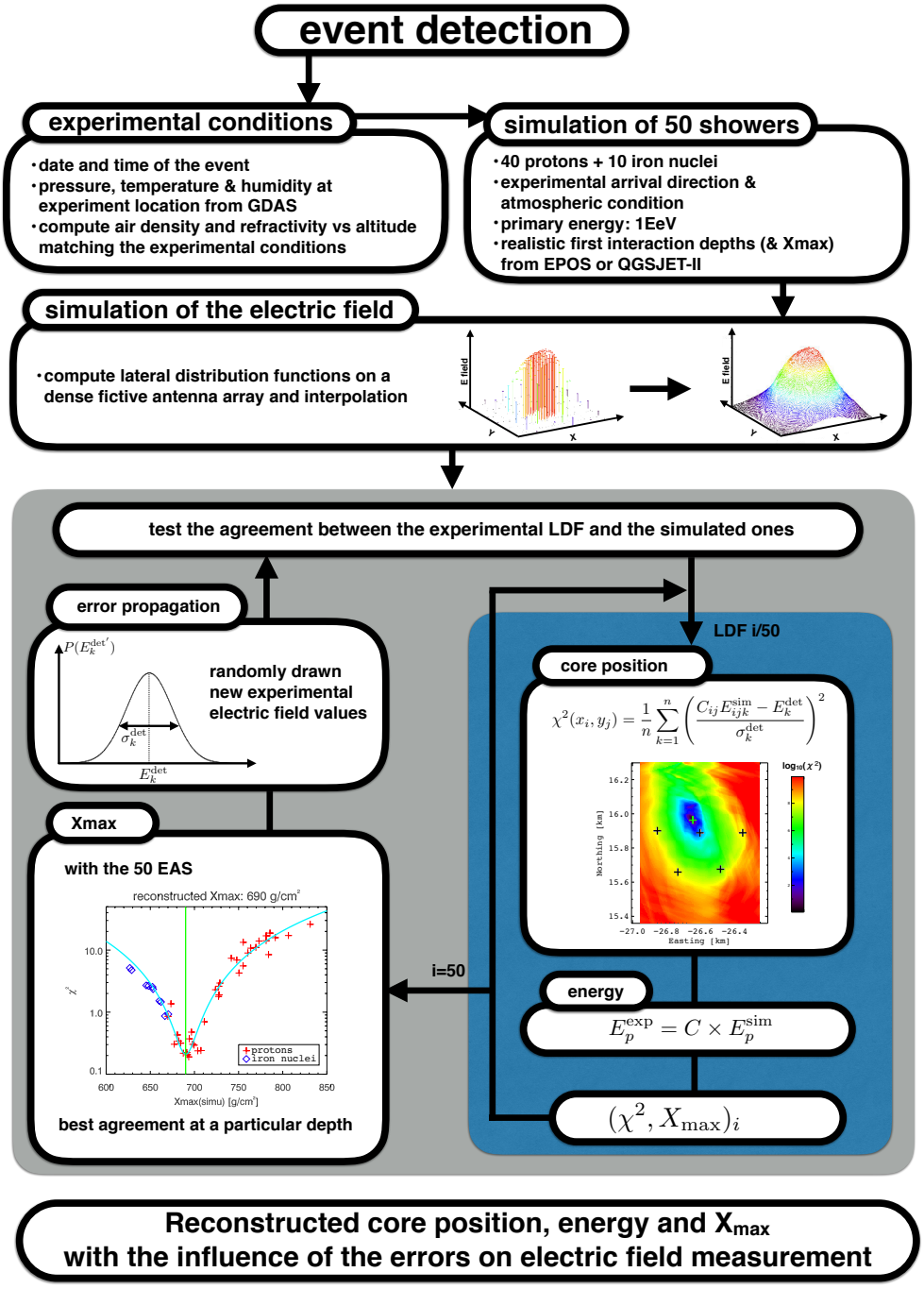

Figure 3.24: Diagram summarizing the steps of the radio method.

3.3.1 Detailed reconstruction of one AERA event

In this Section the full reconstruction of a super hybrid event detected at the Pierre Auger Observatory is detailed. This event has been recorded by the fluorescence telescopes, the Cerenkov tanks and the radio stations. The parameters we wish to reconstruct are thus precisely measured, ensuring a pertinent comparison with experimental results.

3.3.1.1 Experimental data

For this study, high-level reconstructed data are needed. Such data are available from the Advance Data Summary Tree (ADST) files in which are stored quantities reconstructed by an Offline-based analysis for FD, SD and RD. The content of the ADST files is accessible from end-user analysis programs and the relevant quantities for the analysis are:

- arrival direction from RD
- lateral distribution of the electric field from RD
- $X_{\max}$ from FD
- energy of the primary from SD
- core position from SD

Running the radio reconstruction method only require the arrival direction and the distribution of the electric field, the other quantities are just needed for comparison purpose. The LDF is calculated from the three polarizations as described in Section 2.1.2.3.

3.3.1.2 Set of simulated events to reconstruct one experimental event

SELFAS needs to be provided with several input parameters to simulate an EAS induced electric field:

- mass of the primary
- first interaction depth
- geomagnetic field components (bx, by, bz)
- arrival direction: (θ,ϕ)
- energy of the primary
- core position
- relative position of the antennas

- ground altitude
- time step for the electric field computation
- number of secondary particles ($e^{\pm}$)

As explained in Chapter 2, the main cosmic ray candidates at energies beyond 10^{17} eV are protons and iron nuclei. Their interaction cross sections with the atmosphere constituents lead to larger X_{max} depth fluctuations in the case of protons. Thus, 10 iron nuclei and 40 protons cosmic rays are simulated to cover a reasonable X_{max} range in which the experimental event might fit in. To do so, the first interaction depths are provided by CONEX using a high energy interaction model. The available models are EPOS-LHC, QGSJETII-04 and SYBILL. The main differences between EPOS and QGSJETII and the influence of the model choice on the reconstruction method are discussed Section 2.3.1. The geomagnetic field components corresponding to a given location must be provided. As described in [152], the arrival direction of the cosmic ray is very well estimated using radio signals and this direction is the one used for the 50 simulations. The energy of the simulated primary cosmic rays is fixed arbitrarily to 10^{18} eV. At first order, the amplitude of the electric field distribution varies linearly with the energy of the primary. To avoid the simulation of hundreds of events at different energies, the primary energy is fixed and the amplitude of the LDF is treated as a free parameter in the method and used to estimate the energy of the primary cosmic ray. The same logic is applied for the core position, the 50 events are simulated with a core position located at the center of a dense, fictive array and the agreement is tested placing the core position of the simulated events at different locations on the experimental array frame. Finally, one must provide the time step of the simulated traces and the number of electrons and positrons of the shower used for the electric field computation. The simulation time depends on the number of antennas, the time step (1 nanoseconde) and the number of secondary particles. Concerning this latter parameter, a study has shown that 20 millions of particles are enough to avoid significant statistical shower to shower fluctuations. This strategy allows the reconstruction of the latter parameters using a Monte Carlo set of 50 events instead of a set of thousands events for every energy, core position, arrival direction and X_{max} depth. In the following, the method is illustrated though the reconstruction of a super hybrid event detected by the instruments of the Pierre Auger Observatory.

3.3.1.3 Core position and energy

The search for the core position is the first step of the method, the simulated LDFs are linearly interpolated to retrieve electric field values at any position with respect to the center of the virtual array (i.e. not only the positions at which the antennas were simulated). For computational purposes, the minimum value on the interpolated LDF is set to 1. The electric field values are considered in units of μV/m ($\gg 1$ where the emission is coherent). The agreement between the simulated LDF and the detected

electric field is tested at different core positions of the simulated LDFs with a χ^2 test, as written in Eq (1).

$$\chi^2_{ij} = \chi^2(x_i, y_j) = \frac{1}{n}\sum_{k=1}^{n}\left(\frac{C_{ij}E^{\text{sim}}_{ijk} - E^{\text{det}}_k}{\sigma^{\text{det}}_k}\right)^2 \tag{3.13}$$

Where n is the number of antennas, E^{det}_k is the electric field measured by antenna number k, σ^{det}_k is the corresponding uncertainty. E^{sim}_{ijk} is the simulated electric field value at the relative position k matching the one of antenna number k with respect to the tested core position (i, j). C_{ij} is a scaling factor at the position (i, j) and is the same for all antennas at a given tested core position. This parameter allows to compare only the shapes of the LDFs. The scaling factor is calculated as the mean deviation between data and simulation and is applied to the simulated LDF in the χ^2 test calculation. However, one must be careful with the use of the scaling factor as it can produce a very good agreement between the two LDFs at particular tested core positions with respect to the true core position. When the tested core position is very far from the true core, as depicted in Figure 3.25, the experimental data are compared to the lowest values of the simulated LDF (where the electric field is set to 1).

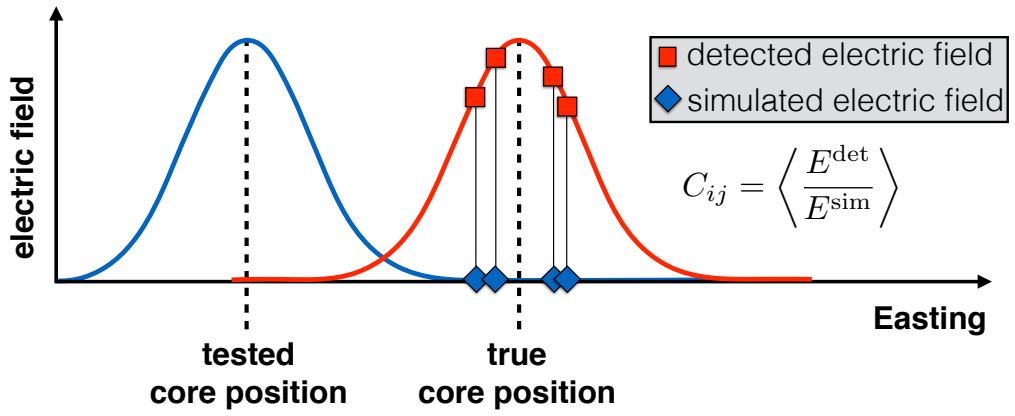

Figure 3.25: Sketch of the case where the low values of the simulated LDF (in blue) are compared to the detected ones (in red).

In this case depicted in Figure 3.25, the scaling factor takes values around $C_{ij} \simeq \langle E^{\text{det}} \rangle$ and is applied to the simulated values. Therefore the χ^2 value is relatively low and indicates as good agreement. This situation must be avoided. To do so, a prior test is executed within the reconstruction algorithm. The χ^2 values, corresponding to the tested core positions and used to reconstruct the true core position must take into account this computational situation. The false good agreements are found for $C_{ij} \simeq \langle E^{\text{det}} \rangle$. A corrective term is thus added to the χ^2 calculation. This term depends on the value of the corrective factor and is written as follow:

$$f(C_{ij}) = 1 + A \times \exp\left[-\frac{C_{ij} - \langle E^{\text{det}} \rangle}{0.2 \times \langle E^{\text{det}} \rangle}\right]^2 \tag{3.14}$$

This function has been built empirically. We fix A to a value of 10^{10}, which corresponds to the value at which the χ^2 values are set before searching for the core position. The final χ^2 values used for the reconstruction, for all tested core positions are calculated as:

$$\chi^2_{ij} = \frac{1}{n}\sum_{k=1}^{n}\left(\frac{C_{ij}E^{\text{sim}}_{ijk} - E^{\text{det}}_k}{\sigma^{\text{det}}_k}\right)^2 \times f(C_{ij}) \tag{3.15}$$

With this precaution, the situation depicted in Figure 3.25 is avoided. This situation is not always encountered, in particular for showers developing at large distances from the simulated array. For this latter case the points in Figure 3.25 (in blue) that are compared to the data (in red) can be located in the coherent area. Both cases can be encountered since the simulated data set is composed of events various first interaction depths. With the taking into account of this problem, we can search for the core position within same spatial window for all the set of simulated events. The two plots presented in Figure 3.26 show the comparison between the measured LDF and one of the simulated ones out of the set for 2 tested core positions.

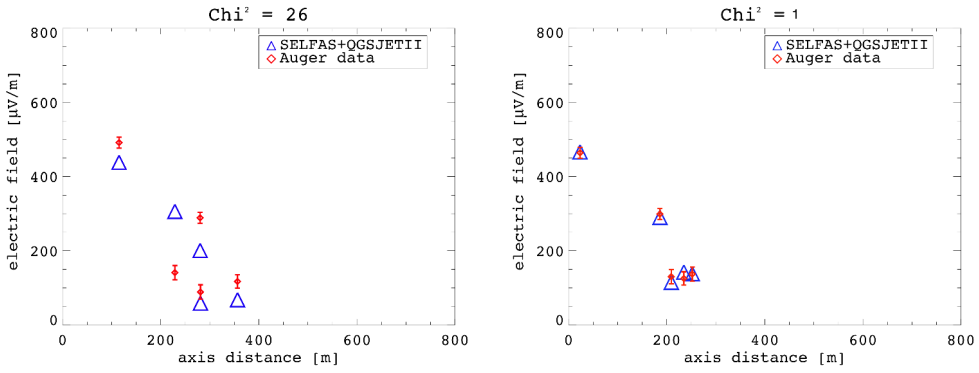

Figure 3.26: Comparison of the electric field distributions at 2 tested core positions and their associated χ^2 test values.

The experimental data are shown in red and the simulation is in blue. On the right plot of Figure 3.26, where the comparison is made at the best core position, it is important to notice that SELFAS is able to reproduce accurately the electric field distribution. This operation is done for every possible core positions and the reduced χ^2 value can be displayed as a function of the tested core position to obtain the χ^2 density map shown Figure 3.27. In this figure, the black crosses indicate the AERA antennas location and the green one is the core position that gives the best agreement.

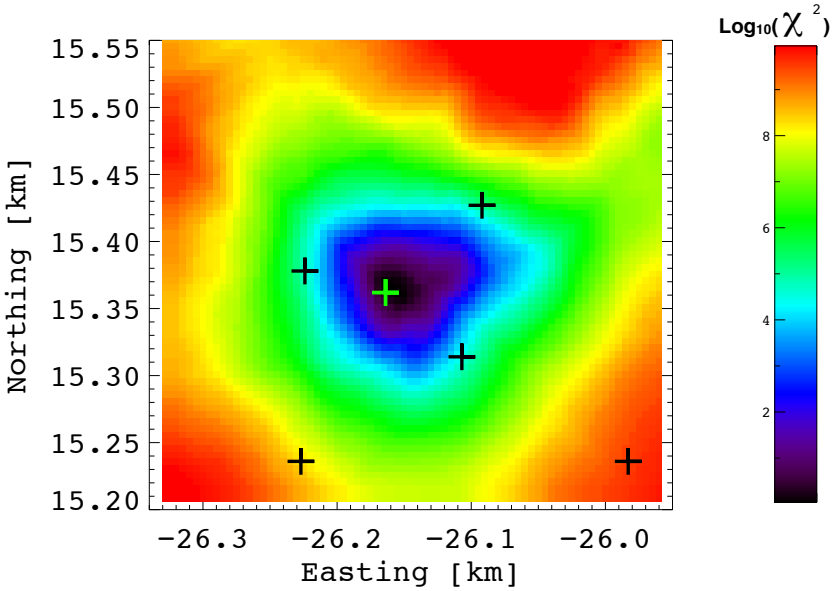

Figure 3.27: χ^2 density map calculated from the comparison of the experimental LDF and the experimental data.

A clear minimization of the most suitable core position appears. The same process is applied to the other 49 simulated events of the set to produce as many χ^2 density maps. The 50 core positions obtained are saved and the operation is repeated to perform errors propagation on the measured electric field. To propagate the errors, this process is done several times. At each step an error is added to the measured electric field values. These errors are randomly calculated within gaussian distributions centered on the experimental values with standard deviations matching the experimental errors of the measurement. After the errors propagation, the reconstructed core position distribution is finally obtain. The reconstructed value is its centroid and the errors is taken as the its standard deviation. The results are shown Figure 3.28.

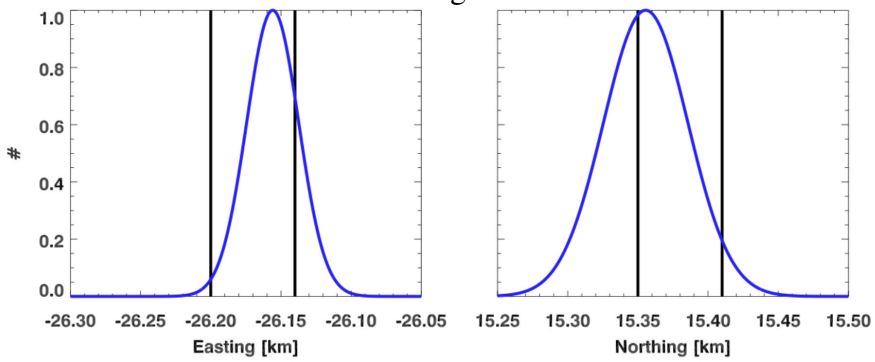

Figure 3.28: Probability distribution of the reconstructed core position in blue compared to the error bars from SD.

The results are in very good agreements and we show in Sections 3.3.1.5 and 3.3.3.2

Detection	Easting [km]	Northing [km]
SD	-26.17 ±0.03	15.38 ±0.03
RD	-26.16 ±0.02	15.36 ±0.03

Table 3.2: Reconstructed core position with the radio method (RD) and with the surface detectors (SD).

that the method is always highly effective to reconstruct the core position (even if the core position is not surrounded by the stations) when at least five stations have detected a significant signal. The very same method is applied to reconstruct the energy of the primary cosmic ray. At each step described previously the scaling factors at the best core positions are gathered and their distribution function is multiplied by the energy at which the set of events has been simulated: 10^{18} eV and the results are shown in Figure 3.29.

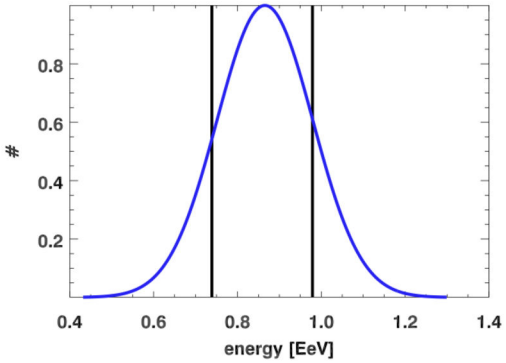

Figure 3.29: Probability distribution of the reconstructed energy in blue compared to the error bars from SD.

Detection	Energy of the primary [EeV]
SD	0.86 ±0.12
RD	0.87 ±0.11

Table 3.3: Energy of the primary cosmic ray reconstructed with the radio method (RD) and with the surface detectors (SD).

3.3.1.4 X_{max} depth

As the process described before is done with the 50 simulated events and as each of them have a particular X_{max} depth value, the agreement between data and simulation is tested as a function of X_{max}. Each step of the errors propagation produces a plot similar

to the one in Figure 3.30.

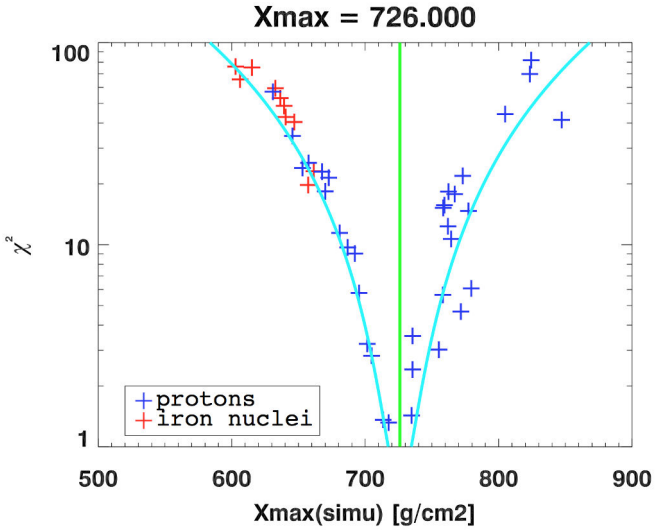

Figure 3.30: Agreement between data and simulation as a function of the $X_{\max}$ values of the simulated events.

The χ^2 values as a function of $X_{\max}$ shows that the best agreement is obtained for a particular $X_{\max}$ value. The errors propagation will change slightly the value at which the best agreement is found as it modifies the shapes of the simulated LDFs. After the propagation the reconstructed $X_{\max}$ distribution is obtained.

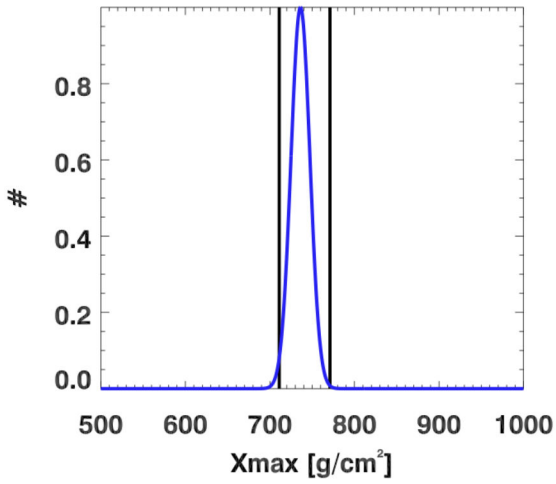

Figure 3.31: Probability distribution of the reconstructed $X_{\max}$ depth value in blue compared to the error bars from FD (black vertical lines).

This example shows the radio data are highly correlated to the core position, energy and the nature of the primary through the measurement of the $X_{\max}$ depth. The reconstructed values are in very good agreement with the ones from the particle and fluorescence detectors and the error bars are very satisfying compared to the two other detectors.

Detection	X_{max} [g/cm^2]
FD	741 ± 30
RD	736 ± 11

Table 3.4: Depth of the shower maximum (X_{max}) reconstructed with the radio method (RD) and measured with the fluorescence detectors (FD).

3.3.1.5 Self consistency

In this Section, we test the ability of the method to reconstruct the parameters of events simulated by SELFAS. The influence of the number of antennas and the pattern of their positions with respect to the shower axis will be studied. First, we generate 30 events with random X_{max}, arrival direction and masses (p or Fe). All of them with an energy of 1 EeV. Their associated sets of 50 simulated events is used as described previously to perform the reconstruction. To do so one simulated event is removed from the set, the LDF is under sampled (in this example only five antennas are kept) and one tries to reconstruct its characteristics using the rest of the simulated set. The fictive antenna array is a star shaped array in the shower plan projected on the ground as shown in Figure 3.32. The five positions are shown in red and match the positions at which five fictive antennas have been simulated. As the interpolation of the electric field is in good agreement with the simulated one at particular positions of the stations, there was no need to simulate the five antennas of the tested event at different locations.

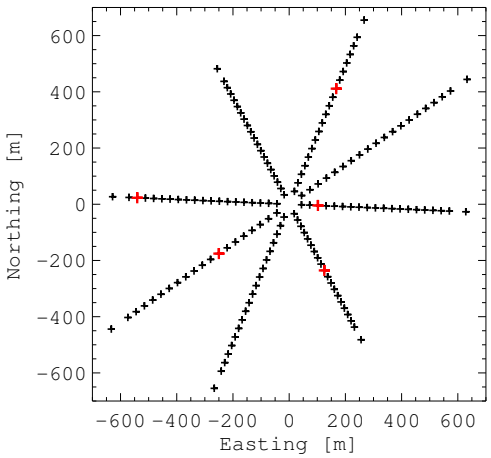

Figure 3.32: Ground position of the fictive array used for the simulations and the antennas used for the under sampling of the mock event in red.

The method described previously is applied on 30 events. Figure 3.33 shows the distribution of the differences between the core position of the control events and the reconstructed one in the East direction and the North direction.

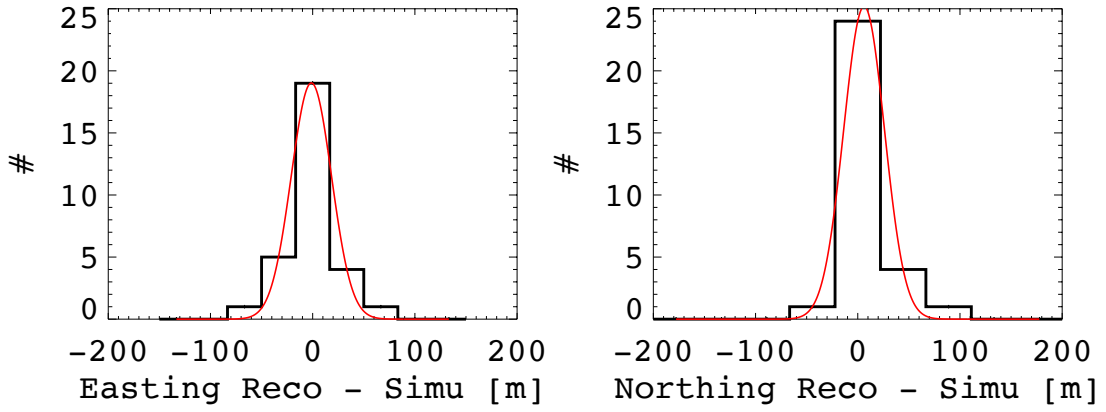

Figure 3.33: Left: distribution of the differences between reconstructed core position and the simulated one along the East direction - Right: distribution of the differences between reconstructed core position and the simulated one along the North direction.

We obtain $\Delta X_{\text{core}} = 1 \pm 20$ m and $\Delta Y_{\text{core}} = 6 \pm 20$ m. The uncertainty is larger in the Northern direction because, in this case, the arrival directions were generated with respect to the arrival direction at the Pierre Auger Observatory and favors events from the south (see Section 2.2 for the explanation of the geomagnetic effect). Thus, the LDF is stretched in this direction leading to a worse precision on this axis. Nevertheless, the accuracy is very satisfactory in both directions. We then test the reconstruction of the energy and the X_{max} of the primary, the distributions of the differences are shown Figure 3.34.

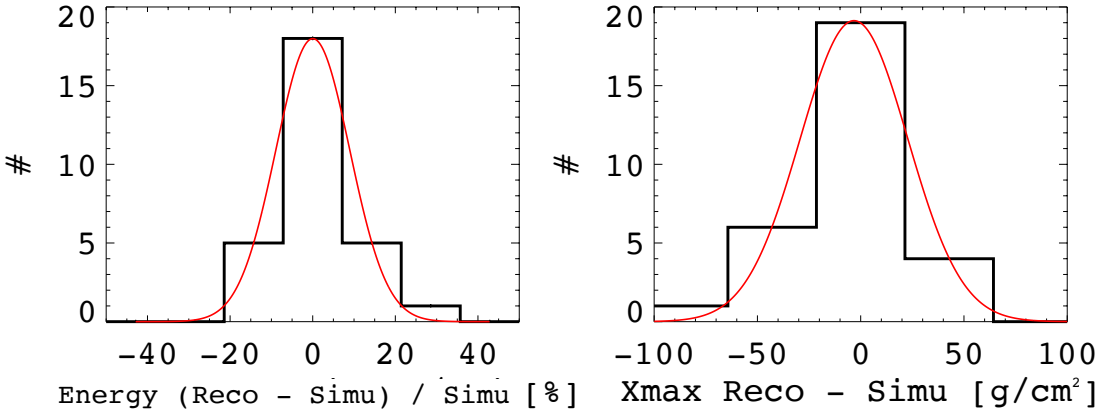

Figure 3.34: Left: distribution of the relative differences between reconstructed and true energy. - Right: distribution of the differences of reconstructed and true X_{max}.

The results give $E_{reco} = E_{simu} \pm 10\%$. The resolution on X_{max} shown in Figure 3.34 is also very good: $\Delta X_{\text{max}} = -3 \pm 26$ g/cm^2 especially with only five antennas. The errors on the reconstructed values are obtain by error propagation on the electric field, considering a reasonable error of 10%. This proves the self-consistency of the method and it will now be apply it on a real data set of showers detected at AERA.

3.3.2 Improvement of the method

For purpose of time calculation, the scan procedure to estimate the core position has been improved. The improvement lies on the fact that the search of the core position is first performed with a large step (around 80 meters) again but with very small steps. The contour of the χ^2 density map are calculated as shown in Figure 3.35 (eft). Then the search for the core position is performed again with a very small step (1 to 5 meters) but only within the contour giving the best χ^2 values. Doing so reduce considerably the size of the search area and thus, the computing time. To do so one must know the coordinates describing the contour. The values are displayed in Figure 3.35 (right).

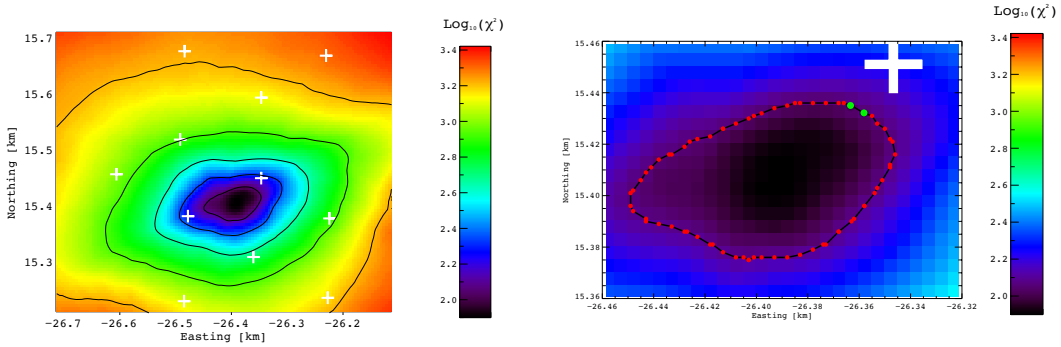

Figure 3.35: Left: The contours of the density map are represented by the black lines. The color scale indicates the values of $\mathrm{Log}_{10}(\chi^2)$. Right: Zoom on the area of the smallest contour of the density map. The coordinates defining the contour are represented by the red and green circles.

The step between two consecutive points is not constant and is larger than one meter. The LDF is interpolated within a grid of 1×1 meter and if one wants to scan the area inside the smallest contour, it is mandatory to determine the scan boundaries in both direction at the meter scale.

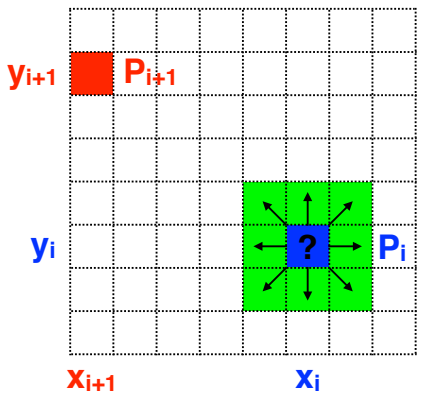

Figure 3.36: Path finding procedure between two of points defining the contour.

To do so, a grid composed of pixels of 1×1 meter is defined and one needs to calculate the shortest path between one point to the following and the boundaries are defined as the coordinates of each obtained after each displacement. To explain the approach, the calculation of the path between the two green points of Figure 3.35 (right) is detailed. The path from $P_i : (x(i), y(i))$ to $P_{i+1} : (x(i+1), y(i+1))$, is calculated pixel by pixel, in one direction, either horizontally, vertically or diagonally. From $P_i : (x(i), y(i))$, the eight possible moves are considered as depicted in Figure 3.36. The coordinates of the possible next positions are evaluated as:

$$\sqrt{(u - x(i+1))^2 + (v - y(i+1))^2} \quad \text{with} \quad u, v = [-1, 0, 1] \tag{3.16}$$

The direction that will get us the closest to the goal is kept and we move form $P_i : (x(i), y(i))$ to (u, v) and the operation is repeated until the following condition is satisfied.

$$\sqrt{(u - x(i+1))^2 + (v - y(i+1))^2} = 0 \tag{3.17}$$

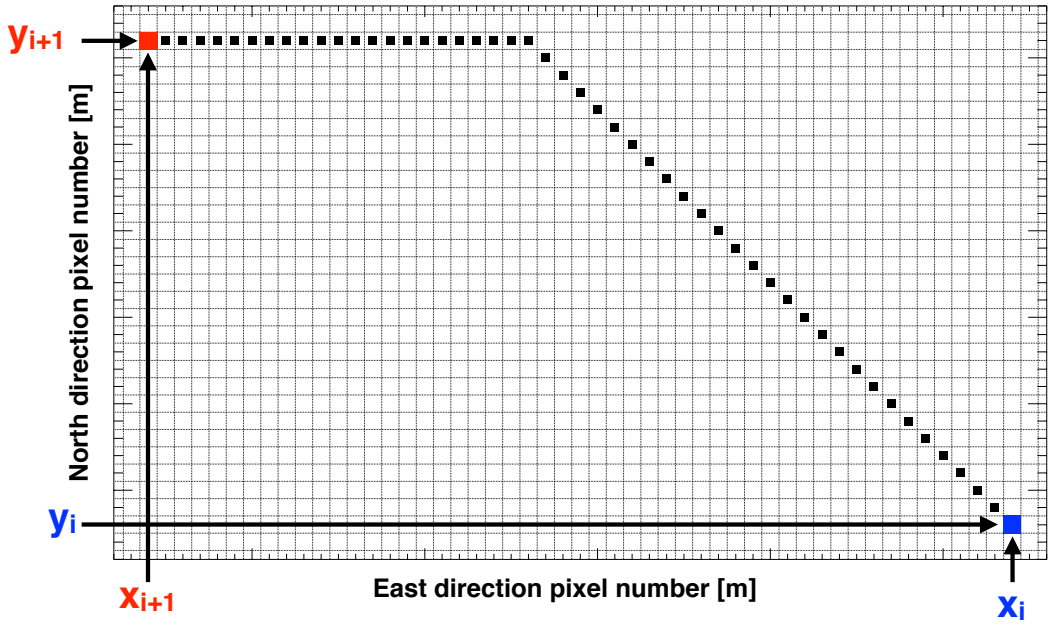

Figure 3.37: Local contour between two points defining the full contour obtained with the pathfinding method.

At the end of the procedure, $P_{i+1} : (x(i+1), y(i+1))$ is reached. The path calculated by the procedure between is shown in Figure 3.37, linking $P_i : (x(i), y(i))$ in blue to $P_{i+1} : (x(i+1), y(i+1))$ in red. The area in which the agreement is maximum and where the core position is the more likely located is now well defined and the scan

is performed in this surface with a 1×1 meter step. For a total reconstruction of the parameters of an event, the calculation time is divided by 7.

3.3.3 Comparison with FD and SD measurements

3.3.3.1 Data set

A selection of high quality super hybrid events (detected in coincidence by the FD, the RD and the SD), has been performed to test the radio reconstruction method by comparing the reconstructed parameters with their actual measurements. A data set, composed of all the events detected in triple coincidence at the Pierre Auger Observatory from the 1st of January 2012 up to the 30th of April 2015. In order to ensure the quality of the data, several quality cuts are applied to the full data set. The FD standard quality cuts are applied, requesting among other criteria that $X_{\max}$ is in the FD field of view and a precision of the measurement better than 40 g/cm^2 (see [153] for the detailed list of the cuts). The radio cuts remove from the data set the events with less than five radio stations with signal and those with a zenith angle determined from radio data higher than 55°. The array of surface detectors is fully efficient for showers with a zenith angle smaller than 55°, which explains the zenith cut applied for this study. The events passing the cuts reach a total number of 29 events. The simulation were done using a array with a high density of antenna close to the shower axis as shown in the shower frame in Figure 3.38 and then projected on the ground.

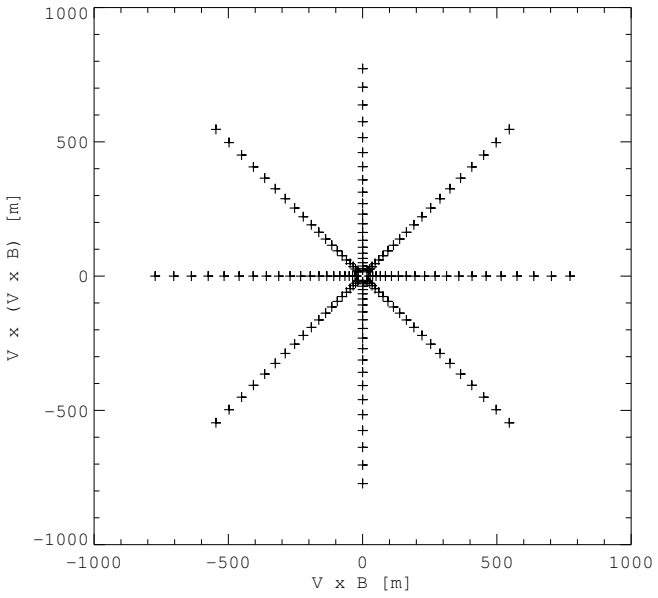

Figure 3.38: The array of simulated antenna used for the comparison in the shower frame.

3.3.3.2 Core position

The core position is calculated by the surface detector. The reconstructed values with the radio method are compared to the SD data. The correlations plots are presented in Figure 3.39.

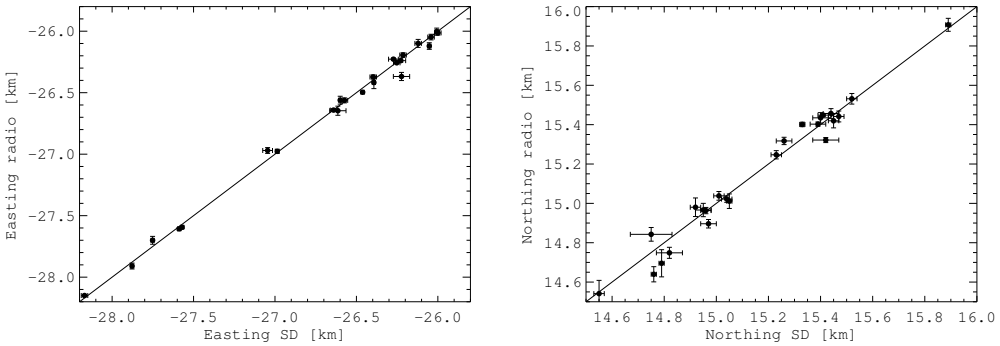

Figure 3.39: Correlation plots between the reconstructed easting and northing core positions with the radio method and the SD data. The straight lines account for a one-to-one correlation.

The correlation plots demonstrate a good agreement between the measured and reconstructed core positions.

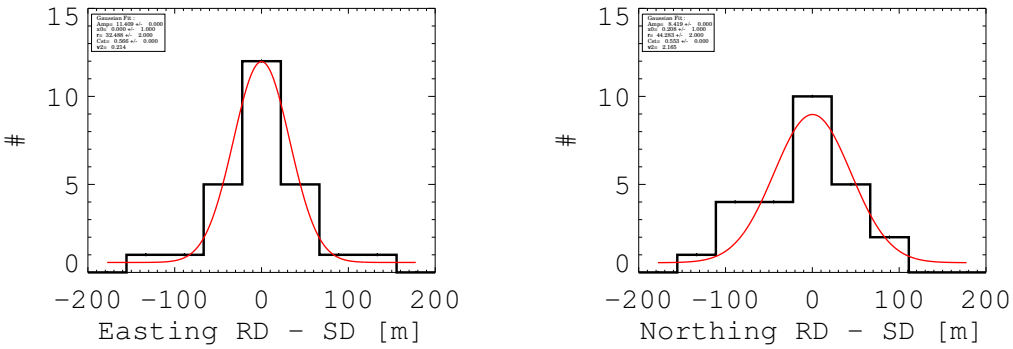

Figure 3.40: distributions of the differences between the SD core positions and RD core positions.

direction	mean	RMS
ΔX [m]	0	32.4
ΔY [m]	0.2	44.4

Table 3.5: Mean and standard deviation of the distributions of the differences between the SD core positions and RD core positions.

The reconstructed core positions are in very nice agreement with the data of the surface detectors. The distributions of the differences are fitted by a gaussian function and the results are summarized in Table 3.5.

3.3.3.3 Energy

We now compare the reconstructed energy to the one measured by the surface detectors with the correlation plot in Figure 3.41 (left). Once again the correlation is very good. The distribution of the differences between the radio reconstruction and the SD measurement is shown in Figure 3.41 (right). The characteristics of the distribution of the differences are summarized in Table 3.6.

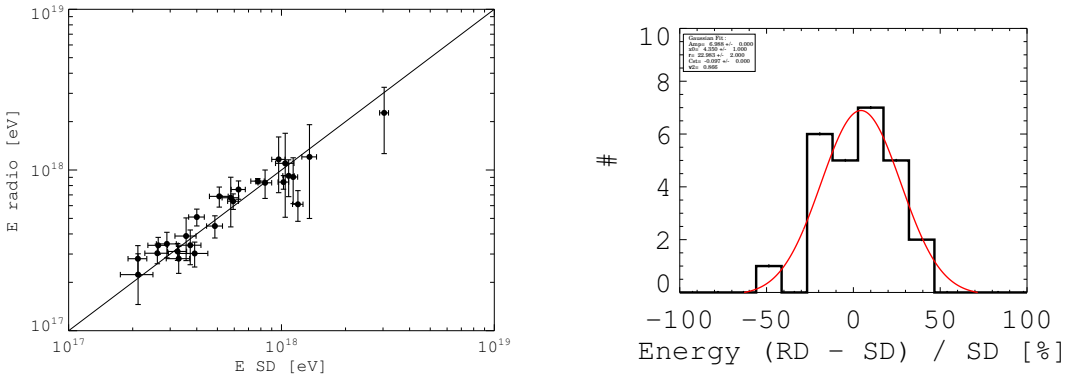

Figure 3.41: Left: correlation plot between the reconstructed energy of the primary cosmic ray with the radio method and the SD data. The straight lines account for a one-to-one correlation. Right: distribution of the differences between the SD energy and RD energy.

	mean	RMS
relative difference [%]	4.3	23

Table 3.6: Mean and standard deviation of the distribution of the differences between the SD energy and RD energy.

The mean deviation from the energy estimated by the surface detectors is of 4% and shows that the radio method is not noticeably biased.

3.3.3.4 X_{max}

The X_{max} obtained by FD measurements are compared to the reconstructed values with the radio method. Some of the reconstructed values are in good agreement with the FD measurements. However some events are poorly reconstructed. One of the two events with a measured X_{max} value greater than 1000 g/cm^2 is reconstructed with a value of few hundreds g/cm^2 and is out of the limits the plot window.

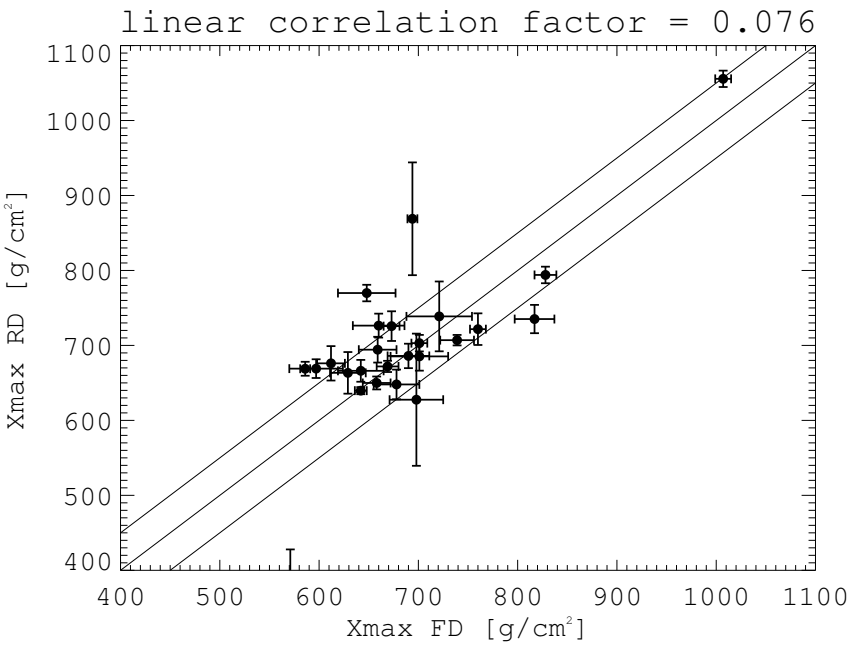

Figure 3.42: Correlation plot between the reconstructed $X_{\max}$ with the radio method and the FD measurements. The middle straight line accounts for a one-to-one correlation and the other two account for differences of $\pm$ 50g/cm^2.

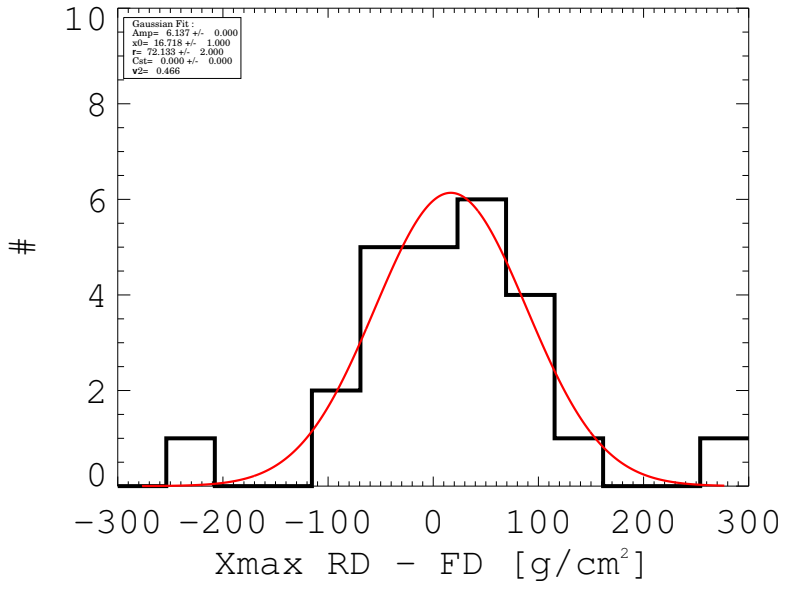

Figure 3.43: Distribution of the differences between the reconstructed $X_{\max}$ the radio method and the FD measurements.

The characteristics of the distribution of the differences are summarized in Table 3.7.

The linear correlation between the measured and reconstructed values is not very good

	mean [g/cm^2]	RMS [g/cm^2]
$X_{\max}^{\mathrm{RD}} - X_{\max}^{\mathrm{FD}}$	16.7	72.1

Table 3.7: Mean and standard deviation of the distribution of the differences between the FD $X_{\max}$ energy and RD $X_{\max}$.

due to the poorly reconstructed events that are taken into account in the reconstruction. A systematic shift of 16 g/cm^2 is observed. No effect was found with the zenith angle nor the azimuth angle.

3.4 Conclusions

The radio method gives very good results, especially for the reconstruction of the core position. The energy of the primary is also reconstructed precisely. The reconstructed depth of the shower maximum is nicely correlated to the FD measurements. However, a systematic shift of 17 g/cm^2 is present. In order to explain and correct this deviation, improvements have been made concerning SELFAS. The efforts have been put in a better description of the atmosphere. A complete spherical description is now considered. A realistic treatment of the air density and refractive index has been added. The FD values take into account the variation of the state of the atmosphere. To reach the FD precision it is now mandatory to simulate the shower using a realistic atmospherical model. In the next chapter the importance of such consideration are detailed and the reconstruction method is performed again on the same set of events.

CHAPTER 4

Dynamic atmosphere simulation

Contents

4.1 Introduction

Ideally, the reconstruction accuracy of the radio method presented in the previous chapter should be close or better than that achieved with the fluorescence technique ($\sim$ 20 g/cm^2). The electric field received by antennas strongly depends on the characteristics of the atmosphere in which secondary particles evolve: air density, optical refractive index, temperature and pressure. For a long time, simulation codes computing this electric field assumed a standard atmosphere, which was a sufficient approximation at that time. Nowadays, with high precision measurements on large radio arrays running continuously such as AERA it becomes important to refine this atmospheric model. Indeed, it is clear that the atmosphere characteristics vary significantly with time (day/night effect and seasonal variations) and these variations are responsible for systematic uncertainties that can prevent an accurate estimation of the $X_{\max}$. Ideally, we need to know the atmosphere state at the time a shower is detected. This is possible using the GDAS data. In this chapter, we show how one can use these data together with a standard atmospheric model for the highest altitudes to compute an accurate air density model as a function of altitude at the time of the detection of the event. The knowledge of the air density allows to compute the realistic air refractive index which is critical for the time structure of the signal and for the Cherenkov ring diameter. Among the existing simulation codes, the descriptions of the atmosphere are summarized below.

code	geometry	density (ρ)	refractivity (N)
SELFAS (old)	flat	4 layers from US standard	constant dry air approx.
SELFAS (new)	curved	GDAS + US standard above 26 km	GDAS pressure and humidity
ZHaireS	curved	4 layers from US standard	air with constant humidity
CoREAS	flat	5 layers from US standard	constant dry air approx.

Table 4.1: Summary of the description of the atmosphere for SELFAS, ZHaireS and CoRSIKA.

The choice of the atmospheric model can induce atmospheric depths uncertainties of the order of $\sim$ 20 g/cm^2 which is typically the uncertainty on the $X_{\max}$ obtained with the fluorescence data. It is therefore very important to use a realistic model.

4.2 Geometry of the atmosphere

The geometric description of the Earth is either flat or curved according to the chosen simulation code. Formerly used in SELFAS, the flat approximation is described in Figure 4.1.

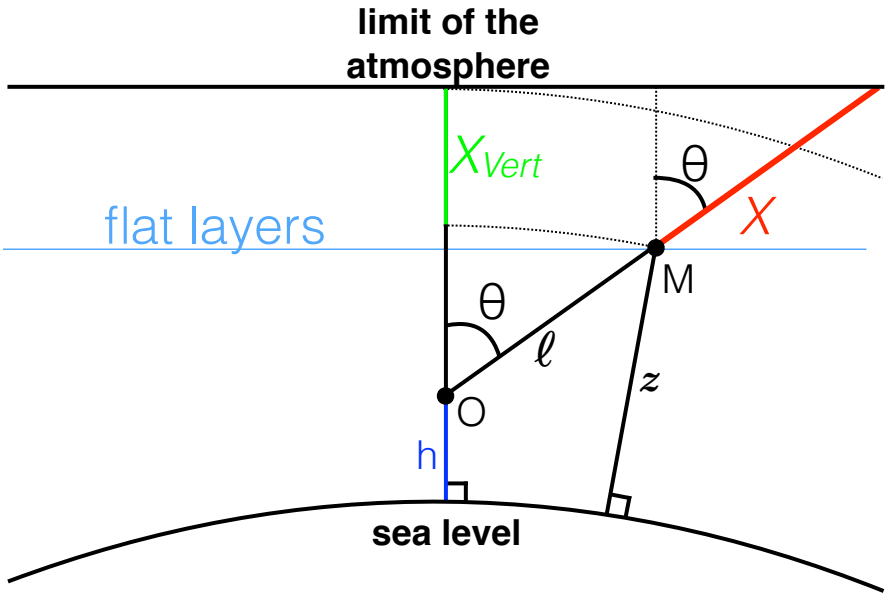

Figure 4.1: The former flat atmosphere geometry used by SELFAS.

The atmospheric depth corresponding to an elementary path $\mathrm{d}\ell$ is given by:

$$\mathrm{d}X = \rho(h(\ell))\,\mathrm{d}\ell \tag{4.1}$$

Where ℓ is the geometrical distance from an observer located at the position O to a position M. In the flat approximation $\mathrm{d}z = \mathrm{d}\ell\cos\theta$ where θ is the angle defined by the normal to the surface of the Earth at the position O and (OM), so that $\mathrm{d}X = \rho(z)\mathrm{d}z/\cos\theta = \mathrm{d}X_v/\cos\theta$. After integration we obtain:

$$X(\ell) = X_{\mathrm{v}}(z(\ell))/\cos\theta \tag{4.2}$$

The model $X_{\mathrm{v}}(z)$ is known as the Linsley's parameterization based on the US Standard atmospheric model. It provides the integrated atmospheric depth from infinity to an altitude z above sea level. The flat approximation is thus correct for vertical showers but considering the accuracy that radio methods are meant to achieve, a comparison to a spherical description is necessary for inclined showers. The expression of the atmospheric depth in Equation (4.2) produces errors for $\theta \neq 0$ because the atmospheric layers are curved and therefore $X_{\mathrm{v}}(z(\ell))/\cos\theta$ is not correct anymore.

The geometry used for the spherical case is shown in Figure 4.2. Moreover at a position M, the zenith angle θ' is not the same than the angle θ at O (see Figure 4.3). We consider an observer O at the altitude h. The radius of the Earth is noted R. A point M on the shower axis is located at an altitude z (above the sea level). The zenith angle at M depends on its position along the shower axis: it is θ for $M = O$ (corresponding to an observer located at an altitude h), θ_{SL} for $M = S$ (corresponding to an observer S at sea level having $z = 0$). The distance SO is noted ℓ_{SL}. Simple geometry gives:

$$
\begin{aligned}
\ell &= \sqrt{(R+z)^2-(R+h)^2\sin^2\theta}-(R+h)\cos\theta \\
z &= \sqrt{\ell^2+(R+h)^2-2\ell(R+h)\cos\theta}-R \\
\ell_{\mathrm{SL}} &= (R+h)\cos\theta-\sqrt{R^2-(R+h)^2\sin^2\theta} \\
\cos\theta' &= \sqrt{1-\left(\frac{R+h}{R+z}\right)^2\sin^2\theta} \\
\text{and in particular, } \cos\theta_{\mathrm{SL}} &= \sqrt{1-\left(1+\frac{h}{R}\right)\sin^2\theta}
\end{aligned}
\tag{4.3}
$$

S exists if $\sin\theta \leqslant R/(R+h)$.

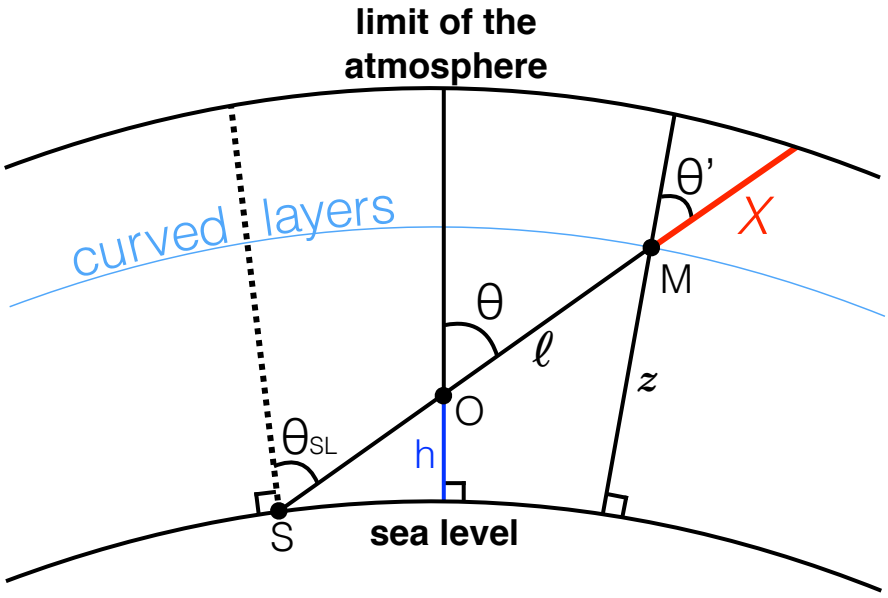

Figure 4.2: The realistic atmosphere geometry adopted for SELFAS.

The atmospheric slant depth is calculated as follows at each step along the shower axis:

$$
X_{\mathrm{slant}} = \int_{\ell}^{\infty} \rho(z(\ell'))\,\mathrm{d}\ell' \tag{4.4}
$$

Where $\rho(z(\ell'))$ is the air density at a given altitude z corresponding to a particle to observer distance ℓ' along the shower axis. A comparison is made between the two descriptions, see Figure 4.3.

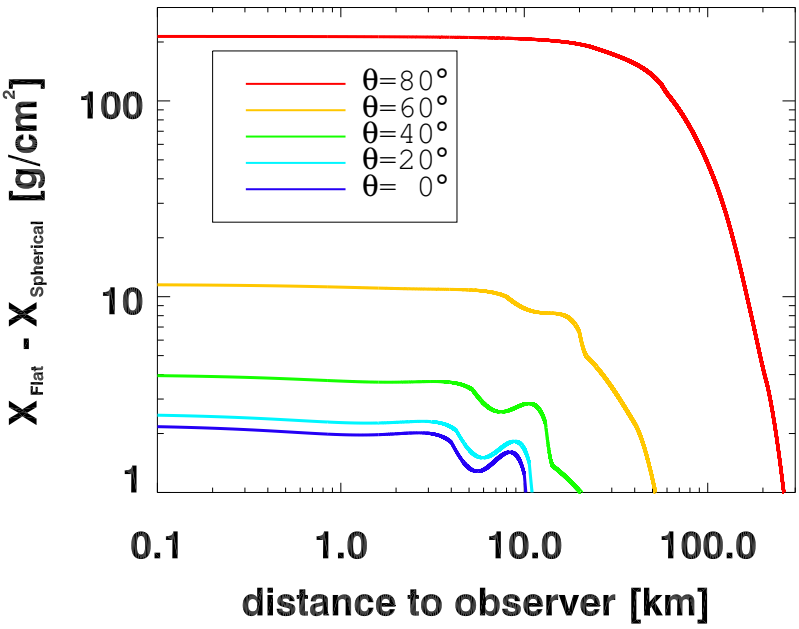

Figure 4.3: Differences of atmospheric depth calculation between the flat approximation (using equation 4.2) and the spherical description (using equation 4.4) for several zenith angles. The observer is located a the sea level and the shower impacts the ground at the position of the observer. The distance to the observer corresponds to the distance ℓ of the Figures 4.1 and 4.2.

Figure 4.3 shows the atmospheric depth crossed from the beginning of the atmosphere (corresponding to an altitude of 100 km) under the angle θ until reaching the position M corresponding to the geometrical distance ℓ to the observer O. The values shown in this figure are obtained for an observer at the sea level ($h = 0$). The two descriptions must give almost equal results for a vertical shower. The small discrepancies are due to two different methods of calculation. In the spherical description, the atmospheric depth corresponds to the integration of the air density whereas in the flat approximation a conversion from altitude to atmospheric depth is obtained using a parameterized function. The vertical case shows the minimum deviation inherent to the differences of the two descriptions. The differences are smaller than 12 g/cm^2 for small angles ($\theta < 60°$). At $\theta = 40°$, the maximum difference between the two values is about 4 g/cm^2. On the contrary for high zenith angles ($\theta > 60°$), the difference is important as it reaches 200 g/cm^2 at $\theta = 80°$. The spherical description gives the most accurate description of the atmosphere as no approximation is done. A set of events have been simulated with SELFAS in the flat approximation and the curved description to study the influence of the geometry on the electric field. The set is composed of showers induced by protons of 1 EeV with a first interaction depth of 10 and 100 g/cm^2 and

arriving from the north with a zenith angle of 30° in the conditions of CODALEMA (magnetic field and altitude). The power spectra obtained with the two geometrical descriptions are shown in Figure 4.4. The same random seed was chosen for these simulations in order to avoid shower to shower fluctuation effects.

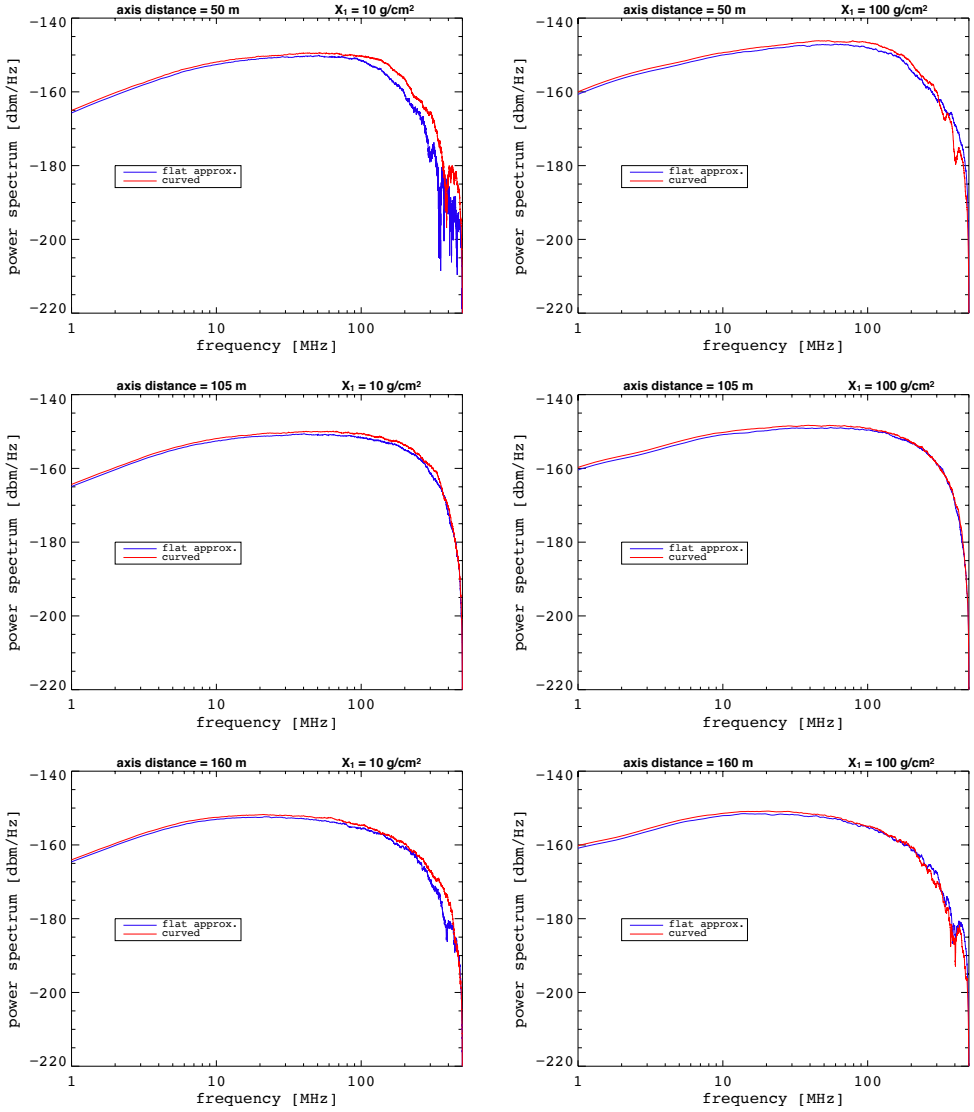

Figure 4.4: Simulated power spectra with the flat approximation (blue curves) and the curved description (red curves) for different distances to the shower axis (50 m, 105 m and 160 m) in the $\boldsymbol{v} \times \boldsymbol{B}$ direction in the east-west polarization. The showers are induced by protons with a first interaction depth of 10 g/cm^2 (left panels) and 100 g/cm^2 (right panels).

In general, the spectra are the same in both geometrical descriptions at frequencies below 80 MHz. The power is larger in the spherical case, this is particularly true above

80 MHz where the difference of the spectral indexes becomes noticeable, especially for a distance to the shower axis of 50 m. The electric field amplitudes are compared in Figure 4.5 for a first interaction point at 10 g/cm^2 and at 100 g/cm^2 in Figure 4.6.

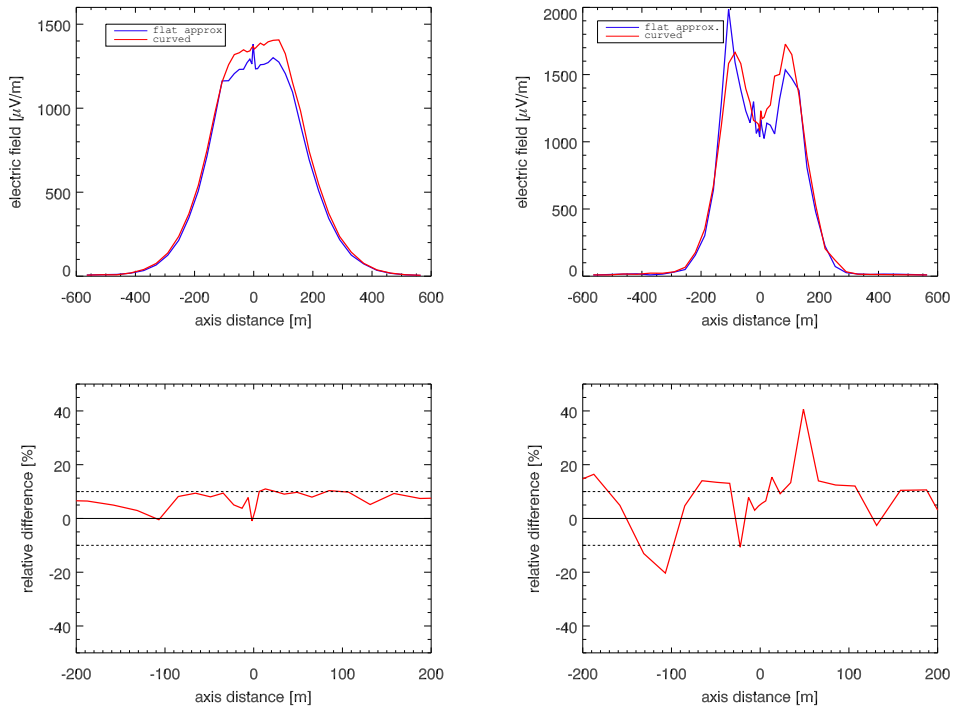

Figure 4.5: Top: Electric field amplitudes simulated with the flat approximation (blue curve) and the curved description (red curve) in the $\boldsymbol{v} \times \boldsymbol{B}$ direction in the shower frame. The showers are induced by protons with a first interaction depth of 10 g/cm^2 and the electric field is filtered in the band [30 - 80] MHz (left) and [120 - 200] MHz (right) using the three polarizations (maximum of the square root of the quadratic sum of the Hilbert envelop of each polarization). - Bottom: the corresponding relative differences of the amplitude of the electric field at a maximum distance of 200 m from the shower axis, where the emission of the electric field is coherent. The dotted lines account for a relative difference of $\pm$ 10%.

The relative difference reaches 10% in the band [30 - 80] MHz and 40% in the band [120 - 200] MHz. In the previous chapter, the error propagation on the electric field (the uncertainties are roughly of 10%) led to an accuracy of the $X_{\max}$ reconstruction of 30 g/cm^2. It means that a variation of 10% of the electric field (detected or simulated) used in the reconstruction method can induce a difference of few dozens of g/cm^2 on the reconstructed $X_{\max}$. This issue is discussed more quantitatively in Section 4.6. In the band [120 - 200] MHz, the asymmetry around the shower axis is inverted and reduced (in this example). It may be due to the discrete distributions of the secondary particles. This effect is not present in the band [30 - 80] MHz. In general, the electric field is stronger when using the spherical description.

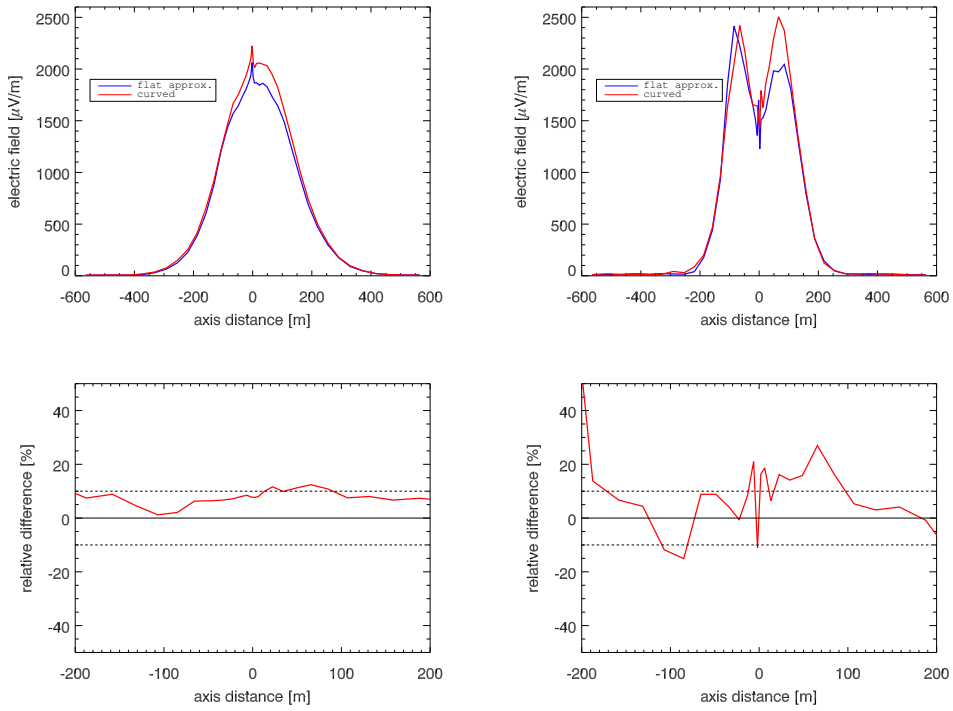

Figure 4.6: Same as Figure 4.5 but for a first interaction depth of 100 g/cm^2.

The results for a first interaction depth of 100 g/cm^2 are essentially the same as for 10 g/cm^2 in the band [30 - 80] MHz. In the band [120 - 200] MHz, the relative difference is smaller and reaches 25% close to the shower axis and 50% at 200 m. Besides being necessary to the simulation of highly inclined showers, the calculation of the atmospheric depth with the spherical description permits to use different air density profiles $\rho(z)$. In this section, only the geometry of the atmosphere has been discussed. In the next section, the importance of the air density profile is studied extensively. In particular, the deviations between the US Standard model, constant along the year, and air density profiles calculated from the global data acquisition system (GDAS) that provides data every three hours and thus accounts for the seasonal and daily variations of the atmospheric density and refractivity.

4.3 The GDAS data

The characteristics of the atmosphere that are needed for the electric field computation are the air refractive index (η) and density (ρ) along the simulated shower axis. These parameters depend on the temperature (T), the total pressure (P) and the relative humidity (Rh). Eventually, the latter quantities will vary on a daily basis as seen in Figures 4.7, 4.8 and 4.9.

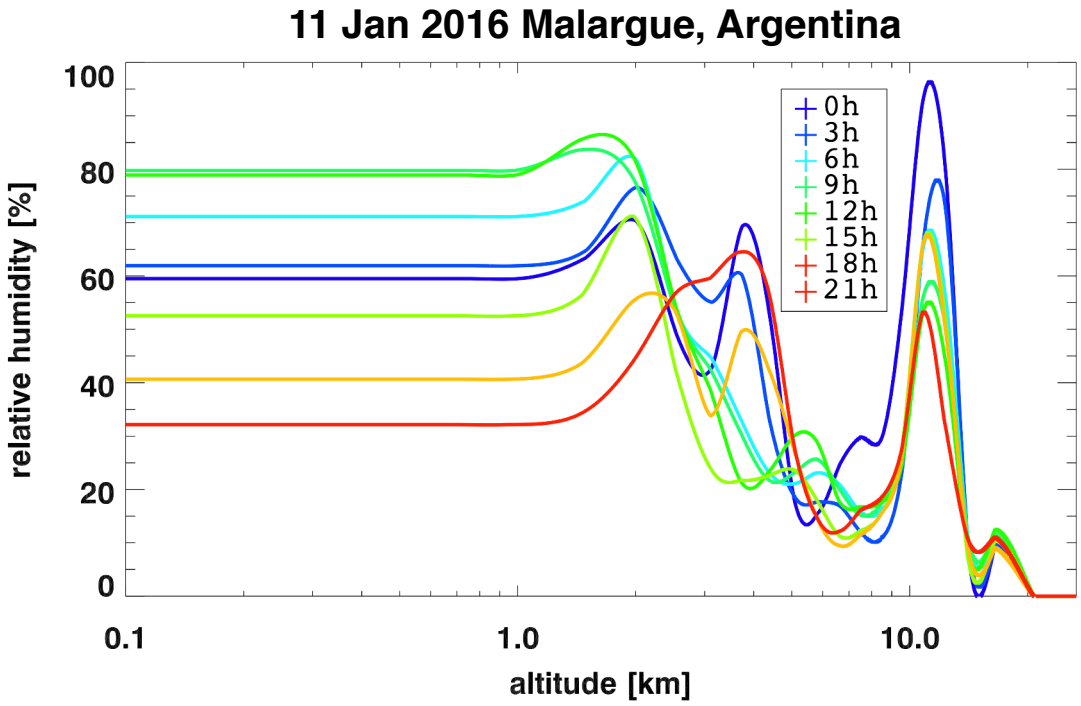

Figure 4.7: Daily variations of the relative humidity as a function of the altitude.

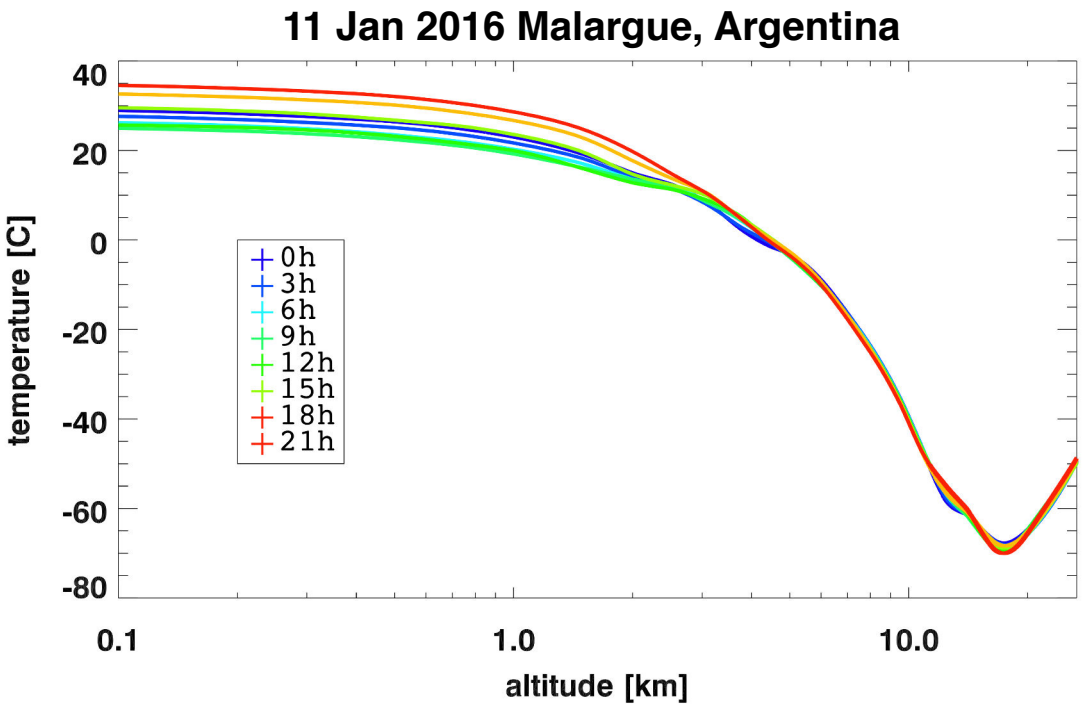

Figure 4.8: Daily variations of the temperature as a function of the altitude.

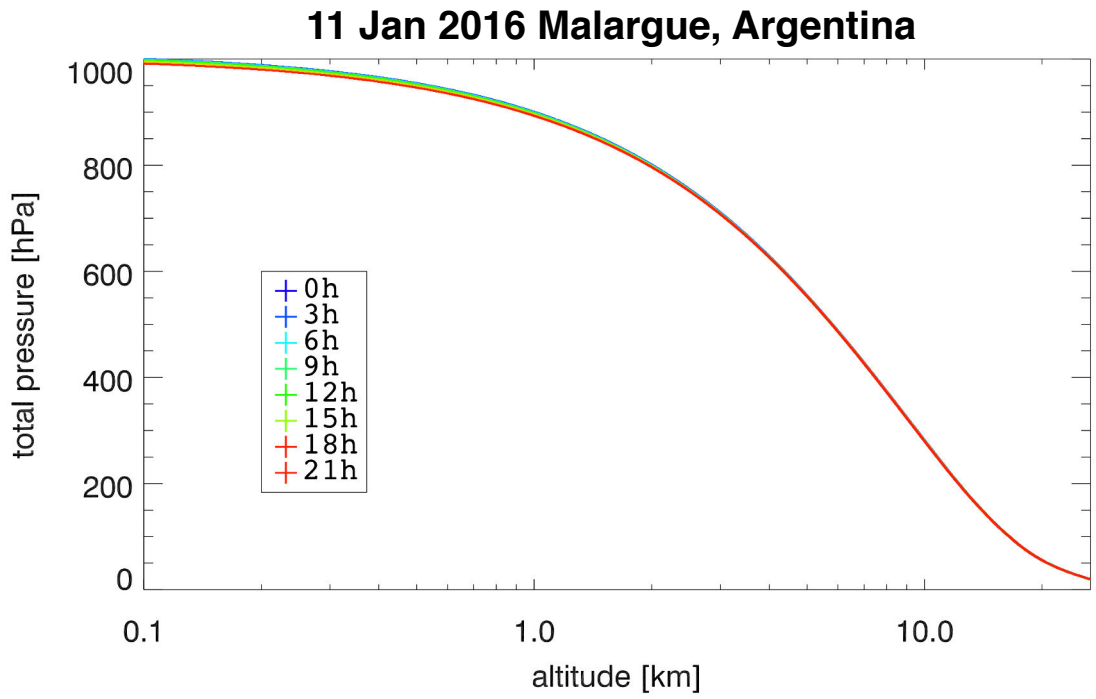

Figure 4.9: Daily variations of the total pressure as a function of the altitude.

The variation of the total pressure is not significative. However, the relative humidity and the temperature variations are important. The latter quantities are of great importance for the air refractive index and density calculations.

The presented values were obtained with the GDAS which provides a data base of measurements of physicochemical characteristics of the atmosphere. Each GDAS file contains a week of data and one must extract the ones corresponding to the desired location. The files contain measurements for every 3 hours at the surface and 23 geopotential heights. The electric field depends on the atmospheric density model in which the shower develops. The adopted approach to provide to SELFAS a realistic air density profile along with a proper geometrical description of the atmospheric layers from the GDAS data is explained in the next sections. A detailed comparisons between the US Standard air density profile and the ones calculated from GDAS data and the consequences on the $X_{\max}$ reconstruction are shown. The details of the available parameters are explained in Appendix A.

Among these parameters, are available in this order: the geopotential height, the temperature, the two horizontal components of the wind speed, the pressure vertical velocity and the relative humidity. The next set of data beginning at line 25 starts again with the surface level (second red line) followed by the 23 vertical levels and shows the data at 3 AM. This pattern is repeated for 7 days with a 3 hours step.

In the end, as the goal is only to calculate the atmosphere density as a function of altitude, we only use the following parameters at all 23 available altitudes:

- Pressure surface (P) [hPa]
- Geopotential height (Gh) [gpm[1]]
- Temperature (T) [K]
- Relative humidity (Rh) [%]

As the GDAS provides data in geopotential meter, one must convert it to meter above sea level (altitude).

4.4 Atmospheric depth from air density

At an altitude of h and a latitude of ϕ, the geopotential height is defined as:

$$Z_g(z,\phi) = \frac{1}{g_0}\int_0^z g(z',\phi)\,\mathrm{d}z' \tag{4.5}$$

Where g_0 and $g(\phi,z)$ are respectively the gravitational acceleration at mean sea level and corrected for altitude z, latitude ϕ and Earth rotation. $g(\phi,z)$ can be estimated by the following relation known as International Gravity Formula 1967:

$$g(z,\phi) = g_0(1 + A\sin^2(\phi) - B\sin^2(2\phi)) - z\,C \tag{4.6}$$

$$\text{With: } A = 0.0053024, \quad B = 0.0000058 \quad \text{and} \quad C = 3.086\times10^{-6}$$

The solutions of z for a given latitude ϕ and geopotential height $Z_g(z)$ are:

$$\begin{aligned} z(Z_g,\phi) \;=\; & \frac{g_0(2+A-B-A\cos(2\phi)+2B\cos(4\phi))}{2C} \\ & - \frac{\sqrt{g_0(-8CZ_g + g_0(2+A-B-A\cos(2\phi)+B\cos(4\phi))^2)}}{2C} \end{aligned} \tag{4.7}$$

Thus for each geopotential height we obtain the corresponding altitude in meters and the air density is calculated as:

$$\rho = \frac{p_d M_d + p_v M_v}{RT} \tag{4.8}$$

Where p_d and p_v are the partial pressures of dry air and water vapor, M_d and M_v are the molar masses of dry air and water vapor, T (in Kelvin) is the temperature and R is the universal gas constant. The formula used to calculate p_{sat} (air saturation vapor

[1] geopotential meters

pressure) can be found in [154] and is a modification of a previous parameterization explained in [155].

$$p_d = P - p_v \quad \text{with} \quad p_v = Rh \times p_{\text{sat}} \quad \text{and}$$
$$p_{\text{sat}} = 6.1121 \exp\left[\left(18.678 - \frac{T}{234.5}\right)\left(\frac{T}{257.14+T}\right)\right] \quad (\text{T in } ^\circ\text{C}) \qquad (4.9)$$

The formula is accurate in the range of -80°C to 50°C which is suitable in our case if we refer to Figure 4.10 below.

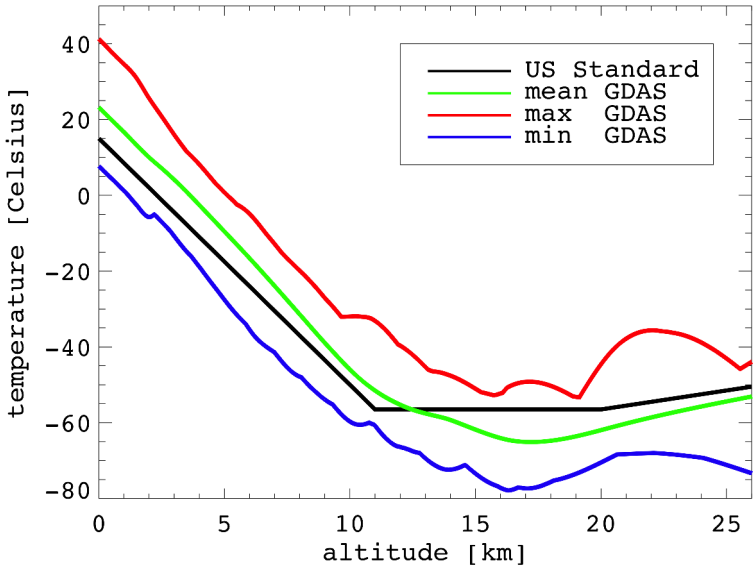

Figure 4.10: US Standard temperature profile compared to the GDAS profiles at Malargüe. The values are calculated from all the GDAS profiles along the year 2014. For each altitude, the mean, minimum and maximum temperatures during this year have been computed.

As we can see in the altitude range in which Eq 4.9 is used, the maximum temperature of year 2014 is 40°C and the minimum is -80°C. The comparison is made from the sea level to an altitude of 26 km as Equations 4.8 and 4.9 are only used up to this altitude which corresponds roughly to the maximum altitude at which data are available from the GDAS. In SELFAS we provide the air density profile up to an altitude of 100 km, well above the GDAS limit, because the air showers can initiate their development quickly after their entry in the atmosphere. Between the sea level and 26 km, we obtain the air density at any altitude by interpolation of the 23 GDAS data points. Above 26 km, we use the US Standard air density profile described in [156] with a scaling factor to ensure boundary conditions with the GDAS data. The US Standard profile can be retrieved easily (see [157]) up to 100 km of altitude but as a function of geopotential meters that one has to convert again in geometric altitude as described in

Section 4.4. After this procedure, the tabulated air density profile is known within a meter step from sea level to an altitude of 100 km. In order to estimate the seasonal and day/night systematics, a comparison is made for every possible GDAS profiles for the year 2014 (i.e. one profile every 3 hours along the year). The extrema of the relative differences between all the profiles from GDAS data and the US Standard model are shown in Figure 4.11.

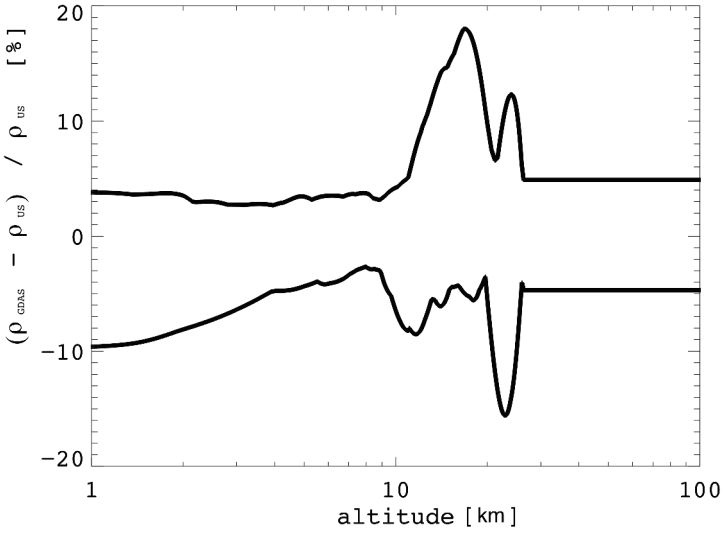

Figure 4.11: Extrema of the differences between the US model air density profile and all the GDAS profiles along the year 2014.

We can see that the difference in air density can reach 20% especially in the range 10-20 km which is a region of interest at which the maximum of the electric field emission typically occurs. The difference above 26 km is constant because beyond this limit we use the same US Standard model, the only difference being the scaling factor to ensure boundary conditions to a GDAS profile at lower altitudes. These deviations will affect the atmospheric depth and the air index corresponding to source to observer geometric distance. In SELFAS, the shower development is sampled in this realistic atmosphere with a 0.5 g/cm^2 step along the axis and calculated as follow, with the spherical description depicted in Figure 4.2 and where $z_{\max}$ is the highest altitude at which data are available from the GDAS.

$$X_{\text{slant}} = f_B \int_{\ell(z_{\max})}^{\infty} \rho_{\text{USstd}}(z(\ell'))\,\mathrm{d}\ell', \qquad z > z_{\max} \quad (4.10)$$

$$X_{\text{slant}} = f_B \int_{\ell(z_{\max})}^{\infty} \rho_{\text{USstd}}(z(\ell'))\,\mathrm{d}\ell' + \int_{\ell}^{\ell(z_{\max})} \rho_{\text{GDAS}}(z(\ell'))\,\mathrm{d}\ell', \quad z < z_{\max} \quad (4.11)$$

Considering the deviations between the GDAS air density profiles and the US Standard profile, relatively important deviations are expected for the calculation of the atmospheric depth. The deviations are quantified as a function of the geometric distance ℓ to the source for different zenith angles and with a spherical description. As depicted in

Figure 4.12 the air density is integrated from the limit of the atmosphere up to the geometrical distance to an observer located at the sea level at O, along the axis for different zenith angles. The integrations are performed following Equations (4.10) and (4.11). The differences of the obtained crossed atmospheric depths using the GDAS profiles (up to $z_{\max}$ and the corrected US Standard profile beyond $z_{\max}$) and the US Standard profile are shown in Figure 4.13 for different zenith angles.

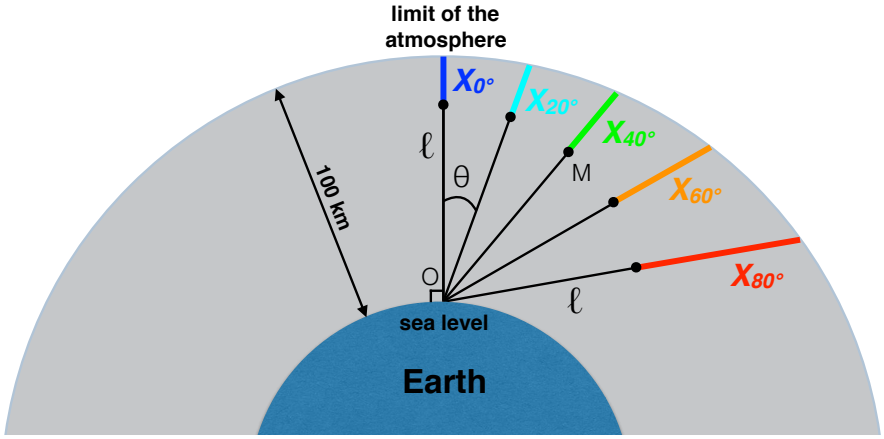

Figure 4.12: Sketch representing the air density integration along the shower axis up to a geometrical distance ℓ to an observer located at the position O for different zenith angle (

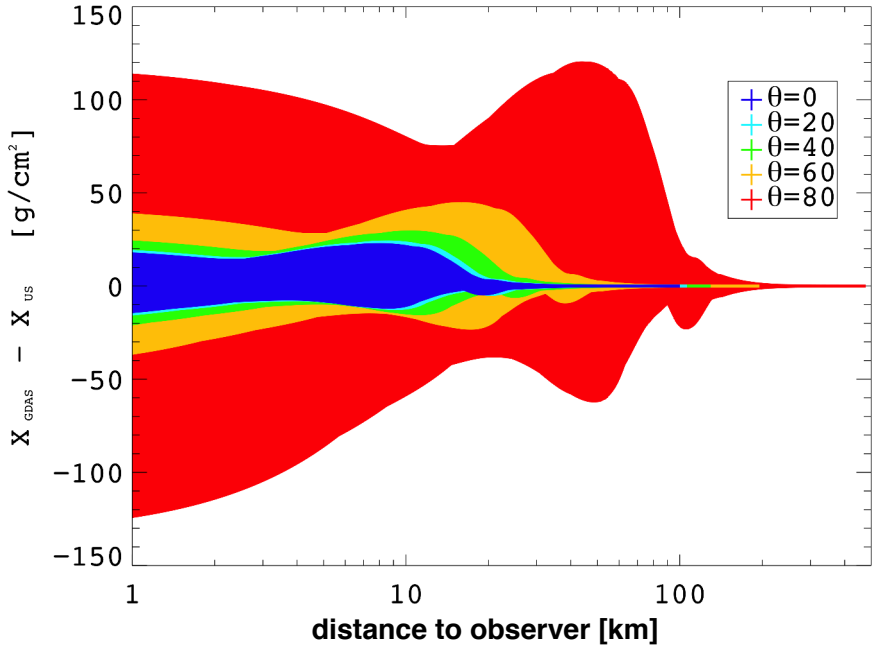

Figure 4.13: Extrema of the atmospheric depth differences between the US Standard model and all GDAS profiles along the year 2014 as a function of source to observer distance ℓ and for various zenith angles.

For a vertical shower, the differences can be as high as 20 g/cm^2. It means that if one wants to reconstruct the $X_{\max}$ depth of a shower, if the maximum emission of the induced electric field is produced at 10 km from the antennas, it is possible to simulate a shower whose $X_{\max}$ is 20 g/cm^2 away from the real value and whose electric field is in good agreement with the experimental one. As expected, the deviations are amplified for higher zenith angles and reach almost 130 g/cm^2 at 80°. The aim of the radio method is to provide the most accurate $X_{\max}$ estimation and such systematic deviations must be corrected for. The use of a completely coherent description of both the atmospheric density and curvature and air refractive index is now mandatory for such analysis.

4.5 Air index

Ideally the air refractive index should be calculated for each secondary particles with respect to their position. The air index intervenes two times for the calculation of the electric field emitted by a secondary particle at a particular position and received at a particular antenna position. In SELFAS, the emitted electric varies proportionally to $(1-\eta\boldsymbol{\beta}\boldsymbol{n})^{-1}$ and is computed taking into account the air refractive index at the emission point η according to the Gladstone and Dale law [144]:

$$\eta(z(l)) = 1 + \kappa \times \rho(z(\ell)) \quad \text{with} \quad \kappa = 0.226\ \text{cm}^3/\text{g} \tag{4.12}$$

The delayed time t_{ret} (see Chapter 3) corresponds to the time at which the electric field has been emitted, with respect to the time t at which it is detected by an observer.

$$t_{\text{ret}} = t - \frac{<\eta> R(t_{\text{ret}})}{c} \tag{4.13}$$

It is computed taking into account the mean value of the air refractive index between the position of the particle and the position of the antenna $<\eta>$. Indeed, the velocity v of a secondary particle can be approximated by $v \simeq c/\eta$ so that $<v> \simeq c/<\eta>$. The mean air index is calculated as:

$$<\eta(z(\ell))> = 1 + \kappa \times \frac{1}{\ell}\int_0^{\ell} \rho(z(\ell'))\,\mathrm{d}\ell' \tag{4.14}$$

The optical path of the electric field from the particle to the antenna is curved due to the spatial variation of the air refractive index. However, it has been demonstrated in [144] that the optical path can be approximated by a straight line. For purposes of code performance, the approximation is made (only for the air refractive index calculation) that each particle is located on the shower axis. Thus, at each shower age, η is calculated only one time and $<\eta>$ is calculated only one time for each relative positions of the simulated antennas. If the spatial distribution of the secondary particle was taken into account, η would be calculated for all particle existing at each shower age, so would be $<\eta>$ (multiplied by the number of simulated antennas). This approximation is mandatory considering the number of simulated secondary particles for a shower

(20×10^6) and the sampling of the atmospheric depth by step of 0.3 g/cm^2 (the total atmospheric depth crossed by a vertical shower is around 1036 g/cm^2 to reach the sea level).

Thanks to the spherical description, we can now calculate air index profiles from the air density calculated with the GDAS data.

However, the Gladstone-Dale constant κ depends on the gas characteristics and the frequency of the light traveling in the medium. The constant κ that was used in SELFAS and in other simulation codes like CORSIKA has been determined in μm domain as shown in Figure 4.14 (found in [158]) and it is not suitable to our studies in the decametric domain (7.5 m at 40 MHz). As described in [159], the dry air index is almost constant from visible to radio wavelengths. Using the Gladstone-Dale law as written in Equation (4.12) is correct if we consider that the atmosphere is purely made of dry air. Obviously it is not the case. A more consistent approach must use a description that takes into account the humidity of the atmosphere. The recent formula introduced in [160] proposes such a description and is now used is SELFAS.

K(cm^3/g)	Wavelength (μm)
0.2239	0.9125
0.2250	0.7034
0.2259	0.6074
0.2274	0.5097
0.2304	0.4079
0.2330	0.3562

Figure 4.14: Gladstone-Dale constant for Air at T = 288 K

$$\eta = 1 + N \times 10^{-6} \quad \text{with} \quad N = \frac{77.6}{T}\left(P + 4810 \times \frac{P_v}{T}\right) \tag{4.15}$$

This equation is parameterized for the high and very high frequencies range (MHz to GHz) and is suitable to our studies. In this formula, if water vapor is present, the term noted as its partial pressure becomes dominant in the air refractive index calculation. GDAS data allow to calculate the air index up to 26 km of height. Beyond this point data for temperature and relative humidity are not accessible. However, the air relative humidity beyond an altitude of 26 km can be taken as null and the highest clouds reach hardly 24 km of height (this altitude accounts for very rare, but possible cases; usually no clouds are observed above 12 km of height). Thus, Equation (4.15) can be simplified beyond the GDAS data points.

$$P_v = 0 \ , \ P = P_d \ , \ T = \frac{P_d M_d}{R\rho} \quad \longrightarrow \quad N = \frac{77.6 \times R}{M_d} \times \rho \tag{4.16}$$

Thus one can calculate the air refractive index profile with the GDAS data below 26 km of height and with the corrected mean US Standard values beyond this point up to 100 km as shown in Figure 4.15.

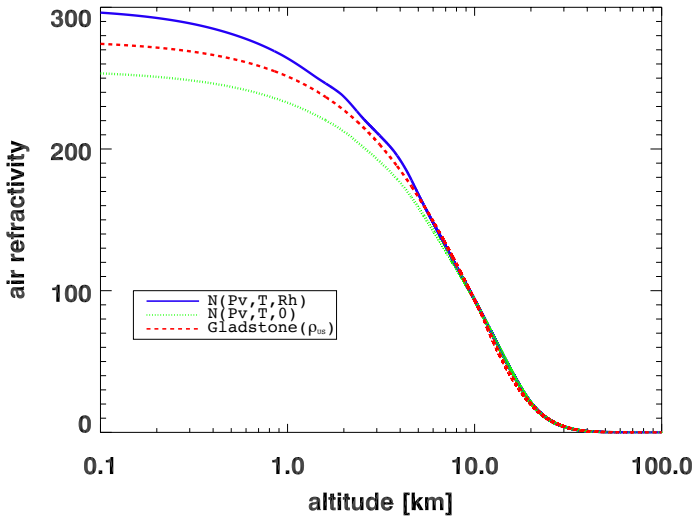

Figure 4.15: Air refractivity up to 100 km of height, calculated and interpolated from GDAS data in blue, considering a purely dry atmosphere in green and from US Standard Model values in red.

We now study the influence of the different hypothesis on the air refractivity profile ($N = (\eta - 1) \times 10^6$). In Figure 4.16, we compare the deviations from the air refractivity calculated with the Gladstone law with ρ_{US} for:

- Gladstone law Eq. (4.12) with ρ_{GDAS}
- high frequency (HF) law Eq. (4.15) with $(P, T, P_V)_{\text{GDAS}}$

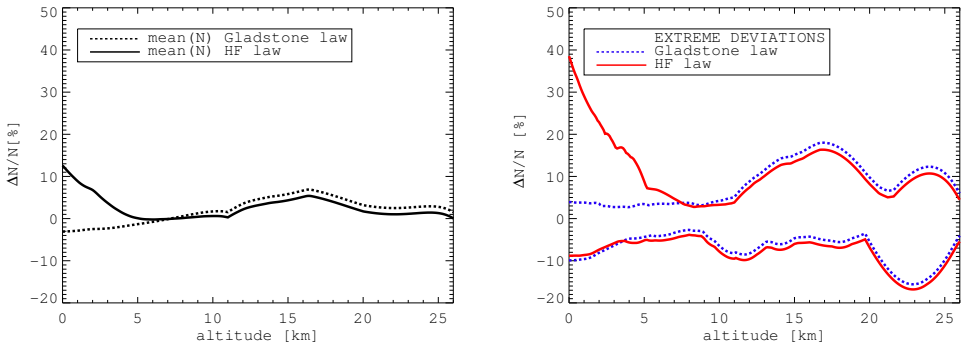

Figure 4.16: Left: mean deviations along the year 2014 of the air refractivity from the Gladstone law with ρ_{US}. Right: extremums of the deviations for the year 2014.

On average, the use of a GDAS profile for the Gladstone law will lead to deviations from the US Standard profile (solid line in Figure 4.16 (left)) that can reach 7% at an altitude of 16 km. The mean deviations in the case of the high frequencies law (dotted line in Figure 4.16 (left)) are a bit lower above 7 km of height but are about 12% higher below this altitude. This is due to the fact that the high frequencies law takes

into account the air humidity and this effect is dominant below 10 km of altitude. As expected from the left plot, one can see on the right plot that the maximum deviations for year 2014 are similar in both cases above 10 km of altitude. The systematic errors that are made relatively to the Gladstone law with the GDAS profiles below 10 km of height is around $\pm 25\%$. Below 10 km and in the case of the high frequencies law, the relative deviations can reach $\pm 50\%$. The main results are summarized in the following table.

$\Delta N/N$	Gladstone(ρ_{GDAS})	$N((P,T,P_V)_{\text{GDAS}})$
$z = 0$ km	$-3.1^{+7.0}_{-6.8}\%$	$12.6^{+25.9}_{-21.4}\%$
$z = 2.5$ km	$-2.4^{+5.4}_{-4.8}\%$	$5.2^{+14.9}_{-11.8}\%$
$z = 5$ km	$-1.3^{+4.7}_{-3.0}\%$	$0.1^{+8.8}_{-5.2}\%$
$z = 7.5$ km	$0.2^{+3.5}_{-3.1}\%$	$0.0^{+3.7}_{-4.2}\%$
$z = 10$ km	$1.7^{+2.5}_{-8.2}\%$	$0.6^{+2.7}_{-8.4}\%$
$z = 12.5$ km	$4.1^{+6.0}_{-11.3}\%$	$2.7^{+6.1}_{-11.3}\%$

Table 4.2: Relative differences of the refractivity for GDAS-based models with the US Standard atmosphere and the Gladestone-Dale law for the air index for several altitudes of interest for air shower physics.

In SELFAS, three contributions to the electric field are calculated: the coulombian contribution of all the secondary particles, the time derivatives of the transverse current and the charge excess. The mathematical expressions of these contributions vary proportionally to $(1-\eta\boldsymbol{\beta}\boldsymbol{n})^{-1}$. Where $\boldsymbol{\beta}$ is the reduced velocity of a secondary particle, $\boldsymbol{n}$ is the unitary orientation vector from the secondary particle to the observer and η is the value of the air refractive index at the emission point. A Cerenkov boost effect of the electric field appears when $(1-\eta\boldsymbol{\beta}\boldsymbol{n})$ is small, i.e. when the angle of emission is the same as the Cerenkov radiation.

$$1-\eta\boldsymbol{\beta}\boldsymbol{n} = 1-\eta\beta\times\cos\theta_{Cb} = 0 \quad \longrightarrow \quad \theta_{Cb} = \text{acos}\left(\frac{1}{\eta\beta}\right) \tag{4.17}$$

The received electric field is highly sensitive to the air refractive index. Figure 4.16 shows the extrema of the relative differences between all the air index profiles from GDAS data with Equations (4.12) and (4.15) and the US model with Equation (4.12). If one considers a point-like source with a vertical arrival direction, at an altitude of 6 km, a difference of 8% of the air refractive index induces a difference of 15% on the radius of the Cerenkov ring at the ground level. Although this result is obtained considering a point-like source and pure geometrical calculation, it now seems important to use a realistic air refractive index in the simulations. The mean value of the realistic air index calculated with the GDAS data is increased compared to the one obtained from the US Standard model with the Gladstone and Dale law. A higher air refractive index at a

given atmospheric depth will produce a sharper electric field distribution. The air index calculations adopted by several simulation codes are summarized in the table below.

code	refractivity (N)
SELFAS	$\frac{77.6}{T}\left(P+4810\times\frac{P_v}{T}\right)$
ZHaireS	$R_s\exp(-z\times K_r)$
CoRSIKA	$\kappa\times\rho_{US}$

Table 4.3: Summary of the description of the air refractivity for SELFAS, ZHaireS and CoRSIKA.

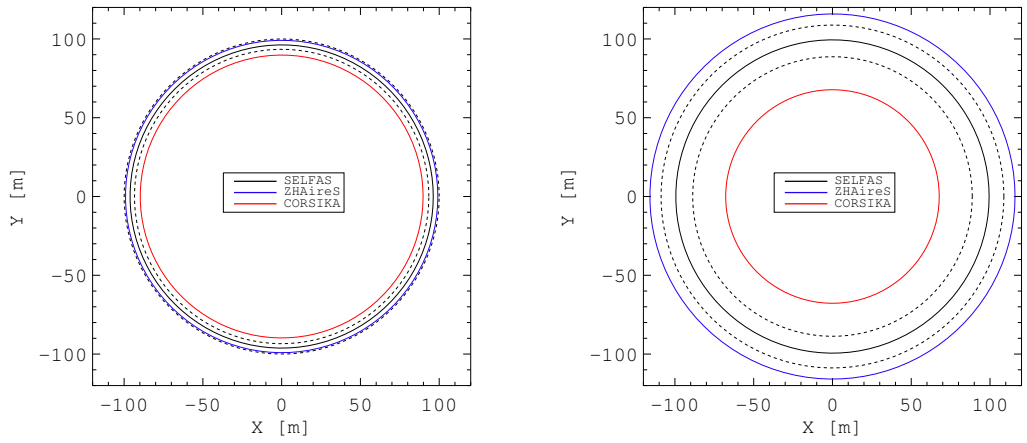

Figure 4.17: Comparison of the Cerenkov ring radius at the sea level for different simulation codes using the GDAS data for the year 2014 at 6 km of height on the left and 16 km of height on the right. In both plots, the dashed lines account for the extrema obtained for year 2014 with SELFAS.

The three calculations are compared in Figure 4.17. For SELFAS, using the GDAS data, the black solid line accounts for the mean air index value at 6 km and 16 km of altitude whereas the black dashed lines account for the minimum and maximum values of the air refractive index during the year 2014, close to the AERA experiment. The radii shown in Figure 4.17 are calculated considering that all particles are located on the shower axis, without a realistic thickness of the shower front and the direction of propagation of the particles is parallel to the shower axis. Before comparing the events simulated with the previous description (US Standard atmosphere, air index using the Gladstone with ρ_{US}) to the events simulated with the new description (GDAS atmosphere, air index calculated from $(P,T,P_V)_{\mathrm{GDAS}}$ and the high frequency law) a comparison is made between the two air index formulas using the GDAS data in both cases. The simulated time series are presented in Figure 4.18 for $X_1 = 10$ g/cm^2 and in Figure 4.18 for $X_1 = 100$ g/cm^2 in full band in the east-west polarization.

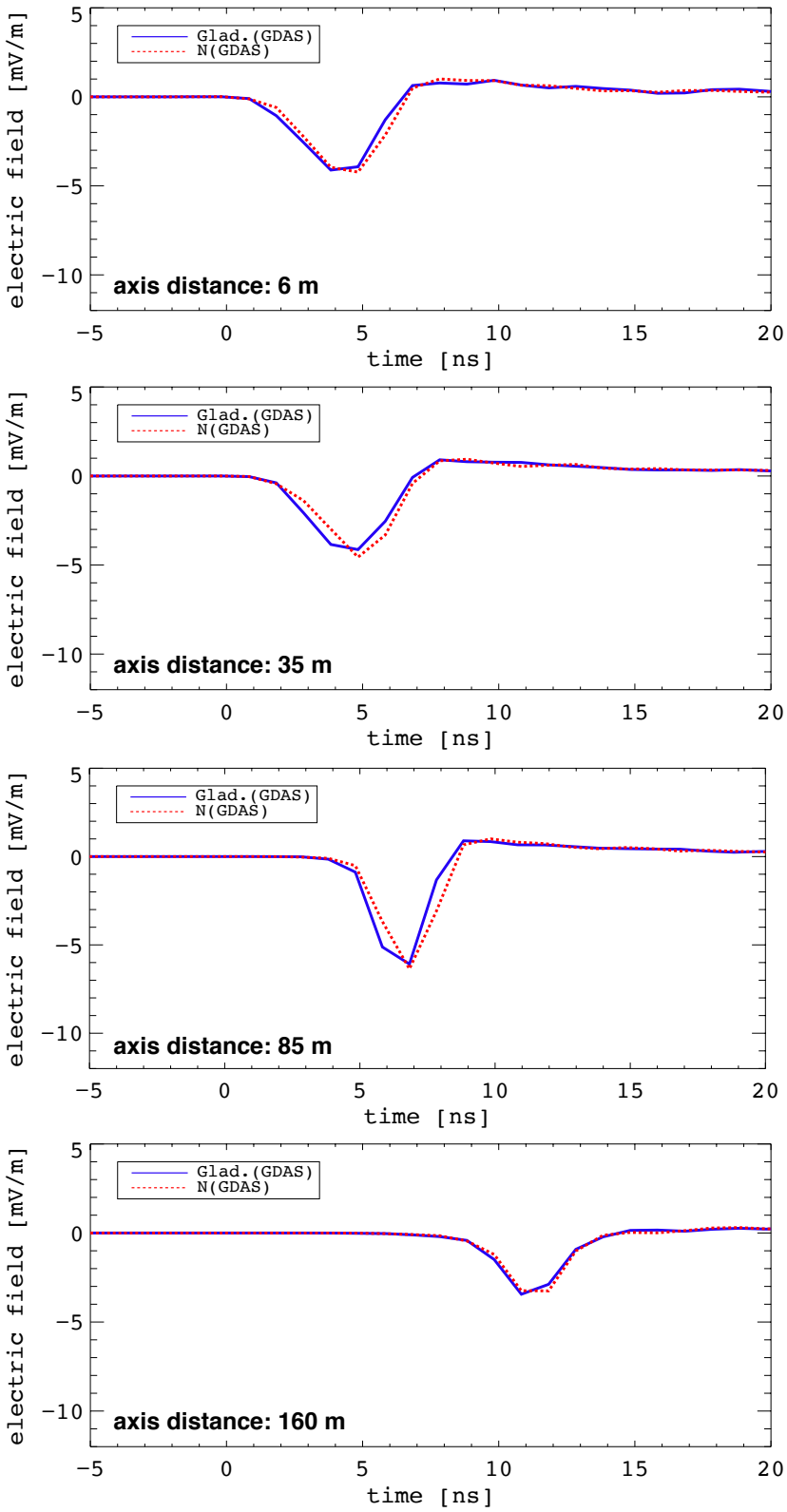

Figure 4.18: Time series of the electric field simulated with Gladstone(ρ_{GDAS}) (blue curves) and with the high frequency law for the air index with $(P,T,P_V)_{\mathrm{GDAS}}$ (red dashed curves) for different distance to the shower axis (6 m, 35 m, 85 m and 160 m) in the $\boldsymbol{v}\times B$ direction in the east-west polarization. The first interaction is fixed at 10 g/cm^2.

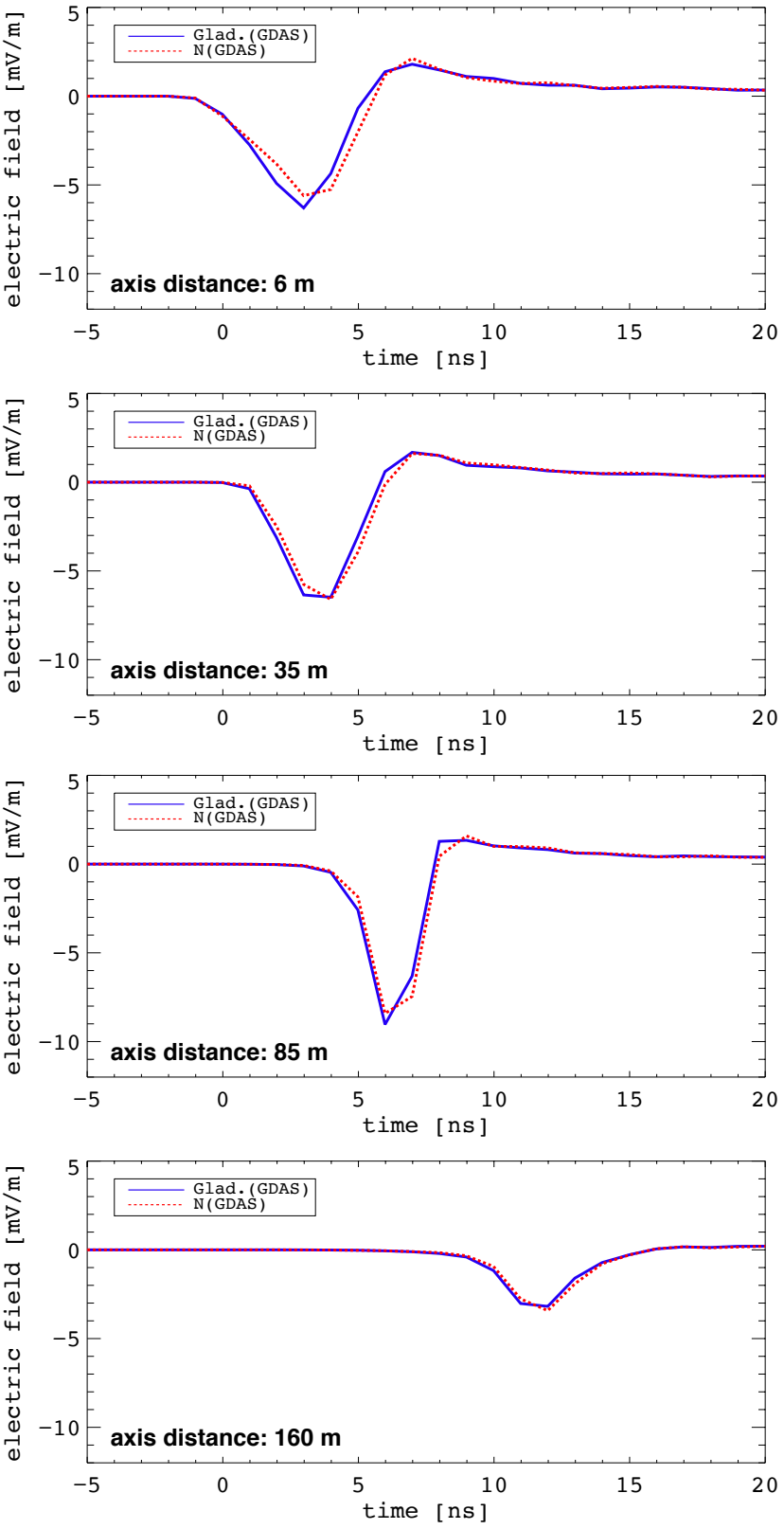

Figure 4.19: Same as Figure 4.18 but for a first interaction depth of 100 g/cm^2.

From Figures 4.18 and 4.19, one can notice small amplitude deviations especially at 35 meters for $X_1 = 10$ g/cm^2 and at 6 m and 85 meters from the shower axis for $X_1 = 100$ g/cm^2. In both Figures, the Cerenkov ring is visible, the electric field is not maximum at the shortest distance to the shower axis. The times of the maxima are shifted by few nano seconds between the two descriptions of the air index which is consistent with the induced small variations of optical path. The comparisons of the events simulated using the US standard atmosphere approximation (ρ_{US} and Glad($_{\mathrm{US}}$)) to the ones using a more realistic description (ρ_{GDAS} and $N(P,T,P_V)_{\mathrm{GDAS}}$) are presented in Figures 4.20, 4.21 and 5.2.

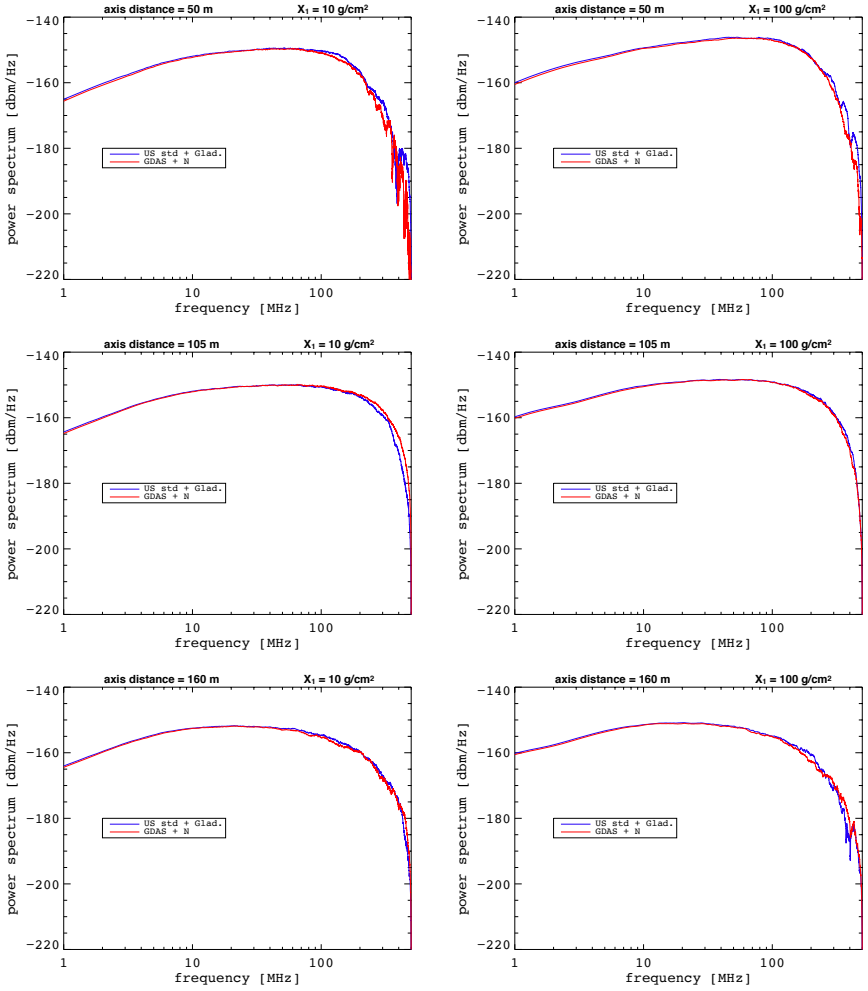

Figure 4.20: Simulated power spectra with US std. atmosphere with Gladstone(ρ_{US}) (blue curves) and the a GDAS atmosphere and the high frequency law for the air index with $(P,T,P_V)_{\mathrm{GDAS}}$ (red curves) for different distances to the shower axis (50 m, 105 m and 160 m) in the $\boldsymbol{v} \times B$ direction in the east-west polarization. The showers are induced by protons with a first interaction depth of 10 g/cm^2 (left panel) and 100 g/cm^2 (right panel).

The deviations between the two atmospheric models are small below 80 MHz. Larger discrepancies are visible above 80 MHz.

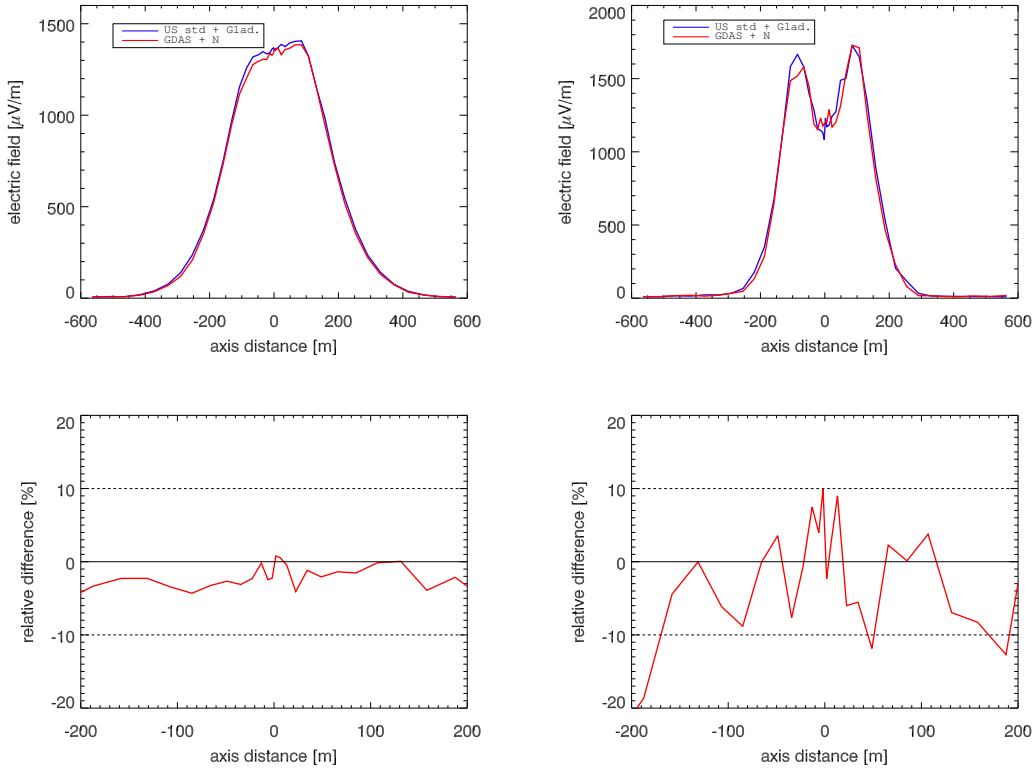

Figure 4.21: Top: LDFs simulated with US std. atmosphere with Gladstone(ρ_{US}) (blue curves) and the a GDAS atmosphere and the high frequencies law for the air index with $(P,T,P_V)_{\mathrm{GDAS}}$ (red curves), computed with several antennas in the $\boldsymbol{v}\times B$ direction. The showers are induced by protons with a first interaction depth of 10 g/cm^2 and the electric field is filtered in the band [30 - 80] MHz (left) and [120 - 200] using the three polarization. - bottom: the corresponding relative differences at a maximum distance of 200 m from the shower axis, where the emission of the electric field is coherent. The dotted lines account for a relative difference of $\pm$ 10%.

The relative differences are smaller than 5% in the band [30 - 80] MHz and smaller than 25% in the band [120 - 200] MHz for a first interaction depth of 10 g/cm^2. The relative differences are smaller than 10% in the band [30 - 80] MHz and smaller than 15% in the band [120 - 200] MHz for a first interaction depth of 100 g/cm^2. As expected from Figure 4.16, the deviations are more important in the case of showers with a large first interaction depth, that develop lower in the atmosphere. The differences induced by the air density and refractive index are not negligible at the antenna scale. In the next Section, the effects on an X_{max} reconstruction are studied.

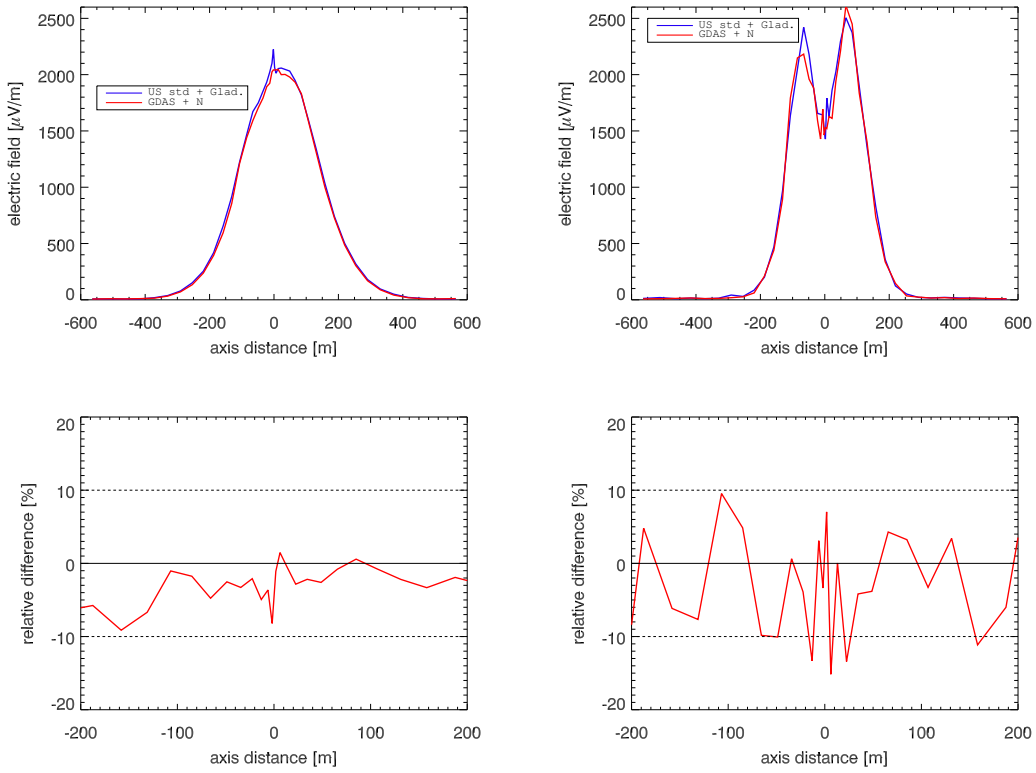

Figure 4.22: Same as Figure 4.21 but for a first interaction depth of 100 g/cm^2.

4.6 Effects on the reconstructed X_{max}

An event is taken from the set of high quality events presented in the last Chapter, the FD measurement gives $X_{max} = 760 \pm 8$ g/cm^2. The different characteristics of the simulations and the reconstructed values from the radio method are summarized in Table 4.4.

geometry	density	refractive index	radio X_{max} (g/cm^2)
flat approx.	US std	Glad(US)	735 ± 25
curved	US std	Glad(US)	750 ± 30
curved	GDAS	Glad(GDAS)	756 ± 18
curved	GDAS	N(GDAS)	757 ± 12

Table 4.4: Summary of the influence of the description of the atmosphere on the reconstructed value of X_{max}.

One can notice that the reconstructed X_{max} value is in better agreement to the FD measurement at each upgrade of the atmospheric model. The order of importance of each parameters is:

- the curved description
- the air density from the GDAS data
- the air index calculated with the high frequency law and the GDAS data

Although the air refractive is not decisive in this case with regards to the mean X_{max} value, one can notice that the precision is better. We now take another event from the previous data set for which the deviation of the reconstructed X_{max} to the FD measurement is particularly important using the US Standard atmosphere. This event has been simulated with the new atmospheric description and the reconstruction method has been performed. The results are summarized in Table 4.5 and compared to the FD measurement.

The agreement between the FD measurement and the reconstructed value is improved using the GDAS data. We obtain a 2 g/cm^2 deviation instead of 32 g/cm^2 with the US Standard model. The difference between the two reconstructed values can be explained with Figure 4.23.

air density	refractive index	X_{max} (g/cm^2)	dispersion (g/cm^2)
US Standard	Glad(ρ_{US})	794	11
GDAS (exp conditions)	$N(\rho_{GDAS})$	826	14
FD measurements		828	11

Table 4.5: Improvement of the X_{max} reconstruction using the new description of the atmosphere.

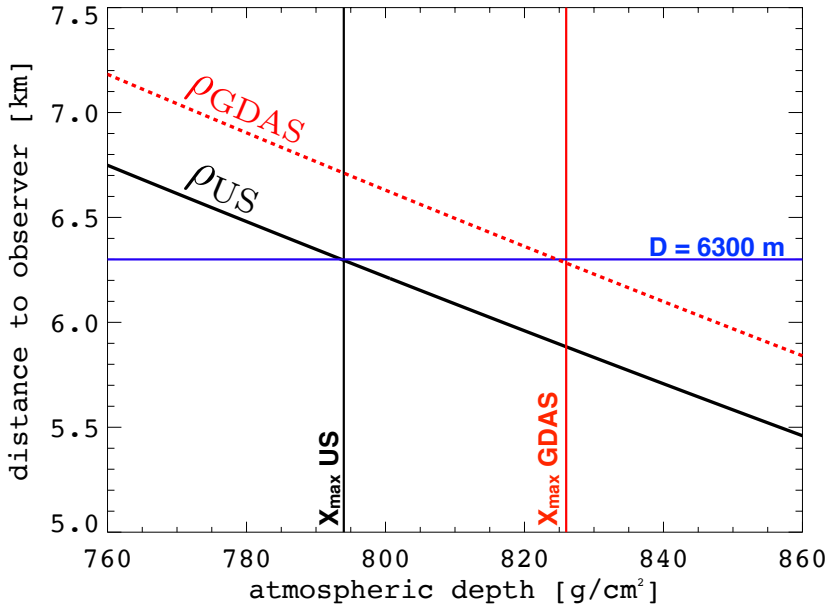

Figure 4.23: Geometric distance to the observer as a function of the atmospheric depth using ρ_{US} (black curve) and ρ_{GDAS} (dashed red line). See text for details.

In the US Standard model description, $X_{max\,US}$ (794 g/cm^2) corresponds to a geometrical distance to the observer of 6300 m. Using the GDAS profile, $X_{max\,GDAS}$ (826 g/cm^2) also corresponds to a distance of 6300 m. The electric field topology at the ground level only depends on the geometrical distance at which occurs the maximum emission (at fixed primary energy and arrival direction). Thus the same shower has been reconstructed with the two descriptions as we obtain the best agreement to the data for the same geometrical distance. Only in the case of the GDAS description, matching the experimental conditions, this distance corresponds to an atmospheric depth of 826 g/cm^2 which is in very good agreement with the FD measurement.

4.7 Conclusions

Constant atmosphere and flat Earth approximations are sufficient to roughly estimate the electric field induced by the development of an extensive air shower. However, in the case of this study, the atmospheric depth that is crossed by an air shower must be determined very precisely. The fluorescence detection takes into account the fluctuations of the air density to provide a precise $X_{\max}$ measurement. Reaching this precision is necessary to the validation of the radio reconstruction method by comparing the reconstructed $X_{\max}$ values to the FD measurements . We have shown that small fluctuations of the amplitude of the electric field (around 10%) are sufficient to shift an $X_{\max}$ reconstructed value by around 10 g/cm^2. Moreover, the precision of the reconstruction is better when using a dynamical atmospheric description. In the next Chapter, the method is tested again with the high quality set of FD events with the version of SELFAS, using air density profiles close to the experimental conditions.

CHAPTER 5

Results of the mass composition using the radio signal

Contents

5.1 Validation of the method

The reconstruction method is applied again of the set of 29 high quality FD events. The simulations are performed using a curved description of the Earth and its atmosphere. The air density is calculated from the GDAS data, so is the refractive index with the high frequencies law. The results are presented in Figure 5.2, and compared to the results previously obtained with the US Standard Model. The improvement of the correlation and between FD and RD is clear. The distribution of the differences is centered at 0, the systematic shift has been corrected. For this data set, the mean RMS of the reconstructed X_{max} with the radio method is 24 g/cm^2 and 17 g/cm^2 with the FD measurements. The new description of the atmosphere gives results in better agreement with the FD X_{max} measurements. The distribution of the differences does not follows a gaussian distribution. Indeed, the values of X_{max} follow a poissonian distribution. The distribution of the differences between FD and RD is a difference of two poissonian distributions, as seen in Figure 5.1, resulting also in a poissonian distribution. This result is thus consistent with the obtained distribution of the differences.

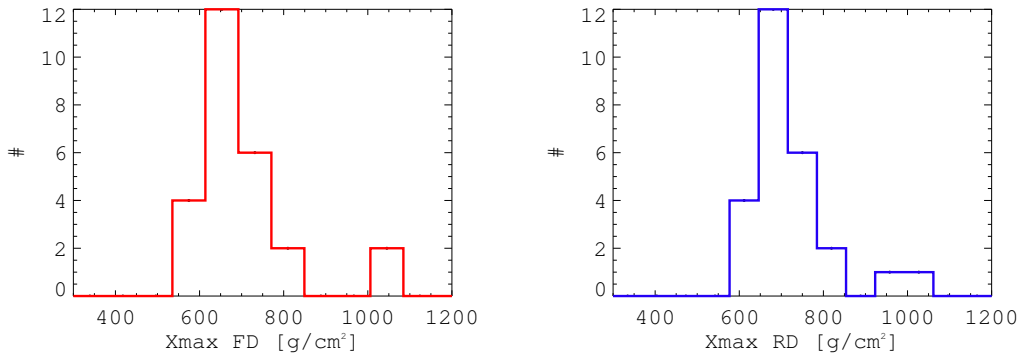

Figure 5.1: Distributions of the measured X_{max} from the FD (left) and reconstructed by the radio method (right) with the same bin size of 70 g/cm^2.

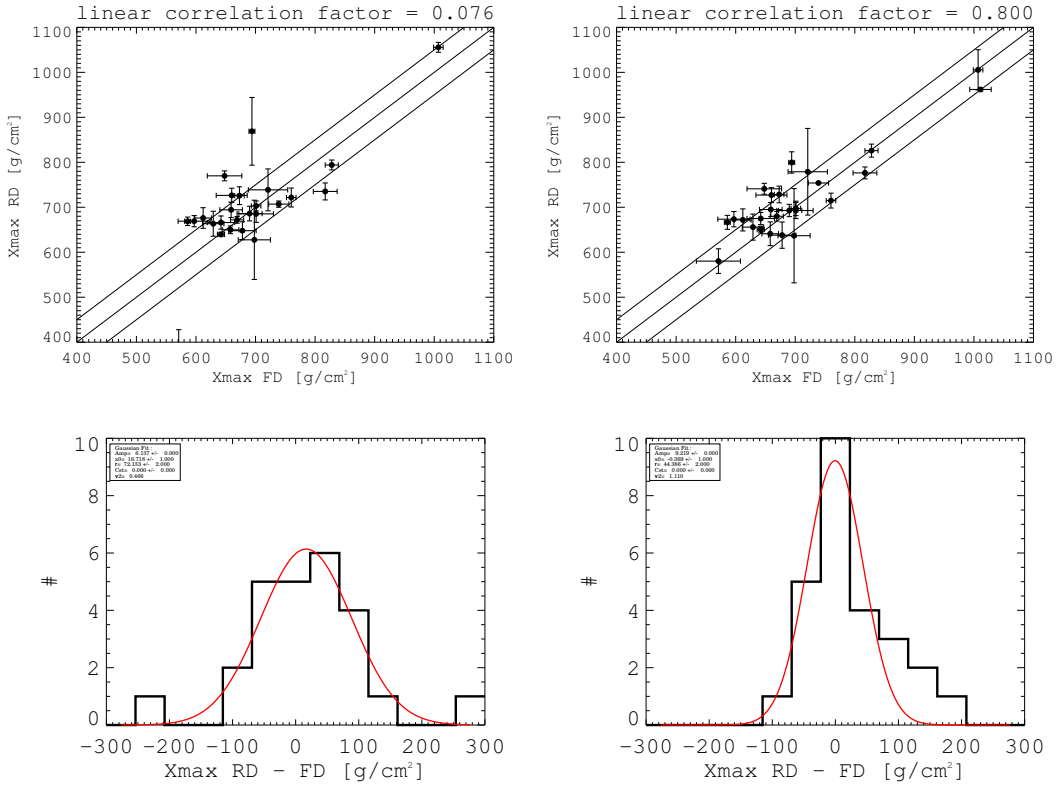

Figure 5.2: Top: reconstructed X_{max} with the radio method as a function of the FD measurements, the middle line accounts for a one-to-one correlation and the others account for a deviation of $\pm$ 50 g/cm^2. Bottom: distributions of the differences between the radio method and the FD measurements. The plots on the left are obtained with the US Standard atmosphere and one the right using the actual GDAS values.

It now appears clearly that the use of a realistic description of the atmosphere is mandatory to perform a reliable reconstruction of X_{max} using the radio signal. The radio reconstruction method can now be used to perform statistical mass discrimination

studies. To do so, a data set is composed with events detected at AERA in coincidence with the surface detectors. It is composed of 150 air showers detected between the 1st of July 2015 and the 31st of December 2015 to ensure a significative seasonal variation of the air density over the data set. Only showers with a zenith angle below 55° are selected and with at least 5 stations with signal. No further quality cuts are applied.

5.2 Blind X_{max} reconstruction

The reconstruction method is applied to the described data set. The X_{max} values are reconstructed together with the energy of the primary. As usual, no assumption was made concerning X_{max}, the core position and the energy of the primary. For the latter parameter an energy of 10^{17} eV was chosen arbitrarily, without consulting the energy measured by the SD. The results that are presented in this Section were obtained through a total blind and radio only reconstruction of the parameters of the air showers. For the simulations the arrival directions calculated from the radio signals are used as inputs. The results are compared to the mass estimated at the Pierre Auger Observatory. The mean X_{max} values are presented in Figure 5.3 with their statistic errors.

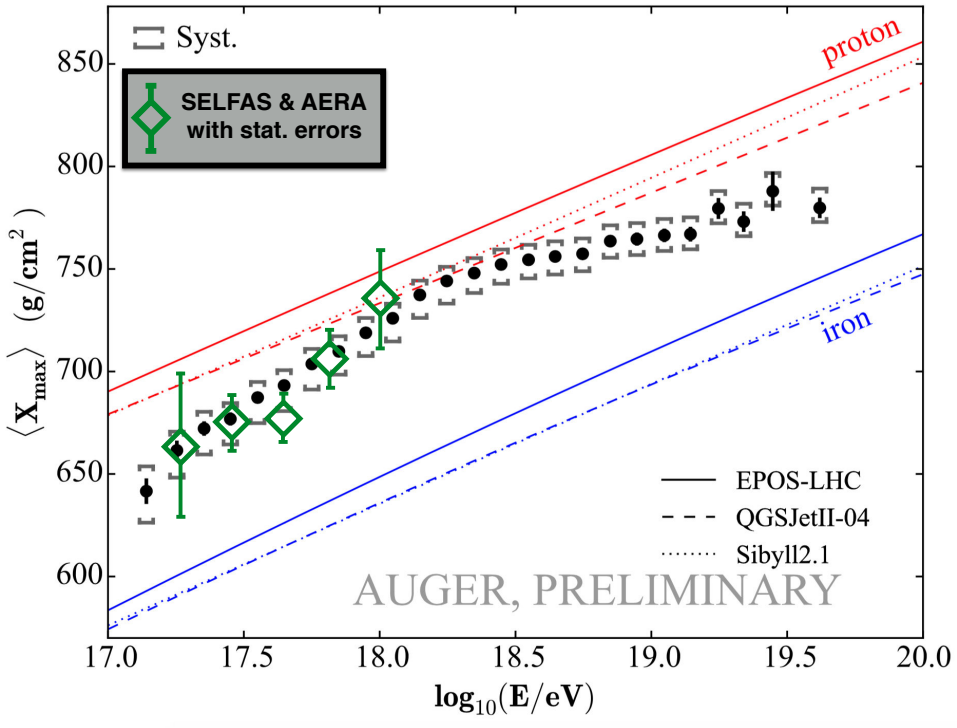

Figure 5.3: X_{max} mean values as a function of the energy of the primary by energy bins. The black dots are the mean X_{max} measurements at the Pierre Auger Observatory obtained with the FD. The green diamonds are the results obtained with the radio method using the AERA data.

The three energy bins are respectively composed of 5, 29, 37, 16 and 6 events. The statistic error $X_{\max}^{stat}$ corresponding to an energy bin is calculated as follow:

$$X_{\max}^{stat} = \frac{1}{\sqrt{n}} \sqrt{\frac{1}{n-1} \sum_{i}^{n} (X_{\max}^{i} - < X_{\max} >)^2} \tag{5.1}$$

The reconstructed values are in very good agreement with the measurements. The statistical fluctuation of $X_{\max}$ is also correlated to the mass of the primary and the reconstructed values are compared to the measurements of the Pierre Auger Observatory in Figure 5.4.

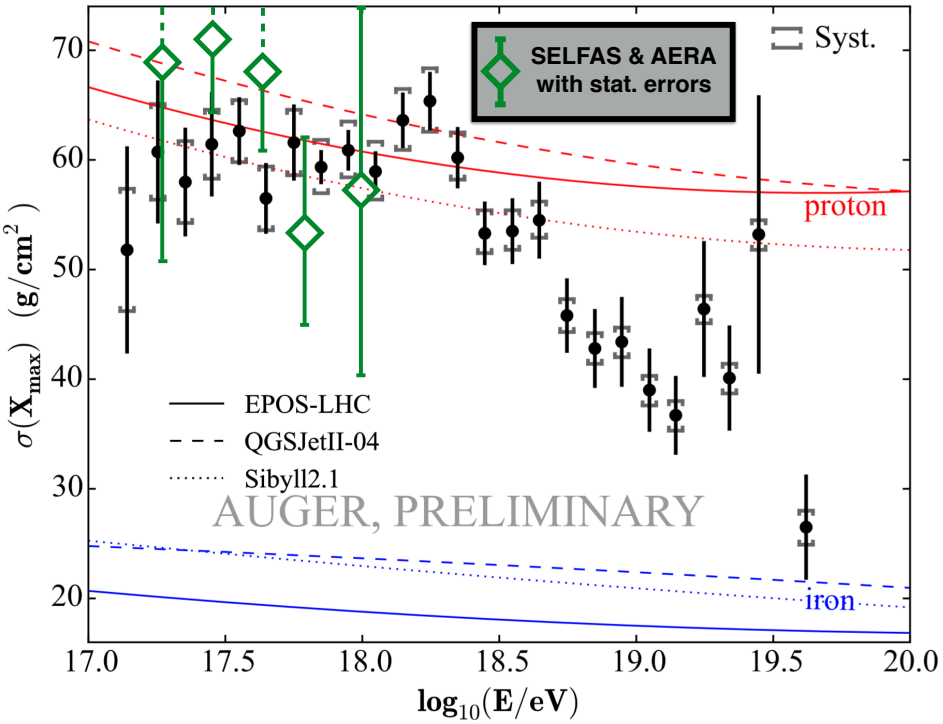

Figure 5.4: RMS($X_{\max}$) mean values as a function of the energy of the primary by energy bins. The black dots are the RMS($X_{\max}$) measurements at the Pierre Auger Observatory with the FD. The green diamonds are the results obtained from the radio method using the AERA data.

The statistic error corresponding to an energy bin σ^{stat} is calculated as follow:

$$\sigma^{stat} = \frac{1}{\sqrt{n}} \sqrt{\frac{1}{n-1} \sum_{i}^{n} (\sigma^{i} - < \sigma >)^2} \tag{5.2}$$

The results also show a good agreement with the measurements. Though in this case the statistic errors are important due to the small number of events, especially for the most energetic bin. In both cases our results, as the results of the Pierre Auger Observatory, are compatible with a light composition in the energy range $\mathrm{Log}_{10}(E) \in [17.5, 18]$. From the results presented in this Chapter, several conclusions can be drawn:

- the radio signal is now well understood and the simulation code SELFAS provides results in agreement the FD and the SD
- the radio signal can be used to estimate efficiently the mass composition of the primary cosmic rays at the highest energies

In the case of AERA, the upper limit of the energy range is limited by the surface covered by the array. The deployment of a larger radio detection array together with a higher energy threshold would allow to focus on the detection of cosmic rays at the highest energies. An experimental setup of this kind could allow a precise determination of the mass composition for energies higher than 10^{18} eV.

Conclusions & Perspectives

The deployment of large detection arrays, such as the Pierre Auger Observatory, has permitted to study the most energetic particles in the Universe. Many progress have been made towards the understanding of the cosmic rays beyond 10^{17} eV. However, the low statistics of detected events does not allow a clear determination of the acceleration mechanisms, the type of sources and the origin of the cut-off of the energy spectrum. The key observable to disentangle the latter topics is the mass composition which is also not clearly established. The depth of the shower maximum (X_{max}) is highly correlated to the mass of the primary and can be used to statistically estimate the composition, which can only be done through the detection of a very high number of showers. This latter condition is not fulfilled at the highest energies by the fluorescence technique, which is the only way to measure X_{max}, due to the very low statistics and a duty cycle of 14%.

In this context, I have developed a method that aims to carry out a complete reconstruction of the air shower parameters: the core position of the shower at the ground level, the energy of the primary cosmic ray and X_{max}. This method is based on a comparison of the radio signal emitted during the development of the air shower and its simulation with the code SELFAS. The duty cycle of the radio detection is close to 100%, ensuring the increase of the number of detected events. Moreover the emission mechanisms of the electric field are well understood.

The radio reconstruction technique appears as very good alternative to perform mass composition studies. The method has been tested on simulated events, and the reconstructed parameters (core position, energy and X_{max}) are in very good agreement with the simulated ones. This basic test allowed to pass a self-consistency test. The method has also been tested on data from the Pierre Auger Observatory. In this purpose, a data set have been composed with super hybrid events, detected in coincidence by the three types of detectors: the radio stations (RD), the fluorescence telescopes (FD) and the particle detectors (SD). The standard FD quality cuts have been applied to ensure a significant comparison of the reconstructed X_{max} values to the measured ones. The reconstructed parameters are in very good agreement with the core positions and energy measured by the SD and X_{max} measured by the FD. These is a systematic shift of 17 g/cm^2 between the X_{max} measured by the FD and the value estimated with the radio data.

In order to understand and correct the systematic deviation, I studied in details the influence of the description of the atmosphere in SELFAS on the computed electric field. Indeed, the fluorescence measurements take into account the seasonal and daily variations of atmosphere density. It thus appeared important to investigate whether or not the variation of the air density could be neglected. Formerly, SELFAS used a

parametrization of the US Standard Atmosphere model, which is constant in time. I used the data provided by the GDAS to compute realistic air density profiles, close to the time of detected events, in order to better match the experimental atmospheric conditions and account for the daily and seasonal variations.

The air refractivity also follows the variations of the air density. In the previous version of SELFAS, the refractivity was scaled linearly to the air density, which was also described by the US parametrization. The slope parameter used for the calculation of the refractivity has been calculated in the μm domain, which was not suitable to our studies in the decametric domain. A law specially parametrized in the decametric domain was adopted. This study has shown that the distribution of the amplitude of the electric field at the ground level is significantly influenced by the air density and refractivity: around 10% in the [30 - 80] MHz frequency band and around 15% in the [120 - 200] MHz frequency band.

The geometry of the atmosphere has also been studied. SELFAS was first developed using a flat Earth approximation, inducing inconsistencies for the calculation of the crossed atmospheric depth along a shower axis. The comparison between the flat approximation and a fully curved description has shown that the discrepancies are negligible for zenith angles smaller than 40° but can reach around 10 g/cm^2 above 60° and 200 g/cm^2 at 80°.

Finally we have demonstrated that taking into account the daily and seasonal variations of the air density and refractivity is mandatory when aiming to reconstruct $X_{\max}$. Indeed, the systematic shift that was obtained using the US Standard Model parameterization vanishes when using realistic air density profiles and a consistent calculation of the air refractivity.

The reconstructed $X_{\max}$ values are now in very good agreement with the FD measurements. The radio method can now be used to perform a statistical mass discrimination of cosmic rays. The method has been applied to a data set of events detected at the AERA experiment and the results of the $X_{\max}$ reconstructions have been compared to the mass estimation performed at the Pierre Auger Observatory as a function of the energy of the primary.

The agreement between the values reconstructed (energy of the primary and $X_{\max}$) by the radio method and the measurements of the Pierre Auger Observatory is very good. Both the mean values of $X_{\max}$ by energy bin and their statistical fluctuations are compatible with a light composition in the energy range $\mathrm{Log}_{10}(E) \in [17.5, 18]$.

This final result is very encouraging and proves that the radio detection technique is able to efficiently estimate the mass composition of cosmic rays. Its high duty cycle is an important asset to increase significantly the statistics that we need to precisely

discriminate the mass of the primaries at the highest energies.

The upgrade of the Pierre Auger Observatory, *AugerPrime*, will provide new informations concerning the muonic component of the extensive air showers and the mass composition. We know since the KASCADE experiment that the pseudo rapidity of the muons is correlated to the mass of the primary. This upgrade also aims to provide new hints about the origin of the cutoff of the energy spectrum.

Another radio signal, produced by the extensive air showers is expected and is starting to be investigated at the CODALEMA experiment. This signal, coming from the *sudden death* of the shower. When hitting the ground, the secondary particles suffer a sudden deceleration. The time variation of the charge and current density is expected to produce a strong electric field at frequencies below 20 MHz. Two low frequency stations have been deployed at CODALEMA to detect this signal in correlation with the signal induced by the development of the extensive air showers. This new observable could help to better constrain the mass composition.

Résumé en Français

La Terre est continuellement bombardée par un flux de particules dont l'origine extraterrestre a été suggérée par Domenico Pacini en 1911 et confirmée par Victor Hess en 1912. L'étude de ce rayonnement est à l'origine de nombreuses avancées majeures de la physique des particules et de l'astrophysique. L'étude des rayons cosmiques est d'ailleurs un domaine d'étude des *astroparticules*. Aujourd'hui, le terme *rayon cosmique* qualifie toutes les particules chargées détectées sur Terre et dont l'origine est extraterrestre. Le spectre en énergie des rayons cosmiques s'étend sur plus de trente-deux ordres de grandeur en flux et douze en énergie. Il est globalement décrit par une loi de puissance dont l'indice spectral varie de 2.8 à 3.3. Le nombre de rayons cosmiques décroît donc très rapidement en fonction de leur énergie. Chaque décade en énergie voit sa statistique divisée par cent. Jusqu'à 10^{17} eV, les sources, les mécanismes d'accélération et la composition en masse des rayons cosmiques sont bien connus. Dans cette gamme en énergie le nombre d'événements détectables est suffisant pour permettre une détection directe (satellites, ballons-sondes...) jusqu'à 10^{15} eV. Au-delà, la detection indirecte est utilisée, grâce à laquelle la détermination des différents paramètres, comme la masse, est possible de manière statistique avec un grand nombre d'événements. La détection indirecte consiste à observer le développement de la cascade de particules secondaire créée lors de l'interaction du rayon cosmique primaire avec les constituants de l'atmosphère. Après avoir pénétré dans l'atmosphère, le rayon cosmique interagit après avoir traversé une profondeur nommée X_1 : c'est le point de première interaction. Le nombre de particules secondaires va croître tant que l'énergie disponible dans le front de gerbe est suffisante, jusqu'à atteindre la profondeur X_{max} à laquelle le nombre de particules est maximal. Passé ce point, l'énergie est trop faible pour créer de nouvelles particules et leur nombre décroît. À partir de 10^{17} eV, la statistique est d'environ une particule / km^2 / jour pour atteindre une particule / km^2 / siècle à 10^{20} eV. Le déploiement de grandes surfaces de détection est donc indispensable pour l'étude des rayons cosmiques d'ultra-haute énergie. C'est le cas de l'Observatoire Pierre Auger, situé en Argentine et qui dispose de 1660 cuves Cerenkov couvrant une surface de 3000 km^2, 27 telescopes de fluorescence répartis sur quatre sites, 153 stations radio et la construction de 61 détecteurs de muons. Les cuves échantillonnent la distribution des particules secondaires qui atteignent le sol. Les détecteurs de muons sont enfouis à 2,5 mètres sous terre, permettant la mesure de la composante muonique de la gerbe, les électrons et positrons étant stoppés avant d'atteindre cette profondeur. Lors du passage de la gerbe dans l'atmosphère, les particules secondaires qui la composent excitent les molécules de diazote. Celles-ci reviennent à leur état fondamental en émettant de la lumière de fluorescence qui est captée par les télescopes. L'intensité de cette lumière est proportionnelle au nombre de particules qui composent la gerbe au moment de l'émission. La technique de détection de la lumière de fluorescence permet donc une mesure calorimétrique du développement de la gerbe dans l'atmosphère

et notamment la mesure directe de la profondeur $X_{\max}$. Cette grandeur est fortement corrélée à la masse du rayon cosmique primaire car elle dépend, au premier ordre, de la section efficace d'interaction du primaire avec l'atmosphère. À l'Observatoire Pierre Auger, la masse des rayons cosmiques d'énergie supérieure à 10^{17} eV est déterminée de manière statistique. Les comportements moyens par gamme en énergie sont comparés aux résultats fournis par des modèles d'interaction hadronique d'ultra-haute énergie. Cette technique est efficace pourvu que le nombre de gerbes détectées soit important, ce qui est le cas jusqu'à quelques EeV (10^{18} eV). Pour les énergies supérieures, la statistique devient faible. Une rupture dans le spectre est observée à 6×10^{19} eV avec un niveau de confiance supérieur à 20σ. La limite GZK prédit cette coupure et l'attribue à l'interaction des rayons cosmiques avec les photons du fond diffus cosmologique dont l'énergie seuil est estimée à 5×10^{19} eV. De plus, le cycle utile des télescopes de fluorescence est d'environ 14% car leur sensibilité ne permet un fonctionnement que par nuit sans lune et sans intempéries. Il en résulte que le nombre d'événements détectés est trop faible au-delà de 6×10^{19} eV pour determiner précisément la masse des rayons cosmiques.

Aujourd'hui encore, certaines questions concernant les rayons cosmiques d'ultra-haute énergie subsistent. La coupure dans le spectre est mise en évidence expérimentalement mais sa cause n'est pas clairement établie. Les données de l'Observatoire Pierre Auger, dans l'hémisphère Sud sont compatibles avec un flux isotrope alors que l'expérience Telescope Array, dans l'hémisphère Nord, annonce un excès dans la direction de l'amas de galaxies Ursa Major. Les modèles de mécanismes d'accélération et de propagation à ces énergies sont également mal contraints dû à un manque de données. Enfin, à ces énergies les deux candidats principaux sont les protons et les noyaux de fer. Les données de l'Observatoire Pierre Auger, aux plus hautes énergies, sont compatibles avec des gerbes initiées par des noyaux lourds comme le fer. Les données de l'expérience Telescope Array sont compatibles avec des protons. La détermination précise de la masse permettrait de contraindre les modèles de mécanismes d'accélération, de propagation et de types de source. C'est donc la priorité de toutes les expériences de détection des rayons cosmiques d'ultra-haute énergie.

Idéalement il faudrait pouvoir mesurer la profondeur $X_{\max}$ avec un cycle utile proche de 100%, ce qui est le cas de la détection radio. Les gerbes atmosphériques sont principalement composées de positrons et d'électrons (constituant 90% de l'énergie de la gerbe avec les photons). L'évolution temporelle de la charge nette du front de particules induit l'émission d'un champ électrique détectable dans le domaine du MHz de l'ordre que quelques centaines de micro Volts par mètre (pour une gerbe verticale initiée par un rayon cosmique de 10^{17} eV et dans la bande de fréquence [30 - 80] MHz). Ce mode de détection est sensible à tout le développement de la gerbe, tout comme la fluorescence.

Les stations radio de l'Observatoire Pierre Auger sont situées sur le site expérimental d'AERA (Auger Engineering Radio Array), proche d'un des sites de télescopes

de fluorescence. Elles permettent des detections en coïncidence avec les télescopes et les cuves Cerenkov. Ces stations possèdent deux antennes de type butterfly ou logarithmic periodic dipole antenna (LPDA) dont l'une est orientée perpendiculairement à l'autre. Les stations enregistrent le champ électrique dans deux polarisations (Nord-Sud et Est-Ouest) dans la bande de fréquence [30 - 80] MHz afin des s'affranchir des parasites radio (bande AM inférieure à 20 MHz et bande FM supérieure à 80 MHz). Les détections faisant intervenir plusieurs antennes permettent de construire la distribution latérale du champ électrique (LDF) calculée comme le champ électrique maximum reçu par chaque antenne en fonction de leur position relative à l'axe de la gerbe.

Au cours de cette thèse, une méthode de reconstruction de la profondeur $X_{\max}$ grâce aux signaux radio a été développée dans le but d'estimer la masse des rayons cosmiques aux énergies supérieures à 10^{17} eV, et ce, avec un cycle utile proche de 100%. Il est maintenant établit que la LDF est fortement corrélée à la profondeur $X_{\max}$. Le champ électrique étant extrêmement focalisé dans la direction de propagation de la gerbe, une grande valeur de $X_{\max}$ donnera lieu à une distribution au sol étroite, car provenant d'une région proche du sol. Au contraire, une faible valeur de $X_{\max}$ correspondra à une LDF moins intense et plus large. La méthode de reconstruction se base sur la comparaison de la LDF échantillonnée par les stations radio et d'un modèle de distribution latérale du champ électrique.

Dans un premier temps, j'ai développé un modèle de densité angulaire de radiation reflétant la manière dont rayonne une gerbe. Le premier mécanisme d'émission est dû à l'excès de charges négatives par rapport aux charges positives, prédit par Askaryan en 1962. En effet, les positrons vont s'annihiler dans le milieu de manière plus importante que les électrons. La variation temporelle du courant induit par la charge nette non nulle du front de gerbe produit un champ électrique polarisé radialement par rapport à l'axe de la gerbe. En 1967, Kahn et Lerche prédisent un autre phénomène. La présence du champ magnétique terrestre provoque la déviation systématique et opposée des électrons et des positrons sous l'effet de la force de Lorenz. Il en résulte l'établissement d'un courant orienté perpendiculairement à la direction de propagation de la gerbe dont la variation temporelle crée un champ électrique polarisé dans la direction $\boldsymbol{v} \times \boldsymbol{B}$, avec $\boldsymbol{v}$, le vecteur vitesse de la gerbe et $\boldsymbol{B}$ le champ magnétique terrestre. Le champ électrique total émis par une gerbe atmosphérique est la superposition de ces deux mécanismes, qui peuvent interférer de manière constructive ou destructive suivant la position autour de l'axe de la gerbe.

Le modèle développé prend en compte ces deux mécanismes et a été paramétrisé grace à une simulation effectuée avec le code SELFAS. Ce code adopte une approche microscopique en sommant les contributions individuelles de chaque particule secondaire au champ électrique total. Il apparaît que le maximum d'émission peut être associé à la profondeur X_{inf}, à laquelle le taux de production de particules secondaires est maximum. La paramétrisation effectuée sur une LDF simulée est donc une image

du rayonnement émis par la gerbe à cette profondeur.

Ce modèle a été testé sur un lot d'événements simulés. Lors de l'ajustement du modèle aux données, un des paramètres libres correspond à la distance géométrique entre le point d'impact de la gerbe sur le sol et le maximum d'émission. Afin de pouvoir comparer des gerbes ayant des angles zénithaux différents, les effets d'atmosphère sont pris en compte pour convertir cette distance en profondeur d'atmosphère. Le modèle d'atmosphère utilisé est une paramétrisation du modèle US Standard, donnant la profondeur d'atmosphère traversée correspondant à une altitude.

La comparaison des profondeurs d'atmosphère reconstruites aux profondeurs X_{inf} simulées montre un très bon accord. En revanche, ce modèle qui prédit une décroissance exponentielle de l'intensité du champ électrique en fonction de la distance à l'axe montre quelques limitations. En effet, l'allure du champ électrique détecté est plus complexe. Un effet comparable à l'emission Cerenkov se produit. En réalité dû à une compression temporelle (les particules secondaires sont relativistes), une augmentation de l'intensité du champ électrique est visible sous un certain angle d'emission, dont la valeur dépend de la vitesse des particules et de l'indice de réfraction de l'air. Dès lors que cet effet se produit, la description proposée par le modèle de densité angulaire de radiation n'est plus valable car il ne prend pas en compte l'indice de réfraction de l'air.

Une autre méthode fut donc adoptée, utilisant directement le code de simulation SELFAS comme prédiction. Cette méthode vise à reconstruire tous les paramètres décrivant une gerbe atmosphérique : la position du cœur de la gerbe sur le réseau, l'énergie du primaire et la profondeur X_{max} permettant une estimation de la masse du primaire. Les données radio permettent une reconstruction précise de la direction d'arrivée en étudiant les temps d'arrivée relatifs du champ électrique au niveau de chaque antenne touchée. La méthode consiste à simuler un lot d'événements composé de gerbes initiées par des noyaux de fer et par des protons avec la même direction d'arrivée que celle déduite expérimentalement. Le champ électrique est calculé pour chaque antenne d'un réseau fictif dense. Après interpolation, les LDFs simulées sont comparées aux données expérimentales. Le point de première interaction de chaque simulation est choisi aléatoirement de manière réaliste grâce à l'utilisation d'un modèle d'interaction hadronique d'ultra-haute énergie. Chaque simulation a donc également une valeur propre de X_{max}. L'énergie des primaires est fixée arbitrairement, l'amplitude du champ électrique variant linéairement avec l'énergie de la particule primaire simulée. L'amplitude du champ simulée est laissée libre lors de l'ajustement. Le meilleur accord est obtenu pour une certaine position du coeur de la gerbe, une valeur de X_{max} et une valeur du facteur d'amplitude.

Les trois paramètres reconstruits (énergie, position du cœur, X_{max}) sont comparés aux valeurs obtenues par les cuves Cerenkov et les télescopes de fluorescence. Les valeurs reconstruites à partir du signal radio présentent un très bon accord avec les

valeurs expérimentales déduites des autres instruments. Les profondeurs $X_{\max}$ reconstruites sont très fortement corrélées aux valeurs des telescopes de fluorescence. Néanmoins un décalage systématique de 17 grammes par centimètre carré est observé.

Afin de tenter d'expliquer et de corriger cette différence, des améliorations ont étés apportées au code de simulation SELFAS. Premièrement, la géométrie de l'atmosphère, auparavant modélisée par une approximation Terre plate où les couches d'atmosphère sont plates, est maintenant modélisée de manière réaliste et totalement sphérique. Deuxièmement, les données produites par les télescopes de fluorescence prennent en compte les variations journalières et saisonnières de la densité d'atmosphère. Les conditions atmosphériques influencent fortement la distribution de champ électrique, il est donc important de les prendre en compte afin de reconstruire précisément les profondeurs $X_{\max}$. Le GDAS (Global Data Assimilation System) rend disponible des données météorologiques d'intérêt partout sur la planète toutes les trois heures. Cette base de données a été utilisée afin de permettre une simulation dynamique de l'atmosphère, au plus proche des conditions expérimentales régnant lors de la detection d'un événement. Troisièmement, une estimation de l'indice de réfraction de l'air plus adaptée au problème traité est proposée. En effet la loi la plus communément utilisée est la loi de Gladstone et Dale qui propose une dépendance linéaire de l'indice de l'air avec la densité atmosphérique. Le pourcentage d'humidité de l'air n'est pas pris en compte alors qu'il joue un rôle important dans le calcul de l'indice de l'air. De plus cette loi est valable pour les longueurs d'ondes optiques, ce qui ne convient pas à la detection dans le domaine décamétrique. Une loi spécialement adaptée aux hautes et ultra-hautes fréquences, prenant en compte la pression, la température et le taux d'humidité a donc été adoptée.

Cette version améliorée de SELFAS est finalement utilisée pour la reconstruction plusieurs événements détectés à l'Observatoire Pierre Auger. L'estimation de la composition en masse des rayons cosmiques d'énergies supérieurs à 10^{17} eV est proposée.

APPENDIX A
GDAS data files

Here I show an example of a GDAS data file, after extracting the data corresponding to a location on the grid.

```
    14     9     1     0     0    859.24   1011.28      0.00      0.11      0.10     73.60
264.00    49.00    -3.24    -1.28   284.40    50.00  1377.05      0.00      0.00
276.95     2.88   437.00   284.20     0.00     0.19     0.00      0.00      0.00
0.00    15.20     2.00    24.00    41.00
    14     9     1     0     1     85.33    292.90     -3.62     -1.46     -0.00     49.00
    14     9     1     0     2    299.96    291.45     -3.62     -1.46     -0.00     49.00
    14     9     1     0     3    519.40    290.00     -3.62     -1.46     -0.00     49.00
    14     9     1     0     4    744.78    288.55     -3.62     -1.46     -0.00     49.00
    14     9     1     0     5    974.33    287.00     -3.62     -1.46     -0.00     49.00
    14     9     1     0     6   1452.80    283.77     -3.87     -1.71     -0.00     49.00
    14     9     1     0     7   1953.73    279.83     -2.12     -5.96      0.00     59.00
    14     9     1     0     8   2480.39    276.17      0.88     -9.21      0.00     63.00
    14     9     1     0     9   3037.03    273.67      0.13    -12.21      0.00     55.00
    14     9     1     0    10   3628.78    271.05     -0.01    -13.52      0.01     52.00
    14     9     1     0    11   4259.88    266.48      0.78    -13.89      0.01     67.00
    14     9     1     0    12   4931.66    260.49      8.71    -17.49      0.01     91.00
    14     9     1     0    13   5652.55    255.81     19.79    -18.58      0.01     94.00
    14     9     1     0    14   6433.15    249.82     24.89    -15.70      0.01     96.00
    14     9     1     0    15   7283.46    243.41     29.34    -12.21      0.00     97.00
    14     9     1     0    16   8223.23    237.45     41.80    -15.70     -0.00     99.00
    14     9     1     0    17   9277.25    229.19     48.60    -22.60     -0.00    100.00
    14     9     1     0    18  10473.04    220.68     47.55    -22.20     -0.00     95.00
    14     9     1     0    19  11932.63    225.51     25.05     -7.35     -0.00     12.00
    14     9     1     0    20  13811.67    218.19     17.49    -21.41      0.00      9.00
    14     9     1     0    21  16368.97    214.93     10.00     -2.92      0.00      7.00
    14     9     1     0    22  20732.15    216.21     -2.33      0.78      0.00      0.00
    14     9     1     0    23  26572.51    220.27     -8.62     -0.51      0.00      0.00
    14     9     1     3     0    854.97   1009.05      0.00      0.04      0.01     -2.40
0.00    51.80    -1.94    -0.55   283.15   100.00  1377.05      0.00      0.00    277.45
1.60   280.40   282.65     0.00     0.19     0.00     0.00      0.00      1.00      7.00
2.00    67.00   100.00
    14     9     1     3     1     73.00    291.77     -2.33     -0.68     -0.00     51.00
    14     9     1     3     2    288.15    290.45     -2.45     -0.68     -0.00     51.00
    14     9     1     3     3    507.04    289.00     -2.45     -0.68     -0.00     51.00
    14     9     1     3     4    731.86    287.55     -2.45     -0.68     -0.00     51.00
    14     9     1     3     5    961.81    286.12     -2.45     -0.68     -0.00     51.00
    14     9     1     3     6   1438.96    282.88     -2.45     -0.68     -0.00     51.00
    14     9     1     3     7   1938.41    279.05     -2.20     -2.93     -0.00     62.00
    14     9     1     3     8   2463.43    275.77      0.80     -6.43     -0.00     66.00
    14     9     1     3     9   3019.72    273.65     -0.20    -11.18      0.00     60.00
    14     9     1     3    10   3611.70    270.80     -0.94    -15.51      0.01     64.00
    14     9     1     3    11   4241.88    266.30      0.29    -14.30      0.01     75.00
    14     9     1     3    12   4913.44    260.38      5.47    -16.00      0.00     93.00
```

Figure A.1: An example of GDAS data after extracting the values corresponding to a specified location

Every set of data corresponding to one hour is composed of 24 lines. I we have a look at the first set (i.e. the first 24 lines), one can see that each line corresponds to an altitude and time and begins with the year (14), month (9) and day (1) in brown, the hour (0) in dark blue and a vertical level (0 to 23) in light blue corresponding to an altitude. The first line in red is the surface and contains the S parameters that can be found in Table 2 in [161]. Each of the next 23 lines correspond to a vertical level (that can be converted in absolute pressure with the Table 3 in [161]) and contains the U parameters in green and can be found also in [161] in Table 2.

Bibliography

[1] Coulomb C. A. (Charles Augustin), Fossier Ill, and Le Gouaz Yves-Marie. Memoires sur l'electricite et le magnetisme. *Academie royale des sciences (France)*, 1789. (Quoted in pages ix, 9 et 10.)

[2] Wulf T. ber die in der atmosphäre vorhandene strahlung von hoher durchdringungsfähigkeit. *Physikalische Zeitschrschift 152-157*, 10, 1909. (Quoted in pages ix et 11.)

[3] CERN courier. Domenico pacini and the origin of cosmic rays. 2012. (Quoted in pages ix, 11 et 12.)

[4] Taken from American Physical Society Sites. 1912: Victor hess's balloon flight during total eclipse to measure cosmic rays. *Springer-Verlag Berlin Heidelberg DOI 10.1007/978-3-642-28371-0 1*, 19, 2010. (Quoted in pages ix et 12.)

[5] Deutsches Elektronen-Synchrotron DESY A Research Centre of the Helmholtz Association Hamburg location Notkestrasse. 100 years of cosmic rays. (Quoted in pages ix et 12.)

[6] Hess V.F. ber beobachtungen der durchdringenden strahlung bei sieben freiballonfahrten. *Physikalische Zeitschrift*, 13, 1912. (Quoted in pages ix et 13.)

[7] Kolhörster W. Messungen der durchdringenden strahlung im freiballon in größeren höhen. *Physikalische Zeitschrift 1153-1156*, 14, 1913. (Quoted in pages ix et 13.)

[8] Kolhörster W. Messungen der durchdringenden strahlung bis in höhen von 9300 m. *Verhandlungen der Deutschen Physikalischen Gesellschaft*, 16, 1914. (Quoted in pages ix et 13.)

[9] Fick H. D. and Hoffmann D. Werner kolhˆrster (1887ñ1945): the german pioneer of cosmic ray physics. *Astroparticle physics 50-54*, 53, 2014. (Quoted in pages ix et 13.)

[10] Compton A.H. and Turner R.N. *Phys. Rev. p.799*, 52, 1937. (Quoted in pages ix et 14.)

[11] Anderson C.D. *Physical Review p.491*, 43, 1933. (Quoted in pages ix et 15.)

[12] Institut de Mecanique Celeste et de calcul des Ephemerides. Histoire de l'observatoire du pic du midi. (Quoted in pages ix et 17.)

[13] CERN courier. The discovery of air-cherenkov radiation. 2012. (Quoted in pages ix et 20.)

[14] FERMILAB. *Physical Review Letters p.146*, 10, 1984. (Quoted in pages ix, 22, 23 et 100.)

[15] The Telescope Array Project Website. Cosmic ray history section - "the fly's eye (1981-1993). *http://www.telescopearray.org*. (Quoted in pages ix et 25.)

[16] Bird D. J., Corbato S. C., Dai H. Y., Elbert J. W., Green K. D., and Huang M. A. Detection of a cosmic ray with measured energy well beyond the expected spectral cutoff due to cosmic microwave radiation. *Astrophys. J.*, 441, 1995. (Quoted in pages x et 26.)

[17] Bird D.J., Corbato S.C., Dai H. Y., Dawson B.R., Elbert J.W., Emerson B.L., Green K.D., Huang M.A., Kieda D.B., Luo M., Ko S., Larsen C.G., Loh E. C., Salamon M.H., Smith J.D., Sokolsky P., Sommers P., Tang J.K.K., and Thomas S.B. The cosmic-ray energy spectrum observed by the fly's eye. *Astrophysical Journal, Part 1 (ISSN 0004-637X)*, 424, 1993. (Quoted in pages x, 26, 27 et 28.)

[18] Takeda M. et al. Extension of the cosmic-ray energy spectrum beyond the predicted greisen-zatsepin-kuz'min cutoff. *Phys. Rev. Lett. p.1163*, 81, 1998. (Quoted in pages x et 29.)

[19] Sokolskya P. For the HiRes Collaboration. Final results from the high resolution fly's eye (hires) experiment. *Nuclear Physics B (Proc. Suppl.) 74-78*, 212-213, 2011. (Quoted in pages x, 29 et 30.)

[20] Danilo Zavrtanik. Ultra high energy cosmic rays. *Contemporary Physics DOI :10.1080/00107514.2010.502783*, 51, 2010. (Quoted in pages x et 31.)

[21] Sciutto S.J. Aires : A system for air shower simulations (version 2.2.0). *arXiv :astro-ph/9911331v1*, 1999. (Quoted in pages x et 33.)

[22] Pierre Auger Collaboration. The fluorescence detector of the pierre auger observatory pierre auger collaboration. *Nucl.Instrum.Meth. A 227-251*, 620, 2010. (Quoted in pages x, xi, 42, 43, 44 et 45.)

[23] Meurer C. and Scharf N. on behalf of the Pierre Auger Collaboration. Heat - a low energy enhancement of the pierre auger observatory. *Astrophysics and Space Sciences Transactions 183-186*, 7, 2011. (Quoted in pages x et 43.)

[24] Unger M [The Pierre Auger Collaboration]. *arXiv:0706.1495 [astro-ph]*, 2007. (Quoted in pages x et 44.)

[25] Karl-Heinz et al. Extensive air showers and ultra high-energy cosmic rays: A historical review. *Eur.Phys.J. H37 359-412*, 2012. (Quoted in pages xi et 45.)

[26] Yves A. Gallant. Particle acceleration at relativistic shocks. *arXiv:astro-ph/0201243v1*, 202. (Quoted in pages xi, 49 et 50.)

[27] Aguilar J.A. Cosmic rays. *Particle Astrophysics Lecture 3 UniversitÈ libre de Bruxelles*. (Quoted in pages xi et 51.)

[28] Jui Charles. Summary of results from the telescope array experiment. *Proceedings of the 34th International Cosmic Ray Conference Highlight paper*, 2015. (Quoted in pages xi, 52, 54 et 57.)

[29] Piera Luisa Ghia. Highlights from the pierre auger observatory. *Proceedings of the 34th International Cosmic Ray Conference Highlight paper*, 2015. (Quoted in pages xi, 53, 55 et 56.)

[30] R. Krause for The Pierre Auger Collaboration. Detection of high-energy cosmic rays with the auger engineering radio array. *Proceedings of the Vienna Conference on Instrumentation, to be published in NIM A*, 2016. (Quoted in pages xi et 64.)

[31] John Kelley Stefan Fliescher Lars Mohrmann Martin Erd-mann Anna Nelles, Klaus Weidenhaupt and Jörg Hörandel. A survey of narrowband and broadband radio-frequency interference at aera. *Internal Auger Note*, 2011. (Quoted in pages xii, 70 et 71.)

[32] The Pierre Auger Collaboration. Measurement of the radiation energy in the radio signal of extensive air showers as a universal estimator of cosmic-ray energy. *Physical Review Letters*, 116, 2016. (Quoted in pages xii, xiii, 72, 73 et 75.)

[33] C. Glaser and the Pierre Auger Collaboration. Energy estimation of cosmic rays with the engineering radio array of the pierre auger observatory. *Physical Review D*, 93, 2016. (Quoted in pages xii, xiii, 72, 73, 74 et 75.)

[34] LOPES Collaboration. Radio detection of cosmic rays with lopes. *Brazilian Journal of Physics*, 36, 2006. (Quoted in pages xii et 73.)

[35] B. Revenu. Overview of mhz air shower radio experiments and results. *ARENA conference*, 2012. (Quoted in pages xii et 73.)

[36] The LOPES Collaboration. Experimental evidence for the sensitivity of the air-shower radio signal to the longitudinal shower development. *Physical Review D*, 85, 2012. (Quoted in pages xiii, 75 et 76.)

[37] The CODALEMA Collaboration. Geomagnetic origin of the radio emission from cosmic ray induced air showers observed by codalema. *Astroparticle Physics*, 31, 2009. (Quoted in pages xiii et 79.)

[38] A. Lecacheux V. Marin L. Martin B. Revenu-D. Torres A. Bellétoile, R. Dallier. Evidence for the charge-excess contribution in air shower radio emission observed by the codalema experiment. *Astroparticle Physics*, 69, 2015. (Quoted in pages xiii, 81 et 82.)

[39] The Pierre Auger Collaboration. Probing the radio emission from air showers with polarization measurements. *Physical Review D*, 89, 2014. (Quoted in pages xiii, 82, 83 et 84.)

[40] Bradt H.L. and Peters B. The heavy nuclei of the primary cosmic radiation. *Physical Review p.54*, 77, 1950. (Quoted in pages xxi et 17.)

[41] Ressource linguistique du Centre National de Ressources Textuelles et Lexicales. Disponible en ligne via http://www.cnrtl.fr/etymologie/ion. *Centre National de La Recherche Scientifique*, 2005. (Quoted in page 10.)

[42] Michael Faraday. Experimental researches in electricity. *London*, 2, 1844. (Quoted in page 10.)

[43] William Crookes. On electrical insulation in high vacua. *Proc. Roy. Soc. of London 347-352*, 28, 1879. (Quoted in page 10.)

[44] Becquerel H. sur les radiations emises par phosphorescence. *Compte-rendu de l'academie des sciences 420-421*, 1896. (Quoted in page 10.)

[45] Becquerel H. sur les radiations invisibles emises par les corps phosphorescents. *Compte-rendu de l'academie des sciences 501-502*, 1896. (Quoted in page 10.)

[46] Pierre Curie, Marie Curie, and Gustave Bemont. Sur une nouvelle substance fortement radioactive contenue dans la pechblende. *Compte-rendu de l'academie des sciences 1215-1217*, 127, 1898. (Quoted in page 10.)

[47] Nobel Prize in Physics. in recognition of the extraordinary services they have rendered by their joint researches on the radiation phenomena discovered by professor henri becquerel. *Fondation Nobel*, 1903. (Quoted in page 10.)

[48] William H. Cropper. Great physicists: The life and times of leading physicists from galileo to hawking. *Oxford University Press p.299*, 2001. (Quoted in page 10.)

[49] Wilson C.T.R. On the leakage of electricity through dust-free air. *Proc. Cambridge Philos. Soc. p.32*, 11, 1900. (Quoted in page 10.)

[50] Elster J. and Geitel H. ber die existenz electrischer ionen in der atmosphere (on the existence of electrical ions in the atmosphere). *Terr. Magn. Atmos. Electr. 212-234*, 4, 1899. (Quoted in page 10.)

[51] Wilson C.T.R. On the ionisation of atmospheric air. *Proc. R. Soc. London doi:10.1098/rspl.1901.0032*, 68, 1901. (Quoted in page 10.)

[52] Wulf T. *Physikalische Zeitschrschift p.251*, 8, 1909. (Quoted in page 10.)

[53] Wulf T. *Physikalische Zeitschrschift p.811*, 11, 1910. (Quoted in page 10.)

[54] De Angelis A., Giglietto N., and Stramaglia S. Domenico pacini, the forgotten pioneer of the discovery of cosmic rays. *ArXiv preprint arXiv:1002.2888v2 [physics.hist-ph]*, 2010. (Quoted in page 12.)

[55] Bertolotti M. Celestial messengers: Cosmic rays, astronomers universe. *Springer-Verlag Berlin Heidelberg DOI 10.1007/978-3-642-28371-0 1*, 1, 2013. (Quoted in page 12.)

[56] John A. Simpson. The cosmic radiation. *The century of space science 117-151*, 2001. (Quoted in page 13.)

[57] Yataro Sekido and Harry Elliot. Early history of cosmic ray studies: Personal reminiscences with old photographs. *Science 77-78*, 2012. (Quoted in page 13.)

[58] Millikan R.A. and Harvey Cameron G. High frequency rays of cosmic origin iii. measurements in snow-fed lakes at high altitudes. *Phys. Rev. p.851*, 28, 1926. (Quoted in page 13.)

[59] Clay J. Penetrating radiation. *Proceedings of the Section of Sciences, Koninklijke Akademie van Wetenschappen te Amsterdam 9-10*, 30, 1927. (Quoted in page 14.)

[60] Clay J. Penetrating radiation ii. *Proc. R. Acad. Amsterdam 1091-1097*, 31, 1928. (Quoted in page 14.)

[61] Clay J. Ultra radiation (penetrating radiation) iii: Annual variation and variation with the geographical latitude. *Proc. R. Acad. Amsterdam 711-718*, 33, 1930. (Quoted in page 14.)

[62] Clay J. and Berlage H.P. Variation der ultrastralung mit der geographischen breite und dem erdmagnetismus. *Naturwissenschaften doi:10.1007/BF01494405*, 20, 1932. (Quoted in page 14.)

[63] Compton A.H. Variation of the cosmic rays with latitude. *Phys. Rev. doi:10.1103/PhysRev.41.111.2*, 43, 1932. (Quoted in page 14.)

[64] Compton A.H. A geographic study of cosmic rays. *Phys. Rev. doi:10.1103/PhysRev.43.387*, 43, 1933. (Quoted in page 14.)

[65] The Nobel Prize in Physics. divided equally between arthur holly compton "for his discovery of the effect named after him" and charles thomson rees wilson "for his method of making the paths of electrically charged particles visible by condensation of vapour". 1927. (Quoted in page 15.)

[66] Dirac P.A.M. *Proceedings of the Royal Society of London A p.60*, 133, 1931. (Quoted in page 15.)

[67] Rossi B. *Physical Review p.212*, 45, 1934. (Quoted in page 16.)

[68] Rossi Bruno. Cosmic rays. *McGraw-Hill Book Company Inc.*, 1964. (Quoted in page 16.)

[69] Auger Pierre. Extensive cosmic-ray showers. *Review of Modern Physics p.288*, 11, 1939. (Quoted in page 16.)

[70] Schein Marcel, Jesse W.P., and Wollan E.O. The nature of the primary cosmic radiation and the origin of the mesotron. *Physical Review p.615*, 59, 1941. (Quoted in page 17.)

[71] Schein Marcel, Jesse W.P., and Wollan E.O. Intensity and rate of production of mesotrons in the stratosphere. *Physical Review p.847*, 57, 1940. (Quoted in page 17.)

[72] Fermi E. On the origin of the cosmic radiation. *Physical Review 1169-1174*, 75, 1949. (Quoted in page 17.)

[73] Parizot E. Acceleration des particules: les mecanismes de fermi physique et astrophysique du rayonnement cosmique. *Ecole CNRS de Goutelas XXVI*, 2003. (Quoted in page 18.)

[74] Webb G.M. First order and second order fermi acceleration of energetic charged particles by shock waves. *Astrophysical Journal 319-338*, 270, 1983. (Quoted in page 20.)

[75] Blackett P.M.S. *Physical Society of London Gassiot Committee Report 34-35*, 34, 1948. (Quoted in page 20.)

[76] Galbraith W. and Jelley J.V. Light pulses from the night sky associated with cosmic rays. *Nature 349-50*, 171, 1953. (Quoted in pages 21 et 60.)

[77] Galbraith W. and Jelley J.V. *J. Atmos. Terr. Physics p.250*, 6, 1955. (Quoted in page 21.)

[78] Galbraith W. and Jelley J.V. *J. Atmos. Terr. Physics p.304*, 6, 1955. (Quoted in page 21.)

[79] Rossi Bruno Benedetto. Moments in the life of a scientist. *Cambridge University Press p.99*, ISBN 978-0-521-36439-3, 1990. (Quoted in page 21.)

[80] CLARK G., EARL J., KRAUSHAAR W., LINSLEY J., ROSSI B., and SCHERB F. An experiment on air showers produced by high-energy cosmic rays. *Nature doi:10.1038/180353a0*, 180, 1957. (Quoted in page 21.)

[81] FERMILAB. Fermilab history and archives project. *Available online http://history.fnal.gov/index.html*. (Quoted in page 22.)

[82] Hillas A.M. *Ann. Rev. Astron. Astrophys. 425-44*, 22, 1984. (Quoted in page 22.)

[83] Penzias A.A. and Wilson R.W. A measurement of excess antenna temperature at 4080 mc/s. *Astrophys. Journal p.419*, 142, 1965. (Quoted in page 22.)

[84] Greisen K. *Proc. 9th ICRC, London, p.609*, 2, 1966. (Quoted in page 22.)

[85] Zatsepin G.T. and Kuzmin V.A. Upper limit of the spectrum of cosmic rays. *JETP Lett. p.78*, 4, 1966. (Quoted in page 22.)

[86] Charles C. H. Jui, HiRes Collaboration, and TA Collaboration. Air fluorescence calorimetry with the high resolution fly's eye and telescope array experiments. *AIP Conf. Proc. http://dx.doi.org/10.1063/1.2396953*, 867, 2006. (Quoted in page 24.)

[87] The University of Utah. The energy spectrum of ultra high energy cosmic rays measured by the high resolution fly's eye observatory in stereoscopic mode. *ProQuest p.333*, 2008. (Quoted in page 26.)

[88] Chiba N. et al. Akeno giant air shower array (agasa) covering 100 km2 area. *Nucl. Instr. Methods A 338-349*, 311, 1992. (Quoted in page 29.)

[89] Gaisser T.K. and Hillas A.M. *Proceedings of the 15th ICRC*, 1977. (Quoted in pages 34 et 44.)

[90] Catalano O. et al. *Proc. of 27th ICRC, Hamburg (Germany) p.498*, 2001, 2001. (Quoted in page 34.)

[91] Rossi B. and Greisen K. Cosmic-ray theory. *Reviews of Modern Physics 13, 240-309*, 13, 1941. (Quoted in page 34.)

[92] Allan H.R. et al. *Nature p. 635*, 222, 1969. (Quoted in page 34.)

[93] Kamata K. and Nishimura J. The lateral and the angular structure functions of electron showers. *Progress of Theoretical Physics Supplement, 6 : 93-155*, 1958. (Quoted in page 35.)

[94] Sergey Ostapchenko. Status of qgsjet. *arXiv:0706.3784*, 2007. (Quoted in pages 37 et 86.)

[95] Pierog T. and Werner K. Model and ultra high energy cosmic rays. *arXiv:0905.1198*, 2009. (Quoted in pages 37 et 87.)

[96] Ranchon S. Etude des collisions atmospheriques de rayons cosmiques d'energie superieure ‡ 1 eev grace aux evenements hybrides de l'observatoire pierre auger. *ThËse de doctorat*, 2005. (Quoted in page 39.)

[97] Apel W.D. et al. *NIMA 11-21*, 620, 2010. (Quoted in page 40.)

[98] Kleifges M. for the Pierre Auger Collaboration. Extension of the pierre auger observatory using high-elevation fluorescence telescopes (heat). *Proc. of the 31st icrc*, 2009. (Quoted in page 42.)

[99] Sommers P. Capabilities of a giant hybrid air shower detector. *Astropart. Phys. 3, 349-360*, 4, 1995. (Quoted in page 44.)

[100] Bonifazi C. Pierre Auger Collaboration. Fermilab-conf-05-301-e-td. *Proceedings of the 29th ICRC*, 2005. (Quoted in page 44.)

[101] Giller M., Wieczorek G., Kacperczyk A., Stojek H., and Tkaczyk W. *J. Phys. G*, 30, 2004. (Quoted in page 44.)

[102] Nerling F., Bluemer J., Engel R., and Risse M. *Astropart. Phys. arXiv:astro-ph/0506729*, 24, 2006. (Quoted in page 44.)

[103] Roberts M.D. *J. Phys. G p.1291*, 31, 2005. (Quoted in page 44.)

[104] Pekala J. et al. *Nucl. Instr. and Meth. A p.388*, 605, 2009. (Quoted in page 44.)

[105] Nagano M. et al. *Astropart. Phys. p.235*, 22, 2004. (Quoted in page 44.)

[106] Ave M. et al. AIRFLY Collaboration. *Nucl. Instr. and Meth. A p.50*, 597, 2008. (Quoted in page 44.)

[107] Ave M. et al. AIRFLY Collaboration. *Nucl. Instr. and Meth. A p.46*, 597, 2008. (Quoted in page 44.)

[108] Gora D. et al. *Astropart. Phys. p.484*, 24, 2006. (Quoted in page 44.)

[109] Roth M. for the Pierre Auger Collaboration. The lateral distribution function of shower signals in the surface detector of the pierre auger observatory. *Proc. of the 28th icrc. Tsukuba, Japan*, 2003. (Quoted in page 46.)

[110] Newton D. et al. The optimum distance at which to determine the size of a giant air shower. *Astropart. Phys. 26 414-419*, 6, 2007. (Quoted in page 46.)

[111] A. R. Bell. The acceleration of cosmic rays in shock fronts. i. *Royal Astronomical Society, Monthly Notices*, 182, 1978. (Quoted in page 49.)

[112] Abraham J. et al. *Science p.398*, 318, 2008. (Quoted in page 53.)

[113] Askaryan G.A. *J. Exp. Theor. Phys. P. 658*, 21, 1962. (Quoted in pages 60 et 79.)

[114] J. V. Jelley et al. Radio pulses from extensive air showers. *Nature*, 205, 1965. (Quoted in page 60.)

[115] H.R. Allan. *Nature*, 212, 1965. (Quoted in page 60.)

[116] Kahn F.D. and Lerche I. Radiation from cosmic-ray air showers. *Proceedings of the royal society of london series a-mathematical and physical sciences*, 289 (1417), 1966. (Quoted in pages 60 et 78.)

[117] H. R. ALLAN. Radio emission from extensive air showers, progress in elementary particle and cosmic ray physics. *Progress in Elementary Particle and Cosmic Ray Physics.*, 10, 1971. (Quoted in page 60.)

[118] D. Ardouin et al. (CODALEMA collaboration). Radio-detection signature of high energy cosmic rays by the codalema experiment. *Nucl. Inst. Meth., Section A*, 555, 2005. (Quoted in pages 61 et 67.)

[119] et al. LOPES Collaboration H.Falcke. *Nature*, 435, 2005. (Quoted in page 61.)

[120] J. Schulz for the Pierre Auger Collaboration. A survey of narrowband and broadband radio-frequency interference at aera. *Proc. of the 34th ICRC, The Hague, The Netherlands, PoS(ICRC2015) 615*, 2015. (Quoted in page 61.)

[121] The Pierre Auger Collaboration. Antennas for the detection of radio emission pulses from cosmic-ray induced air showers at the pierre auger observatory. *JINST*, 7, 2012. (Quoted in page 62.)

[122] G Arfken. Convolution theorem. *Mathematical Methods for Physicists, 3rd ed. Orlando, FL: Academic Press*, 1985. (Quoted in page 63.)

[123] C. Timmermanns and J. Kelley. Calibration of the aera phase i digitizer. *Internal note of the Pierre Auger Collaboration, GAP-2011-028*, 2011. (Quoted in page 64.)

[124] Nec2++. *http://elec.otago.ac.nz/w/index.php/Necpp.* (Quoted in page 65.)

[125] The Pierre Auger Collaboration. Nanosecond-level time synchronization of autonomous radio detector stations for extensive air showers. *JINST*, 11, 2016. (Quoted in page 65.)

[126] D. Ardouin et al. (CODALEMA collaboration). Features of radio-detected extensive air shower observed with the detector codalema. *Astropart. Phys. p. 341-350*, 26, 2006. (Quoted in page 67.)

[127] nelles et al. *Astropart. Phys*, 60, 2015. (Quoted in page 72.)

[128] The Pierre Auger Collaboration. Results of a self-triggered prototype system for radio-detection of extensive air showers at the pierre auger observatory. *JINST*, 2012. (Quoted in page 73.)

[129] C. Glaser and the Pierre Auger Collaboration. Energy estimation for cosmic rays measured with the auger engineering radio array. *ARENA conference*, 2012. (Quoted in page 73.)

[130] W. D. Apel et al. KASCADE-Grande Collaboration. *Astroparticle Physics*, 34, 2011. (Quoted in page 76.)

[131] J. Zabierowski et al. KASCADE-Grande Collaboration. *Proceedings of the 31st ICRC*, 2009. (Quoted in page 76.)

[132] J. Zabierowski et al. KASCADE-Grande Collaboration. *Proceedings of the 32nd ICRC*, 2011. (Quoted in page 76.)

[133] S. Buitink and H. Falcke J.R. Hörandel T. Huege A. Nelles-J.P. Rachen P. Schellart O. Scholten S. ter Veen S. Thoudam T.N.G. Trinh A. Corstanje, J.E. Enriquez. Method for high precision reconstruction of air shower xmax using two-dimensional radio intensity profiles. *Physical Review D*, 90, 2014. (Quoted in page 76.)

[134] P.A. Bezyazeekov, et al. - Tunka-Rex Coll. Radio measurements of the energy and depth of maximum of cosmic-ray air showers by Tunka-Rex. *JCAP*, 01:052, 2016. (Quoted in page 76.)

[135] W.D. Apel, et al. - LOPES Coll. The wavefront of the radio signal emitted by cosmic ray air showers. *JCAP*, 09:025, 2014. (Quoted in page 76.)

[136] S. Grebe et al. -Pierre Auger Coll. Spectral index analysis of the data from the Auger Engineering Radio Array. *AIP Conference Proceedings*, 1535:73–77, 2013. (Quoted in page 76.)

[137] Kaidalov A.B. and Ter-Martirosyan K.A. *Sov. J. Nucl. Phys. p. 979*, 39, 1984. (Quoted in page 86.)

[138] Engel R., Gaisser T.K., Lipari P., and Stanev T. *Proc. of 26-th Int. Cosmic Ray Conf. (Salt Lake City) p. 415*, 1, 1999. (Quoted in page 86.)

[139] Gaisser T.K. and Halzen F. *Phys. Rev. Lett. p. 1754*, 54, 1985. (Quoted in page 86.)

[140] Ostapchenko S. High energy cosmic ray interactions - an overview. *Journal of Physics: Conference Series*, 60, 2007. (Quoted in page 87.)

[141] B Revenu V. Marin. Simulation of radio emission from cosmic ray air shower with selfas2. *Astroparticle Physics*, 35, 2012. (Quoted in pages 87 et 88.)

[142] T. Bergmann et al. One-dimensional hybrid approach to extensive air shower simulation. *Astropart. Phys*, 26:420–432, 2007. (Quoted in page 87.)

[143] H. Falcke J. Horandel T. Huege J. Kuijpers S. Lafebre, R. Engel and R. Ulrich. Universality of electron positron distributions in extensive air showers. *Astroparticle Physics*, 31, 2009. (Quoted in page 87.)

[144] K. Werner and O. Scholten. Macroscopic treatment of radio emission from cosmic ray air showers based on shower simulations. *Astroparticle Physics*, 29, 2008. (Quoted in pages 90 et 147.)

[145] K. D. de Vries K. Werner and O. Scholten. Radio emission from cosmic ray air showers based on shower simulations : On the importance of a realistic atmos- pheric index of refraction. *submitted to Astroparticle Physics, 2012. arXiv :1201.4471v1*, 2012. (Quoted in page 90.)

[146] M.Ludwig and T.Huege. Reas3:a revised implementation of the geosynchrotron model for radio emission from air showers. *Nuclear Instruments and Methods in Physics Research Section A : Accelerators, Spectrometers, Detectors and Associated Equipment.*, 2010. (Quoted in page 90.)

[147] W. R. Carvalho Jr J. Alvarez Muniz and E. Zas. Monte carlo simulations of radio pulses in atmospheric showers using zhaires. *Astroparticle Physics*, 35, 2012. (Quoted in page 90.)

[148] F. Halzen E. Zas and T. Stanev. Electromagnetic pulses from high-energy showers : Implications for neutrino detection. *Phys. Rev. D*, 45, 1992. (Quoted in page 90.)

[149] B Rossi and K Greisen. Cosmic-ray theory. *Reviews of Modern Physics*, 4, 1941. (Quoted in page 94.)

[150] John David Jackson. Classical electrodynamics. *chapter 6.3*. (Quoted in page 94.)

[151] US Standard atmosphere. 1976. (Quoted in page 100.)

[152] The CODALEMA collaboration. Geomagnetic origin of the radio emission from cosmic ray induced air showers observed by codalema. *Astropart. Phys.*, 31, 2009. (Quoted in page 117.)

[153] Alessio Porcelli. Measurement of the depth of shower maximum in the transition region between galactic and extragalactic cosmic rays with the pierre auger observatory. *PhD thesis*, 2014. (Quoted in page 127.)

[154] A. L Buck. *Buck Research CR-1A User's Manual, Appendix 1.*, 1996. (Quoted in page 144.)

[155] A. L Buck. New equations for computing vapor pressure and enhancement factor. *J. Appl. Meteorol. 20: 1527–1532*, 1981. (Quoted in page 144.)

[156] Us standard atmosphere 1976. 1976. (Quoted in page 144.)

[157] *http://www.digitaldutch.com/atmoscalc/table.htm*, 1976. (Quoted in page 144.)

[158] Wolfgang Merzkirch. *Table (3.1) in Flow Visualization, Second Edition*. (Quoted in page 148.)

[159] N. C. Gerson. Variation in the index of refraction in the atmosphere. (Quoted in page 148.)

[160] L. Freeman. *formula (1.14) in Radio System Design for Telecommunications, Third Edition*. (Quoted in page 148.)

[161] NOAA. *GDAS Archive Information http://ready.arl.noaa.gov/gdas1.php*. (Quoted in page 177.)

UNIVERSITE BRETAGNE LOIRE

MINES Nantes

Thèse de Doctorat

Florian GATÉ

Estimation of the composition of cosmic rays using the radio signal

Estimation de la composition des rayons cosmiques avec le signal radio émis par les gerbes

Résumé

Plus d'un siècle après leur découverte, les rayons cosmiques continuent d'intriguer les physiciens. Le flux de ces particules d'origine extraterrestre décroît fortement en fonction de leur énergie. Au-delà de 1 PeV (10^{15} eV), le flux devient trop faible pour permettre la détection directe sur des échelles de temps raisonnables. Cependant, les cascades de particules secondaires créées après l'interaction des rayons cosmiques avec les constituants de l'atmosphère sont détectables depuis le sol, c'est la détection indirecte. A partir de 100 PeV, le nombre d'observations est trop faible pour estimer de manière précise la masse des rayons cosmiques et ainsi contraindre les modèles de mécanismes d'accélération, de propagation et de type de sources. La détermination de la composition est effectuée à l'Observatoire Pierre Auger par les télescopes de fluorescence via la mesure de la variable X_{max} avec un cycle utile de 14%. X_{max} est la profondeur d'atmosphère traversée à laquelle le nombre de particules secondaires atteint sa valeur maximale. Cette observable est fortement corrélée à la masse du rayon cosmique qui a initié la gerbe. Un grand nombre d'observations est requis pour effectuer une détermination précise de la masse car les fluctuations statistiques de X_{max} sont importantes. La radio détection apparaît alors comme une excellente alternative à la détection par fluorescence, puisque la technique mesurant ce signal a un cycle utile proche de 100%. Cette thèse propose une méthode d'estimation de la masse des rayons cosmiques d'ultra haute énergie basée seulement sur l'étude des signaux radio et leur simulation, afin de reconstruire de manière systématique l'énergie, le cœur et la profondeur X_{max} des gerbes détectées par l'expérience AERA sur le site de l'Observatoire Pierre Auger. L'influence de la modélisation de l'atmosphère dans le code de simulation SELFAS sur les valeurs reconstruites est étudiée. Notamment la géométrie des couches atmosphériques, la manière de traiter l'indice de réfraction et la densité de l'air ainsi que leurs variations journalières et saisonnières.

Mots clés
rayons cosmiques, gerbes atmosphériques, radio détection, composition en masse

Abstract

More than a century after their discovery, cosmic-rays are still puzzling physicists. The flux of these particles coming from extraterrestrial sources strongly decreases as a function of their energy. Above 1 PeV (10^{15} eV), the particle flux becomes too low to allow a direct detection on a reasonable time scale. However, the cascades of secondary particles produced after the interaction of cosmic-rays with the constituents of the atmosphere are detectable at the ground level; it is the indirect detection. Above 100 PeV, the number of observations is too low to accurately estimate the mass of the cosmic rays and then to constrain the prediction models of acceleration mechanisms, propagation and type of sources. The determination of their composition is achieved at the Pierre Auger Observatory using fluorescence telescopes from the measurement of the X_{max} observable with a duty cycle of 14%. X_{max}, defined as the atmosphere depth at which the number of secondary particles reaches its maximal value, is highly correlated to the mass of the cosmic ray that has created the air shower. A large number of observations is required for a precise estimation of the mass as the X_{max} statistical fluctuations are important. The radio detection is a perfect alternative to the fluorescence method as the duty cycle of a typical radio detector is close to 100%. This thesis proposes a method to estimate the mass of ultra-high energy cosmic rays using only the radio signals and their simulation. The goal is to systematically reconstruct the X_{max} depth of each air shower detected by the AERA experiment within the site of the Pierre Auger Observatory in Argentina. The influence of the description of the atmosphere on the reconstructed shower parameters, in the SELFAS code, has been studied. It includes the geometry of the atmospheric layers, the way to calculate the air refractive index and density, as well as their daily and seasonal fluctuations.

Key Words
cosmic rays, air showers, radio detection, mass composition